



UNIVERSITAT DE
BARCELONA

Functional connectivity at multiple scales: From neuronal cultures to human brain

Marc Montalà Flaquer

ADVERTIMENT. La consulta d'aquesta tesi queda condicionada a l'acceptació de les següents condicions d'ús: La difusió d'aquesta tesi per mitjà del servei TDX (www.tdx.cat) i a través del Dipòsit Digital de la UB (diposit.ub.edu) ha estat autoritzada pels titulars dels drets de propietat intel·lectual únicament per a usos privats emmarcats en activitats d'investigació i docència. No s'autoritza la seva reproducció amb finalitats de lucre ni la seva difusió i posada a disposició des d'un lloc aliè al servei TDX ni al Dipòsit Digital de la UB. No s'autoritza la presentació del seu contingut en una finestra o marc aliè a TDX o al Dipòsit Digital de la UB (framing). Aquesta reserva de drets afecta tant al resum de presentació de la tesi com als seus continguts. En la utilització o cita de parts de la tesi és obligat indicar el nom de la persona autora.

ADVERTENCIA. La consulta de esta tesis queda condicionada a la aceptación de las siguientes condiciones de uso: La difusión de esta tesis por medio del servicio TDR (www.tdx.cat) y a través del Repositorio Digital de la UB (diposit.ub.edu) ha sido autorizada por los titulares de los derechos de propiedad intelectual únicamente para usos privados enmarcados en actividades de investigación y docencia. No se autoriza su reproducción con finalidades de lucro ni su difusión y puesta a disposición desde un sitio ajeno al servicio TDR o al Repositorio Digital de la UB. No se autoriza la presentación de su contenido en una ventana o marco ajeno a TDR o al Repositorio Digital de la UB (framing). Esta reserva de derechos afecta tanto al resumen de presentación de la tesis como a sus contenidos. En la utilización o cita de partes de la tesis es obligado indicar el nombre de la persona autora.

WARNING. On having consulted this thesis you're accepting the following use conditions: Spreading this thesis by the TDX (www.tdx.cat) service and by the UB Digital Repository (diposit.ub.edu) has been authorized by the titular of the intellectual property rights only for private uses placed in investigation and teaching activities. Reproduction with lucrative aims is not authorized nor its spreading and availability from a site foreign to the TDX service or to the UB Digital Repository. Introducing its content in a window or frame foreign to the TDX service or to the UB Digital Repository is not authorized (framing). Those rights affect to the presentation summary of the thesis as well as to its contents. In the using or citation of parts of the thesis it's obliged to indicate the name of the author.

Functional connectivity at multiple scales: From neuronal cultures to human brain



**UNIVERSITAT DE
BARCELONA**

Marc Montalà Flaquer

Departament de Física de la Matèria Condensada
Departament de Psicologia Social i Psicologia Quantitativa
Universitat de Barcelona

PhD Advisors

Joan Guàrdia Olmos, Jordi Soriano Fradera

Tutor

Joan Guàrdia Olmos

Programa de Doctorat en Biomedicina

Desembre 2023

The experimental work exposed in this Doctoral Thesis has been funded by the "Ministerio de Ciencia, Innovación y Universidades" under the Project PGC2018-095829-B-I00, the "Ministerio de Economía y Competitividad" under the project PID2019-108842GB-C21 and the "Conselleria de Recerca i Universitats" of the Generalitat de Catalunya under the Projects 2017-SGR-1061 and 2021SGR 366.

Marc Montalà Flaquer was granted the APIF scholarship "*Ajuts de Personal Investigador en Formació*" from the University of Barcelona. The results from this thesis have yielded the following scientific publications:

List of publications

- Farras-Permanyer, L., Mancho-Fora, N., Montalà-Flaquer, M., Bartrés-Faz, D., Vaqué-Alcázar, L., Peró-Cebollero, M., and Guàrdia-Olmos, J. (2019). Age-related changes in resting-state functional connectivity in older adults. *Neural regeneration research*, 14(9):1544
- Farràs-Permanyer, L., Mancho-Fora, N., Montalà-Flaquer, M., Gudayol-Ferré, E., Gallardo-Moreno, G. B., Zarabozo-Hurtado, D., Villuendas-González, E., Peró-Cebollero, M., and Guàrdia-Olmos, J. (2019). Estimation of brain functional connectivity in patients with mild cognitive impairment. *Brain Sciences*, 9(12):350
- Pedersini, C. A., Guàrdia-Olmos, J., Montalà-Flaquer, M., Cardobi, N., Sanchez-Lopez, J., Parisi, G., Savazzi, S., and Marzi, C. A. (2020). Functional interactions in patients with hemianopia: A graph theory-based connectivity study of resting fmri signal. *PLoS one*, 15(1):e0226816
- Mancho-Fora, N., Montalà-Flaquer, M., Farràs-Permanyer, L., Bartrés-Faz, D., Vaqué-Alcázar, L., Peró-Cebollero, M., and Guàrdia-Olmos, J. (2020b). Resting-state functional connectivity dynamics in healthy aging: An approach through network change point detection. *Brain Connectivity*, 10(3):134–142
- Mancho-Fora, N., Montalà Flaquer, M., Farràs Permanyer, L., Bartrés Faz, D., Vaqué Alcázar, L., Peró, M., and Guàrdia Olmos, J. (2020a). Resting-state functional dynamic connectivity and healthy aging: A sliding-window network analysis. *Psicothema*, 2020, vol. 32, num. 3, p. 337-345

- Mancho-Fora, N., Montalà-Flaquer, M., Farràs-Permanyer, L., Zarabozo-Hurtado, D., Gallardo-Moreno, G. B., Gudayol-Farré, E., Peró-Cebollero, M., and Guàrdia-Olmos, J. (2020c). Network change point detection in resting-state functional connectivity dynamics of mild cognitive impairment patients. *International Journal of Clinical and Health Psychology*, 20(3):200–212
- Ayasreh, S., Jurado, I., López-León, C. F., Montalà-Flaquer, M., and Soriano, J. (2022). Dynamic and functional alterations of neuronal networks in vitro upon physical damage: A proof of concept. *Micromachines*, 13(12):2259
- Montalà-Flaquer, M., López-León, C. F., Tornero, D., Houben, A. M., Fardet, T., Monceau, P., Bottani, S., and Soriano, J. (2022). Rich dynamics and functional organization on topographically designed neuronal networks in vitro. *IScience*, 25(12):105680
- Montalà-Flaquer, M., Cañete-Massé, C., Vaqué-Alcázar, L., Bartrés-Faz, D., Peró-Cebollero, M., and Guàrdia-Olmos, J. (2023). Spontaneous brain activity in healthy aging: An overview through fluctuations and regional homogeneity. *Frontiers in aging neuroscience*, 14:1002811
- Clara F. López Leon, Akke Mats Houben, Marc Montalà-Flaquer, Mireia Olivares, Anna Christina Haeb and Jordi Soriano (2023). Emergent complex Dynamics in neuronal cultures and its relation to neuroengineering and medicine. *Nonlinear Dynamics* (**In press**, Book chapter)
- Montalà-Flaquer, M., Cañete-Massé, C., Vaqué-Alcázar, L., Bartrés-Faz, D., Peró-Cebollero, M. and Guàrdia-Olmos, J. Exploring graph analysis thresholding techniques in fMRI: A game of confidence intervals (**In preparation**)

Als meus pares, Lluïsa i Josep, i a la meva àvia, Emília,
per animar-me a mirar sempre més enllà.

"The Force is not a power you have. It's not about lifting rocks. It's the Energy between all things, a tension, a balance that binds the universe together."

–Luke Skywalker

Acknowledgements

Ha arribat el moment de posar el punt final a aquesta tesi. Ha estat un procés llarg i costós, amb obstacles, amb pujades i baixades de vertigen, però alhora molt gratificant. Al llarg d'aquesta etapa m'han acompanyat i ajudat moltes persones, a les quals voldria dedicar unes paraules.

En primer lloc, un especial agraïment als meus directors de tesi, el Dr. Joan Guàrdia i el Dr. Jordi Soriano. Joan, des del dia que vaig entrar a l'aula d'Anàlisi de Senyals i em vas dir que t'interessava molt parlar amb mi vaig veure clar que tenia davant una oportunitat enorme per créixer. M'has ensenyat aquest ofici, la recerca científica i la docència a l'aula. De tu he pogut aprendre moltíssims detalls de com funciona el procés d'ensenyament-aprenentatge i de com s'han d'entendre les regles del joc per a poder prendre decisions encertades. Jordi, mai et podré agrair prou tot el suport que m'has brindat al llarg d'aquests anys, sempre amb un somriure. Ets un exemple de força de voluntat i de constància amb la feina ben feta, ha estat un plaer poder treballar al teu costat i poder compartir discussions científiques al llarg d'aquesta tesi. Gràcies pels teus incansables ànims durant l'etapa final i també per la teva voluntat de mantenir un grup de treball unit que va més enllà de les parets del laboratori.

Voldria fer un especial agraïment, també, a la Maribel. Ha estat meravellós poder compartir amb tu una part d'aquest viatge. La teva entrega amb tot el que fas és total i espero haver-me pogut contagiar una mica de tota la teva força i la determinació que quan es fa una feina s'ha de fer ben feta. Gràcies també a totes les que m'heu acompanyat pel meu pas al "Despatx": Raquel, Silvia, Mar, Oscar, Cristina Mumbardó, Maria Carbó, María Figueroa, Patricia i Sonia. M'heu enriquit molt durant aquests anys i espero que ens continuem trobant cada any com fins ara. Moltes gràcies, Laia i Núria, per acollir-me amb els braços oberts en la meva arribada al grup i per teixir entre totes una amistat que va més enllà de la tesi i de la universitat. Finalment, un gran gràcies a tu, Cristina. Els últims anys has estat un dels meus grans suports i hem pogut treballar plegats d'una manera increïble. Hem compartit molts moments d'anàlisi de dades i de docència, que ens han permès discutir llargues hores tant a la facultat com en virtual. Fer equip amb tu mola molt i crec que hauríem d'instaurar els esmorzars de tonyina amb anxoves.

Aprofito per agrair a totes les persones que formen part del departament de Psicologia Social i Psicologia Quantitativa per fer-me sentir com a casa, per tot el seu suport i tots els bons moments entre passadissos i aules. En especial, un gran gràcies a tu, Pilar, per ser-hi sempre i per buscar les millors solucions quan anava atabalat per fer alguna gestió. Gràcies per la teva calidesa i la teva alegria. El departament no seria el mateix sense tu, i el meu pas per Mundet, tampoc hauria estat el mateix. Un especial gracias a las compis del despacho de becarias investigadoras predoc, en especial a Ana, Belén y Manu. Por compartir tantos momentos, buenos y malos, por darnos apoyo entre nosotras y por convencernos de que nuestras vidas van más allá de nuestras tesis doctorales.

Tampoc hauria pogut assolir aquesta tesi sense les meves companyes de la facultat de Física. Moltes gràcies, Sara, per acollir-me i ensenyar-me com espavilar-me al laboratori. Gràcies també per totes les discussions que vam tenir sobre el funcionament dels cultius, per tots els moments de te i cafè amb el Pacheco i l'Estefanía i per l'acompanyament en el meu pas per l'UBICS. Gràcies, Lluís per instruir-me com a jove *padawan* i iniciar-me en el món dels cultius neuronals i l'anàlisi de senyals.

Estefanía, no sé ni por dónde empezar. Mil gracias por toda la compañía y todo tu apoyo, especialmente cuando las cosas no iban bien. Eres la viva imagen de lo que significa trabajo en equipo y ha sido un auténtico placer compartir estos años a tu lado. Me quedo con nuestras sesiones de creatividad intentando hacer "sándwiches" de neuronas con PDMS y nuestros mensajes de apoyo en la pizarra del Lab.

Clara, ha sido maravilloso tenerte de compañera en esta fase final y siento que entre una cosa y otra he estado más ausente y no hemos coincidido tanto como me hubiera gustado. Tu alegría es desbordante y contagiosa, y me has rescatado de mis momentos de estrés en incontables ocasiones. Mil gracias por mantener el laboratorio funcionando y que no faltara de nada. Me quedo con las infinitas risas el día que intentamos esterilizar puntas en el autoclave y les pusimos un corcho de 'porex' para que no se escaparan de la caja. Eres maravillosa y estoy seguro de que conseguirás todo aquello que te propongas. I want to give special thanks to Akke Houben. Akke, even though we haven't met in person I have learned a lot from your work on numerical simulations, which have provided a great understanding on the network measures hereby described. I hope we can meet very soon and keep sharing our research. Also, I would like to thank Adriaan, Paul and Anna for their contribution during this journey. I wish the best to all of you. No querría olvidarme de todas aquellas personas que han pasado por el grupo de investigación y que han aportado su granito de arena a esta tesis: Gemma, Ruksanda, Berta, Ana, Salem e Imanol.

Un especial agradecimiento al Dr. Daniel Tornero. Dani, muchas gracias por estar siempre dispuesto a ayudar y por aportar toda tu experiencia en la multitud de discusiones

que hemos tenido a lo largo de estos años. Aprofito per agrair a totes les persones que conformen els dos equips de l'Hospital Clínic amb qui hem col·laborat aquests anys i amb qui espero poder mantenir el contacte.

I want to thank Professor Samuel Bottani and all the "*Matières et Systèmes Complexes*" research group at Université de Paris, especially to Dr. Stéphane Métens, Dr. Pascal Monceau and Dr. Mallory Dazza, for having me in my internship and giving me the great opportunity of growing up professionally and personally.

Voldria agrair també al servei d'estabulari de les facultats de Farmàcia i Biologia per tota l'ajuda, el suport i la seva professionalitat. Especialment a la Teresa Calduch i la Marta per la seva cura amb els animals i per garantir que la nostra recerca sigui possible. També vull enviar un agraïment a tot el personal de neteja de les facultats, que es preocupa que les instal·lacions es mantinguin netes i en bon estat sempre amb un somriure i amb paraules amables.

No em puc oblidar de donar les gràcies al meu grup d'amistats de Física. Vam començar plegades un viatge ple d'aventures i vivències. Ple de caps d'any, d'escapades i de dinars i sopars que m'han fet carregar piles. Sou família i fem família cada vegada que ens ajuntem. Mil gràcies especialment a en Sergi, Irene, Adri, Pérez i Popep. L'últim tram ha estat molt dur i us he sentit ben a prop, m'heu animat i arrencat de l'escriptori quan feia falta, amb aquella petita dosi d'energia quan més la necessitava.

Gracias a mi pequeña familia de París, nuestra estancia fue breve, pero entre sopas y pizzas conseguimos forjar una bonita amistad que espero que dure para siempre. Muchas gracias a toda la gente del Colegio de España por acogerme y regalarme tanto amor y tanta vitalidad. Os quiero muchísimo y espero que sigamos descubriendo mundo (prometo no perderme ninguna otra reunión de *Turras*).

Quiero agradecer también toda la fuerza de Silvia y Tommaso, por estos momentos de reunión que hemos tenido últimamente. Por esos comentarios de ánimo en el sprint final y por una amistad preciosa que crecerá mucho (¡Bienvenidos a Barcelona!). Muchas gracias, Marcos por estar siempre ahí. Crecimos juntos, casi como hermanos, y a pesar de que cada uno hemos seguido nuestro camino, siempre has encontrado la forma de reconectar y estar presente. Tu tenacidad y bondad me han acompañado siempre, eres un referente y una inspiración. ¡Te quiero nano! Agrair també als col·legues de la infantesa de Bonastre: Magí, Menji, David i Josep per ser-hi i per recordar-me que també és important desconnectar, de tant en tant, de tots els maldecaps. Espero haver-me guanyat el dret de defensar amb un dau negre a partir d'ara! Un agraïment especial a en German, la Juanita i a la Teresa i la Judith, per ajudar-me a treure forces d'on jo ja pensava que no en quedaven i per esperonar-me a continuar lluitant fins al final.

Si hay alguien a quien le debo un enorme GRACIAS es a ti, Julia. No hay suficientes palabras para describir todo lo que me has apoyado en esta carrera de fondo. Gracias por entenderme, por tu infinita paciencia, por motivarme cada día para conseguir este logro y por tu criterio siempre acertado con las figuras y formatos. He podido llegar hasta el final con la cabeza cuerda (más o menos) gracias a que te he tenido siempre a mi lado. Ets increïble i em sento profundament afortunat de poder caminar al teu costat. Bendito Hechizo. Gràcies Floki i Mirthu per l'amor incondicional que em doneu cada dia i per fer-me riure amb les vostres malifetes.

Per últim, vull donar les gràcies a la meva família, perquè si he pogut arribar fins aquí també és gràcies a ells i elles. Especialment a la Lluïsa, en Josep i la meva àvia Emília. Gràcies per educar-me en la cultura de l'esforç, de la curiositat i de la responsabilitat. Gràcies per haver-me donat totes aquestes oportunitats de formar-me acadèmicament i personalment i per haver-me recolzat en totes i cada una de les decisions que he anat prenent. No em podria sentir més orgullós d'aquesta família i de les meves arrels. Us estimo molt.

Gràcies a tots i totes per formar part d'aquesta aventura i espero que ben aviat n'encetem de noves.

Resum

Departament de Física de la Matèria Condensada
Departament de Psicologia Social i Psicologia Quantitativa
Universitat de Barcelona

Connectivitat funcional a múltiples escales: dels cultius neuronals al cervell humà

per Marc Montalà Flaquer

Un dels grans reptes en el camp de la neurociència consisteix a obtenir una descripció funcional del cervell més acurada que ens permeti entendre el funcionament de processos cognitius de complexitat superior com la memòria o la consciència. Són moltes les tècniques emprades en els paradigmes experimentals, entre les quals destaca l'adquisició d'imatges mitjançant ressonància magnètica funcional (fMRI). Un altre procediment habitual consisteix a utilitzar la fluorescència amb ions de calci, una tècnica que permet monitorar l'activació neuronal al llarg del temps gràcies al canvi en la concentració de calci a l'espai postsinàptic.

Aquesta tesi té per objectiu l'estudi de la connectivitat funcional d'un sistema complex multiescala, el cervell, en un paradigma d'envelliment sa. Per aconseguir aquest objectiu s'han seguit dues línies de recerca complementàries: un enfocament mesoscòpic amb cultius neuronals primaris de rata i un estudi *whole-brain*, és a dir de tot el cervell, a gran escala, emprant senyal cerebral de participants sans.

Al llarg de la primera línia de recerca s'han desenvolupat cultius neuronals en superfícies amb una topografia determinada —línies i obstacles quadrats— que han permès caracteritzar els trets funcionals i la riquesa dinàmica de l'activitat espontània subjacent. En la segona línia de recerca s'ha abordat l'anàlisi del senyal fMRI provinent de participants sans així com la caracterització de les xarxes funcionals que es deriven de les matrius de connectivitat. Com a objectiu secundari, s'ha analitzat com els mètodes de filtratge sobre de les matrius de connectivitat afecten a aquests indicadors funcionals.

Pel que fa al patró de línies, hem observat com la dinàmica d'activació és substancialment diferent de la dels cultius en superfície llisa. Les línies paral·leles trenquen totalment la isotropia de la superfície on creixen les neurones, creant una direcció privilegiada en les connexions amb les neurones veïnes. Malgrat tot, hi ha una certa possibilitat que les connexions es donin transversalment originant activacions al llarg de tot el cultiu. Cal

destacar que en aquest paradigma ja no es pot assumir que la propagació es doni seguint un front circular, de fet s'ha constatat que hi ha una velocitat de propagació ràpida al llarg de la pista i una velocitat més lenta de propagació en la direcció transversal.

Per últim, s'han analitzat mesures locals i globals de segregació i integració tals com l'eficiència global, el coeficient d'agregació o el grau de connectivitat. Aquest estudi ens ha permès entendre millor la comunicació al llarg del cultiu i les variacions dinàmiques de les activacions espontànies. Gràcies a l'ús d'algoritmes de transferència d'entropia per a quantificar el flux d'informació en la xarxa neuronal, s'ha trobat que els cultius amb patrons quadrats i línies mostren una organització funcional efectiva modular, mentre que els cultius homogenis sobre superfície llisa mostren una organització més aleatòria. Les anàlisis de connectivitat efectiva han revelat l'aparició de mòduls funcionals espacialment compactes i que es poden associar a les característiques topogràfiques i als fronts d'activitat espai-temporal.

Tots aquests resultats donen suport al supòsit que la introducció de patrons com a pertorbació física modifiquen la dinàmica funcional dels cultius neuronals i els doten d'una major riquesa dinàmica.

Respecte a l'anàlisi de senyal fMRI, els resultats semblen indicar que els mètodes d'anàlisi fALFF (de l'anglès *fractional Amplitude of low-frequency fluctuations*) i ReHo (*Regional Homogeneity*) descriuen correctament el procés d'envelliment sa (sense declivi del rendiment cognitiu) d'una població i posen de manifest dos elements interessants. D'una banda, fALFF mostra que hi ha una diferència significativa en les fluctuacions de baixa intensitat a mesura que es dona l'envelliment. Altres estudis han reportat una pèrdua de connectivitat funcional sense que hi hagi un declivi en les mesures neuropsicològiques ni en el rendiment del participant. D'altra banda, ReHo indica un augment de la sincronia regional quan es compara el grup de més edat amb la resta de grups d'edat. Aquest augment de sincronització s'ha descrit en altres estudis com un mecanisme compensatori en el qual determinades regions necessiten major coherència per a continuar funcionant sense que s'aprecii cap baixada en indicadors de rendiment neuropsicològic. Creiem, doncs, que ReHo podria estar descrivint el procés d'envelliment sa.

Amb relació a l'exploració dels mètodes de filtratge, hem pogut constatar que la tècnica més estable és la de TMFG (de les sigles en anglès de *Triangulated Maximally Filtered Graph*). També és la tècnica que més s'allunya del model nul, és a dir de la distribució aleatòria de correlació de senyals, en els indicadors de connectivitat estudiats. A més, l'avantatge d'aquesta tècnica és que conserva la màxima informació continguda en la matriu de connectivitat tot eliminant les connexions redundants o espúries.

Resumen

Departamento de Física de la Materia Condensada
Departamento de Psicología Social y Psicología Cuantitativa
Universidad de Barcelona

Connectividad funcional en múltiples escalas: de los cultivos neuronales al cerebro humano

por Marc Montalà Flaquer

Uno de los mayores retos en el campo de la neurociencia consiste en obtener una descripción funcional del cerebro más precisa que nos permita entender el funcionamiento de procesos cognitivos de complejidad superior, como la memoria o la consciencia. Son muchas las técnicas utilizadas en los paradigmas experimentales, entre las cuales destaca la adquisición de imágenes mediante resonancia magnética funcional (*fMRI*). Otro procedimiento habitual consiste en utilizar la fluorescencia con iones de calcio, una técnica que permite monitorear la activación neuronal a lo largo del tiempo gracias al cambio en la concentración de calcio en el espacio postsináptico.

Esta tesis tiene por objetivo el estudio de la conectividad funcional de un sistema complejo multiescala, el cerebro, en un paradigma de envejecimiento sano. Para conseguir este objetivo se han seguido dos líneas de investigación complementarias: un enfoque mesoscópico con cultivos neuronales primarios de rata y un estudio *whole-brain*, es decir, de todo el cerebro y a gran escala, empleando señales cerebrales de participantes sanos.

En la primera línea de investigación, los cultivos neuronales se han desarrollado sobre superficies con una topografía específica —líneas y obstáculos cuadrados— que nos han permitido caracterizar los rasgos funcionales y la riqueza dinámica de la actividad espontánea subyacente. El segundo enfoque ha abordado el análisis de la señal *fMRI* procedente de participantes sanos, así como la caracterización de las redes funcionales derivadas de las matrices de conectividad de la actividad espontánea subyacente. Como objetivo secundario, hemos analizado cómo afectan a estos indicadores funcionales los métodos de filtrado de las matrices de conectividad.

En cuanto al patrón de líneas, observamos que la dinámica de activación es sustancialmente diferente a la de los cultivos de superficie lisa. Las líneas paralelas rompen completamente la isotropía de la superficie en la que crecen las neuronas, creando una

dirección privilegiada en las conexiones con las neuronas vecinas. Sin embargo, existe cierta posibilidad de que las conexiones se den transversalmente, originando activaciones a lo largo de todo el cultivo. En este paradigma ya no es posible asumir que la propagación sigue un frente circular, de hecho, se ha comprobado que existe una velocidad de propagación rápida a lo largo de las pistas y una velocidad de propagación más lenta en la dirección transversal.

Por último, se han analizado medidas locales y globales de segregación e integración como la eficiencia global, el coeficiente de agregación o el grado de conectividad. Este estudio nos ha permitido entender mejor la comunicación a lo largo del cultivo y las variaciones dinámicas de las activaciones espontáneas. Gracias al uso de algoritmos de transferencia de entropía para cuantificar el flujo de información en la red neuronal, se ha encontrado que los cultivos con patrones cuadrados y líneas muestran una organización funcional efectiva modular, mientras que los cultivos homogéneos sobre superficie lisa muestran una organización más aleatoria. Los análisis de conectividad efectiva han revelado la aparición de módulos funcionales espacialmente compactos que se pueden asociar a las características topográficas y a los frentes de actividad espaciotemporal. Estos resultados apoyan al supuesto que la introducción de patrones como perturbación física modifican la dinámica funcional de los cultivos neuronales y los dotan de mayor riqueza dinámica.

Respecto al análisis de señal fMRI, los resultados indican que los métodos de análisis fALFF (del inglés *fractional Amplitude of low-frequency fluctuations*) y ReHo (*Regional Homogeneity*) describen correctamente el proceso de envejecimiento sano, es decir, sin declive del rendimiento cognitivo, de una población y ponen de manifiesto dos elementos interesantes. Por un lado, fALFF muestra que hay una diferencia significativa en las fluctuaciones de baja intensidad a medida que se da el envejecimiento. Otros estudios han reportado una pérdida de conectividad funcional sin que haya un declive en las medidas neuropsicológicas ni en el rendimiento del participante. Por otro lado, ReHo indica un aumento de la sincronía regional cuando se compara el grupo de más edad con el resto de grupos de edad. Este aumento de sincronización se ha descrito en otros estudios como un mecanismo compensatorio en el cual determinadas regiones necesitan mayor coherencia para continuar funcionando sin que se aprecie una disminución en indicadores de rendimiento neuropsicológico. Creemos, pues, que ReHo podría estar describiendo el proceso de envejecimiento sano.

Con relación a la exploración de los métodos de filtraje, hemos podido constatar que TMFG (*Triangulated Maximally Filtered Graph*) es la técnica más estable. También es el método que más se aleja del modelo nulo, es decir, de la distribución aleatoria de correlación de señales, en los indicadores de conectividad estudiados. Además, esta técnica conserva la máxima información contenida en la matriz de conectividad, eliminando las conexiones redundantes o espurias.

Abstract

Department of Condensed Matter Physics

Department of Social Psychology and Quantitative Psychology

University of Barcelona

Functional connectivity at multiple scales: From neuronal cultures to human brain

by Marc Montalà Flaquer

One of the greatest challenges in the field of neuroscience is to obtain an accurate functional description of the brain that allows us to understand the functioning of higher complexity cognitive processes such as memory or consciousness. Many techniques are used to fit in the various experimental paradigms, among which the functional magnetic resonance (fMRI) imaging stands out. Another standard procedure is the calcium fluorescence imaging, a technique that allows the monitoring of neuronal activations over time thanks to the changes in calcium concentration in the synaptic cleft.

This thesis aims to study the functional connectivity of a complex multiscale system, the brain, in a healthy aging paradigm. To achieve this objective, two complementary lines of research have been followed: a mesoscopic approach with primary rat neuronal cultures and a *whole-brain* study, *i.e.*, at a large scale, using brain spontaneous activity from healthy participants.

Throughout the first line of research, neuronal cultures have been developed on surfaces with a certain topography —track and square obstacles— that enabled to characterize the functional features and the dynamical richness of the emerging spontaneous activity. The second line of research has addressed the analysis of the fMRI signal from healthy participants as well as the characterization of the functional networks that derive from connectivity matrices. As a secondary objective, we analysed how the filtering methods affected these functional indicators extracted from the connectivity matrices.

In neuronal cultures, and regarding the track's configuration, we have observed that the activation dynamics was substantially different from the one observed in standard, flat surface cultures. The parallel lines completely break the isotropy of the surface creating a privileged direction in the connections with neighbouring neurons. However, there is a certain possibility that neurons connect transversely, which originate activations throughout

the entire neuronal culture. We note that in this paradigm it is no longer possible to assume that the propagation takes place following a circular wave front. Indeed, we found a rapid propagation velocity along the track and a slower speed of propagation in the transverse direction.

Finally, local and global measures of segregation and integration such as global efficiency, aggregation coefficient or degree of connectivity have been analysed. This study has allowed us to better understand communication throughout the culture and the dynamic changes of spontaneous activity. Thanks to transfer entropy algorithms to unveil information flow, we have found that cultures with square and track configurations show an effective modular organization, while homogeneous cultures on a flat surface show a more random organization. Effective connectivity analyses have revealed the emergence of spatially compact functional modules that can be associated with topographical features and spatiotemporal activity fronts.

All these results support the assumption that the introduction of patterns as physical perturbation modifies the functional dynamics of neuronal cultures and endows them with greater dynamical richness.

Regarding the analysis of fMRI signal, the results seem to indicate that the analysis methods fALFF (fractional Amplitude of low-frequency fluctuations) and ReHo (Region Homogeneity) correctly describe the aging process of a healthy population, that is, without decline of cognitive performance, and highlight two interesting facts. On the one hand, fALFF shows that there is a significant difference in low-intensity fluctuations as aging occurs. Other studies have reported a loss of functional connectivity without the manifestation of a decline in neuropsychological measurements or participant performance. On the other hand, ReHo indicates an increase in regional synchrony when comparing the oldest group with the other age groups. This increase in synchronization has been described in other studies as a compensatory mechanism, in which certain regions need greater coherence to continue operating without any decline in neuropsychological performance indicators. We therefore believe that ReHo could be describing the process of healthy aging.

In relation to the exploration of filtering methods, we have been able to verify that the most stable technique is TMFG (Triangulated Maximally Filtered Graph). It is also the technique that is furthest away from the null model, *i.e.*, the random distribution of signal correlation, throughout all the connectivity indicators studied. In addition, the advantage of this technique is that it preserves the maximum information stored in the connectivity matrix by eliminating redundant or spurious connections.

Table of contents

List of tables	xxiii
List of figures	xxv
List of acronyms and abbreviations	xxxi
1 Introduction	1
1.1 Conceptual framework	1
1.2 The need of <i>in vitro</i> approaches: neuronal cultures	5
1.3 Cortical neuronal cultures	7
1.3.1 Homogeneous cultures	8
1.3.2 Patterned cultures	10
1.4 Spontaneous activity in neuronal cultures	11
1.4.1 Initiation of spontaneous activity	11
1.4.2 Structure of propagating fronts	12
1.5 Connectivity	13
1.5.1 Structural connectivity	14
1.5.2 Functional and effective connectivity	14
1.6 From neuronal cultures to the brain	16
1.7 The mammalian brain	17
1.7.1 The mammalian cerebral cortex	17
1.8 Animal models	18
1.9 fMRI and BOLD signal	19
1.10 Healthy aging	23
1.10.1 Brain changes in healthy aging	24
1.11 The brain as a complex system	25
1.11.1 The segregation–integration balance	26
1.11.2 Brain complex network traits	26

1.12	Outlook of the present Thesis	27
2	Objectives	29
3	Experimental Procedures <i>in vitro</i>	31
3.1	Rat primary cultures	31
3.1.1	Primary neuronal cell cultures	32
3.1.2	Immunocytochemistry	33
3.2	Modulating neuronal culture substrates	35
3.2.1	PDMS topographical reliefs	35
3.2.2	Stamping of patterned surfaces	38
3.3	Data acquisition	39
3.3.1	Neuronal action potentials	40
3.3.2	Fluorescence calcium imaging	41
3.3.3	Confocal microscopy	42
3.4	Data analysis tools	44
3.4.1	Calcium imaging	44
3.4.2	Calcium imaging data analysis and activity events detection	44
3.4.3	Population activity, network bursts, and distribution of burst amplitudes	46
3.4.4	Bursts' analysis as spatiotemporal fronts	47
3.4.5	Similarity of spatiotemporal fronts	49
3.4.6	Velocity of propagating fronts	50
3.4.7	Numerical simulations	51
3.4.8	Neuronal model	53
4	Experimental Procedures <i>in vivo</i>	55
4.1	fMRI data description	55
4.1.1	Participants	56
4.1.2	Instruments	57
4.2	MRI acquisition	57
4.3	Data analysis tools	58
4.3.1	Data preprocessing	58
4.3.2	Voxel-based Morphometry	59
4.4	Seed-based analysis	59
4.4.1	The amplitude of low-frequency fluctuations	60
4.4.2	Regional homogeneity	61
4.5	Node-based analysis	61

4.5.1	Graph extraction	62
4.5.2	Filtering methods	63
4.5.3	Graph metrics	64
4.6	Generation of the null–hypothesis distribution model	64
4.7	Thresholding accuracy measure	65
5	Network and statistical analysis	67
5.1	Dynamical richness in neuronal cultures	68
5.2	Effective Connectivity in neuronal cultures	69
5.3	Functional connectivity in fMRI recordings	72
5.4	Network measures	72
5.5	Spatial compactness of functional modules	77
5.6	Statistical analysis	78
6	Results I: Understanding complex functional organization in neuronal assemblies	83
6.1	Coherent activity disruption in patterned cultures	84
6.1.1	The effect of PDMS topographical molds	84
6.1.2	Bursting sizes and dynamical richness	87
6.2	Topography induces a rich repertoire of activity patterns	88
6.3	PDMS topography induces connectivity traits	92
6.4	PDMS topography impacts on burst initiation and velocity of burst propagation	94
6.5	Effective connectivity analysis identifies unique network organization traits	97
6.5.1	Euclidean distance analysis in topographical cultures	99
6.5.2	Numerical simulations	102
6.5.3	Local topological properties in patterned cultures	104
6.6	Discussion	108
6.6.1	Limitations of the study	112
6.7	List of videos from experimental recordings	113
7	Results II: Understanding complex functional organization in aging brain	115
7.1	ALFF and ReHo approaches to fMRI data	117
7.1.1	Participant characteristics analysis	117
7.1.2	fALFF results between groups	120
7.1.3	ReHo results between groups	121
7.1.4	Correlation analysis with neuropsychological outcome	123
7.1.5	Correlations and regressions: fALFF, ReHo, and aging	124

7.2	Graph-based analysis of fMRI data and thresholding	126
7.2.1	Characteristic path length L	127
7.2.2	Clustering coefficient CC	128
7.2.3	Global Efficiency G_E	129
7.2.4	Modularity Q	129
7.2.5	Transitivity T	131
7.2.6	Smallworldness	133
7.2.7	Accuracy measure	136
7.3	Discussion	138
7.3.1	Discussion fALFF and ReHo	138
7.3.2	Discussion on thresholds	141
8	General discussion	149
8.1	General discussion	149
8.2	Limitations of the Thesis	152
9	Conclusions	155
9.1	Conclusions	155
	References	159
	Appendix A Informed consent documents	185

List of tables

1.1	Life expectancy at birth (in years) in Spain (1996-2021)	23
3.1	Primary cultures media	34
3.2	Primary antibodies	35
4.1	fMRI acquisition protocols	58
7.1	Description of participant and movement between age groups	118
7.2	Description of neuropsychological measures between age groups	119
7.3	Description of level of education between age groups	119
7.4	Significant between-group differences in fALFF	121
7.5	Significant between-group differences in ReHo	122
7.6	Parameter estimation (β) of the best stepwise linear model for age	126
7.7	Total accuracy for every threshold considering all the graph indicators	136
7.8	Accuracy for every threshold in every connectivity indicator	137

List of figures

1.1	Structural and functional scales involving the brain	4
1.2	Cortical neuron drawings by Santiago Ramón y Cajal	6
1.3	Primary neuronal culture preparations on PDMS	9
1.4	Modes of brain connectivity	15
1.5	The mammalian brain: humans and rodents	19
1.6	Blood oxygen level–dependent signal	21
1.7	Timing of the hemodynamic response function	22
3.1	Summary of the neuronal culture and brain features	32
3.2	Sketch of the experimental setup and procedure	34
3.3	Shaping patterned substrates	36
3.4	Preparation of topographical PDMS substrates	37
3.5	Neurons on the ‘tracks’ PDMS topography	38
3.6	Engineering of patterns with stamps	39
3.7	Schematic depiction of voltage-dependending calcium channels	40
3.8	Sketch of the neurotransmitter release	41
3.9	Fluorescence calcium imaging and spike inference	42
3.10	Fluorescence microscopy	43
3.11	Data analysis	45
3.12	From fluorescence to spikes	46
3.13	Population activity	47
3.14	Activity fronts and initiation	48
3.15	Spatiotemporal front classification	50
3.16	Velocity of propagating fronts	51
3.17	Construction of <i>in silico</i> networks	52
4.1	Pipeline of the MRI preprocessing	59
4.2	Pipeline of the graph extraction	62

5.1	Concept map of the main functional connectivity measures explored	67
5.2	Schematic representation of Dynamical richness values in two different neuronal culture configuration	68
5.3	Pipeline of the effective connectivity extraction in the <i>in-vitro</i> experiments .	69
5.4	z–score transformation of the Transfer Entropy data	70
5.5	Extraction of functional modules of the <i>in-vitro</i> experiments	71
5.6	Measures of complex network topology	73
5.7	Schematic representation of important concepts in complex networks	76
5.8	Compactness of effective networks in a 6 mm neuronal culture	79
6.1	Patterned culture activation	85
6.2	ROI generation and data analysis	86
6.3	Dynamical richness repertoire	88
6.4	Repertoire of spatiotemporal patterns in control cultures	89
6.5	Repertoire of spatiotemporal patterns in cultures with tracks configuration‘ .	90
6.6	Repertoire of spatiotemporal patterns in cultures with squares configuration	91
6.7	Anisotropic connectivity in PDMS topographical cultures revealed by immunostaining	93
6.8	Burst initiation point distribution and Gini coefficient	95
6.9	Velocity of propagation bursts in PDMS topographical cultures	96
6.10	Velocity of propagation bursts in tracks configuration	97
6.11	Effective connectivity analysis in PDMS topographical cultures	98
6.12	Relationship between effective connectivity and dynamics in ‘tracks’ configuration	100
6.13	Local and global functional features in PDMS topographical cultures	101
6.14	Evolution of Euclidean distance between effectively connected neurons . .	102
6.15	Dependence of effective connectivity distance on average axonal length . .	103
6.16	In–degree connectivity distributions and evolution of average connectivity along development	105
6.17	Local network properties for effective connectivity in experimental data at DIV 14	107
6.18	Comparison between structural and effective clustering coefficients	108
7.1	fALFF analysis across significant age groups	120
7.2	ReHo analysis through age groups	123
7.3	Correlation analysis between significant clusters	125
7.4	Scatter plot and regression for age	126

7.5	Graphical representation of the subjects' characteristic path length L	128
7.6	Graphical representation of the subjects' clustering coefficient CC	130
7.7	Graphical representation of the subjects' global efficiency G_E	131
7.8	Graphical representation of the subjects' modularity Q	132
7.9	Graphical representation of the subjects' transitivity T	133
7.10	Graphical representation of the subjects' small-world SW	135
8.1	Simplification and expansion processes to understand the brain functioning	150

List of acronyms and abbreviations

AAL: Automatic Anatomical Labeling

AAV: Adeno-associated virus

AD: Alzheimer's Disease

AIC: Akaike Information Criteria

AMPA: α -amino-3-hydroxy-5-methyl-4-isoxazolepropionic acid

ANOVA Analysis Of Variances

APOE Apolipoprotein E

BC: Betweenness Centrality

BNT: Boston Naming Test

BOLD: Blood Oxygen Level-Dependent

CC: Clustering Coefficient

CNS: Central Nervous System

CR: Cognitive Reserve

CSF: Cerebrospinal Fluid

DARTEL: Diffeomorphic Anatomical Registration Through Exponentiated Lie algebra

DIV: Day In Vitro

DMN: Default Mode Network

DMSO: Dimethyl Sulfoxide

DoF: Depth of Field

DPABI: Data Processing and Analysis for Brain Imaging

DPARSF: Data Processing Assistant for Resting-State fMRI

DTI: Diffusion Tensor Imaging

ECM: Extracellular Matrix

EEG: Electroencephalography

fALFF: fractional Amplitude of Low-Frequency Fluctuations

FBS: Fetal Bovine Serum

FC: Functional Connectivity

FD: Framewise Displacement

fMRI: functional Magnetic Resonance Imaging

FOV: Field Of View

FWER: Family-Wise Error Rate

FWHM: Full Width at Half Maximum

GABA: Gamma-aminobutyric acid

GECI: Genetically Encoded Calcium Indicator

GM: Grey Matter

GTE: Generalized Transfer Entropy

hiPSC: human induced Pluripotent Stem Cells

HS: Horse Serum

ICC: Immunocytochemistry

LFP: Local Field Potential

LSM: Laser Scanning Microscopy

MEA: Micro-electrode Array

MEM: Minimum Essential Medium

MMSE: Mini-Mental State Examination

MNI: Montreal Neurological Institute

MPRAGE: Magnetization–Prepared Rapid Acquisition Gradient Echo

NART: National Adult Reading Test

PBS: Phosphate-buffered saline

PDMS: Polydimethylsiloxane

PFA: Paraformaldehyde

PLL: Poly-L-Lysine

RAVLT: Rey Auditory Verbal Learning Test

ReHo: Regional Homogeneity

ROI: Region Of Interest

rs-fMRI: resting state functional Magnetic Resonance Imaging

SCA: Seed–based Correlation Analysis

SD: Standard Deviation

SW: Smallworldness

TE: Time of Echo

TFCE: Threshold–Free Cluster Enhancement

TMFG: Triangulated Maximally Filtered Graph

TR: Time of Repetition

VBM: Voxel Based Morphometry

WAIS: Wechsler Adult Intelligence Scale

WHO: World Health Organization

WM: White Matter

"Saruman believes that it is only a great power that can hold evil in check, but that is not what I have found. I have found that it is the small things, every-day deed of ordinary folks that keep the darkness at bay. Small acts of kindness and love." - Gandalf.

*—J.R.R. Tolkien, *The Hobbit* (1937).*

Chapter 1

Introduction

1.1 Conceptual framework

Physics of complex systems has emerged in the last decades as a powerful branch of knowledge to model and predict both the natural world and human-made technologies. From social interactions to the brain and internet, complex systems deal with the understanding of how an ensemble of interacting units are able to exhibit a collective behaviour that is much richer than the sum of its individual components (Siegenfeld and Bar-Yam, 2020). With the support of powerful tools grounded in dynamical systems (Strogatz, 2018), data science (Zanin et al., 2016) and complex networks (Boccaletti et al., 2006), research in complex systems has both revolutionized our view of the world and provided insight into its evolution, playing a fundamental role in understanding problems as diverse as the propagation of epidemics (Soriano-Paños et al., 2022), climate change (Fan et al., 2021), the vulnerability of internet (Li et al., 2021) or the understanding and prognosis of neurological disorders (Medaglia and Bassett, 2018; Stam, 2014).

A dream for any scientist working in complex systems is the capacity to *play* with such a system, *i.e.*, to shape and control the interactions among its building blocks as well as to act on the system to dissect the mechanisms that shape its complexity and repertoire of behaviours. This is particularly attractive in biological systems, in which processes at different spatial and temporal scales coexist, from molecular interactions to multicellular communication. One of such *model complex system* is a neuronal culture, *i.e.*, the growth of neurons in a controlled, *in vitro* environment.

Surprisingly, neuronal cultures were already developed about a century ago (Millet and Gillette, 2012b), when neuroscientists started dissociating rodent neurons and plating them on sterile surfaces where they could be maintained and monitored. The idea behind that novel technique was to verify that neurons were the building blocks of a nervous system, then to

understand their intrinsic dynamical behaviour, and finally to investigate their capacity to connect to one another and shape intricate information processing networks (Yuste, 2015). The capacity of neurons to reconnect after dissociation and, in a matter of days, exhibit robust spontaneous activity patterns, has fascinated the neuroscience and the complex system communities alike (Mazzoni et al., 2007; Rolston et al., 2007).

Indeed, along this century of neuronal cultures, the scientific community has acknowledged their importance as a toolbox to understand the brain and its dysfunctions. And it is precisely the fact that one can act on neuronal cultures what has made them so attractive. Several multidisciplinary approaches have united to the technological revolution, such as advanced microscopy or optogenetics, as well as game-changing biological achievements, such as genetically encoded calcium indicators (Chen et al., 2013), have boosted neuroscience even further. For instance, various electronic and optical technologies allow to monitor the evolution of a neuronal culture from a community of isolated cells to a networked assembly with rich topological and dynamical characteristics. The continued monitoring has provided invaluable insight in aspects such as self-organization, spontaneous activity, the emergence of rich non-random network traits, critical behaviour, computation, or the repertoire of activity patterns. Additionally, with the advent of microfabrication technologies and bioengineering, neuronal cultures have been used to explore in detail the relationship between structural connectivity and collective dynamics, the quest towards mimicking brain-like circuits *in vitro*, or the vulnerability of neuronal networks to perturbations, damage or disease. The latter is related to a wealth of multidisciplinary efforts aimed at understanding and treating neurological disorders, in which neuronal cultures provide an environment to explore both the mechanisms behind network alterations and the goodness of therapeutic interventions.

Neuronal cultures can be viewed as a coin in which ‘complex systems’ are one of the sides. The other side is neuroscience, representing all the efforts to understand neuronal behaviour, from the molecular processes up to cognition, with the brain the ultimate mystery to decode. Indeed, the brain might be considered the most complex system in nature. This organ is able to receive and store exceptional amounts of information, process and modify it with great adaptability, and finally generate simple yet precise actions, like motor movement, or more elevated functions such our own consciousness and thoughts (Ornstein and Thompson, 1986). Unveiling the fundamental mechanisms that allow our Central Nervous System (CNS) to perform such sophisticated functions is an extraordinarily defying challenge.

The organization of the brain is complex, and the interconnectivity of its functional elements extends across multiple scales. Some events, like synapse coupling and neurotransmitter release, take place at a single-neuron scale (microscale), the flow of information between cortical columns takes place at a scale of tens of neurons, (mesoscale), and the

communication between memory and motor areas to perform a superior function takes place at a macroscopic scale. Therefore, the processing of information and the collective phenomena of interacting communities occur at diverse temporal and spatial scales.

To understand the mechanisms governing the brain, two main strategies have been developed. The first one, the top–down approach, focuses on the macroscopic study of the CNS by exploring large–scale activity recordings, such as functional magnetic resonance imaging (fMRI) or electroencephalography (EEG), to understand and identify the contribution of smaller subsets. The second strategy, the bottom–up approach, relies on the exploration of the emergence of collective phenomena, especially spontaneous activity, that appear in larger ensembles of neurons, at the mesoscale.

In the present Thesis, we delved into the study of functional connectivity at multiple scales in an attempt to describe neuronal functional organizations from different perspectives, as illustrated in Figure 1.1. In the following chapters, we will provide, first, examples of different neuronal culture preparations and the tools that we used to analyse their dynamics. We will then introduce numerical simulations to illustrate their capacity to model and predict experimental results. Next, we will present the analysis of fMRI recordings of healthy aging brains from a graph theory point of view. Finally, we will describe the tools that we used to process the data and the effect that aging may alter in different graph functional measures.

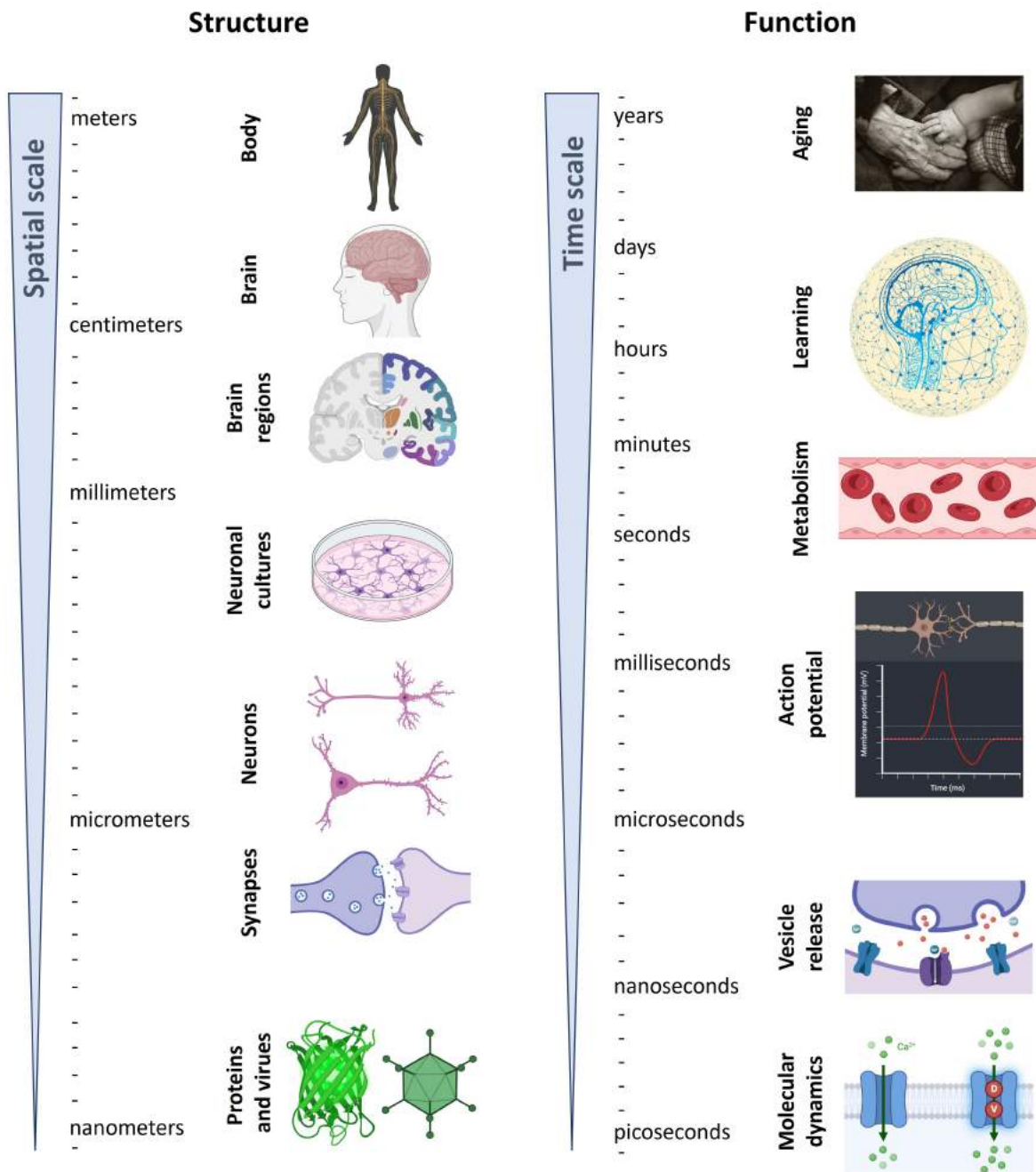


Fig. 1.1 Structural and functional scales involving the brain. The brain is an intrinsically multi-scale, multi-level organ operating across several spatial scales, ranging from nanometres (proteins) to metres (the human body); and temporal scales, from picoseconds (molecular interactions) to years (the lifespan of a human being). Generated with *BioRender.com*.

1.2 The need of *in vitro* approaches: neuronal cultures

Mesoscale (bottom–up) approaches include theoretical models, computational simulations, and experiments in simple living systems, *i.e.*, *in vitro* preparations in the form of slices or neuronal cultures. The three views often work together, reinforcing the validity of the derived tools as well as their applicability (Markram et al., 2015).

Typically, *in vitro* preparations are derived from dissociated rat cortical or hippocampal tissues and they are called ‘primary neuronal cultures’. Primary cultures lose the initial topology layout but both connectivity and spontaneous activity emerge *de novo* in a still poorly disclosed self–organizing process. Neurons can be maintained alive in a nutritious environment for several weeks and their activity monitored by recording techniques that enable the tracking of either single cell behaviour (Eckmann et al., 2007) or collective phenomena. The versatility of neuronal cultures to fit diverse experimental scenarios has made them very attractive for a large number of investigations, most notably the emergence and richness of spontaneous activity patterns (Orlandi et al., 2013; Wagenaar et al., 2006), the interplay activity–connectivity (Volman et al., 2005), the network’s self–organizing potential (Pasquale et al., 2008) and criticality (Tetzlaff et al., 2010).

Historically, humankind has been fascinated and inspired to unveil the complex functionality of the brain. Santiago Ramón y Cajal, born in the 1800s, proved with his sketches (Figure 1.2) that single neurons were the structural and functional units of the CNS. Nowadays we know that neuronal cells are the constituents of a bigger building block: the neuronal circuits. They shape in great measure the functionality of the brain, from simple motor tasks to complex abstract thinking (Yuste, 2015).

Despite considerable advances, the link between connectivity, neuronal activity, and brain function remains elusive. Understanding this intricate puzzle would shed some light to the understanding of not only the regular behaviour and cognition but also the impaired ones. To achieve this understanding, it is required to study neuronal circuits in simpler living systems at a mesoscale level. In such systems, even though complexity is vastly reduced when compared to the entire brain, they exhibit rich spontaneous activity. Also, their manipulation and reproducibility are increased, making them highly attractive to study cellular and connectivity aspects related to healthy and diseased neuronal circuits. Additionally, the connectivity of the circuit can be tuned in a plastic manner by neuronal dynamics and the strength of the connections can be reinforced or weakened either physically, with the aid of light or electrical stimulation, or through chemical action.

Despite the enormous gap between neurons in *in vitro* designs and in the brain, neuronal cultures may help to understand brain alterations by mimicking deficiencies of brain pathologies. They may also allow to study the implications of damage–induced injuries as well as to

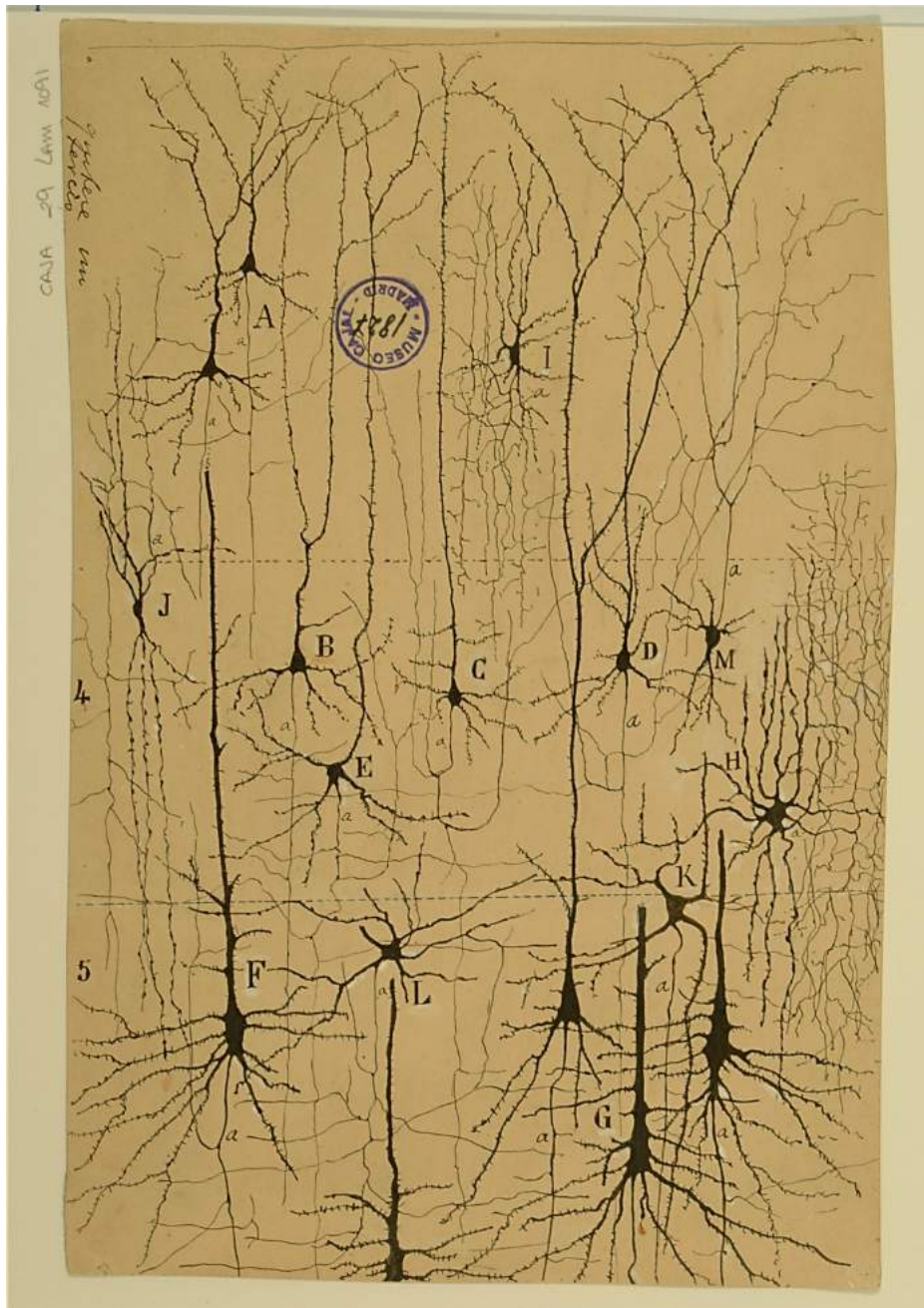


Fig. 1.2 Cortical neuron drawings by Santiago Ramón y Cajal. Some of the original drawings, known as *The Cajal Legacy*, are housed at the Cajal Institute (CSIC) in Madrid, Spain. Other examples with full descriptions can be consulted in Ramón y Cajal books (Ramon y Cajal, 1899). Copyright by Legado Cajal-CSIC, inventory nº LC03678. Reproduced with permission.

investigate possible recovery strategies using pharmacological drugs (Srinivas et al., 2007) or even stimulation (Mazzatenta et al., 2007). In this context, neuronal cultures have assisted in the comprehension of circuit dysfunction in epilepsy (Srinivas et al., 2007; Sun et al., 2002,

2004) or neurodegenerative diseases, particularly Alzheimer's (Dahlgren et al., 2002; Hartley et al., 1999).

Hence, neuronal cultures serve as a true living lab to investigate universal phenomena in neuronal systems, their physical modelling, and the sensitivity of network behaviour to failure at a circuitry or neuronal level.

In terms of activity, individual neurons respond to particular stimuli like a switch, in an on-off manner, a fact that displays its dynamical non-linearity and complexity. However, this inherent behaviour does not confer a neuron a predominant role in a neuronal circuit. Indeed, the single-neuron conceptual framework started to lose popularity by 1930, when multi-neuron imaging technologies were brought to light and brain spontaneous activity started to be measured (Fox and Raichle, 2007). This emergent activity is characterized by the coherent activation of large neuronal assemblies in the absence of stimuli and cannot be explained from a single-neuron perspective. More importantly, individual neurons never seem to respond identically to the same stimulus (Gross and Kowalski, 1999), and the activation of a single neuron often leads to the activation of an entire population (Feldt et al., 2011). Thus, one of the big assertions of modern neuroscience is that information is distributed in cell assemblies rather than encoded by single cells, although the nature of coding or the information processing in these neuronal circuits remains unclear.

The topological organization of the connections among neuronal populations is one of the key ingredients for information processing. The architecture of the underlying neuronal circuitry can indeed substantially constrain the resulting dynamics (Sporns et al., 2000; Sporns and Zwi, 2004). Thus, a neuronal circuit can be seen as a hard-wired but tunable system where dynamics may continuously modify the synaptic coupling strengths, shaping activity patterns that may in turn reshape the physical connections.

1.3 Cortical neuronal cultures

As introduced before, cortical neuronal cultures are a low-cost, valuable tool to study living neuronal circuits in a controlled manner, with a reduced number of elements (neurons), much more accessible than in the brain, and highly reproducible. Although the original *in vivo* complex connectivity circuitry of the mature cortex is lost during the dissociation process, neuronal phenotypes, morphology and sensing capabilities are preserved (Kriegstein and Dichter, 1983). The fact that the neuronal properties are conserved through the process of dissociation and plating is crucial to guarantee that spontaneous dynamics in both complex systems, brain and neuronal culture, are comparable (Mazzoni et al., 2007). Therefore,

despite structural simplicity, cortical neuronal cultures are an adequate platform to investigate the emergence of collective activity and its spatiotemporal characteristics.

The use of cortical cultures is widespread and covers a great variety of applications and investigations, shaping its multidisciplinary core. For example, Soriano et al. (2008) investigated the self-organization potential of neuronal cultures during development, and Orlandi et al. (2013) and Pasquale et al. (2008) delved in the emergence and overall features of spontaneous activity. Also, others studies treated synchronized activity (Baruchi et al., 2008) and oscillations (Czarnecki et al., 2012). On the other hand, criticality in neuronal networks was also explored through cortical cultures (Tetzlaff et al., 2010), and some studies used *in vitro* preparations to explore network traits in the framework of network theory (Downes et al., 2012; Teller et al., 2014). *In vitro* cultures also helped in the study of neuronal diseases in a controlled environment, such as the Alzheimer's disease (Huang and Mucke, 2012; Teller et al., 2015). Finally, cultures proved also to be useful in studies involving drug toxicity tests (Frega et al., 2012).

In the present Thesis, two culture preparations were utilised to address different features in an optimal way (Figure 1.3). The first kind of cultures are *homogeneous cultures*, which consist of uniformly distributed neurons on a substrate (Cohen et al., 2008a; Orlandi et al., 2013; Tibau et al., 2013). Homogeneous cultures are particularly useful for assessing the initiation and propagation of spontaneous activity in neuronal networks, since they provide a simple neuronal model where single-cell activity can be tracked and collective behaviour investigated. On the other hand, the second kind of explored cultures are *patterned cultures*, which consist of heterogeneously immobilized neurons on the plating surface following a pre-defined architecture. Patterned cultures are specifically useful for assessing network features and functional connectivity traits —such as modularity, community detection or global efficiency— in relation to the underlying physical constraints.

1.3.1 Homogeneous cultures

Homogeneous neuronal cultures (Figure 1.3, left) represent the most standard and most used culture preparation. It is necessary to control adhesion and morphogenesis in the plating environment to obtain homogeneously distributed neurons, which is achieved by coating substrates such as PLL (Poly-L-lysine) or laminin, proteins that promote anchorage of neurons, on a variety of surfaces (Sun et al., 2012). As stated before, homogeneous cultures have proven to be very useful in addressing questions related to the generation and propagation of spontaneous activity patterns. Their activity is distinctive, a phenomenon called network bursts, which is characterized by the collective activation of all the neurons in a short time window (Ben-Ari, 2001; Gross and Kowalski, 1999; Kamioka et al., 1996; Streit

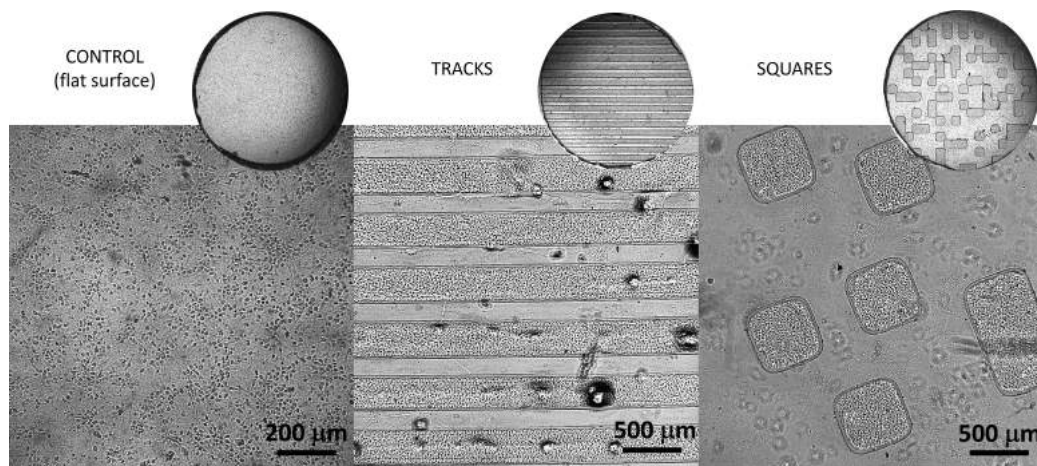


Fig. 1.3 Primary neuronal culture preparations on PDMS. Bright field images of homogeneous neuronal cultures ($\varnothing = 6$ mm) grown on PDMS for three different topographies: control flat surface (left), tracks (centre) and squares (right). On top, the outline of the full culture is shown whereas the central images provide a detailed zoom-in of neurons plated on the surface.

et al., 2001; Wagenaar et al., 2006). For clarity, in this particular preparation, when a neuron activates it triggers a series of action potentials or spikes. A train of such spikes in a neuron is termed *burst*, whereas the collective network activation refers to the term ‘*network burst*’.

Various research groups studied the initiation of these spontaneous network bursts, and elaborated important conceptual frameworks that include the existence of initiation zones (Feinerman et al., 2007), synchronization of different type of neurons and networks (Segev et al., 2004), or the presence of a small subset of highly active neurons called ‘leader neurons’ (Eckmann et al., 2008, 2010; Ham et al., 2008) or ‘functional hubs’ (Sun et al., 2010). These frameworks are introduced in Section 1.4.1.

Researchers have also studied in detail the propagation characteristics of the aforementioned network bursts. Some studies claim that bursts propagate throughout the network as a circular wave (Maeda et al., 1995; Orlandi et al., 2013), while others support that the wave propagation occurs in avalanche-like manner and drives the culture towards a critical state following a power law distributed in time (Mazzoni et al., 2007; Pasquale et al., 2008; Pu et al., 2013; Tetzlaff et al., 2010). In particular, these studies have pointed out that the age of the neuronal culture sets different critical regimes in terms of dynamical repertoire. This criticality was previously shown in brain slices (Beggs and Plenz, 2003, 2004) and has been strongly related with memory and optimal computational capabilities.

Despite all these important studies, homogeneous cultures have two major limitations. First, as already mentioned before, the homogeneous organization is a much simpler complex system and the inter-connectivity is far from *in vivo* networks. And second, the restriction of

motility impedes the formation of richer physical circuits which, in turn, could favor a wider spectrum of activity patterns and functional connectivity traits.

1.3.2 Patterned cultures

An interesting plan of action to evaluate changes in activity patterns in custom-made scenarios is to impose a topographical layout at the surface where neurons are to be plated (Eckmann et al., 2007; Wheeler and Brewer, 2010). An example in the context of this Thesis is provided in Figure 1.3 (central and rightmost panels), where PDMS topographical patterns are used to guide neuronal connectivity. Patterning technique enables the possibility to understand how the spatial arrangement of neurons in a culture influences activity patterns (Schröter et al., 2017) to, later, ascribe them functional topological characteristics. By promoting heterogeneity in the distribution of the neurons, a much richer repertoire of connectivity and activity patterns can be obtained. For instance, modular architectures can arise by sparsely interconnecting small subsets of highly connected neurons (Okujeni and Egert, 2019; Okujeni et al., 2017).

Several approaches and tools have been employed to immobilize neurons in specific locations, or to make them grow on predefined areas. Some of these approaches include the physical barriers to isolate regions of neurons and guide their connections (Gabay et al., 2005; Shein et al., 2009; Shein-Idelson et al., 2011). Other techniques apply biochemical substrates to combine cell-attracting with cell-repelling surfaces (Macis et al., 2007), and some others implement lithographic techniques at the plating environment (Wheeler and Brewer, 2010; Yamamoto et al., 2018). The major concern when working with patterned neuronal cultures is to preserve neurons in their initial locations since they present a high motility that can compromise the study of connectivity and dynamical activations over time (Shein-Idelson et al., 2011).

Some studies observed that spatial heterogeneity enhances connectivity and metric correlations among nearby neurons (Hernández-Navarro et al., 2017; Tibau et al., 2018) when evaluating the distribution of neurons in the coating substrates. Also, in the absence of adhesive proteins at the plating surface, neuronal aggregates were formed and showed distinctive modularity traits in comparison with homogeneously distributed cells (Teller et al., 2014). *In vitro* experiments in a patterned modular neuronal network demonstrated that micro-fabricated patterns could alter the integration-segregation balance and give rise to a much richer repertoire of activations (Yamamoto et al., 2018). Microfabrication was also successful in establishing neuronal density gradients and even provided promising resources for modeling neurological disorders on-a-chip (Yi et al., 2015). Although it is not possible to finely tune neuronal network repertoire of activity, these results show that it is possible

to obtain a great variety of activity regimes by imposing specific architectures to neuronal circuitry.

1.4 Spontaneous activity in neuronal cultures

From a microscopic perspective, spontaneous activity is established on calcium transients that travel through axons from the cell body, the soma, to the pre-synaptic cleft. In homogeneous cultures, neurons' individual activity is usually presented as a short series of concatenated action potentials, *i.e.*, a train of spikes or burst. Eventually, the interaction of those individual bursts might trigger an activation of the whole culture in the form of a spontaneous network burst (Kamioka et al., 1996; Wagenaar et al., 2006), a phenomenon that was also observed in the hippocampus (Mazzoni et al., 2007) and in the neocortex since young embryonic stages (Corlew et al., 2004). For the latter, some studies argue that synchronized spontaneous activity precedes the onset of sensory experience (Kirwan et al., 2015). The mechanisms dictating network burst' initiation and the subsequent propagation are still an open research field, which we will try to explore in this Thesis, especially in patterned neuronal cultures.

1.4.1 Initiation of spontaneous activity

Several models based on experimental observations have been proposed to unveil the mechanism of spontaneous activity. Some suggested the existence of specialized components that promoted the activity such as network burst initiation areas (Feinerman et al., 2007; Lonardoni et al., 2017), or leader neurons, a sort of specialized neurons that orchestrate activity (Eckmann et al., 2008, 2010; Ham et al., 2008). On the other hand, other studies pointed out that neuronal population interactions triggered network activity (Eytan and Marom, 2006; Segev et al., 2004), or that the formation of functional hubs dictated the raise of spontaneous activity (Sun et al., 2010). Finally, another group of studies proposed a noise-focusing scenario, which suggests that synaptic neuronal noise is amplified through topological traits until network bursts are triggered (Orlandi et al., 2013). The advantage of the noise-focusing framework is that it does not assume the need of primordial constituents such as leader neurons for spontaneous activations to occur. On the other hand, it assumes that there is sufficient noise and connectivity amplification features for spontaneous activity to initiate.

Although the detailed mechanisms for the initiation of network bursts is still unclear, there is a general consensus that spontaneous collective phenomena is grounded on synaptic interactions and alterations of the excitatory-inhibitory balance, neuronal noise and amplifi-

cation phenomena through specific network pathways (Mazzoni et al., 2007; Orlandi et al., 2013). Indeed, individual activations apparently arise from synaptic noise, mainly in the form of spontaneous release of neurotransmitters from input neurons. This release to the synaptic cleft generates post-synaptic currents (Otsu and Murphy, 2003; Serra et al., 2010) which are amplified and increase the firing probability of its neighbors, generating propagation waves (Wu et al., 2008).

In cultured networks, neuronal activity appears as action potentials arranged in discrete time series on the millisecond timescale spaced by extended latency periods. As already mentioned, these repetitive activations emerge from self-organized neurons and conform spike trains or *bursts*. The interaction of individual spikes can give rise to coordinated neuronal activations through all the culture in the form of highly synchronous *network bursts* (Orlandi et al., 2013; Rolston et al., 2007). Certainly, these coordinated events of high neuronal participation have been observed not only in cultures (Orlandi et al., 2013; Rolston et al., 2007) but also in slice preparations (Corlew et al., 2004) and *in vivo* (Leinekugel et al., 2002) at multiple frequency regimes.

1.4.2 Structure of propagating fronts

Typically, simultaneous recordings of multiple neurons are necessary to assess the propagation of collective spontaneous activity. The first evidences of studies exploring propagation were obtained in simultaneous recordings of 2 – 3 neurons (Dichter, 1978). By using extracellular tools, some groups were able to identify activity patterns by monitoring one neuron at a time (Habets et al., 1987). Thanks to the improvement and consolidation of various techniques, specially optical fluorometry linked with extracellular calcium (Ca^{2+}), the number of simultaneously monitored neurons substantially increased (Murphy et al., 1992; Ogura et al., 1987).

The presence of synchronized whole-culture bursts was reported by Robinson et al. (1993) on a study grounded on simultaneous measures of electric activity using patch clamp and intracellular calcium recordings. They described the existence of activity propagating fronts with random onset locations inside the culture. Other posterior studies focused on a more local scale and explored full-synchronization approaches (Opitz et al., 2002; Segev et al., 2004; Wagenaar et al., 2006), disregarding the suggested propagation profile. Caution should be taken when assessing large-scale propagation events since sufficient spatiotemporal resolution must be granted to correctly evaluate simultaneous activations.

Indeed, a key feature when exploring the propagation of activations is the characteristic lengthscale of the neuronal culture. Eckmann et al. (2007) and Feinerman and Moses (2003) designed unidimensional homogeneous cultures whose with a total length of \sim

10 cm, much larger than the average extension of axons, ~ 1 mm. In this experimental design, they observed two differentiated velocity regimes: a first one of fast neuronal propagation at ~ 80 mm/s that was preceded by a second one related to slow recruitment (~ 20 mm/s) of asynchronous activations. Based on the experimental observations, it was then suggested that the measured velocities basically depended on three key factors: the excitation–inhibition balance of the network, the strength of connections, and the degree of synaptic depression (Alvarez-Lacalle and Moses, 2009). Moreover, the initiation of network bursts was located in highly specific (and usually dense) regions of the culture, which were therefore labeled as ‘burst initiation zones’ (Feinerman et al., 2005, 2007).

The experiments presented and analysed in this Thesis are grounded on neuronal cultures grown on two–dimensional substrates ($\varnothing = 6$ mm) using three different surface topographies: flat surface homogeneous cultures, squared obstacles and straight lines (see Chapter 3, Section 3.2.1 for detailed information). Typically, in large cortical cultures ($\varnothing \geq 3$ mm), network bursts nucleate on specific finite areas (≈ 0.3 mm²) and then propagate through the whole neuronal network at an approximate velocity in the range 10 – 100 mm/s (Orlandi et al., 2013). In homogeneous cultures, this propagation is usually observed as a circular wave front that activates the entire system in a short time window (Maeda et al., 1995; Orlandi et al., 2013), although some studies alleged that temporal activations follow a power–law distribution and present a complex spatiotemporal structure (Mazzoni et al., 2007; Okujeni et al., 2017; Pasquale et al., 2008; Pu et al., 2013; Tetzlaff et al., 2010).

1.5 Connectivity

The relation between neuronal wiring structure and the corresponding dynamics is not straightforward. The interaction between single neurons generates emergent events where the collective system presents a greater complexity than the sum of its parts. For example, a fixed structural connectivity of a neuronal population provides a wide spectrum of sustained dynamical states (Battaglia et al., 2012; Deco and Jirsa, 2012); whereas similar dynamic regimes may arise from completely different structural layouts (Stetter et al., 2012).

One of the main challenges in neuroscience has been the study of the connectivity traits of neuronal networks and, consequently, the human brain. Although the structural information of a network is very important, it is not enough to properly characterize neuronal activity. The missing component is the intrinsic dynamics of the system. Neuronal activity, noise and the interaction of both may dictate the dynamics of the neural culture and, by extension, the whole brain. Consequently, it is necessary to consider both the architecture and the flow of information during activity.

Three visions stand in the spotlight when analysing neuronal circuits in the framework of network science (Figure 1.4): *structural*, where the nodes are actual neurons (or aggregates of them) and connections are the anatomical paths that connect them (neurites); *functional*, where the nodes are dynamic elements, and connections are statistical relations (such as cross correlation) between them; and *effective*, where the connections are causal interactions, *i.e.*, that a node directly influences the behaviour of another one (such as in information-based transmission). These three levels of representation can lead to very different networks (see Figure 1.4, although they may not be entirely independent and can influence one another).

1.5.1 Structural connectivity

The structural connectivity is the outline of the physical connections between all cell-pairs of a neuronal network. It is mainly related with the topography dictated by axons and dendrites. In this context, dissociated neuronal cultures emerge as a very appealing tool to study structural connectivity and its relationship with emerging network behaviour. Since cultures are highly manipulable, topological features can be imprinted at some extent with neuroengineering (Wheeler and Brewer, 2010), *i.e.*, in patterned cultures, giving rise in turn to a richer dynamic repertoire.

Structural neuronal networks have been described at different scales. At the microscopic scale, nodes correspond to single neurons, and the anatomical connections to neurites. Because of the extensive molecular and biological actors at play, the microscale description may fail at providing a clear picture of emergent collective phenomena. At the other extreme, at the macroscopic scale, brain regions are considered to be the nodes and the connections are associated with white matter, the connectivity tracts inside the brain. Consequently, the macroscale approach can provide interesting insights in terms of large-scale organization, but may lack the details to fully understand the human brain's functional dynamics and its information processing capabilities. The necessary scale that complements both descriptions is the mesoscale, where nodes correspond to neuronal populations, and the links to fibres of axons. In addition, emergent functional features typically occur at this scale, making the exploration of such systems of extreme interest.

1.5.2 Functional and effective connectivity

Functional and effective neuronal networks are grounded on dynamical observations. When information flow or causality is ignored, functional connectivity may be defined by means of statistical dependence between nodes that present activity (either firing single-cells, neuronal populations, network modules or macroscopic brain regions Friston (2011)). When causality

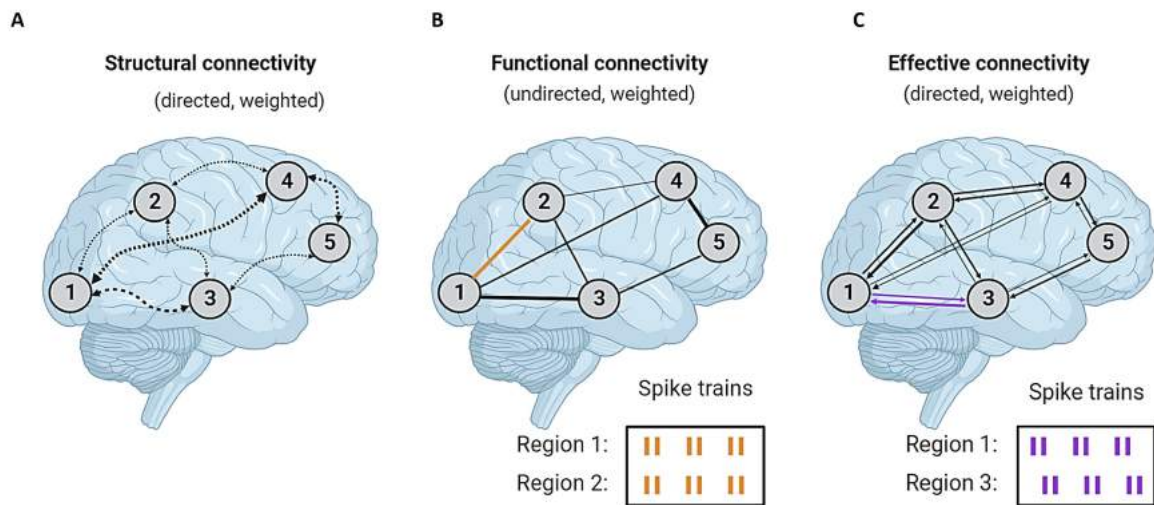


Fig. 1.4 Modes of brain connectivity. Sketches of the brain illustrate the classification of neuronal connectivity. **(A)** The structural connectivity of a neuronal network relies on fibre pathways between brain areas. Structural links are directed and weighted. **(B)** Functional connectivity is based on the statistical correlation between the signal of two brain regions. In the example, the spike trains of neurons on regions 1 and 2 are identical and activate at the same instant, meaning they are statistically connected, and thus functionally connected. Functional links are undirected and typically weighted, the latter represented in the sketch by different link widths between brain regions. **(C)** The effective connectivity is grounded on the causal information flow between brain regions. In the example, the profile of activation of region 3 is the same as the one of region 1 but with a temporal shift. That shift on the spike trains indicates that activity on region 1 causally affects the activation on region 3, so region 1 activates region 3. Effective connections are directed and weighted, the latter represented in the sketch by different link widths.

is included, effective connectivity is brought to light, which infers a directed relationship among firing neurons, *i.e.*, the influence that a node exerts on another (Figure 1.4). Thus, functional connectivity represents firing neurons that co-activate together, while the effective connectivity relates to ‘who activated who’ (Friston, 2011; Vicente et al., 2011). The functional or effective connectivity maps can be seen as a good proxy of neuronal dynamics and a wide spectrum of techniques have been developed with their advantages and limitations.

At lower scales, the neuronal firing of single neurons or the events associated to populations of neurons are measured typically through fluorescence calcium imaging or through micro-electrode arrays (MEAs). In particular, calcium imaging techniques have incredibly improved in the last decade which, combined with better fluorescence probes such as genetically encoded calcium indicators (Tian et al., 2009), have provided important advances in single-cell resolution and visualization of neuronal activity.

Regarding neuronal cultures, one of the main techniques used in the study of functional or effective connectivity is calcium imaging. This technique is grounded on the monitoring

of intracellular calcium concentration to detect neuronal activity (Gobel and Helmchen, 2007; Smetters et al., 1999). Specifically, single-cell internal Ca^{2+} concentration is measured by means of fluorescent probes. In the present Thesis, genetically encoded calcium indicators (GECIs) (Kotlikoff, 2007) have been used because they provide a similar spatial resolution with a fair temporal resolution compared to chemical calcium indicators like Fluo-8. Additionally, the GECI probes are not noxious, meaning that neuronal cultures do not suffer oxidative stress. This condition grants a better health of the living components and enables the possibility to monitor the evolution of the same culture over several weeks.

At the macroscale, these functional or effective maps are inferred from neuronal activity data provided by imaging techniques such as functional magnetic resonance imaging (fMRI) or electro-physiological techniques such as electroencephalography (EEG). The latter focuses on a multi-electrode array around the skull (Thakor and Tong, 2004) to detect electrical currents and voltage variations in different brain regions. On the other hand, fMRI is grounded on an indirect measure of neuronal activity by taking into account the blood rich-oxygenation needed when performing a specific task. Further details on this technique are explained in Chapter 1, Section 1.9.

In the present Thesis, we approached the functional connectivity of the human brain using fMRI imaging. fMRI is a non-invasive technique and has no side-effects to individuals that participate in the study. Additionally, it has a great spatial resolution and provides valuable information on the location of the detected fluctuations. On the other hand, temporal resolution is not that precise and therefore researchers often combine fMRI with EEG, which has a better temporal performance.

1.6 From neuronal cultures to the brain

As mentioned before, the interaction between functional/effective connectivity and the underlying structure —either in neuronal cultures or in the brain— can yield a vast repertoire of dynamical states difficult to explore. Neuronal cultures constitute a complementary tool for brain research since one can examine specific structural layouts and afterwards analyse their impact on the resulting functional/effective connectivity.

Nowadays, multiple research fields, such as physics, computational neuroscience, medicine, biology and psychology, embrace the use of cultures to understand brain functioning. For example, neuronal cultures have been used to identify key biochemical players in neurological disorders (Teller et al., 2015), allowed to model the role of noise in the spontaneous activity (Orlandi et al., 2013) and to reveal network architectural traits (Okujeni and Egert, 2019).

Nevertheless, the urge of understanding large-scale mechanisms compels the researchers to complement their studies by analysing the human brain.

1.7 The mammalian brain

The human brain is considered the most complex system in nature, which is composed by billions of cells (neurons) and millions of inter-cellular connections. These interactions between different units and regions contribute to information processing. Neuronal activity shapes main tasks such as perceiving sensory inputs, evoking memory or performing fine motor skills, among others. Thus, the brain provides an agile system of communication fast enough to receive and process information to rapidly interact with the environment we live in. However, the rules governing these processes and their underlying dynamical organization are yet not fully understood.

Neurons constituting the brain are highly specialized cells thanks to its morphology, and communicate to one another by transforming electrical signals into chemical ones and vice-versa. Neurotransmitters are signalling molecules that intervene in the communication between neurons. When a neuron receives a chemical input, it generates and propagates an electrical signal through its axon until it reaches its terminal. Then, the signal is again converted to a chemical signal and, through vesicles, neurotransmitters are released to the synaptic cleft to bind specific receptors and trigger new electrical signals.

However, individual neurons have rather slow dynamics (Von Neumann and Kurzweil, 2012) when compared to the speed of decision-making in the brain, where information is processed quickly. Some hypotheses point towards the idea that the brain uses parallel processing units to retrieve information and compute specific tasks. Hence, the functional behaviour of the brain may be the result of a collective phenomena, *i.e.*, its networking traits, rather than the isolated activations of the primordial elements, the neurons. A great example of this networking capacity is found in the cerebral cortex, the most external layer of the brain, as exposed next.

1.7.1 The mammalian cerebral cortex

The cerebral cortex corresponds to the outermost layer of the brain, composed of creased grey matter of 2 – 4 mm thick. It is folded forming ridges (gyri) and crevices (sulcus). In humans and other mammals, the cortex is separated into two hemispheres by the longitudinal fissure. Additionally, the cranial suture lines divide it into lobes with distinct functionality: frontal, parietal, occipital and temporal. The cortex plays a crucial role in various simple

functions, such as sensory information (vision or hearing) and somatic sensation (pressure or vibration) and also rather high-order functions, being responsible complex processes such as memory, language, cognition and motor control.

The cortex contains 10 – 20 billion neurons (S. von Bartheld et al., 2016) organized in six layers enumerated *I – VI* from the outer surface inwards. Each cortical layer presents differentiated neuronal shapes, sizes and densities as well as characteristic connectivity paths (Greig et al., 2013; Mountcastle, 1997). Roughly, neurons are essentially classified as excitatory pyramidal neurons, being those the vast majority, and inhibitory cortical interneurons locally connected within the neocortex (Lodato and Arlotta, 2015). Also, neurons from different horizontal layers connect vertically forming cortical columns (de No and Fulton, 1938; Mountcastle, 1997), considered to be the minimum functional element in the brain (DeFelipe et al., 2012; Mountcastle, 1997). From a functional point of view, the interconnection of repeated cortical columns gives rise to local neural circuits, a connectivity profile known as *modules*. Quite interestingly, functional properties of the cortex change drastically between adjacent horizontal points while they remain continuous along the perpendicular direction, *i.e.*, following the same cortical column.

When the concept of columns as functional modules is extrapolated to the whole-brain, it seems reasonable to expect the appearance of specialized regions and the need of hierarchical organization from one level of complexity to the next. From a cost-efficiency point of view, the segregation into inter-twinned functional modules provides a versatile reusing of resources and pathway routes. However, the parcellation of the cerebral cortex into functionally segregated networks presents a drawback when addressing the complex cortical integration to achieve higher functions. Anatomical studies (Gevins et al., 1990; Goldman-Rakic et al., 1993) have indeed revealed that subnetworks connecting different areas conform large-scale cortical networks. This observation strengthens the hypothesis that large-scale parallel processing of information may be supported by the anatomical architecture of the cerebral cortex. Additionally, some studies (Damasio, 1989; Liu et al., 2018) demonstrated the functional co-activation of multiple areas in large-scale networks, and neuropsychological studies (Mesulam, 1990; Posner and Rothbart, 1994) confirmed that coordinated large-scale networks mediate several different complex cognitive functions.

1.8 Animal models

The deterioration of the sophisticated network of connections that ensure a proper performance of the brain promotes the emergence of neurological disorders (Palop and Mucke, 2016). Consequently, many diseases are closely related to abnormalities in the cerebral cortex

that lead to cognitive decline or motor deficits. In this regard, animal models are a valuable tool to study neuronal dynamics during development, maturation and disease. In particular, rodents (mice and rats) present genetic and physiological similarities to humans and for this reason have been the most examined species in neuroscience research, especially given the lack of accessible human tissue. Rodents have been used both *in vivo* and *in vitro* to mimic neuronal diseases by replicating pathological symptoms (Dawson Ted M., 2018) applying biochemical strategies.

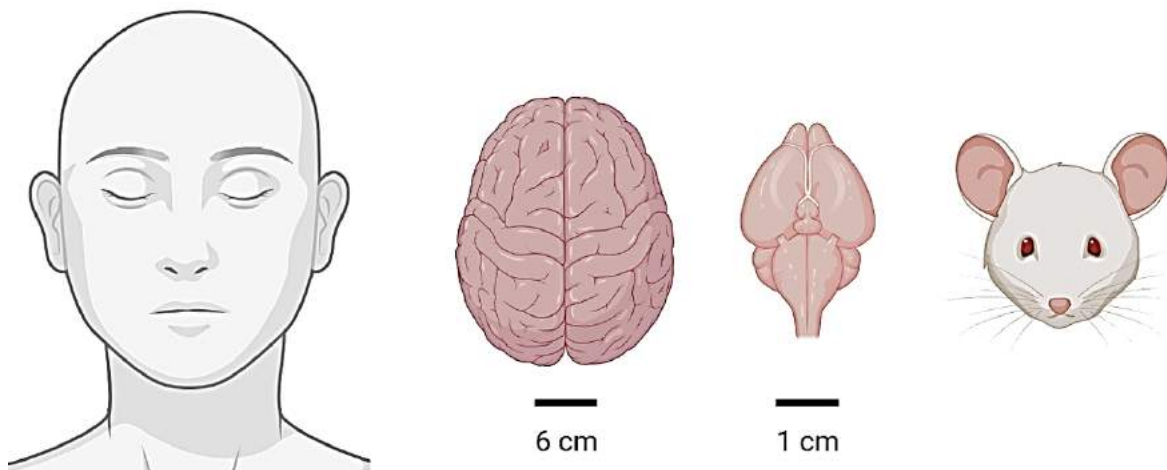


Fig. 1.5 The mammalian brain: humans and rodents. Illustration of the human brain and the rat brain, which at a glance have differences in size and shape. Additionally, the rat cortex is very smooth compared to the human brain, which has many sulci and gyri. Generated with *BioRender.com*.

As a word of caution, there are differences between a rat and a human brain. The former brain is smaller, the cortex is smoother instead of folded (Figure 1.5) and the thickness of the layers and the number of neurons varies considerably (DeFelipe, 2011). Human pyramidal cells are also anatomically different from rodents, as they have unique membrane properties and larger number of synapses per cell (Deitcher et al., 2017; Eyal et al., 2016). Although the process of cortex development seems to be consistent between rodents and humans, the generation of induced cortical neurons *in vitro* is slower in humans. Thus, on the basis of the clear differences between human and rodent's cortex the extrapolation and interpretation of results in this animal model should be done carefully.

1.9 fMRI and BOLD signal

Activity in the brain is characterized by rich spatiotemporal patterns that comprise diverse neuronal populations and timescales (Blankenship and Feller, 2010; Deco et al., 2008).

Interestingly, spontaneous activity is very broad and much more structured than neuronal activity when performing a specific task. Some studies concluded that these activations represent a fundamental mechanism for brain functioning as opposed to the previous idea that it was just background noise. Spontaneous activity in the brain is often called *resting state* (Deco and Jirsa, 2012; Deco et al., 2010), and it is believed to facilitate efficient communication among brain regions, provide alertness, quick response to stimuli and maintenance of neuronal circuits (Cohen and D’Esposito, 2016; Deco et al., 2010). The advances in brain functional and mapping techniques such as fMRI, EEG, or diffusion tensor imaging (DTI), together with resources from graph theory and signal processing, have facilitated the study of the relationship between resting state and brain functional decline. The deterioration of spontaneous activity is so crucial that may causes broad motor and cognitive alterations, as occurs in Parkinson’s, Alzheimer’s and other diseases (Deco et al., 2010; Fox and Greicius, 2010; Seeley et al., 2009).

fMRI is a non-invasive technique that measures the local fluctuations in cerebral blood flow. Within this technique, two paradigms are commonly studied, namely *task-related* responses and *resting state*. For the former, the human subjects under study are asked to perform a task during the fMRI registration. For the latter, subjects confront no stimuli and are asked to avoid any task-oriented activity (from motor movement to mental concentration) while the fMRI instrument measures brain activity.

Since no specific task is conducted during ‘resting state’ measurements, this technique has been widely used to measure patterns of synchronous and spontaneous activations (Yang et al., 2020). A substantial number of studies in healthy participants (Onoda and Yamaguchi, 2013; Oschmann et al., 2020; Vaqué-Alcázar et al., 2020) and populations involving cognitive decline pathologies and other disorders, such as mild cognitive impairment, Alzheimer’s disease or major depression (Damoiseaux, 2012; Siegle et al., 2006; Zhou et al., 2008) have been published using this technique. Therefore, the resting state approach has become popular not only to pinpoint neurological disorders, their progress, and the goodness of therapies, but also to disentangle age-related differences in functional connectivity, as described for instance in Farras-Permanyer et al. (2019) and Geerligs et al. (2017).

The fMRI technique uses the hemodynamic response of the brain to infer its dynamic state, although this response is not directly related to the neuronal activity. Conceptually, the post-synaptic activity between neurons generates a localized increase in blood flow oxygenation level (Figure 1.6). Then, and more importantly, oxygen-rich blood shows different magnetic properties than oxygen-poor blood, which is caused by the presence of the hemoglobin that binds to oxygen. Thus, the tiny differences in the magnetic properties of the neuronal tissue can be detected with the appropriate instrument. However, it must

be clear that the measurement of activity is *indirect*, *i.e.*, the observed changes in magnetic resonance signal are an effect related to the changes in blood flow that follow the changes in neural activity (Matthews et al., 1999). This ‘indirect’ nature of the signal makes it prone to artifacts and miss-interpretations, as discussed, *e.g.*, in the important work of Logothetis (2008).

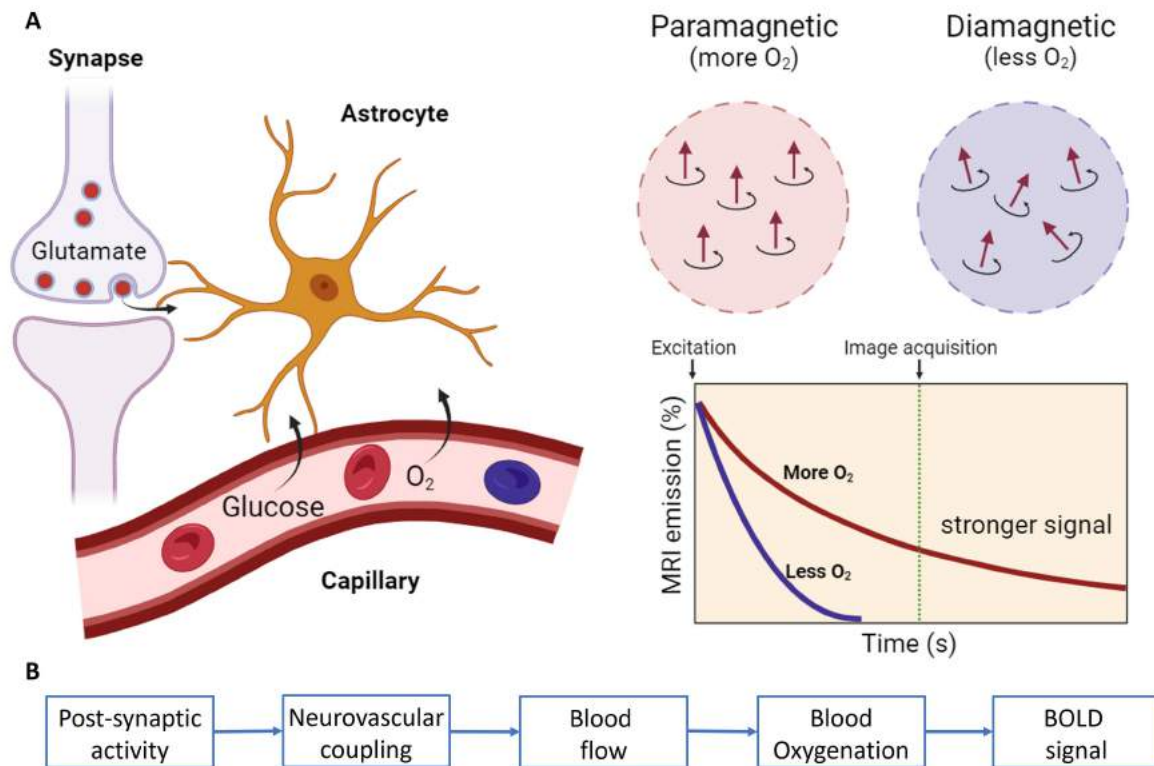


Fig. 1.6 Blood oxygen level-dependent signal. (A) Sketch of BOLD signal properties. Blood stream has to provide oxygen and glucose to neuron cells, which means that an increase in neuronal activity correlates with a decrease of oxygen levels in blood vessels. To indirectly measure this neuronal activity fMRI, scanners use a nuclear magnetic pulse to evaluate the magnetic behaviour of the tissue. Haemoglobin, the protein that transports oxygen in red cells is paramagnetic when empty of oxygen and diamagnetic when has it and changes its orientation under a magnetic field. Therefore, oxygen-free haemoglobin shows weaker signal allowing to indirectly detect neural activity. Image generated with *BioRender.com*. (B) BOLD signal chart flow. Some complex biological processes as neurovascular coupling take place and yield a localized increase in blood oxygenation that are measured in the BOLD fMRI technique. Adapted from Bijsterbosch et al. (2017).

To obtain meaningful data from a fMRI instrument, the hemodynamic response (Figure 1.7) represents the transfer function that links the neuronal activity with the magnetic resonance signal (Blamire et al., 1992). At the microscopic level, a neuron consists of a cell body that receives upstream inputs through dendrites and passes action potentials through

axonal tracts to other downstream cells using neurotransmitters such as glutamate. These microscopic processes result in a localized increase in blood flow that exceeds the oxygen demands of neuronal activity, leading to a local increase in blood oxygenation level. Several studies have shown a strong link between spontaneous fluctuations in resting state BOLD data and slow fluctuations in the local field potential (LFP). Therefore, the BOLD signal is thought to primarily reflect the excitatory inputs of the neural population, a concept termed *synchronized post-synaptic activity* (Bijsterbosch et al., 2017).

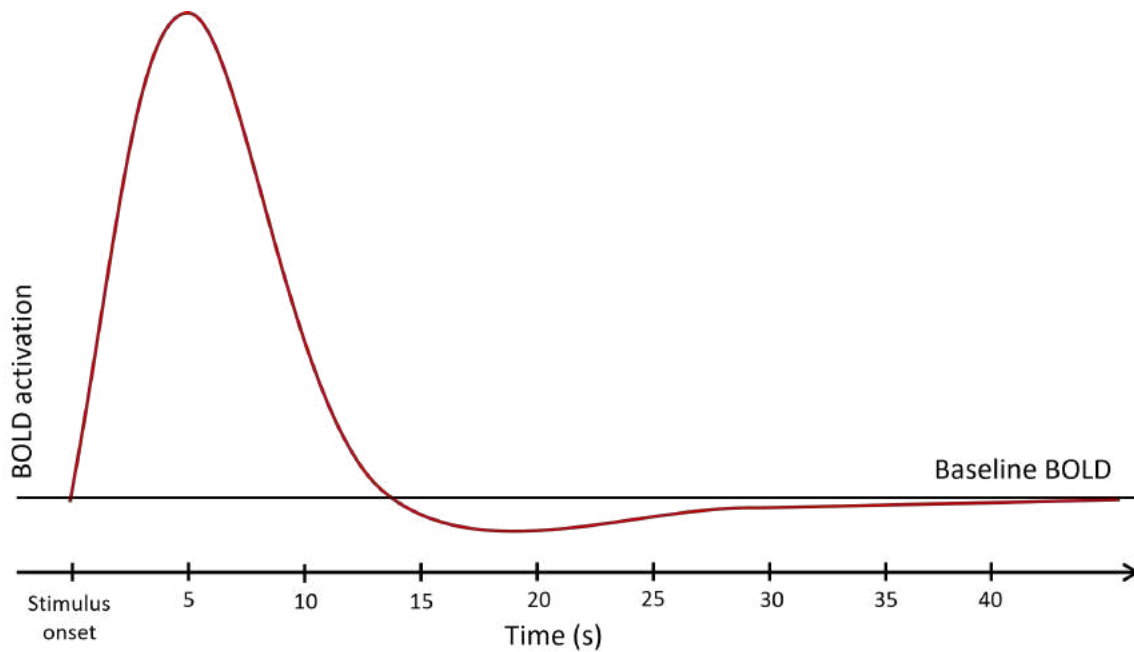


Fig. 1.7 Timing of the hemodynamic response function. The standard form of the hemodynamic response function is shown. The BOLD signal takes approximately 5 seconds to reach its maximum after the stimulus onset. Adapted from Bijsterbosch et al. (2017).

An important aspect of the BOLD signal, and that makes data analysis and interpretation difficult, is the different timescales at which processes occur. Indeed, blood flow starts to increase within seconds after the increase of neuronal activity and it peaks around 5 seconds after it. However, neural firing occurs at the rate of milliseconds, which implies that the BOLD signal measured in fMRI is not only an indirect measure, but also a delayed and temporally imprecise measure of neuronal activity.

1.10 Healthy aging

In the last decade, the average health life expectancy at birth of the worldwide population, especially in developed countries, has raised significantly. In Spain, life expectancy at birth has followed a sustained increasing tendency for the last 20 years (see Table 1.1; Ministerio de sanidad (2021); Ministerio de sanidad política social e igualdad (2010)). The main factors contributing to this increase in population's life expectancy are, among others, the medical advances achieved along the last years, the development of more effective drugs —or with fewer side effects— which grants better quality of life to people, and specially to the elderly ones.

Table 1.1 Life expectancy at birth (in years) in Spain (1996-2021)

Year	1986	1999	2007	2015	2021
Total	76,4	79,4	81,1	82,8	83,2
Males	73,2	76,1	77,8	80,1	80,3
Females	79,6	82,8	84,3	85,5	86,1

This rapid aging process is having a substantial impact on society in many aspects such as economical, by the investment in retirement aids; social, by increasing demand of specialists who take care of the ones in need and in the health care system, by developing new drugs for chronic diseases. Additionally, some individual changes are also remarkable. Physically, elderly people tend to suffer from loss of muscular strength (Brooks and Faulkner, 1994), visual alterations and an impairment on fine motor skills (Association et al., 2017). In addition, some significant changes in the personality traits are worth mentioning. Elderly people are prone to experience short-term memory loss, a reduced capability of learning new skills (Association et al., 2017) or a higher risk of suffering from depression (Kessler et al., 2010).

Another key factor that has to be accounted for when analysing the aging process are the changes the brain undergoes through the passing of time. Fjell and Walhovd (2010) reported the loss of volume in some brain regions —hippocampus, thalamus and amygdala—, an increase of the ventricles and the sulci and the loss of grey and white matter, *i.e.*, the loss of neuronal tissue and its connections, that is, myelinated axons. Despite aging may be associated with the appearance of a pathology, either physical or psychological, it is important to keep in mind that the aging process itself entails several intrinsic changes often referred as *healthy aging*. The world health organization (WHO) and the scientific community defined healthy aging as the process of aging that preserves the cognitive capabilities of the individ-

ual and under the condition of not developing any psychopathology or neurodegenerative disease (World Health Organization, 2016). Nonetheless, the brain changes with the passing of the years and some cognitive capabilities start to decline.

Some research groups focused on exploring the connectivity through the healthy aging process and found an increase in inter-network connections with a decrease in intra-network links (Geerligs et al., 2015; Huang et al., 2015). Seidler et al. (2010) hypothesized that this increase in connectivity was a compensatory mechanism, where the brain needs to use more resources to perform the same task with no evidence of cognitive alteration. In an exhaustive bibliographic review, Damoiseaux (2017) concluded that functional changes mainly affect the default mode network (DMN), a network of diverse functional networks, *e.g.*, sensorimotor or visual, that is specifically active when the individual is at rest (Farras-Permanyer et al., 2019). Elder participants of the latter study would have their DMN connectivity compromised, showing less inter-network links and thus, less functional segregation. Additionally, the correlation between the increase in connectivity and age might indicate the appearance of a present or a future cognitive impairment.

Another factor that might play a key role in cognitive performance and functioning of the brain is the cognitive reserve (CR). CR is the resilience of the adult brain against specific pathologies to minimize its symptoms or appearance (Stern, 2002). The CR was postulated to explain the evidence that there was no direct relationship between the severity of brain damage and the clinical manifestation of the neurological alteration. Additionally, CR varies through individuals and it is thought to be related to several factors (Valenzuela and Sachdev, 2006), such as the education level, the development of high-demand cognitive activities or the presence of social networking.

1.10.1 Brain changes in healthy aging

Understanding the age related anatomical, functional and neuropsychological changes of the brain might help in developing accurate detection tools and biomarkers (Blazer et al., 2015). Regarding structural changes related with age, Damoiseaux et al. (2008) found a reduction on grey matter, especially in the occipital lobe, anterior and posterior cingulate cortex, precuneus, insula and the central sulci. Also, a performance decline involving memory, processing speed, attention and executive functioning when exploring the changes in neuropsychological performance was observed (Damoiseaux et al., 2008).

Considering functional connectivity, a decline of connectivity in the resting state networks—such as DMN, auditive salience networks, sensorimotor and visual subnetworks— was detected (Farras-Permanyer et al., 2019; Huang et al., 2015). Additionally, some studies have applied network analysis to explore the functional connectivity between brain regions

and found interesting results concerning some networking traits. The definition of such networking measures are discussed in Chapter 5, Section 5.4.

Xu et al. (2015) demonstrated a decrease in the global brain network density, specifically in the occipital and temporal lobes. Sala-Llonch et al. (2015) observed a paradoxical increase with age in both segregation and integration of the network and Onoda and Yamaguchi (2013); Xu et al. (2015) noticed a decrease in the small-world coefficient of the network. Also, a decrease of both modularity and local efficiency of the DMN network was observed when comparing elder and younger participants (Cao et al., 2014; Song et al., 2014a), meaning that the network becomes less specific as brain ages. In addition, synchronization between neuronal assemblies in the developing hippocampus has been related to the existence of superconnected nodes in a scale-free topology (Bonifazi et al., 2009); efficient information transfer has been associated to circuits with small-world features (Latora and Marchiori, 2001) and Hagmann et al. (2008); Meunier et al. (2010) hypothesized that the coexistence of both segregated and integrated activity in the brain is strongly related to a modular circuit architecture.

1.11 The brain as a complex system

It is known that the brain circuitry is comprised by around 10^{11} neurons and 10^{14} synapses (Herculano-Houzel, 2009; Pakkenberg et al., 2003). However, the complexity of the human brain resides not only in the high number of neurons and connections, but also in their interactions, *i.e.*, the great repertoire of dynamical states that occur at different temporal and spatial scales (Buzsaki and Draguhn, 2004; Honey et al., 2007). Exploring the brain as a complex system is one of the major challenges of the last decade and multiple approaches have emerged, specially at the mesoscale.

First, graph theoretical analysis aimed to examine the anatomical connection patterns between brain areas in the cat cerebral cortex and monkey (Hilgetag et al., 2000; Scannell et al., 1995; Young, 1993). Later, structural analysis (Gong et al., 2009; He et al., 2007) and functional human brain explorations (Achard et al., 2006) were performed. Specifically, the topological organization in functional human brain networks is inferred from data measured in healthy human volunteers while not performing any particular task, *i.e.*, 'at rest' (Deco et al., 2011; Wang et al., 2009).

Many research groups are devoted to exploring and developing statistical or biochemical metrics that contribute to the understanding and interpretation of functional connectivity networks. Consequently, these connectivity markers might help characterizing, classifying and providing conceptual significance to neuronal networks. A broad variety of brain

network studies —either using fMRI, EEG or DTI— are grounded on graph theoretical approaches (Cao and Slobounov, 2009; Sotiropoulos et al., 2010; Vecchio et al., 2015). Rubinov and Sporns (2010) defined and analysed the main networks metrics and their interpretation in the framework of computational neuroscience. Complementary, Fornito et al. (2016) grounded the interpretation of functional network traits on various factors, such as the segregating–integrating balance, the community distribution, the link density or the presence of some nodes that play a critical role in the structure of the network (Deco et al., 2015; Friston, 2009).

1.11.1 The segregation–integration balance

From a complex networking approach, a crucial aspect to analyse is how neuronal networks are able to retrieve, process and communicate information. To perform such computational tasks, the organization of anatomical and functional cortical networks is guided by two basic principles: segregation and integration (Friston, 1997; Tononi et al., 1994).

The term segregation refers to a specialized, organized neuronal population (community or module) which selectively respond to specific input features or combination of features. Nevertheless, a coordinated activation —functional integration— of large neuronal groups from the cerebral cortex is required to achieve superior high–performance tasks, such as coherent perception and cognitive states (Bressler, 1995; Srinivasan et al., 1999).

As a whole, large–scale cortical networks exhibit highly heterogeneous structures as well as distinct clusters with hierarchical organization (Hilgetag et al., 2000), a specific composition of structural and functional motifs (Sporns and Kötter, 2004). A highly integrated network with specialized modules is likely to provide high complexity dynamics. This segregation–integration balance (Deco et al., 2015) may happen at different scales, and it is believed that optimal brain function, synchronization and correct information flow are consequences of a fast switching between integration and segregation regimes (Sporns, 2013; Stam, 2014).

1.11.2 Brain complex network traits

The complex network theory (Alon, 2007; Barrat et al., 2008; Dorogovtsev and Mendes, 2003; Newman, 2010) is founded in the representation of the elements of a system as nodes of a network, and the interactions between those nodes as links or connections. The number of links connected to a node is termed *degree*. The *degree distribution* $p(k)$ is the probability to find a node with degree k randomly chosen. Many complex networks follow a ‘scale–free’ distribution, defined by a power law $p(k) \sim k^{-\gamma}$, with typically $2 < \gamma < 3$. This particular

distribution leads to a high number of low-degree nodes with a small number of high-degree ones. The high-degree nodes, often termed *hubs*, ensure a high level of global connectivity since they cope with much of the information flow (Barabási and Albert, 1999; Barabási and Bonabeau, 2003; Grigorov, 2005; Van Den Heuvel et al., 2013).

A prominent example of such correlations is assortativity (Teller et al., 2014), which describes networks in which nodes preferably attach to other nodes with similar degree. Assortativity is believed to play an important role in brain networks since it may provide a subnetwork of highly connected nodes where information flow can be reorganized in case of damage.

Indeed, the segregation–integration balance seems to govern the functionality of the brain (Stam, 2014; Tononi et al., 1994) and the integration of multiple functional regions leads towards a hierarchical network (Hilgetag et al., 2000). Modern network science has pinpointed that healthy brain networks exhibit small–world features which shape a cost–efficient configuration (Watts and Strogatz, 1998). Specifically, a small–world blueprint implies a strong local connectivity —high clustering coefficients—, with efficient long distance connections, *i.e.*, the information needs fewer steps to reach the furthest nodes —short path lengths— (Achard et al., 2006; Hagmann et al., 2008; Meunier et al., 2010; Sporns and Zwi, 2004). Since small–world networks present short average distances (like random graphs) and high clustering coefficients (like regular lattices), these networks have a high value of global and local efficiency (Watts and Strogatz, 1998). Then, small–world networks are extremely efficient in exchanging information both at a global and at a local scale (Boccaletti et al., 2006; Latora and Marchiori, 2001).

Related to efficiency of neuronal networks, modularity is a network trait that implies the aforementioned community association of neurons mediated by a few inter–module links that govern their integration (Blondel et al., 2008). Modularity is considered a measurement of segregation of the network and, typically, efficient networks tend to be modular, since they allow faster adaptability to environmental changes. Healthy brains are thought to present a hierarchical modular dynamics, where modules are associated to specific cortical functions such as motor tasks or sensory processing (He et al., 2009; Meunier et al., 2010).

1.12 Outlook of the present Thesis

One of the greatest challenges in the field of neuroscience is to obtain a more accurate functional description of the brain that allows us to understand the functioning of higher–complexity cognitive processes such as memory or consciousness. fMRI–BOLD signal acquisition and calcium fluorescence recording are two of the main techniques that stand out

when exploring functional connectivity of complex systems. Although both methodologies are grounded in different physical principles, and occur at different length scales, they may be complementary when describing neuronal functional connectivity.

Henceforth, the main objective of this Ph.D. Thesis was to consider approaches that connected a mesoscopic representation with a macroscopic one, but both grounded in the functional organization of two different yet complementary complex systems, namely neuronal cultures and the brain, and in the context of a healthy development. To achieve this objective, two parallel lines of research were conducted: (i) The development of primary neuronal cultures on top of topographical surfaces and the characterization of the functional traits and dynamical richness of the underlying spontaneous activity. (ii) The analysis of fMRI signal of healthy participants and the characterization of the functional networks that arise from the connectivity matrices.

The Thesis is organized as follows. Chapter 2 enunciates the objectives of the present Thesis. Chapter 3 describes all experimental protocols and tools for culturing rat primary cells in 2D. Chapter 4 details all experimental protocols and tools to acquire, process and analyse fMRI data. Chapter 5 reports the set of network traits and statistical analysis implemented in the Thesis to understand both *in vivo* and *in vitro* approaches. Chapter 6 describes the successes with neuronal cultures on topographical reliefs in which we could explore the impact of physical constraint on the dynamic repertoire of spontaneous activity. Chapter 7 details our successes with the analysis of fMRI recordings on a sample of healthy participants in which we could advance in the exploration of possible biomarkers that predict healthy aging. Chapter 8 elaborates a general discussion that provides a bridge between the mesoscopic analysis conducted with primary neuronal cultures and the large-scale approach rendered by the fMRI data. Finally, Chapter 9 summarises the main conclusions and take-home messages.

Chapter 2

Objectives

This Thesis covers a multi-scale experimental and analytical study at the interface between physics of complex systems and clinical neuroscience, from neuronal cultures to the whole brain. Its main objectives are:

- Establish a baseline firing behavior (control group) of 2D homogeneous cultures on a flat surface by monitoring the resting state (spontaneous activity) of neuronal networks derived from rat primary neurons (Chapter 3, Section 3.4.).
- Generate physical perturbations in the form of topographical modulations as ‘square’ or ‘tracks’ patterns, and monitor their behaviour (Chapter 3, Subsection 3.2.1).
- Characterize the spatiotemporal complexity of the topographical cultures, and interpret them in the context of the underlying, imprinted anisotropies in connectivity (Chapter 3, Section 3.4).
- Analyse and compare the propagation velocity and the initiation points of spontaneous activity in all neuronal cultures (homogeneous, square and track configurations) (Chapter 3, Subsection 3.4.6).
- Develop a computational framework to understand the impact of spatial constraints on the connectivity and dynamics of the neuronal cultures recorded in the laboratory. (Chapter 3, Subsection 3.4.7).
- Characterize the properties of the fMRI brain signal as a tool to understand the brain functioning as a complex system (Chapter 4, Chapter 5).
- Analyse the low-frequency fluctuations and homogeneity of the fMRI signal in healthy population to describe the process of healthy aging (Chapter 4, Section 4.4).

- Analyse the impact of filtering and thresholding in the fMRI functional network (Chapter 4, Section 4.5).
- Extract functional connectivity traits in healthy aging populations and compare different approaches (Chapter 5).

Chapter 3

Experimental Procedures *in vitro*

Neuronal cultures are one of the most celebrated techniques in several multidisciplinary research fields, including physics of complex systems, neuroengineering and medicine. Despite their divergence from a fully grown brain in terms of scale and organization, neuronal cultures constitute a closed, simple and highly reproducible environment of interconnected neurons that can be easily accessed in the laboratory (Figure 3.1). Overall, neuronal cultures shape a powerful tool to *play* with a living complex system, allowing to design wide spectrum of connectivity configurations and measure their spontaneous activity, from which functional connectivity traits and an analysis of the structure–function can be carried out.

This Chapter aims to provide a detailed description of the experimental procedures *in vitro* used in this Thesis. We will also present the tools and strategies that were devised to monitor their behaviour in a microscope and extract their most important characteristics.

3.1 Rat primary cultures

In this Thesis we have explored primary neuronal cultures derived from embryonic rat cortical cells. Since neurons at embryonic stages 18–19 present fewer connections compared to maturer ones, it is easier and less harmful to mechanically dissociate them after extraction and successfully plate them on a surface, ensuring their survivability and capacity to establish a *de novo* network.

The simplest neuronal cultures that one can design are termed *homogeneous cultures* in which neurons, after dissociation, are plated uniformly on top of the surface they are going to develop. Indeed, neurons can move freely on the substrate since neurites' tension promotes neuron's motility and coalescence (de Santos-Sierra et al., 2014; Segev et al., 2003), a mechanism of aggregation that, if it is not prevented, gives birth to clustered cultures (Teller et al., 2014). To maintain homogeneity throughout the maturation of the culture it is necessary



Neuronal culture	Brain
~ 5000 neurons	~ 10^{11} neurons
Scarce neuronal cell types and neurotransmitters	Rich repertoire of neuronal cell types and neurotransmitters
Absence of external input/stimuli	Sensory input + resting state
Excitatory and inhibitory neurons	Excitatory and inhibitory neurons
Bursting spontaneous activity	Multi-scale spontaneous activity
2-dimensional cellular structure	3-dimensional cellular structure

Fig. 3.1 Summary of the neuronal culture and brain features. Representative characteristics of the *in vitro* neuronal cultures and brain as complex systems.

that the substrate is coated with adhesive proteins. The protocols for the preparation of these cultures are described later, but were essentially adapted with minor modifications from Refs. Breskin et al. (2006), Cohen et al. (2008b) and Soriano et al. (2008).

All experimental procedures with primary neuronal cultures were carried out in accordance with the regulations of the Ethical Committee for Animal Experimentation of the University of Barcelona (protocol code B-RP-094/15-7125 of July 10th, 2015) and the laws for animal experimentation of the Generalitat de Catalunya (Catalonia, Spain). All neuronal cultures used in our experiments were prepared, maintained and monitored at Jordi Soriano's Lab, at the Physics Faculty of the University of Barcelona.

3.1.1 Primary neuronal cell cultures

Neurons were extracted from cortical tissue of Sprague–Dawley embryonic rats at days 18–19 of development. Cortical neurons were used for two reasons. On the one hand, embryonic cortices are located on a peripheral region of the brain and makes them easily accessible for extraction without damaging the neuronal tissue. On the other hand, the embryonic cortical neurons extracted present a stable combination of two neuronal cell types: 80% excitatory pyramidal neurons and 20% inhibitory interneurons, a ratio that is maintained *in vitro* (Soriano et al., 2008), allowing to investigate the impact of excitatory–inhibitory balance on network's collective dynamics. Rats were provided by the animal farm of the

University of Barcelona, deceased with CO₂ at the same facility and gently transported to Soriano's laboratory for dissection. For clarity, all chemicals and solutions used for the culture preparations are summarized in Table 3.1.

Dissection was carried out in ice-cold L-15 medium (Gibco), cortical tissue dissociated mechanically by repeated pipetting, and neurons suspended in plating medium [90% Eagle's Minimum Essential Medium (MEM, Invitrogen) with 5% Horse Serum (HS, Invitrogen), 5% Bovine Calf Serum (Invitrogen) and 1 μ l/ml B27 (Sigma)]. Prior culturing, the substrate in which neurons would be plated was submerged overnight in a solution containing the adhesive protein Poly-L-Lysine (PLL, Sigma-Aldrich) at a concentration of 10 mg/ml PLL in Borate Buffer. Neurons were plated with a neuronal density of about 400 neurons/mm² and were homogeneously distributed over the surface, although some aggregation existed. One day after plating, cultures were infected with the adeno-associated virus bearing the GCaMP6s calcium sensor under synapsin-I promoter (AAV9.Syn.GCaMP6s.WPRE.SV40, Addgene). Four days afterwards, at day *in vitro* (DIV) 5, plating medium was replaced by changing medium (90% MEM, 10% HS and 0.5% FUDR) to limit glial growth. At DIV 8 the medium was switched again to final medium (90% MEM and 10% HS) and refreshed periodically every 3 days. Table 3.1 summarizes the media and its composition utilised in this Thesis.

Only neurons expressed the calcium sensor under the synapsin-I promoter. Thus, although cultures contained both neurons and glia, only neuronal activity was visualized. As explained later in Section 3.2, neurons were plated on substrates that were either flat or that contained physical constraints. In either case, the substrates were made of polydimethylsiloxane (PDMS). To maximize laboratory resources, these PDMS substrates were shaped as discs of 6 mm in diameter and 1 mm high that were attached to glass coverslips. Each pair of PDMS discs, after coating and neuronal seeding, were placed on 4-well plates (Nunc), in which only two wells were used, thus totalling 4 PDMS cultures. This facilitated the consecutive recording of different cultures while minimizing possible alterations in those wells that were not recorded at that moment. Additionally, depending on the experiments planned, between one and three 4-well plates were prepared per week (from 4 to 6 effective cultures). Neuronal cultures were incubated at 37°C, 5% CO₂, and 95% humidity. Spontaneous activity emerged by DIV 5, but GCaMP6s expression was not sufficiently strong for reliable imaging until DIV 7.

3.1.2 Immunocytochemistry

Immunocytochemistry (ICC) is a technique used in biochemistry research that uses antibodies to identify specific antigens or proteins in a sample cellular population. Primary antibodies

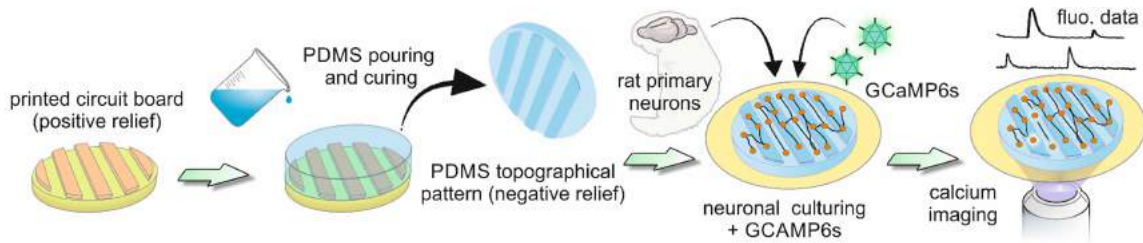


Fig. 3.2 Sketch of the experimental setup and procedure. A printed board circuit with a topographical relief $70\ \mu\text{m}$ high (orange) was used as a master mold to pour and cure PDMS on it, leading to a design (blue) that is the negative relief of the original mold. Neurons were cultured on it in combination with GCaMP6s, delivered through adeno-associated viruses (AAVs). Spontaneous neuronal activity was then monitored through calcium fluorescence imaging.

Table 3.1 Primary cultures media

Medium	Composition
L-15 Solution	L-15, 0.6% Glucose, 0.5% Gentamicine, O_2
MEM+3G	MEM, 1% glutamax, 4%, Glucose, 0.4% Gentamicine
Plating medium	MEM+3G, 5% Fetal Bovine Serum, 5% Horse Serum, 0.1% B27
Changing medium	MEM+3G, 0.5% Uridine, 0.5% FUDR, 10% Horse Serum
Final medium	MEM+3G, 10% Horse Serum
PLL solution	Borate Buffer, 16.6%, Poly-L-Lysine

bind to target proteins while secondary antibodies are conjugated to a fluorophore that emits at a given wavelength λ . Before staining, it is necessary to fix the cell culture in order to preserve cell structure and permeate the membrane so that antibodies can penetrate the membrane and reach inner compartments. ICC was used in our experiments to verify the successful plating of healthy neurons and gain insight on connectivity traits in relation to imprinted spatial constraints.

ICC was performed at the facilities of the Faculty of Medicine under the supervision of our collaborator Dr. Daniel Tornero. Neuronal cultures were fixed with 4% Paraformaldehyde (PFA, F8775 Sigma-Aldrich) for 15 min at room temperature. Afterwards, cultures were rinsed twice with Phosphate-buffered saline (PBS) and stored at $4\ ^\circ\text{C}$. For the staining process, samples were incubated with blocking solution containing 0.03% Triton (Sigma) and 5% Normal Donkey Serum (Jackson Immunoresearch) in PBS for 45 minutes at room temperature. Primary antibodies against neuronal cytoskeleton (β 3-Tubulin and MAP2, Table 3.2) were applied diluted in blocking solution at ratios 1:100-1:1000 and incubated overnight at $4\ ^\circ\text{C}$. Hereafter, cultured samples were washed three times with PBS and incubated for 90 minutes at room temperature with a blocking solution containing diluted

Alexa488-conjugated secondary antibody against mouse (Sigma, A10667). For astrocytic staining, samples were post-fixed again and incubated with anti-GFAP antibody directly conjugated with Cy3 (Table 3.2) overnight at 4°C.

Before imaging, immunostained cultures were rinsed again three times with PBS, submerged in milli-Q water to remove salts and mounted on glass microscope slides (Superfrost Plus, Fisher Scientific) using a drop of DAPI-fluoromount–G (ShouthernBiotech). Finally, ICC images were acquired on a Zeiss confocal microscope (LSM-880) at the Faculty of Medicine. Table 3.2 summarizes the immunostaining combinations applied to the present Thesis.

Table 3.2 Primary antibodies

Antigen	Stains for	Company	Origin	Code
Tuj1	Neurons and processes	Sigma	Mouse	T8660
MAP2	Neurons' nuclei	Sigma	Mouse	M1416
GFAP-Cy3	Glia	Sigma	Mouse	C9205

3.2 Modulating neuronal culture substrates

Neuronal cultures are well-known for their capacity to exhibit spontaneous activity. However, neurons grown on flat surfaces exhibit a strongly coherent activity (Orlandi et al., 2013; Tibau et al., 2013) in which neurons activate all at the same time in the form of a *network burst* and remain quiescent in between bursts. To approach our main objective and tune the functional richness of naturally formed neuronal circuits, we explored different methods to imprint anisotropies in the surface where neurons were plated. On the one hand, we prepared polydimethylsiloxane (PDMS) topographical reliefs with two different configurations, ‘tracks’ and ‘squares’, which emerged from the flat surface by typically 70 μm and effectually set the neurons in two layers (Figures 3.2 and 3.3A). On the other hand, we aimed at replicating the work of Yamamoto et al. (2018) by chemically stamping predesigned reliefs on a 13 mm glass coverslips with assistance of adhesive proteins (Figure 3.3B).

3.2.1 PDMS topographical reliefs

Topographical substrates were prepared by using a specially designed printed circuit board—manufactured by 2CI Circuitos Impresos (Barcelona, Spain)—that served as a negative mold for the desired topographical design. As shown in Figure 3.4A, the printed circuit was

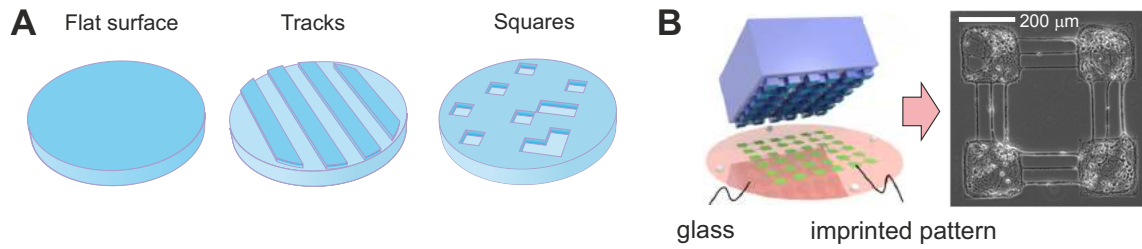


Fig. 3.3 Shaping patterned substrates. (A) Conceptual illustration of PDMS topographical reliefs, comparing a flat standard culture (left), a ‘tracks’ configuration (centre) and a ‘squares’ one (right). The structure of crevices and valleys break the isotropy of a standard culture and promotes a more complexity connectivity. (B) Patterned networks made by imprinting adhesive proteins on a glass substrate, producing a modular network. Adapted from Yamamoto et al. (2018).

formed by two layers, a bottom one of uniform fiberglass 2 mm thick and a top one of copper deposits 70 μm high that shaped different designs. This height of the copper was constant along the board. For the present Thesis, two main designs were used and termed ‘tracks’ and ‘squares’ (Figure 3.4B). ‘Tracks’ consisted of parallel rectangular bands 300 μm wide and 20 mm long and separated by 300 μm . ‘Squares’ consisted of randomly positioned squared blocks of either 300 or 600 μm in lateral size. Blocks were placed following a grid of 300 or 600 μm spacing, so that there was no overlap between blocks and the spatial dimensions of the resulting designs were all multiple of the basic square dimensions. The blocks were laid on a $20 \times 20 \text{ mm}^2$ area and occupied 15% of it. PDMS (Sylgard 184, Farnell) with a mixture of 90% base and 10% curing agent was poured on the printed circuit board and cured at 90°C for 2h (Figure 3.4C). The PDMS was then gently removed, shaping a topographical relief in which the copper and fiberglass on the original board corresponded to depressions and crevices on the PDMS, respectively.

PDMS discs of 6 mm in diameter and typically 1 mm thick were then pierced using stainless steel punchers (Bahco 400.003.020), carefully washed, dried, and attached to glass coverslips (#1 Marienfeld-Superior). A coverslip contained two PDMS discs (Figure 3.4D). Different sets of coverslips containing PDMS were prepared and sterilized in an autoclave (Selecta 4002515), which in turn strongly bond the PDMS to the glass surface. A detail of the ‘Tracks’ and ‘Squares’ designs ready for culturing are provided in Figure 3.4E. The shown bright-field images are accompanied of simple sketches to clarify which are the top and down areas of the designs. Since the copper in the printed board was very smooth, the corresponding PDMS depressions were transparent when observed under bright-field microscopy, whereas the slight roughness of the fiberglass led to PDMS crevices that appeared opaquer. These slight differences in opacity did not affect calcium fluorescence imaging on neurons over the relief. To compare neuronal network dynamics with and without topography, flat PDMS discs

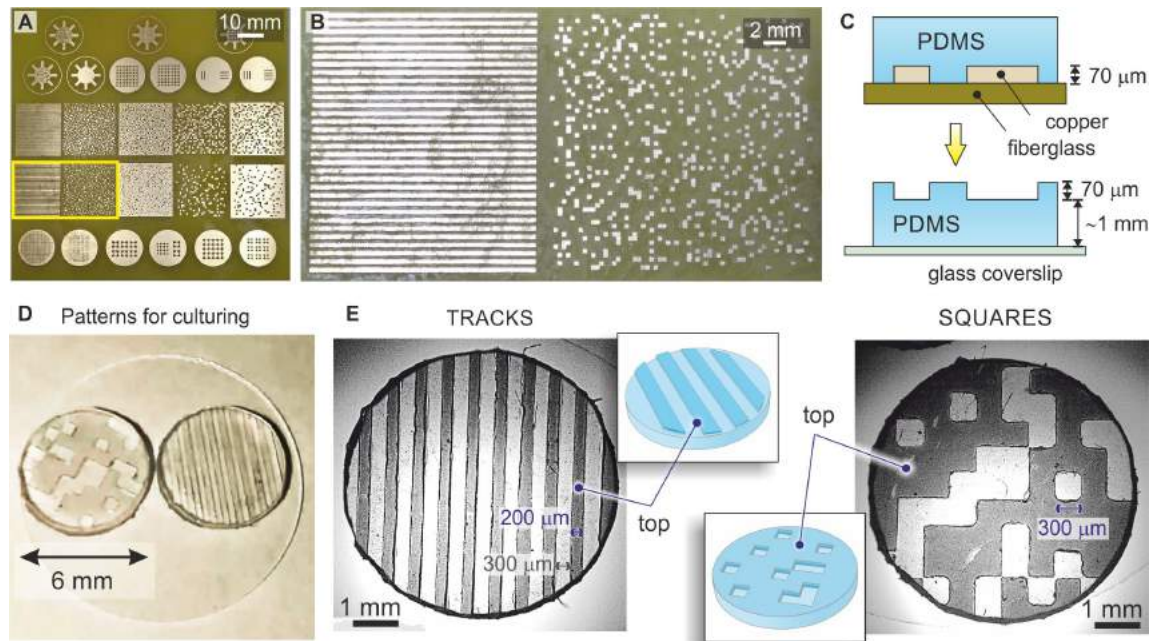


Fig. 3.4 Preparation of topographical PDMS substrates. (A) Printed circuit board containing different designs. Copper (bright gold) elevates over the fiberglass (dark green) by $70\ \mu\text{m}$. The yellow rectangle highlights the designs used in the present study. (B) Detail of ‘tracks’ (left) and ‘squares’ (right) designs. For tracks, copper tracks elevations are $200\ \mu\text{m}$ thick and are separated by crevices $200\ \mu\text{m}$ wide. For squares, they are $300 \times 300\ \mu\text{m}$ unit size and randomly positioned without overlap and occupying 15% of the available area. (C) Sketch of PDMS casting from the printed circuit board. (D) A couple of topographical cultures 6 mm in diameter attached to a glass coverslip. (E) Bright-field images of the cultures. Transparent and dark areas correspond to PDMS in contact with copper and fiberglass, respectively, and shape the bottom and top regions of the topographical relief.

were also prepared on plastic petri dishes and pierced with the aforementioned punchers. These neuronal cultures will be referred as ‘controls’ along the Thesis.

Examples of PDMS reliefs with seeded neurons on their surface, and ready for calcium imaging, are provided in Figure 3.5A. The snapshots were taken with different filters in a wide-field optical microscope. Although the roughness of the PDMS tracks at the top parts makes the visualization of the neurons difficult, we can observe that neurons and processes (mostly axons) are present both at the top and at the bottom of the tracks. Neurons tend to aggregate, which possibly indicates that PDMS coating with PLL was not sufficiently uniform. Nevertheless, the important aspect is that the tracks imparted strong anisotropy in the connectivity of the network by funnelling axons along the direction of the tracks. This is clear in the immunostained images of Figure 3.5B, in which neuronal axons appear in green and neuronal nuclei in blue. Clearly, despite aggregation, the majority of axons follow the tracks and only a minor fraction of them crosses the tracks transversally.

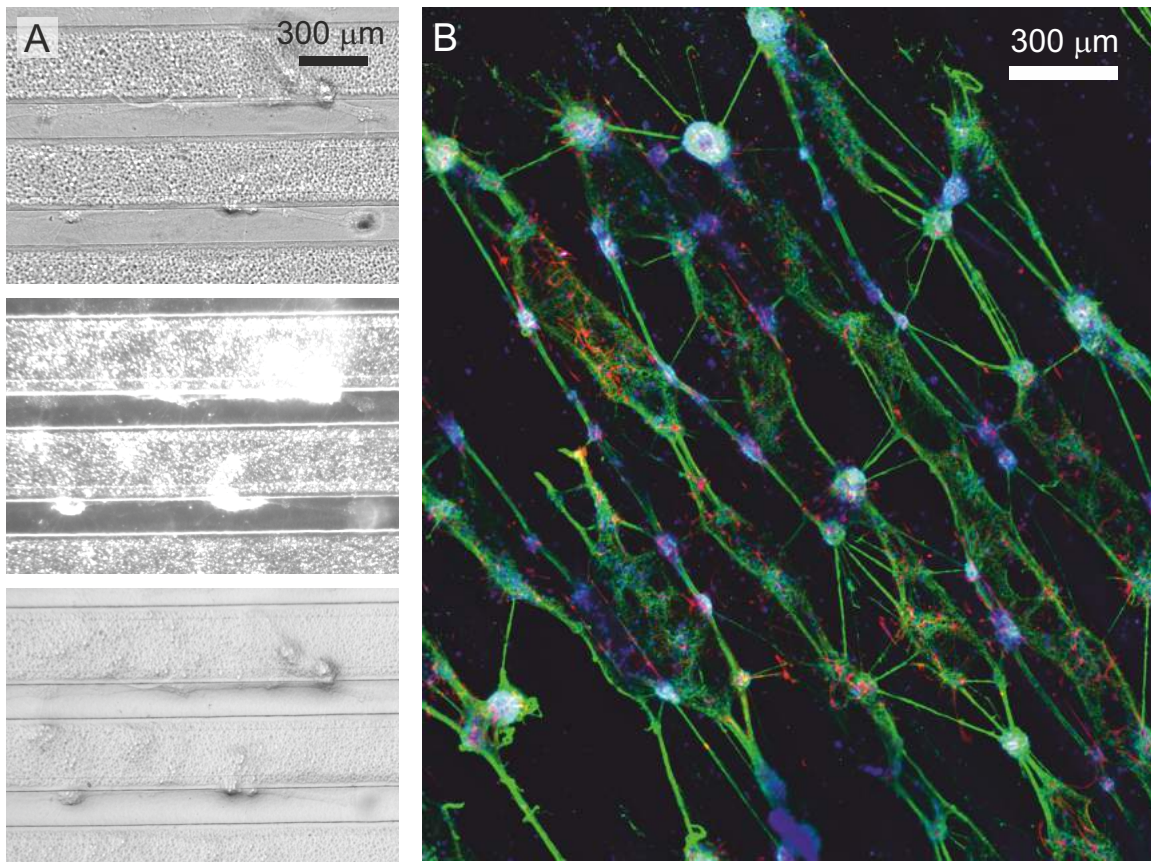


Fig. 3.5 Neurons on the 'tracks' PDMS topography. (A) Optical images with different filters. Top: bright-field; centre: phase contrast; bottom: differential interference contrast. (B) Fluorescence images of the same culture. Green are neuronal processes (axons and dendrites) and blue are neuronal nuclei. Neuronal aggregation is clear, as well as the tendency for the axons to grow aligned to the tracks.

3.2.2 Stamping of patterned surfaces

Microcontact printing was used to create a pattern a mixture of poly-D-lysine and extracellular matrix (ECM) on an agarose-coated glass coverslip using a PDMS stamp fabricated according to the protocol described by Yamamoto et al. (2016). These PDMS stamps had a cubic shape and the desired micropattern imprinted on one of its faces (Figure 3.3B). For the printing process, a glass coverslip was first cleaned by sonication in 100% ethanol and dried at room temperature. Afterwards, four dots of paraffin wax (P355, Sigma-Aldrich) were placed at the periphery of the coverslip and then the surface was coated with a 0.2% agarose (A9918, Sigma-Aldrich). After overnight drying the agarose, the coverslips were sterilized using ultraviolet irradiation for 30 minutes.

The protein ink used for the stamping was prepared using a mixture of ECM gel (E12770, Sigma Aldrich; 1:100 dilution) and poly-D-lysine (50 μ g/ml; P0899, Sigma Aldrich). The

face with the topographical relief on the PDMS stamps was impregnated with the protein ink and, with a specially designed micromanipulator, the pattern was stamped on the agarose coated coverslip. Finally, the coverslip was dried overnight in a fume hood and subsequently immersed in the neuronal plating medium four days before cell plating.

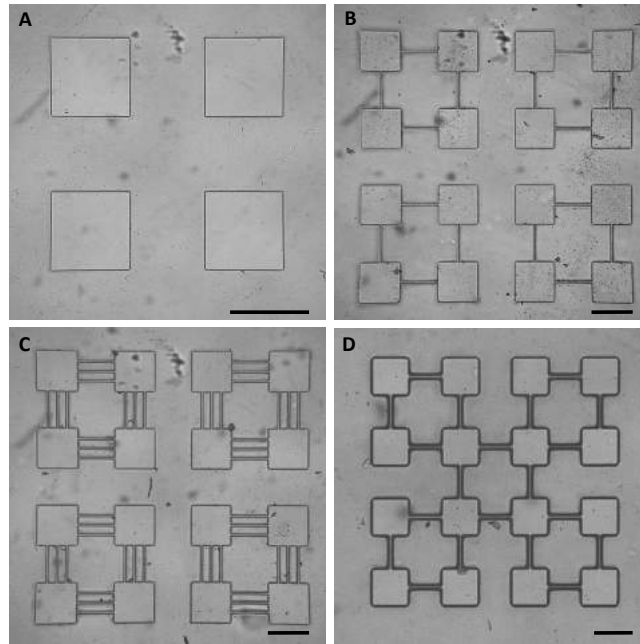


Fig. 3.6 Engineering of patterns with stamps. (A) Modular design with four $200\ \mu\text{m}$ by $200\ \mu\text{m}$ squares spatially segregated with no bond between them. (B) Detail of a modular design consisting of four squares connected by a single bond of $5\ \mu\text{m}$. (C) Modular design of four squares with a triple bond of $5\ \mu\text{m}$ between them. (D) Modular design of a hierarchical pattern connecting 16 squares with a single bond through the 4 central modules. All scales in the figure represent the same size of $200\ \mu\text{m}$.

3.3 Data acquisition

Spontaneous neuronal activity was monitored by fluorescence calcium imaging (Rochefort et al., 2008; Smetters et al., 1999), an experimental technique that allows to detect real-time neuronal firings with a high signal-to-noise ratio and single cell resolution. Calcium is an essential intracellular messenger in mammalian neurons and its concentration rises by two orders of magnitude during electrical activity (Grienberger and Konnerth, 2012). With the help of calcium indicators and an imaging setup for fluorescence, neuronal activity can be identified and monitored.

3.3.1 Neuronal action potentials

The neuronal membrane is a semipermeable structure that separates the inner cell space, the cytoplasm, from the extracellular environment. The membrane potential of a neuron is the voltage difference between the two sides of this structure and is due to an imbalance of ionic concentrations of Na^+ , Cl^- , Ca^{2+} and K^+ , among others. At rest, the value of the action potential is typically -70 mV and the neuron is considered to be polarized. The input signals from upstream connected neurons causes a flow of charged ion particles, which cross the membrane into the cytoplasm through the action of membrane pumps and channels (Figure 3.7). This leads to an increase of positive charges inside the cytoplasm, which rapidly increases the value of the membrane potential (depolarization). When a given threshold is reached, voltage-gated ion channels trigger and action potential, which propagates as a fast signal along the axon, stimulating the release of neurotransmitter-carrying vesicles in the axonal presynaptic terminal. These neurotransmitters bind the corresponding receptors on the postsynaptic cleft and generate the electrical signal that may lead to a new activation on the downstream neurons.

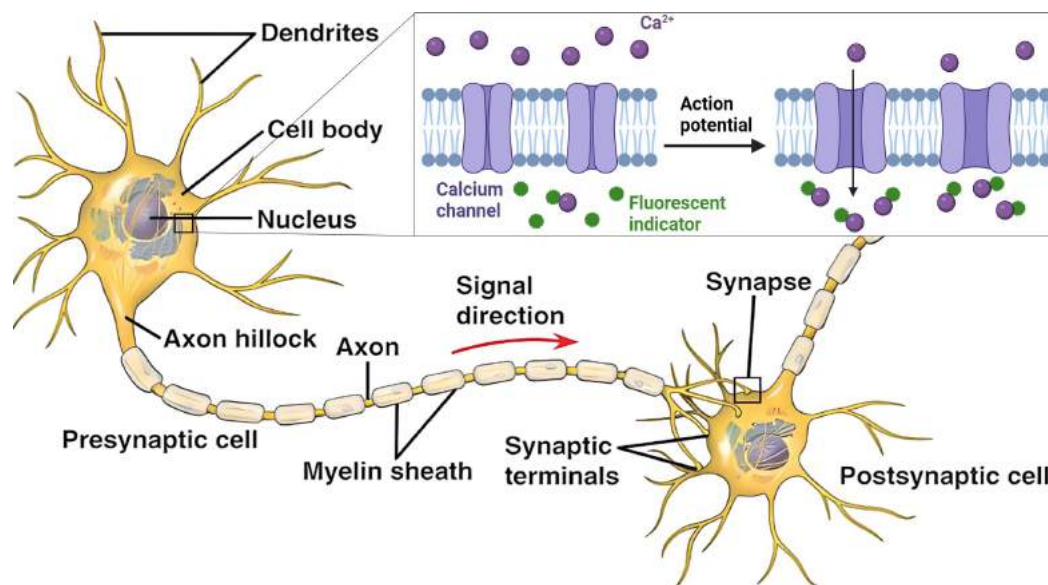


Fig. 3.7 Schematic depiction of voltage-dependent calcium channels. The action potential transmission causes calcium dependent channels in the cell membrane to open. The fluorescence indicator, GCaMP6s, reacts to the incoming intracellular calcium ions increasing the intensity of the fluorescence signal. Adapted from Kandel et al. (2000) with *BioRender.com*.

Vesicles' release is mediated by Ca^{2+} ions inside the cell's axonal terminals (Figure 3.8). Upon generation of vesicles, Ca^{2+} concentration increases by two-to-four orders of magnitude as compared to the free calcium concentration at rest (Berridge et al., 2000). Fluoro-

rescence calcium imaging takes advantage of this intake and uses proper calcium indicators (fluorophores) that are only fluorescent when they bind to free Ca^{2+} ions.

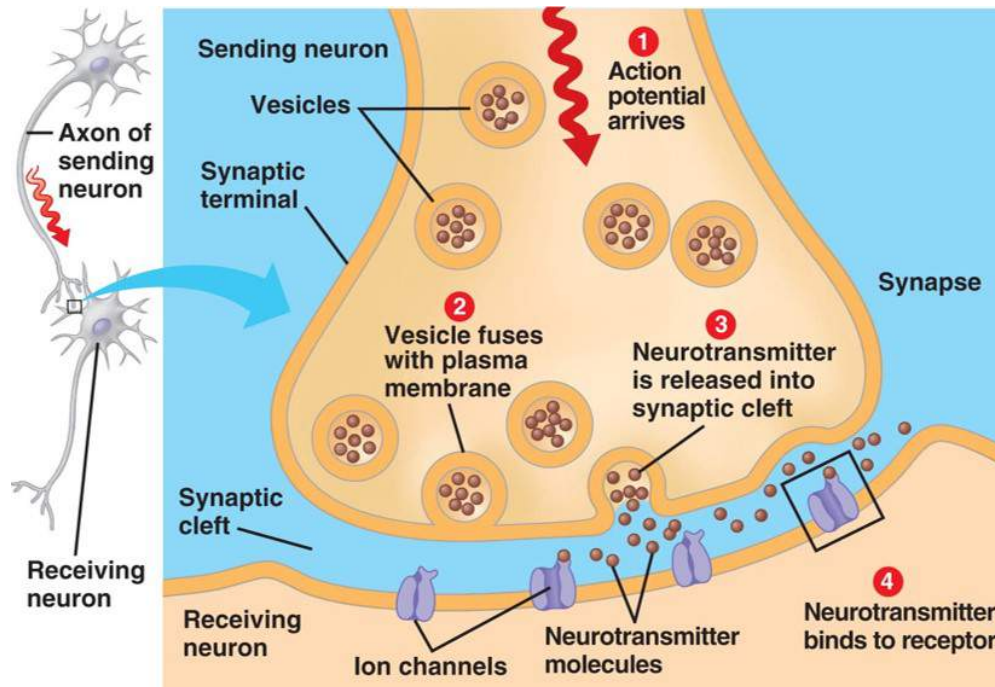


Fig. 3.8 Sketch of the neurotransmitter release. Vesicles carry the action potential neurotransmitters, *i.e.*, Ca^{2+} , through the axon of the sending neuron until the synaptic terminal. Afterwards, vesicles fuse with the plasma membrane and release the positive calcium ions to the synaptic cleft, where they are detected by the receptors of the post-synaptic neuron. Extracted from Simon et al. (2013)

3.3.2 Fluorescence calcium imaging

This technique was used to record spontaneous neuronal activity in Soriano's Lab. Typically, GFP-like proteins were used, such as the Fluo-4 chemical indicator or the genetically-encoded calcium indicator (GECI) GCaMP6s. Both emit green light ($\lambda = 514 \text{ nm}$) when excited by blue light ($\lambda = 490 \text{ nm}$). Excitation light is provided by a mercury lamp (OSRAM) attached to the microscope (Figure 3.10). Calcium imaging allows to detect the sharp increase in fluorescence emission, within a few milliseconds, as the membrane depolarizes *i.e.*, when the neuron fires (Figure 3.9). However, it has a setback. After neuronal firing, the repolarization is significantly much slower since ions, specially Ca^{2+} , have to return to their resting concentrations and the fluorophore has to unbind calcium. This process leaves a slowly decaying fluorescence that can last up to 10 s and may hinder the detection of concatenated neuronal firing events.

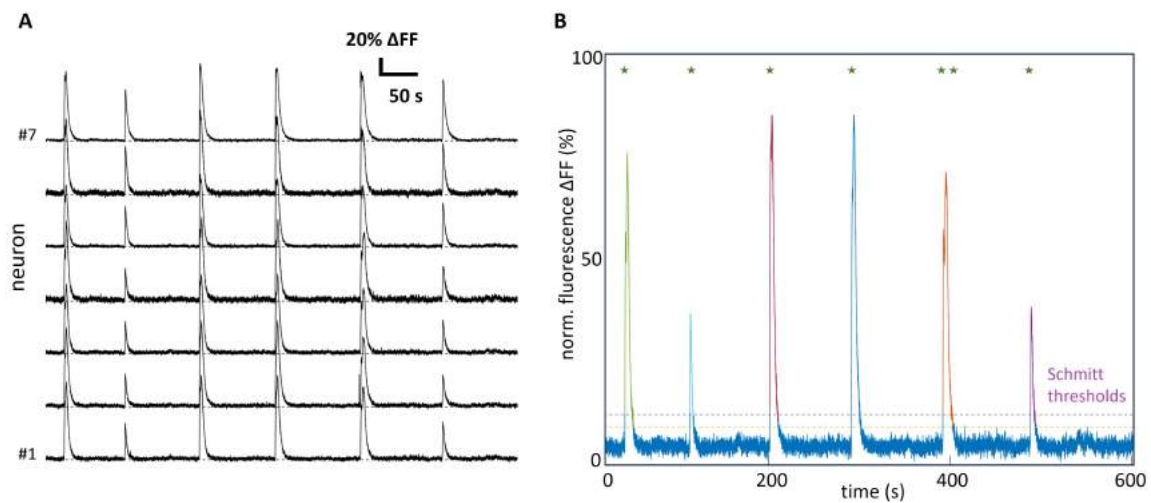


Fig. 3.9 Fluorescence calcium imaging and spike inference. (A) Example of normalized fluorescence traces for seven neurons in an experiment with primary cultures. Fluorescence data was acquired with the genetically encoded calcium indicator GCaMP6s. (B) Neuronal spike inference in which the original fluorescence trace (blue signal) is analysed to obtain the spikes via the Schmitt thresholding method (purple dashed line and stars). This method uses two thresholds to avoid ascribing noisy fluctuations as valid spikes.

Deciding the nature of the fluorescence indicators to be used, chemical or GECIs, is crucial. The first ones can be easily loaded into the cell with the use of Dimethyl sulfoxide (DMSO) and provide a fairly good signal-to-noise ratio, which enables their use to detect rapid neuronal firings. Their major drawback is a long-term toxicity since the DMSO needed to load the calcium indicator into the cytoplasm ultimately damages the cell membrane. This limitation impedes the monitoring of activity in the same culture more than once. The second indicators, the GECIs, are those that are expressed by the neurons themselves, either because the corresponding genetic material is already present in the cell's genome (*e.g.*, cell lines) or because it was incorporated to the cells through viral infection, *e.g.*, by using adeno-associated viruses. In this Thesis we used the latter strategy for its simplicity and safety. The important advantage of GECIs is that they allow to monitor the same culture along two weeks or more, and therefore are ideal to investigate changes in neuronal network behaviour along development.

3.3.3 Confocal microscopy

This technique was used to obtain immunostaining images. Confocal laser scanning microscopy (LSM) is a type of wide-field fluorescence microscopy that scans sample points sequentially. High-intensity monochromatic lasers emit a tight beam of excitation light at a

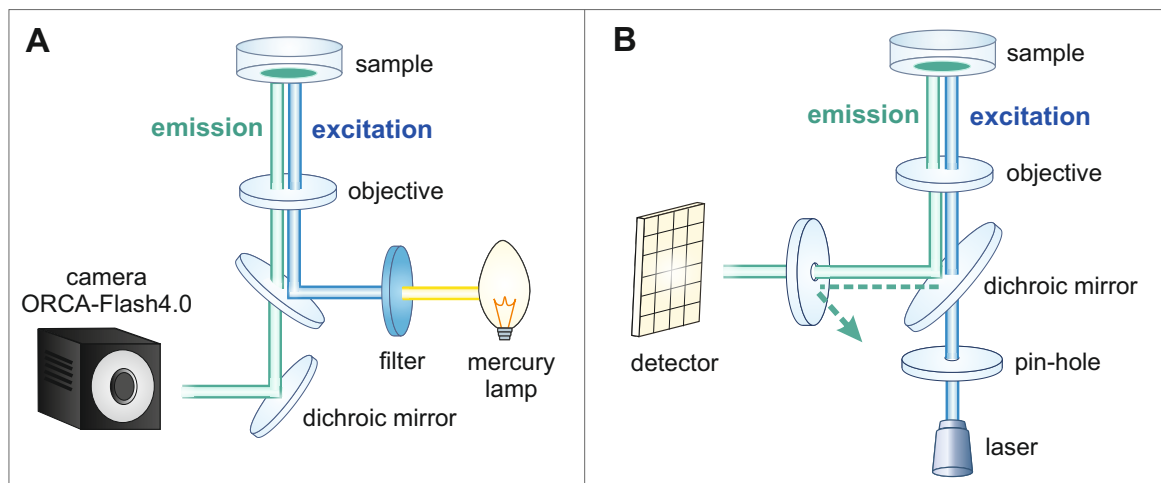


Fig. 3.10 Fluorescence microscopy. (A) Illustration of Wide-Field fluorescence microscopy where a mercury lamp is the source of the fluorescence light. A colour filter selects the wavelength of the incoming white light. The dichroic mirrors guide the beam into the objective, stimulating the sample. Emitted fluorescence light is collected by the camera sensor. The camera is connected to a computer, which captures fluorescence images with the program Hokawo. (B) Illustration of confocal microscopy where a high-intensity laser is the source of the fluorescence light. There are several lasers within the same setup because each laser has a particular wavelength, but only one works at a time. The light crosses a pin-hole making the beam extremely accurate. Then, the dichroic mirrors guide the beam into the objective targeting the sample and backwards to a sensor, passing the information directly to the computer. Adapted from Estefanía Estévez's PhD Thesis.

low rate of expansion to lessen the scattering. The power and gain of the laser is adjusted individually based on a preliminary image, because every fluorophore has a different intrinsic intensity. The emitted light from the sample goes back through a pinhole that only lets pass the beam from the focal point. This tiny aperture helps eliminate the background caused by out-of-focus light and scattering, obtaining sharp images with great contrast. Finally, the beam reaches a dichroic mirror, an optical bifurcation that reflects forward the light to the alignment path and into the camera sensor (Figure 3.10B).

The slit of the pinhole can be regulated manually, the reduction of the aperture provides higher resolution but consequently the detector collects fewer photons, so the exposure time is to be increased to obtain brighter images. The pinhole aperture also affects the distance between the nearest and the furthest focused planes, *i.e.*, the depth of field (DoF). Single images had $\text{DoF} = 4\mu\text{m}$.

Once the optical sections from different focal planes have been collected, they are compiled into a 3D reconstruction or z-projection. Given that a neuron's size is around $20\mu\text{m}$, that is the minimum height for a complete scanned volume, so we captured 5 sections of $4\mu\text{m}$. Neurons grown on top of PDMS patterns may increase the height up to $80\mu\text{m}$.

Images were taken at Hospital Clinic in Barcelona with the laser scanning confocal microscope ZEISS LSM 880, controlled by the software ZEN 2.3. The whole system stands on top of an optical table to prevent vibrations while scanning. Image resolution was 1024×1024 pixels in uncompressed TIF format.

3.4 Data analysis tools

3.4.1 Calcium imaging

Spontaneous activity in neuronal cultures grown on PDMS topographical substrates was recorded daily at 25°C along two weeks, from DIV 7 (the onset of strong GCaMP6s calcium signal) to 21 (the beginning of culture degradation). Since monitoring the same culture was crucial, the set of prepared wells was inspected in detail before any recording, and cultures that did not have a homogeneous distribution of neurons or that were inactive at DIV 7 were discarded. For the selected cultures, the 4-well plate in which they sit was mounted on a Zeiss Axiovert C25 inverted microscope equipped with a high-speed CMOS camera (Hamamatsu Orca Flash 4.1). The combination of a 2.5X objective and an optical zoom allowed for the visualization of an entire 6 mm diameter culture with a spatial resolution of $5.9 \mu\text{m}/\text{pixel}$, an image size of $1,024 \times 1,024$ pixels, and 8-bit grey scale format. Spontaneous activity recordings were carried out for 30 min at 100 images/s and repeated every 24h. The orientation of a given culture relative to the camera was maintained along the 2-week culture evolution to facilitate data analysis.

3.4.2 Calcium imaging data analysis and activity events detection

Fluorescence recordings were analysed with the custom-made software Netcal run in MATLAB (Fernández-García et al., 2020; Orlandi et al., 2017). For convenience, and since the scope of the experiments carried out in this Thesis was to investigate collective behaviour, a set of 1,300 Regions of Interest (ROIs) was laid out on the image (see Figure 3.11A). The ROIs shaped a grid centred at the culture and extending its entire circular shape of 6 mm diameter. A ROI had a typical size of $150 \times 150 \mu\text{m}$ and contained about 5–10 neurons. The average fluorescence intensity of each ROI i along the 30 min recording duration was then extracted, and the obtained fluorescence trace $F_i(t)$ was corrected from drifts and normalized as $\Delta F F_i(t) \equiv (F_i(t) - F_{i,0})/F_{i,0}$, where $F_{i,0}$ is the basal fluorescence level, *i.e.*, without neuronal activity (Figure 3.11B).

The fluorescence data of each ROI was converted into time series of neuronal activity—a process generally called *spike inference*—by using the Schmitt trigger method, which

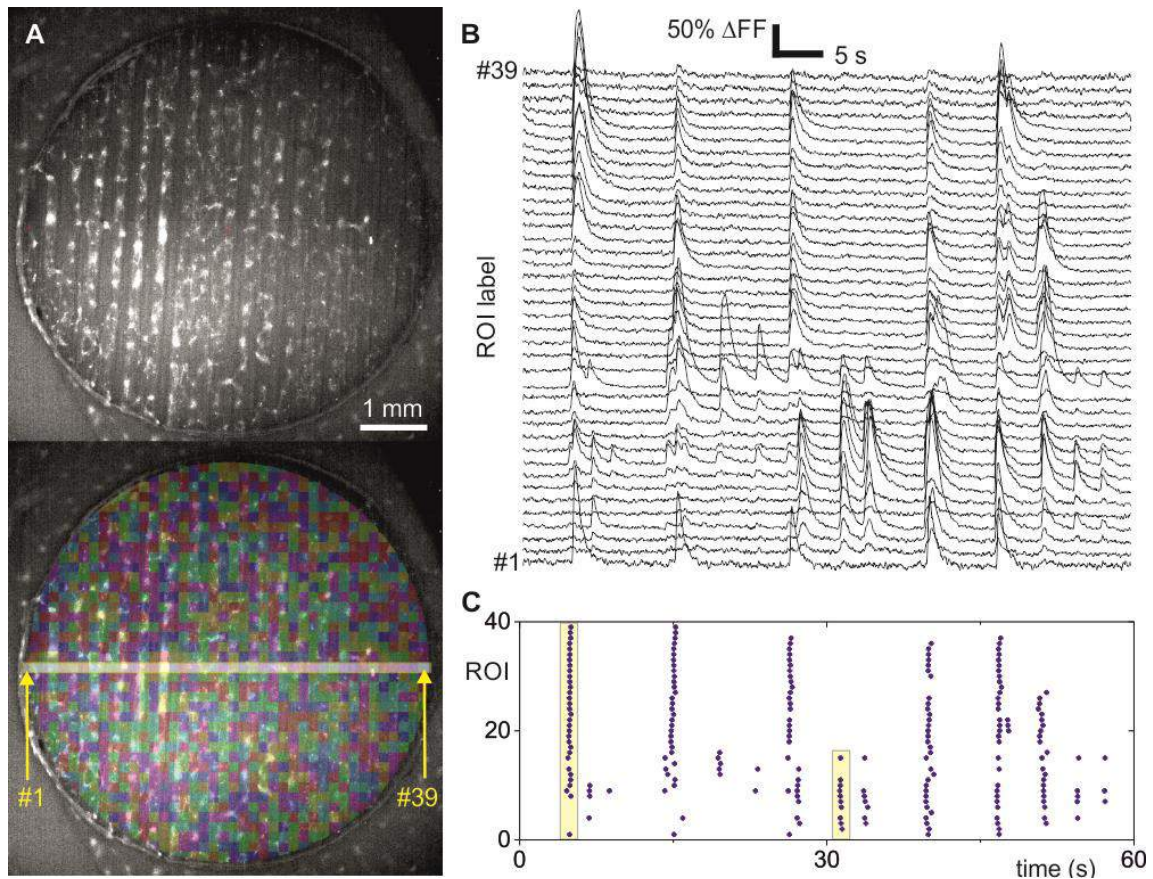


Fig. 3.11 Data analysis. (A) Top, highly contrasted fluorescence image of a ‘tracks’ culture. Bottom, Regions of Interest (ROIs) set as squared boxes and covering the entire circular culture, with a total number of 1,300. The 39 ROIs at the centre of the culture are used to provide representative fluorescence traces. (B) Normalized fluorescence traces for the 39 ROIs at the centre of the culture along the first minute of the recording, vertically shifted for clarity. Sharp peaks indicate neuronal activity. (C) Corresponding raster plot. Examples of coordinated neuronal activity events of large and small sizes are highlighted with yellow boxes.

accepts a sharp change in fluorescence as an activity episode whenever the fluorescence stays elevated for at least 100 ms between a lower and a higher threshold (Grewe et al., 2010) (Figure 3.12). The two thresholds (marked as two horizontal lines in the figure) are necessary to prevent that camera noise or other artifacts are identified as activity events. By using this Schmitt approach, the inferred spikes effectually provided a single event per fluorescence peak, which is marked in the figure as green stars. For comparison, the figure also shows an alternative method known as Oasis (Friedrich et al., 2017), which uses a biophysical model to reconstruct the fluorescence signal. This model takes into account the typical fluorescence amplitude of a single spike as well as the decay time of fluorescence. The red trace in the figure corresponds to the Oasis–reconstructed signal, with the inferred spikes marked as black dots. Although the model captures well the signal, it often takes noisy fluctuations as

spikes (black arrowhead). After several tests comparing Schmitt, Oasis and other methods, it was decided to take the Schmitt method to prevent a large number of artificial spikes, which added problematic noise. Also, for the computation of functional connectivity, it was also tested that Schmitt was more convenient (Ludl and Soriano, 2020). The reason is that a single spike per active neuron revealed causal interactions between neuronal pairs, while many concatenated spikes per neuron revealed causal interactions within the spike trains themselves, giving rise to problematic artifacts that had nothing to do with a characterization of whole-network exchange of information.

Thus, the Schmitt trigger method captured the onset time of activity in each ROI, independently on the amplitude of the fluorescence peak as far as it was sufficiently high, *i.e.*, above noise level. The train of detected events, extended to all ROIs in the network, was visualized as raster plots (Figure 3.11C) and framed the core dataset for in-depth analysis of the neuronal cultures.

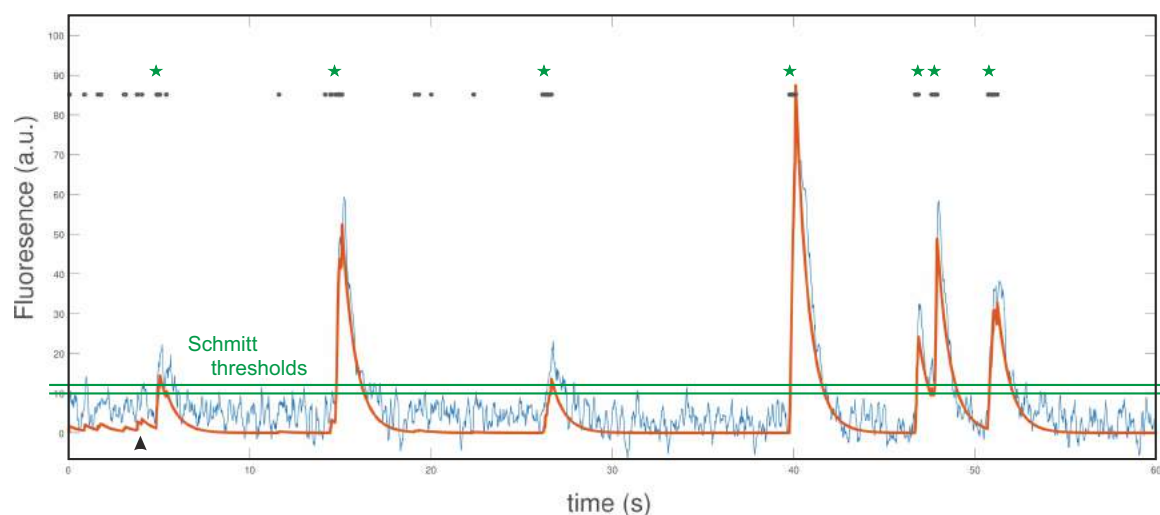


Fig. 3.12 From fluorescence to spikes. The blue signal corresponds to the recorded experimental data. The red one is the reconstructed signal assuming the Oasis biophysical model that takes into account the fast rise and slow decay of fluorescence upon neuronal activation. The corresponding spike events are shown as black dots. The green horizontal lines are the thresholds for Schmitt inference. The corresponding spike events are shown as green stars. The black arrowhead on the bottom-left marks a misidentified spiking event by the Oasis method.

3.4.3 Population activity, network bursts, and distribution of burst amplitudes

The population activity A quantified the capacity of the neurons in the network to exhibit collective activity, *i.e.*, the coordinated activation of a fraction of the network within a

window of 100 ms. The population activity was computed as the fraction of ROIs in the network that activated together without repetition in a sliding window 1 s wide and 0.1 s step (Figure 3.13). A varied between 0 (no activity) and 1 (full network activation). Sharp peaks in A identified strong coordinated activity and were denoted as *network bursts*. These bursts were deemed significant when their amplitude A_b verified $A_b > \mu_{\text{bgnd}} + 3 \cdot \text{SD}_{\text{bgnd}}$, where μ_{bgnd} and SD_{bgnd} are the mean and standard deviation of background activity. In general, for most of the experiments, significant bursts were those with $A_b > 0.1$, *i.e.*, 10% of the network active. All significant burst amplitudes A_b , across realizations and for a given experimental condition, were pooled together to build the distribution of amplitudes. These distributions were finally compared between the different experimental conditions, for instance standard control cultures and topographical ones. For the latter, and as shown in Figure 3.13, the variety in A_b values was much more richer than in controls.

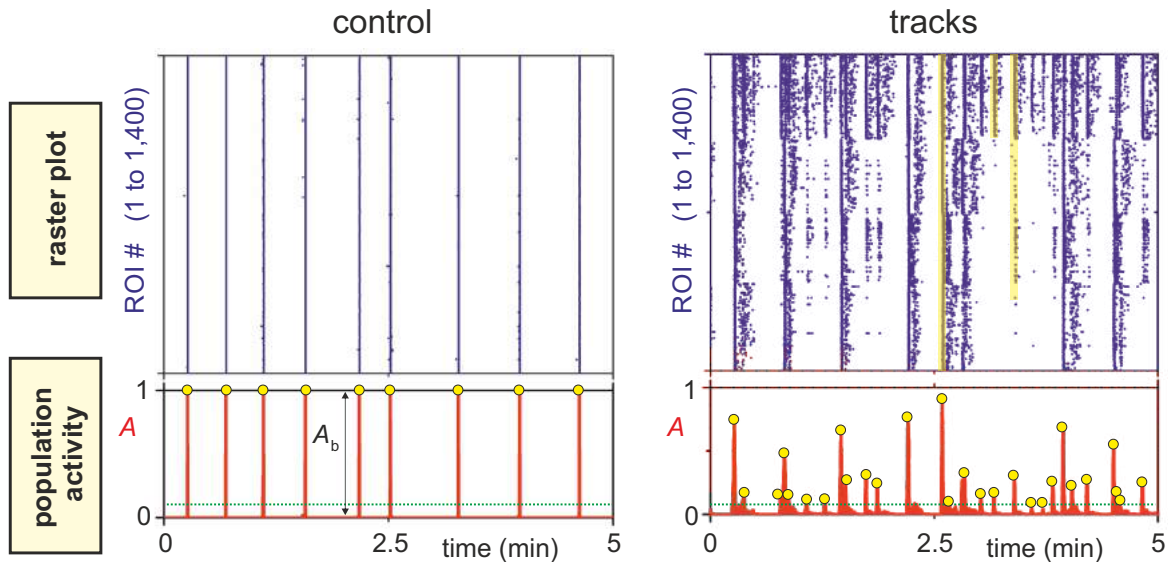


Fig. 3.13 Population activity. Illustrative examples of raster plots (top) and population activity A (bottom) for a control and a PDMS topographical ‘tracks’ cultures. Yellow bands in ‘tracks’ highlight bursting events of different sizes, one encompassing the 95% of the network and another one encompassing about 30%.

3.4.4 Bursts’ analysis as spatiotemporal fronts

Network bursts propagated throughout the PDMS surface as spatiotemporal fronts whose structure and velocity depended on the underpinned topographical design. The propagation of a given burst was depicted as an image plot (Figure 3.14A), in which each active ROI was shown in the Euclidean $x - y$ space and coloured according to its activation time. Dark

colours represented those regions that activated first, and yellow–white colours those that activated the latest. Inactive ROIs or regions of the map without ROIs were shown in dark grey. The origin of activity, termed ‘burst initiation point’, was computed by considering a group of 10 ROIs with the shortest activation times and by analysing all combinations of 4 ROIs within the group, computing for each combination the average inter–ROI Euclidean distance d_0 and average activation time t_0 . The combination that procured the lowest d_0 and shortest t_0 (termed t_0^{min}) was selected as initiator and the ROIs’ centroid (x_0, y_0) was evaluated. This centroid was ascribed as the burst initiation point and was shown in the image plots of Figure 3.14A as a grey circle. Finally, the activation times t_i of all ROIs i were then shifted according to the origin of activity as $t_i^* = t_i - t_0$. ROIs with negative time t_i^* values were set to 0.

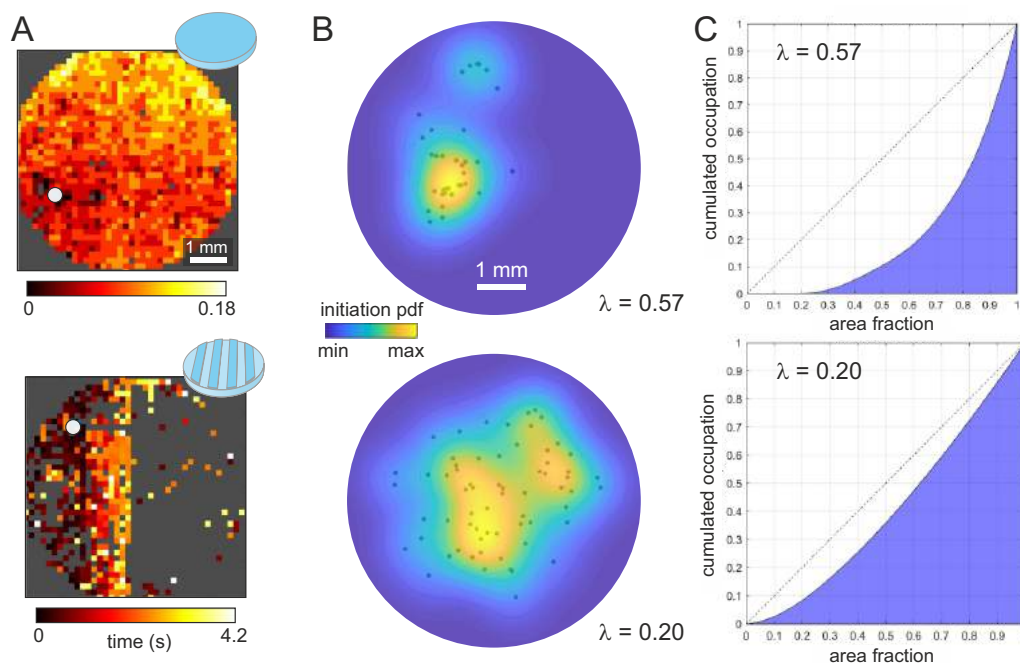


Fig. 3.14 Activity fronts and initiation. (A) Examples of spatiotemporal activity fronts for control and ‘tracks’ cultures. (B) Spatial distribution of activity initiation. Each black dot is the initiation point of a burst (the equivalent of the white dot on panel A), and the blue–yellow contour is the corresponding probability density function. The more yellow an area is, the higher the probability for activity to start in that spot. (C) Lorenz curves and Gini coefficient λ of burst initiation, for the same data as in panel B. Conceptually, if the blue area occupies half the diagram, initiation is similar anywhere in the culture, *i.e.*, the initiation points are uniformly distributed. Gradually smaller blue areas correspond to more concentrated initiation points.

The collection of burst initiation points for each experiment was further analysed to study their spatial distribution and quantify the tendency for the spontaneous activity to start in

the same area of the culture (Figure 3.14B). Following (Faci-Lázaro et al., 2019; Orlandi et al., 2013), the distribution of points was converted to a probability density function of burst initiation, from which the Gini coefficient λ was extracted as a measure of activity focalization (Figure 3.14C). $\lambda \rightarrow 1$ indicated a tendency towards a strongly focalized initiation in the same spot, whereas $\lambda \rightarrow 0$ indicated a tendency towards an equiprobable distribution of initiation across the culture.

3.4.5 Similarity of spatiotemporal fronts

The richness of activity repertoire in a culture was quantified by analysing the similarity among bursts' spatiotemporal structure. A coarse approach (Figure 3.15B) consisted in plotting the bursts as blue–red colour bands, where the width of the band is the number of active ROIs and its colour patterning indicates the propagation of activity. Each band has its own ROI ordering, from the one that started activity to the last. Bursts with similar band widths and colour schemes indicated a comparable propagation structure, *i.e.*, similar number of active ROIs and temporal evolution.

A more refined approach was carried out as follows. First, each burst i was treated as a vector v_i whose elements contained the activation time of each ROI. Non–active ROIs were set to -1 . All bursts' vectors preserved the same indexing of ROIs, *i.e.*, a given position in all vectors contained the activation time of the same ROI. Second, for each pair of bursts' vectors v_i and v_j , the number of common active ROIs (non–negative entries in both vectors) was determined, and this number was divided by the burst that had the largest number of active ROIs. This procured a ‘common ROIs’ matrix $\mathbf{C} = c_{ij}$, in which bursts that shared most of the ROI indexes had $c_{i,j} \rightarrow 1$, otherwise $c_{i,j} \rightarrow 0$. Third, cross correlation was carried out between all pairs of bursts' vectors but using only those ROIs that were active in both vectors, leading to a correlation coefficients matrix $\mathbf{R} = r_{i,j}$. Values of $r_{i,j} \rightarrow 1$ indicated pairs of bursts with almost identical spatiotemporal structure (same active ROIs and propagation times), while $r_{i,j} \rightarrow 0$ indicated bursts that shared few ROIs or that propagated in a completely different way. A final matrix \mathbf{S} of similarity among burst pairs was obtained as the element–wise multiplication of \mathbf{C} and \mathbf{R} , *i.e.*, $S = \mathbf{C} \circ \mathbf{R}$.

To classify the bursts and visualize the matrix \mathbf{S} , community structure analysis was carried out in \mathbf{S} using a fast implementation of the Louvain algorithm (Blondel et al., 2008), procuring a new matrix whose elements were ordered according to the detected communities (Figure 3.15C). For clarity of data visualization, bursts' indexes in Figure 3.15B were also sorted according to the detected communities in Figure 3.15C.

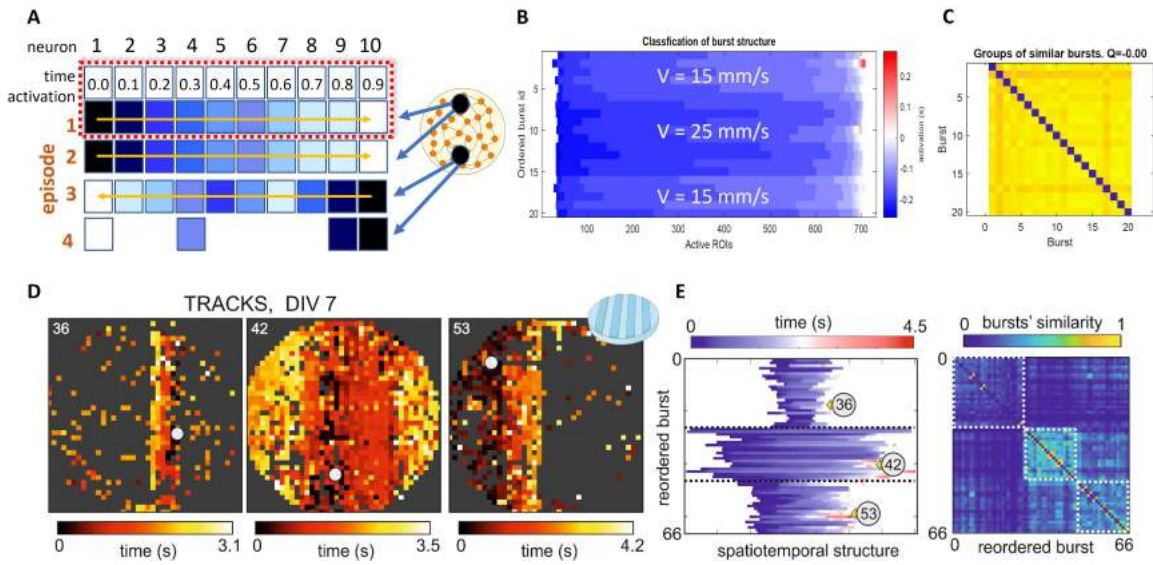


Fig. 3.15 Spatiotemporal front classification. (A) Sketch that illustrates three bursting episodes with its corresponding colour palette depending on the initiation bursting time. (B) The plot depicts the burst structure of the sorted burst id. The colour indicates the time in which each ROI activated, being blue the ones that activated first and red the ones that activated later. (C) Similarity matrix of the burst in the example. Since the majority of the burst present the same structure the value of similarity is close to one. (D) Representative examples of spatiotemporal activity fronts for a track configuration culture. Each coloured dot in the image plots is an active ROI, with the colour coded according to the time of activation (from black to yellow). Grey regions indicate absence of active ROIs. The number on the top-left corner of each panel identifies the burst, while the big white dot signals the origin of activity. In this case, image plots are drawn for the topographical tracks to coincide with the vertical direction. (E) Classification of burst sizes and propagation (left) and similarity matrix of the bursts (right). Each band corresponds to a burst, its width indicates the ROIs involved in the burst while its colour indicates the propagation time. Bands with similar colour scheme portray bursts with akin spatiotemporal structure. Circled numbers indicate the position of the bursts represented in panel D. The dotted black lines separate the different groups of bursts. Regarding the similarity matrix, the brighter the colour, the higher the similarity among bursts. White dashed boxes identify the groups of similar bursts.

3.4.6 Velocity of propagating fronts

The propagation speed of activity fronts was analysed by computing the Euclidean distance ρ_i of each ROI i to the origin of activity (x_0, y_0) and by plotting next ρ_i as a function of t_i^* , the activation times relative to the origin of activity (Figure 3.16). An estimation of the global propagation velocity was obtained by the slope of a linear fit $\rho_i(t_i^*)$, and with the intercept forced at $(0,0)$. Only fits with Pearson's regression coefficients $r \geq 0.70$ were accepted, with the best fits corresponding to bursts that propagated as neat circular fronts (Orlandi et al., 2013) and that were typically observed in control cultures. The determination of parallel and

transverse velocities for the ‘tracks’ configuration was carried out similarly but after selecting either a row of ROIs in the culture (parallel velocity) or a column (transverse velocity).

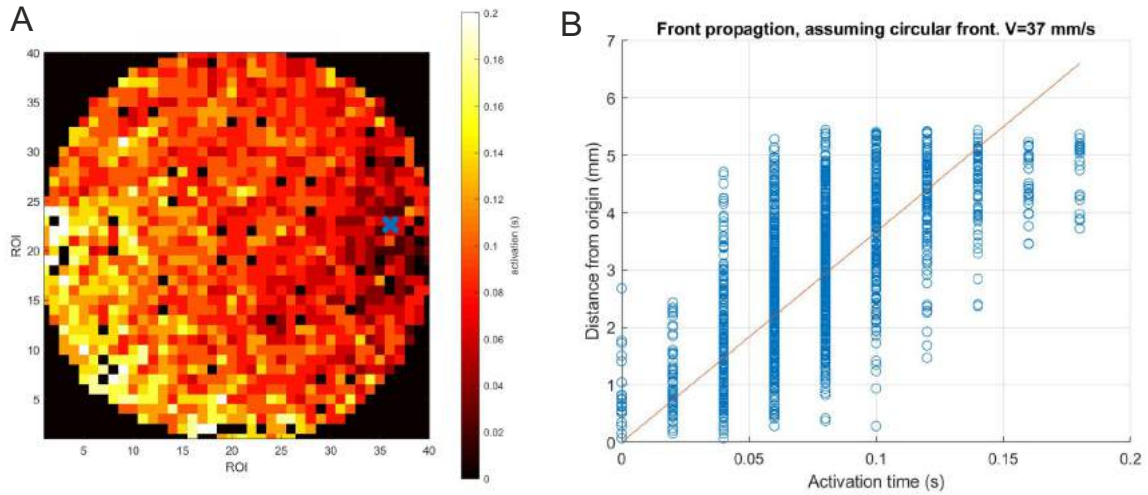


Fig. 3.16 Velocity of propagating fronts. (A) Representative propagation map of activity for a neuronal culture grown on a flat surface. The blue cross marks the initiation point of activity. (B) Corresponding plot $\rho_i(t_i^*)$ and its linear fit to extract the velocity of propagation. In this fit, $r \simeq 0.72$.

3.4.7 Numerical simulations

Numerical simulations were carried out by the PhD student Akke Houben, in Soriano’s group, to provide a framework to understand some experimental results. In the simulations, $N \approx 10^4$ spatially-embedded neurons were laid on a surface following the biologically realistic construction of Orlandi et al. (2013) and Ludl and Soriano (2020). Neurons were modelled as Izhikevich, single spiking integrate-and-fire units with added pre-synaptic depression dynamics. The latter accounted for the depletion of neurotransmitter following repetitive firing. Excitatory neurons comprised 80% of the network and the remaining 20% were inhibitory. The excitatory or inhibitory role of the neurons in the network was randomly chosen. The neurons at rest received no inputs, except for a white noise intrinsic to each neuron.

Each simulation was carried out for 1.2×10^5 time-steps, corresponding to a simulated time of 120 s. The spatially embedded networks were constructed by placing neurons randomly in a circular area with a diameter of 6 mm, as in the experiments, resulting in a uniform density of 400 neurons/mm². Next, for each neuron, axonal growth was modelled by successively placing 10 μm line segments, each with an angle drawn from a zero mean Gaussian distribution with 0.1 radians standard deviation with respect to the direction of the

previous segment, up to a total length drawn for each neuron independently from a Rayleigh distribution with mean 1 mm (Orlandi et al., 2013). This resulted in nearly straight axons.

A circular area around each neuron with a radius drawn from a Gaussian distribution with mean 150 μm and 40 μm standard deviation functioned as the dendritic tree. Once the axon of a neuron crossed into this dendritic area of another neuron, a connection from the first to the latter was established with a probability 0.1. The topographical PDMS patterns were implemented by placing virtual borders in the culture area corresponding to either bottom-to-top or top-to-bottom transitions. When, during the formation of the axons, a line segment was placed such that it crossed one of these borders it would cross with a probability P , and be deflected with the inverse probability $1 - P$. The crossing probability was dependent on the direction of crossing: for bottom-to-top transitions $P = 0.6$, while for bottom-to-top $P = 0.8$. Simulations procured raster plots and collective dynamics that qualitatively resembled those from experiments. For connectivity analysis, 1000 neurons were randomly sampled from the raster plots. The z-score used was the same as for the experimental data analysis.

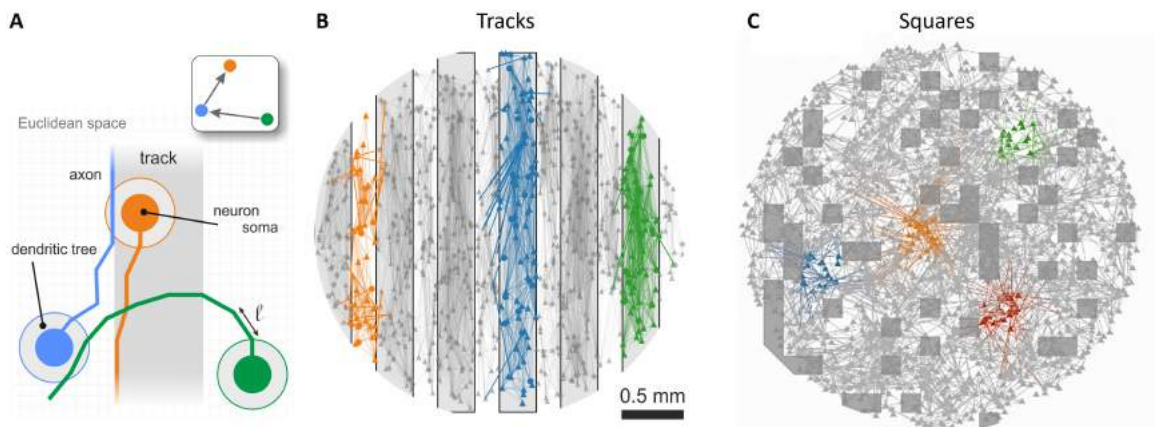


Fig. 3.17 Construction of *in silico* networks. (A) Neurons (solid discs) are placed on a bi-dimensional surface and neurons grown by concatenating segments of length $\Delta\ell$. Axons have a given probability to either follow the tracks' obstacles (blue and orange) or cross the tracks towards neighbouring areas (green). Whenever an axon of neuron i intersects the dendritic tree (colour circles) of neuron j , a connection $i \rightarrow j$ is established with probability 0.5 (top-right sketch). (B) Final network grown on a 3 mm diameter circular area mimicking track obstacles at the surface. Up-triangles and circles indicate excitatory and inhibitory neurons, respectively, and lines connections. Colours indicate groups of neurons strongly connected within their physical area. (C) Final network grown on a 3 mm diameter circular area mimicking square obstacles at the surface. Again, up-triangles and circles indicate excitatory and inhibitory neurons, respectively, and lines connections. colours indicate groups of neurons strongly connected within their physical area.

3.4.8 Neuronal model

Each neuron was modelled as a Izhikevich model neuron (Izhikevich, 2003) for which the membrane potential v_i and adaptation current u_i of a neuron i evolved according to

$$\begin{aligned}\frac{dv_i}{dt} &= 0.04v_i^2 + 5v_i + 140 - u_i + I_i^{\text{syn}} + \sigma\eta_i(t), \\ \frac{du_i}{dt} &= a(bv_i - u_i),\end{aligned}\tag{3.1}$$

where I_i^{syn} is the synaptic input received from other neurons, $\eta_i(t)$ a white noise process, a and b model parameters, and σ the noise magnitude. Dynamically, whenever the membrane potential of neuron i crosses a preset threshold v_{th} the neuron is said to spike and the membrane potential v_i and adaptation current u_i are reset as

$$v_i > v_{th} \implies \begin{cases} v_i \leftarrow v_{\text{reset}} \\ u_i \leftarrow u_i + d. \end{cases}\tag{3.2}$$

The synaptic inputs

$$I_i^{\text{syn}} = \sum_j g_j W_{ij} P_j(t)\tag{3.3}$$

a neuron received depended on the connectivity matrix \mathbf{W} , the construction of which is explained below. The synaptic strength g_i depends on the pre-synaptic neuron type, with $g_i = g_{\text{AMPA}}$ for excitatory and $g_i = g_{\text{GABA}}$ for inhibitory neurons.

The synaptic potentials $P_i(t)$ followed exponential decay with time-constant τ_p . Upon firing of the pre-synaptic neuron i the synaptic potential P_i is increased with a factor depending on a variable $R_i(t)$ that captures the number of available neurotransmitter vesicles for release.

This variable follows

$$\tau_R \frac{dR_i}{dt} = 1 - R_i,\tag{3.4}$$

and P_i , R_i are updated following a spike of neuron i as

$$v_i > v_{th} \implies \begin{cases} P_i \leftarrow P_i + \delta_P R_i(t) P_i(t) \\ R_i \leftarrow R_i - \delta_R R_i(t), \end{cases}\tag{3.5}$$

Chapter 4

Experimental Procedures *in vivo*

This Chapter aims to provide a detailed description of the experimental procedures *in vivo* used in this Thesis. Since most of the data was obtained from experiments in human subjects using functional magnetic resonance imaging (fMRI), in this chapter we will also introduce the tools and strategies that were devised to analyse and interpret such data.

4.1 fMRI data description

The magnetic resonance imaging (MRI) is a harmless technique since it does not use X-ray or any ionizing radiation. However, if the participant presented any medical incompatibility—having a pacemaker, an automatic defibrillator or neuraxial clips implanted or any non-removable metallic prosthesis—it was excluded from the study since it could be dangerous for the participant's integrity. The major inconvenient that could arise from the scanning procedure was the feeling of claustrophobia, since the scanner is shallow and the space was reduced. In addition, during the recording, despite a noise-cancellation headphones were granted to the participants, the loud noise of the scanner can be annoying and uncomfortable.

For the data employed in this Thesis, the approximate duration of the session was about 30 minutes in which the participants were asked to rest laying down trying not to move at all and facing up with the eyes open, to prevent the person to fall asleep. The exploration with the MRI technique provided spatially accurate images that permitted the evaluation of the structural integrity of the brain and also the performance of functional analysis of the brain regions while the participant was at rest.

Two main paradigms emerge when an fMRI study is designed: task related and resting-state. On the one hand, task-related fMRI studies require participants to perform a task during the registration and assign functions to a specific brain region. On the other hand, the resting-state measures indirect brain activity when there is no presentation of stimuli to the

subjects. In the resting-state approach, since there is no task-related event, the technique measures spontaneous activation (Yang et al., 2020) of different brain regions. Afterwards the timeseries can be analysed by means of cross-correlation to explore the similarity of the BOLD signals and evince the functional correlation between brain regions (Biswal et al., 1995; Greicius et al., 2003). A final consideration is that the fMRI recording must be long and accurate enough to generate large-scale functional maps (Smith et al., 2009).

4.1.1 Participants

The original data used in this part of the Thesis is comprised of resting state (rs) fMRI sequences (rs-fMRI) of 121 healthy individuals pooled together from three different studies conducted at the Department of Medicine, School of Medicine and Health Sciences, University of Barcelona. However, two subjects were discarded because the T1-weighted acquisition, *i.e.*, the imaging protocol that provides the structure of the brain tissue, was noisy. Additionally, four subjects were excluded due to excessive movement during the registration (Jenkinson et al., 2002), and four more subjects were excluded due to incomplete recordings, leaving a total sample of 112 participants. The protocols associated to the three studies were approved by the Ethics Committee (*Comissió de Bioètica*) of Universitat de Barcelona, approval No. PSI2012-38257, and the Ethics Committee from Barcelona's Hospital Clínic, approvals No. 2009-5306 and 2011-6604.

The above exclusion criteria included illiteracy or an inability to either understand the protocol or undergo neuropsychological tests, as explained in the next section, which could arise from cerebrovascular accident, any relevant psychiatric illness, advanced cognitive deterioration, dementia, or other neurodegenerative diseases (*e.g.*, Parkinson's disease). Additionally, exclusion could also be account for subjects that had chronic illnesses expected to shorten survival (grave diseases such as heart failure, chronic liver disease, kidney failure, blood disease or cancer) as well as any MRI-related incompatibility (the presence of metallic objects within the body, pacemaker or claustrophobia).

The final participant sample of 112 healthy individuals aged 48 – 89 years (68.80 ± 7.99) years (50% females). The participants were split into 6 age groups (< 60, 60 to 64, 65 to 69, 70 to 74, 75 to 79, and ≥ 80) with the following group sizes: $n_1 = 12$; $n_2 = 21$; $n_3 = 30$; $n_4 = 21$; $n_5 = 18$ and $n_6 = 10$, respectively. The age intervals were chosen to detect slight differences in relatively short aging intervals. This categorization had been used in previous studies and is coherent with the suggestion made by Sala-Llonch et al. (2015). Only 2 participants were younger than 55 years in the first group, and only 4 participants were older than 85 years.

4.1.2 Instruments

The three protocols contained a neuropsychological assessment of major cognitive domains, including the vocabulary scale in the Wechsler Adult Intelligence Scale (WAIS) (Lezak, 2004), the mini-mental state examination (MMSE) (Folstein et al., 1975; Tombaugh and McIntyre, 1992), the National Adult Reading Test (NART) (Nelson and Willison, 1991) and the Boston Naming Test (BNT) (Goodglass et al., 1983). However, specifically, the participants of the first and third protocols were also assessed with the Rey Auditory Verbal Learning Test (RAVLT) (n=80; Rey (1958)), and the participants of the second protocol were also assessed with the Grober and Buschke Test (n=32; Grober and Buschke (1987)). To ensure that all participants had a normal cognitive profile, neuropsychological tests were administered and only participants with MMSE scores over 25 (Mitchell, 2009), as well as performances on neuropsychological tests no more than 1.5 standard deviations (SD) below normative scores on any of the tests administered, were accepted in the study. In other words, participants were sufficiently healthy to do not fulfill criteria for mild cognitive impairment (Petersen and Morris, 2005).

4.2 MRI acquisition

All structural and functional data recordings were performed at the *Unitat d'Imatge per Ressonància Magnètica IDIBAPS* (Hospital Clínic, Barcelona) by the research team directed by Dr. David Bartrés Faz.

The three protocols used a Siemens Magnetom Trio Tim syngo 3-T system scanner. Firstly, a high-resolution T1-weighted (T1-w) structural image was obtained with a magnetization-prepared rapid acquisition gradient echo (MPRAGE) three-dimensional protocol with repetition time (TR) = 2300 ms, echo time (TE) = 2.98 ms, 240 slices, slice thickness = 1 mm, and field of view (FOV) = 256 mm. Secondly, for the resting-state acquisition, participants were instructed to lie down with their eyes closed and not to fall asleep. The fMRI recordings were obtained with TR = 2000 ms, slice thickness = 3 mm, interslices gap = 25% and FOV = 220 mm. Notably, the BOLD signal acquisition was slightly different for each protocol, as summarized in Table 4.1.

Although the total recording time is established in terms of minutes usually the term dynamics points is used to refer the acquisition data points from the scanner. Consequently, in this case, each dynamical point represents 2 seconds of recording. Additionally, while Protocols 1 and 3 recorded 150 dynamic points, Protocol 2 recorded a total of 300 dynamic points. This difference between protocols complicated the statistical processing of the data. Thus, the temporal registries of Protocol 2 were truncated, and only the first 150 dynamical

Table 4.1 fMRI acquisition protocols

Protocol	n (participants)	TE (ms)	Total recording (minutes)
Protocol 1	32	16	5
Protocol 2	57	16	10
Protocol 3	23	19	5

points were used. Additionally, a difference in the echo time (TE) on Protocol 3 was reported, but it was so slight that no further effect was seen on the sample data between protocols. Furthermore, this parameter was included as a covariate in the analysis to assess potential confound effects. The structural T2 images of every participant were revised to identify any possible abnormality before including the participant in the statistical analysis. No structural abnormalities or alterations were found in any participant.

4.3 Data analysis tools

4.3.1 Data preprocessing

Image preprocessing was performed using the Data Processing Assistant for Resting–State fMRI (DPARF; <http://rfmri.org/DPARF>; Yan and Zang (2010)). Essentially, the pipeline (Figure 4.1) was based on MATLAB, SPM12 and DPABI, a toolbox for *Data processing and analysis for brain imaging*. Primarily, the first 10 functional images were discarded to avoid possible effects from participants adapting to the scanner. Also, this ensures the magnetization to equilibrate properly and guarantees that the magnetic field from the scanner is homogeneous and steady. Then, the remaining functional images were corrected for slice time by means of their timing acquisition to secure the correct reconstruction of the brain images. Additionally, a head motion assessment was carried out to detect possible movement from the participants through the scanning procedure. Nuisance signals were regressed out considering white matter and cerebrospinal fluid signals, linear trends and, finally, signals associated with the 24 Friston head–motion parameters (Friston et al., 1996).

Afterwards, the T1–w structural images were segmented and transformed (normalized) into a common coordinate space, the Montreal Neurological Institute (MNI) space, using Diffeomorphic Anatomical Registration Through Exponentiated Lie algebra (DARTEL) tool. Consequently, the derived functional images were also normalized to MNI space with warped parameters and resampled to 3 mm cubic voxels. Thus, the derived functional images were correctly coregistered with their corresponding structural images. To assess excessive

movement from the functional recording, participants exceeding the group mean plus two standard deviations (Yan et al., 2013) were excluded from the study. The mean movement group value was estimated with Jenkinson's framewise displacement (FD; Jenkinson et al. (2002)), and the mean FD is shown in Table 7.1 for each group (see Chapter 7). As mentioned in the participants description (Section 4.1.1), 10 participants were discarded through the preprocessing procedure, and the final sample was 112 healthy people. Therefore, further statistical analyses were performed with the covariate of mean Jenkinson's FD for every subject.

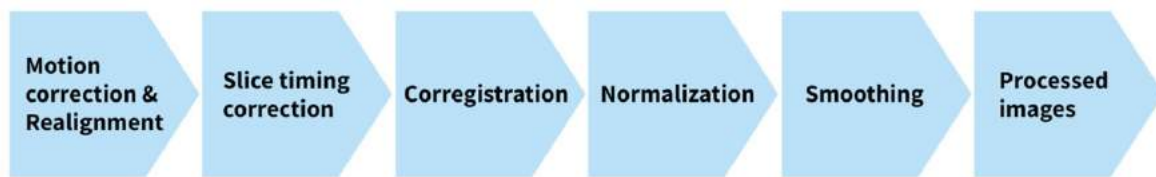


Fig. 4.1 Pipeline of the MRI preprocessing. This sketch illustrates the steps of the pipeline followed to preprocess the fMRI recordings. Generated with *Genially*.

4.3.2 Voxel-based Morphometry

The T1w-structural images were automatically processed with DPABI (Yan et al., 2016). The images were reoriented and individually checked for quality control. Afterwards, reoriented T1 images were segmented into grey matter (GM), white matter (WM) and cerebrospinal fluid (CSF; Ashburner and Friston (2005)). Finally, the DPABI module used the DARTEL tool (Ashburner, 2007) to compute transformations from individual native space to MNI space. Finally, grey matter segmentations were resliced and smoothed to match the parameters with the functional images. Additionally, total grey matter volumes and parcellation volumes were calculated using SPM12 (<http://www.fil.ion.ucl.ac.uk/spm>) and SPM12 based scripts (Maldjian et al., 2004, 2003).

4.4 Seed-based analysis

In a seed-based correlation analysis (SCA), one region of interest (seed region) is chosen to drive the resulting functional connectivity map. This seed region may be a single voxel, a group of them or even a functional region defined in the brain.

This technique aims to extract a whole-brain map that describes the strength of the functional connectivity of each voxel with the selected seed region of interest. To do so, the BOLD timeseries of all the voxels or functional ROIs are extracted for each subject.

Afterwards, the *Pearson* correlation coefficient between these timeseries and the seed voxel is computed, allowing to generate a whole-brain connectivity map.

Once the resulting seed-based connectivity map is extracted for every subject it can be used in subsequent group-level analysis. Typically, the values of the connectivity maps are transformed to *Z*-scores using *Fisher's r-to-Z transformation*. With this transformation, *Pearson* correlation coefficients, that range from -1 to $+1$, convert to a normally distributed variable, *z*-score, that is not bound by lower or upper limits.

This approach has been used in many fMRI studies involving healthy aging (Hirsiger et al., 2016), Alzheimer's disease (Dennis and Thompson, 2014; Tang et al., 2021) and psychiatric diseases (Yu et al., 2020).

4.4.1 The amplitude of low-frequency fluctuations

Several measures of rs-functional connectivity focus on detecting similarities in the fluctuations of the BOLD signal between two brain regions. However, it is also possible to extract potential valuable information from an individual region. Since BOLD signal is dominated by the low-frequency fluctuations (due to the slow timescale of the hemodynamic response function) it can be interesting to measure the amplitude of low-frequency fluctuations (ALFF) for each voxel. In some sense, this measure attempts to estimate the neuronal component from the BOLD signal by determining how much of the power is in the low-frequency range (Bijsterbosch et al., 2017).

ALFF is estimated by calculating the Fourier transform, *i.e.*, the power spectrum, of each voxel timeseries, reflecting the different composition of the signal in terms of frequencies. Moreover, ALFF can be calculated by taking the average square root power within the low-frequency range (0.01 – 0.1 Hz) and afterwards standardized by dividing it by the global mean of ALFF. However, ALFF is sensitive to noise fluctuations, particularly near arteries and veins. The fractional amplitude of low-frequency fluctuations (fALFF) is considered to be more sensitive to those fluctuations whose origin is neuronal (Zou et al., 2008). Fractional ALFF is a normalized version of ALFF since it is defined as the average square root power in the low-frequency range divided by the square root power across the entire frequency range. It can be estimated as follows:

$$fALFF = \frac{\text{total power in the low frequency range (0.01 – 0.1 Hz)}}{\text{total power across the entire frequency range}} \quad (4.1)$$

The estimation of fALFF values was performed using DPABI. To estimate ALFF, additional spatial smoothing of the voxels was performed with a 4 mm full width at half maximum

Gaussian kernel. After that, the time series of each voxel was transformed to the frequency domain with a fast Fourier transform to compute the power spectrum. To compute ALFF, this power spectrum, with an initial frequency range of 0 – 0.25 Hz, was square-rooted at each frequency and then averaged across 0.01 – 0.08 Hz at each voxel. Finally, to obtain fALFF, the latter ALFF values were divided by the whole frequency range observed in the signal (0 – 0.25 Hz; Zou et al. (2008)). Finally, individual fALFF maps were standardized into z-score maps by subtracting the mean and dividing by the standard deviation.

4.4.2 Regional homogeneity

Most rs-fMRI methods investigate functional connectivity across the entire brain and thus are especially sensitive to long-range connections. However, the Regional homogeneity (ReHo) technique aims to describe the functional connectivity between neighbouring voxels, *i.e.*, local scale functional connectivity. ReHo is defined as the correlation of a voxel timeseries with the ones of its local vicinity and is measured by the *Kendall's coefficient of concordance* (KCC). Therefore, the output of a ReHo analysis is a single whole-brain map where the higher values represent voxels with a strong temporal correlation with their immediate neighbourhood of voxels.

Also, the estimation of ReHo values was performed using DPABI. The KCC of the time series of all voxels and their neighbours ($n = 27$) was calculated following the procedure described by Zang et al. (2004). All ReHo maps were smoothed with a Gaussian Kernel of 4 mm full width at half maximum (FWHM). Afterwards, the normalized functional images were then bandpass filtered (0.01 – 0.1 Hz). Finally, individual ReHo maps were standardized into z-score maps by subtracting the mean and dividing by the standard deviation.

4.5 Node-based analysis

Node-based connectivity analyses try to address the structure of the connectivity or information flow between different functional regions. Typically, this approach models connectivity through nodes and edges, the first ones representing brain regions (voxels or ROIs) and the latter the connection strength between nodes. Node-based analyses are a form of graph-based connectivity modelling, where the connectivity matrix is built from the signal correlation from nodes and edges defined by the brain regions of interest.

4.5.1 Graph extraction

Graph analysis techniques provide a theoretical framework to extract higher level measures that enable the description of aspects of network functioning. Depending on their specific characteristics, networks can be either directed or undirected and binary or weighted.

On the one hand, directed networks take into account the direction of information flow between nodes, where the link value from node *A* to *B* is different than the link from node *B* to *A*. Undirected networks consider the existence of one link value between two nodes that are connected and does not consider directionality, so the link value is the same from node *A* to *B* and vice-versa.

On the other hand, a binary network is the one that considers whether if there is or is not a connection between two nodes while a weighted network quantifies the degree of the existing relation between them. The first are mathematically represented by a matrix full of zeros and ones where 0 indicates the absence of link and 1 indicates the existence of link. The latter usually pick normalized values ranging from 0 to 1 to quantify the strength of the link between nodes.

Usually, graph theory analysis uses correlation to calculate the matrix edges. Afterwards, this matrix is filtered to retain significant connections with the less amount of information. The election of the threshold used to filter the connectivity matrices is sometimes arbitrary, and usually an absolute threshold is applied. The discussion of three different thresholding techniques will be discussed in Section 4.5.2

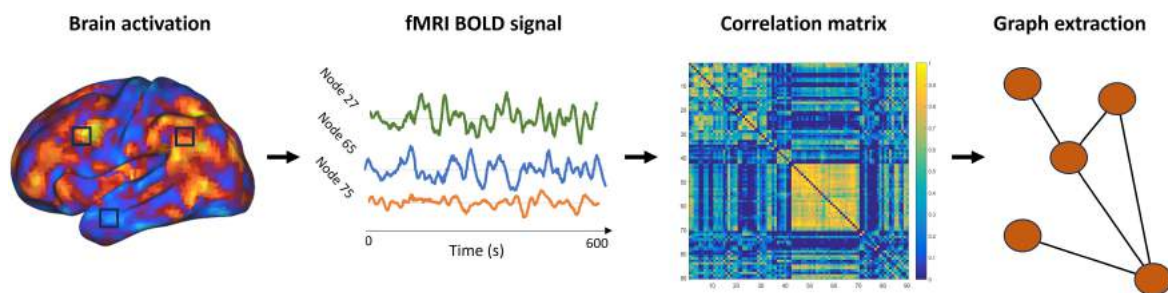


Fig. 4.2 Pipeline of the graph extraction. This sketch illustrates the pipeline followed to extract graphs. First, brain activations are indirectly recorded with the scanner and a 4D image of the brain is acquired. Next, the acquired functional images are processed and the BOLD signal is extracted from the ROIs. After preprocessing, Pearson correlations are calculated from the BOLD signal and the correlation matrices are generated. Finally, after filtering the matrices, graph representations are extracted from the correlation matrices to analyse functional properties of the network.

The Pearson correlation was computed for each individual BOLD time series obtaining an $M \times M$ square matrix, where M is the 90 ROIs defined by the AAL atlas (Tzourio-Mazoyer

et al., 2002). All correlation matrices were considered weighted and undirected throughout this study. Afterwards, these connectivity matrices were then expressed in terms of graphs, conceptualizing every brain region, *i.e.*, Region of Interest (ROI), as a node and the correlation weight as the edge or link between nodes (Figure 4.2).

4.5.2 Filtering methods

We must note that graph analysis, the mathematical framework to understand the data, applies a threshold to every correlation matrix in order to retain those interactions that are significant. In this sense, as the aim of our work was to find which was the adequate threshold in the fMRI-derived connectivity matrices, different approaches for thresholding were considered:

- **Absolute thresholding:** This filtering technique consists on setting a value to cut off the correlation matrices. Typically, absolute thresholding assumes that all correlations above the cut off are strong and significant, and therefore exists a connection between nodes, whereas the ones below of it are removed meaning there is not a connection. In this Thesis, two absolute thresholds were considered. In order to choose the best absolute thresholding, we followed the effect size of Cohen's criterion (Cohen, 1988) and the absolute thresholding further used in the bibliography. In the first place, an absolute $r_t = 0.5$ threshold was used, which preserves all the correlations $r \geq r_t$, from 0.5 to 1 (Pedersini et al., 2020). Following Cohen's criterion, the minimum effect size of the correlations (r^2) included would be of medium intensity. The second absolute threshold used for this study sets the filtering value at $r_t = 0.7$, meaning it preserves the correlations from 0.7 until 1. This criterion was used in many other studies (Aurich et al., 2015), because the effect size (r^2) derived from the lowest correlation included is considered as high intensity (Cohen, 1988). In both thresholds, the proportion of links conserved for every subject varies depending on their potential correlation, which hinders the analysis through subjects. In our samples, the mean and deviation for the absolute thresholding 0.5 were (0.210 ± 0.089) [mean \pm sd] and for the 0.7 were (0.073 ± 0.058) . A great deviation was found in both.
- **Proportional or relative thresholding (10 – 50%):** The aim of this filtering technique is to set a ratio that defines the strongest correlations we intend to preserve out of the total correlation matrix values. By tuning the value of the threshold, we can decide how much information we want to retain. Proportional thresholds do not take into account absolute differences in correlation values, so information about overall group differences may be lost (Garrison et al., 2015). A range of proportional thresholds have been reported, from 5 – 40% (Fornito et al., 2010) The proportion of thresholds used

in this Thesis were set from 10 to 50% in steps of 5%. In this threshold, obviously, the proportion of links was preserved for all the subjects.

- *Triangulated maximally filtered graph* (TMFG): Filtering technique applied to the adjacency matrices that maximizes the significant information between the nodes of a network while minimizing the spurious correlations (Massara et al., 2016). This method sorts the weighted correlation values in descending order and finds the four nodes that have greater sum of edge weights with all other nodes. Afterwards, these four nodes are connected forming a tetrahedron. Then, the algorithm iteratively identifies and adds the node that maximizes the sum of its connections to the three nodes already included in the network (Christensen, 2018). This algorithm uses the joint probability distribution, concept derived from the information theory, to describe the observed behaviour of the variable, in this case the correlation coefficients. Thus, it enhances the computational performance and reduces the computational time. In addition, in the case of this method, the proportion of links is also conserved through all the subjects.

4.5.3 Graph metrics

Six commonly used network graph measures were calculated throughout this fMRI study, namely characteristic path length, clustering coefficient, efficiency, modularity, transitivity, and smallworldness. They were chosen because of the are commonly used in the literature and because they all provided distinct features of the network. Their description and mathematical definitions are described in Chapter 5 and according to Rubinov and Sporns (2010). An openly available MATLAB toolbox named GraphVar (Kruschwitz et al., 2015) was used to extract graph metrics.

4.6 Generation of the null-hypothesis distribution model

Null models are random networks with fixed parameters, and they allow discriminating which graph attributes *could not occur* by chance or, in other words, exceed the expected values given by the null model (Sporns, 2018). They allow comparison with real networks, preserving some fixed parameters, but having random topological properties (Wandelt et al., 2019). Generating a null-hypothesis distribution model, or in short *null-model* of the studied functional network, permits to understand how close or far are the extracted individual network measures from a random distribution. Thus, if the graph measures computed from the filtered matrices, such as clustering coefficient or modularity, would resemble the ones

from a random distribution then the applied filtering method was too severe and no significant information was preserved rather than noise.

Additionally, for each individual thresholded graph matrix also an undirected null-hypothesis distribution model was computed. We note that null hypothesis networks preserve basic characteristics of the original network despite having simple random topologies (Rubinov and Sporns, 2010). A function of the brain connectivity toolbox implemented in *GraphVar* (Kruschwitz et al., 2015) was used to compute these null-hypothesis networks. Specifically, this function randomizes an undirected network with positive and negative weights while preserving the degree and strength distributions of the original network. In this sense, two input parameters were needed for this function: the number of bin swaps, *i.e.*, the average number of swaps of each edge in binary randomization, and the weight frequency, which is the periodicity of weight sorting in the randomization.

For statistical and computational purposes, 10 null-hypothesis models with 1000 iterations were extracted per each individual dataset on each thresholding scenario.

4.7 Thresholding accuracy measure

An accuracy measure was developed in order to evaluate all the threshold values, per graph measure (except for the smallworldness). In this sense, the mean of the ten individual graph measures of the null model and their standard deviation (SD) were used to estimate the percentage of values correctly classified. For every threshold and every graph measure, an individual cut-off point was estimated by adding two or three SDs to the individual null model graph measure. Later, individual subject values were evaluated to know whether they were within or outside the null model interval. The graph measure values that fell inside the null model interval were considered as incorrectly classified and the others were considered as accurate. Finally, a ratio between the accurately classified subjects was computed overall the total subjects and expressed as a percentage. Nevertheless, since the null model values of the efficiency graph measure were greater than the subjects' values, instead of using the addition of the SD, a subtraction was made for this analysis.

Chapter 5

Network and statistical analysis

Here we describe the set of statistical measures that were used to understand the experimental results, both *in vitro* and *in vivo*. These measures allowed to compare different conditions, for instance the impact of topographical obstacles in neuronal cultures or the difference in network properties between healthy subjects and affected patients in fMRI recordings. Figure 5.1 provides a summary of the statistical measures used within the context of network theory, where some magnitudes were common to both the *in vitro* and *in vivo* studies.

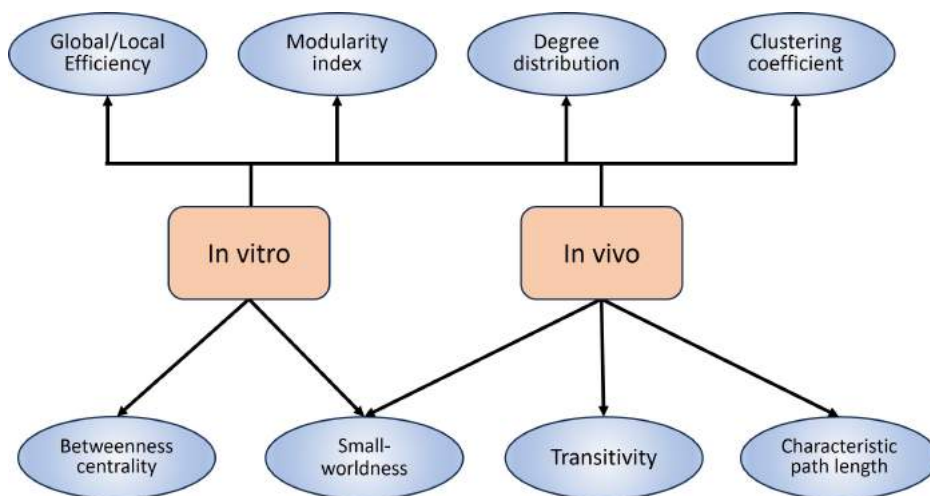


Fig. 5.1 Concept map of the main functional connectivity measures explored. Representation of the functional connectivity measures extracted from the *in vitro* experiments using rat neurons (left) and from the *in vivo* BOLD fMRI recordings (right).

5.1 Dynamical richness in neuronal cultures

The dynamical richness Θ provides a measure for the spatiotemporal variability of network activity, *i.e.*, the existence of a broad range of coactivation patterns and dynamical states, and is defined as (Yamamoto et al., 2018):

$$\Theta = \left(1 - \frac{n_b}{2(n_b - 1)} \sum_{\mu=1}^{n_b} \left| p_{\mu}(CC_{ij}) - \frac{1}{n_b} \right| \right) \left(1 - \frac{n_b}{2(n_b - 1)} \sum_{\mu=1}^{n_b} \left| p_{\mu}(A_b) - \frac{1}{n_b} \right| \right), \quad (5.1)$$

where $p(CC_{ij})$ is the distribution of Pearson's correlation coefficients between the activity trains of all pairs of ROIs i and j , $p(A_b)$ the distribution of burst sizes A_b , $|\cdot|$ denotes the absolute value and $n_b = 20$ is the number of bins used for estimating the distributions.

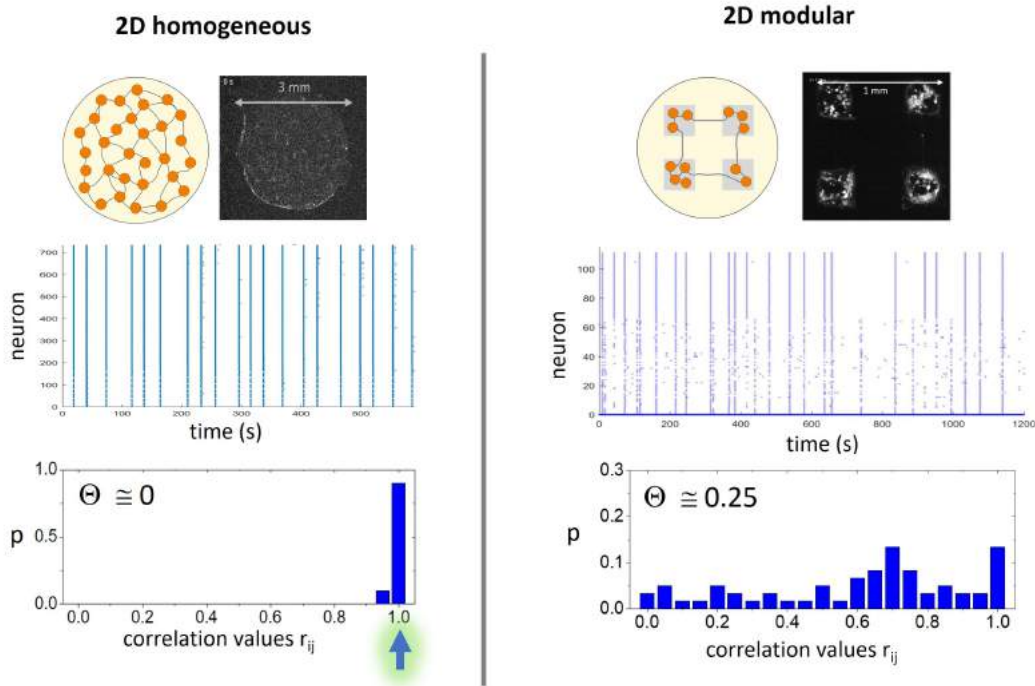


Fig. 5.2 Schematic representation of Dynamical richness values in two different neuronal culture configuration. Left: Homogeneous neuronal culture of 3 mm diameter plated on top of a glass coverslip. Raster plot shows a totally synchronous activation behaviour with the entire population involved. The correlation value distribution is mainly centred around 1, meaning there is no variation in the coactivation pattern and, consequently, dynamical richness is very close to 0. Right: Modular culture with 4 chambers of $200\mu\text{m}$ connected with a single corridor of $5\mu\text{m}$. Raster plot shows a much more richer activation pattern of the neuronal culture, with firing events that involve a smaller fraction of the entire culture. The cross-correlation distribution shows a much diverse landscape with values ranging from 0 to 1, which is traduced with a Θ value of 0.25, meaning a richer dynamical behaviour.

Θ varies between 0 (no richness) and 1 (full richness). Conceptually, as illustrated in Figure 5.2, $\Theta \simeq 0$ corresponds to a scenario of random activity or coherent, whole-network activations, whereas $\Theta \simeq 1$ corresponds to a network state in which neurons coactivate in groups of richly varying size and temporal occurrence.

5.2 Effective Connectivity in neuronal cultures

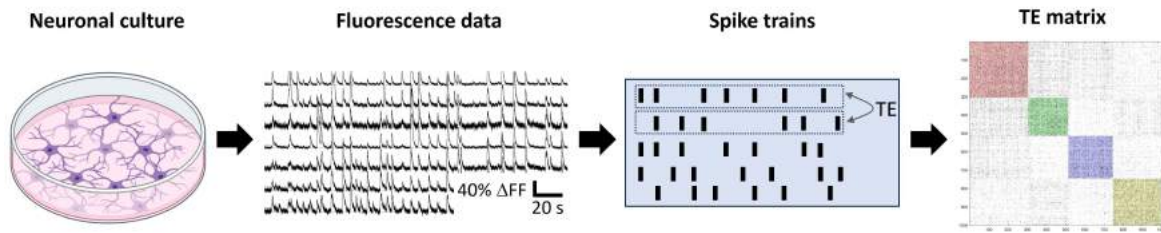


Fig. 5.3 Pipeline of the effective connectivity extraction in the *in-vitro* experiments. Neuronal cultures are prepared on a substrate within a circular well and maintained in an incubator. The culture contains a nutritive solution in combination with viruses that encode for the fluorescence calcium indicator GCaMP6s. Neurons become active during their developmental process, and their spontaneous activity is revealed as sharp peaks in the fluorescence signal of selected ROIs. These peaks are ascribed as neuronal activations and binarized, shaping a set of ‘spike trains’ for each ROI. In a further processing step, generalized transfer entropy (GTE) is used to all pairs of spike trains to infer the effective connectivity between ROIs. Finally, significant causal relationships between ROIs are represented in a sorted binary matrix that highlights the presence of a modular organization or other network traits.

Causal relationships among pairs of ROIs’ activity trains were computed by using a modified version of Generalized Transfer Entropy (GTE) (Ludl and Soriano, 2020; Stetter et al., 2012; Tibau et al., 2018) run in MATLAB. Figure 5.3 provides a summary of the steps carried out to obtain such data. Binarized vectors for the 30 min activity trains (‘1’ for the presence of a spike, ‘0’ for absence) were constructed using a time bin of 20 ms, and an effective connection from ROI I to ROI J ($TE_{I \rightarrow J}$) was established whenever the information contained in I significantly increased the capacity to predict future states of J . Instant feedback was present, and Markov Order was set to 2 (Stetter et al., 2012). The significance z for effective connections was established by comparing the transfer entropy estimate $TE_{(I \rightarrow J)}$ with the joint distribution of all input X to J and output I to Y (for any X and Y), as

$$z = \frac{TE_{I \rightarrow J} - \langle TE_{joint} \rangle}{\sigma_{joint}}, \quad (5.2)$$

where $\langle TE_{joint} \rangle$ is the average value of the joint distribution and σ_{joint} its standard deviation. Significant connections were then set as those with $z \geq z_{th}$, with $z_{th} = 2$ (Figure 5.4). This threshold was considered optimal to capture effective communication both at a local and a global scales (Ludl and Soriano, 2020), *i.e.*, whole–network collective activity and interactions in small groups. Significant TE scores were finally set to 0 (absence of connection) or 1 (connection present), shaping directed yet unweighted connectivity matrices. These matrices were visualized in the form of network maps with Gephi (Bastian et al., 2009), as illustrated in Figure 5.5.

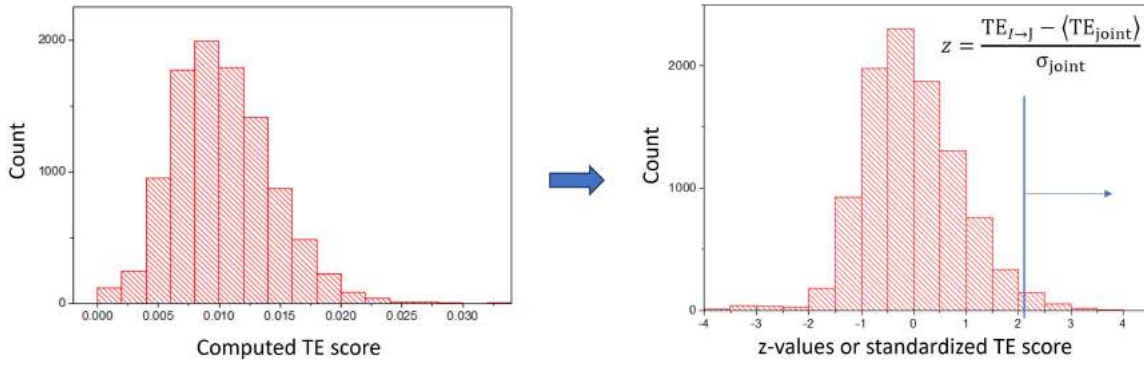


Fig. 5.4 z–score transformation of the Transfer Entropy data. The distribution of raw Transfer Entropy values (left) is normalized as a z–score z (right) and thresholded to consider only those causal interactions with $z \geq z_{th}$, with $z_{th} = 2$ (vertical blue bar). Typically, for $0.5 < z_{th} < 1$ a mixture of weak and strong interactions is observed, but essentially capturing global network communication. For $z_{th} \geq 2$ only strong causal interactions are preserved, and typically portraying the most relevant whole–network communication together with interactions in small groups.

The effective connectivity data was used to computer a number of network measures, described next, as well as basic descriptors related to the intrinsic spatial embedding of the cultures. These descriptors included the Euclidean distance between effectively connected ROIs, d_{ij}^E (in mm), which was simply given by:

$$d_{ij}^E = [(x_j - x_i)^2 + (y_j - y_i)^2]^{1/2}, \quad (5.3)$$

where x_i, y_i are the spatial coordinates of a ROI i on the culture’s surface; and the angle between effectively connected neurons θ_{ij} , which was computed as the angle (in degrees) formed by the vectors of the effective connection $i \rightarrow j$ and the positive x axis of the culture’s surface. An angle of 90° or -90° in the tracks configuration, for instance, indicated that neuronal communication occurred preferentially along the direction of the tracks. For both d^E and θ descriptors, the probability distribution functions were computed by building the histograms of either d^E (bin size 0.2 mm) or θ (bin size 10 degrees) and normalizing them.

We arbitrarily set an effective connection with Euclidean distance d^E to be considered 'long range' whenever d^E was larger than 75% the diameter of the culture. Thus, for our 6 mm diameter cultures, this 'long range' threshold corresponded to 4.5 mm.

It is important to note that effective connectivity informed about the flow of neuronal communication across the culture. It may be related, but do not directly reflect, the underpinned structural connectivity, *e.g.*, axonal lengths or synaptic strengths.

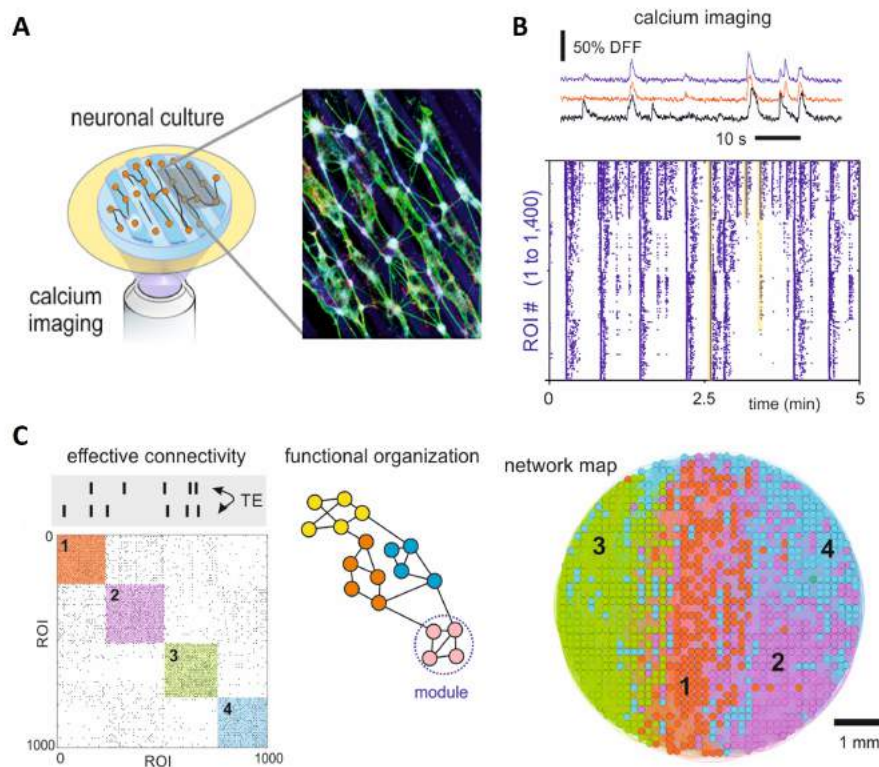


Fig. 5.5 Extraction of functional modules of the *in-vitro* experiments. (A) Representation of the observation of a neuronal culture in the confocal microscope to explore its structure. A coloured immunocytochemistry is shown where the axonal projection can be seen. (B) The example shows the traces of three firing neurons (top) and the raster plot (bottom) of the activations of all culture population (ROIs) through the full recording. (C) The effective connectivity is extracted using a Generalized Transfer Entropy algorithm that analyses causality between the signal from different ROIs. This effective connectivity is represented in a square matrix (left) and sorted by similarity, which enables to detect communities of neurons arranged in functional modules (coloured boxes with numbers). These functional modules can also be represented as a graph (centre) and described by network traits such as clustering coefficient or modularity. Finally, neurons of each functional module can also be identified and plotted in the physical space of the neuronal culture to see the extent of the communities (right).

5.3 Functional connectivity in fMRI recordings

Statistical relationship between pairs of ROIs' BOLD signal were computed by using the Pearson correlation coefficient in RStudio. A weighted squared matrix for all ROI pairs along the 5 min fMRI activity was computed, being the correlation coefficient the weights of the functional connectivity. The Pearson coefficients ranged from -1 to 1 , but the functional matrix only took into account the positive coefficients. Also, autocorrelations were not considered, setting the elements of the principal diagonal of the matrix as 0 . The final preserved weights represented the intensity of the statistical relation between brain regions (from '0' for the absence of correlation to '1' for full correlation).

For clarity, the functional connectivity extracted from the fMRI data is a weighted statistical relationship, thus no directionality can be inferred between brain regions. On the other hand, the effective connectivity computed from neuronal spikes in the *in vitro* experiments does indeed represent the flow of information between ROIs and hence the functional network is directed.

5.4 Network measures

Effective connectivity matrices were analysed using the 'Brain Connectivity Toolbox' (Rubinov and Sporns, 2010), run in MATLAB, to quantify their topological organization. These analysis of network properties applied to both *in vitro* recording and fMRI measurements. The following network measures were used.

For clarity, we emphasize here that *in vitro* effective networks were directed and unweighted, whereas *in vivo* ones were both undirected and weighted. Additionally, for *in vitro* experiments we refer as a node each individual neuron or small groups of neurons ($2 - 3$ cells) since the selected ROI size is paired with its cellular body. On the other hand, for *in vivo* experiments, we considered that a node is either a brain voxel or one of the 90 brain region defined by the AAL atlas (Tzourio-Mazoyer et al., 2002), depending on the analysis performed (seed-based or node-based).

- *Degree distribution $p(k)$:*

It portrayed the histogram of connections in a given network, and mathematically it accounted for the probability to observe a given node (neuron or brain region) with a specific connectivity. For directed networks, one must consider both the ingoing (in-degree) k_i^{in} and outgoing (out-degree) k_i^{out} of node i .

We must note that, for *in vitro* data, we considered —and compared— only in-degree distributions since in a previous numerical study (Ludl and Soriano, 2020) we showed

that k_{in} better captured the differences among cultures, *e.g.*, homogeneous or with patterning. The probability distribution function $p(k^{in})$ of in-degree values k^{in} for a given network was obtained by computing the histogram of observed k^{in} values with bin size 2 and normalizing it.

For *in vivo* data, since the network matrices were weighted, we considered the degree to be the sum of the Pearson correlation values around the node i . In this case, the *degree* was used as a measure of density or strength of the links between nodes.

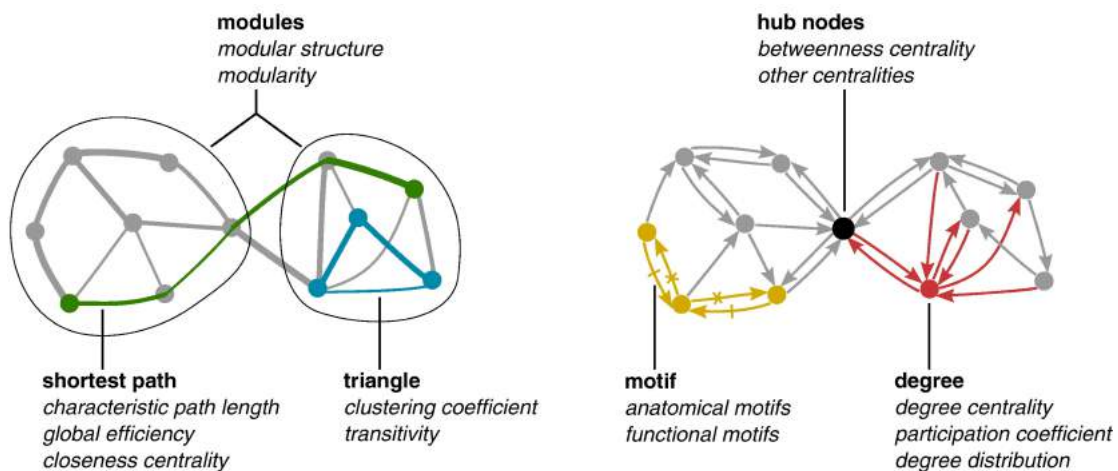


Fig. 5.6 Measures of complex network topology. Top: An illustration of key complex network measures (in italics) described in Rubinov and Sporns (2010). These measures are typically based on basic properties of network connectivity (in bold type). Thus, measures of integration are based on shortest path lengths (green), while measures of segregation are often based on triangle counts (blue) but also include more sophisticated decomposition into modules (ovals). Bottom: Measures of centrality may be based on node degree (red) or on the length and number of shortest paths between nodes. Hub nodes (black) often lie on a high number of shortest paths and consequently often have high betweenness centrality. Patterns of local connectivity are quantified by network motifs (yellow). An example three-node and four-link anatomical motif contains six possible functional motifs, of which two are shown—one motif containing dashed links, and one motif containing crossed links. Adapted from Rubinov and Sporns (2010).

- *Clustering coefficient CC:*

It quantified whether connected nodes to a given pair i, j were also connected among themselves, *i.e.*, they formed triangles. Thus, conceptually, CC measured the cohesiveness of the network at a local scale, with large CC values reflecting groups of neurons that strongly interacted to one another. CC was computed as the ratio between the number of triangles with i as one vertex and the number of all possible triangles that i could form, as described in (Ludl and Soriano, 2020). The probability distribution

function of CC values was evaluated but computing the histogram of observed CC values in a given network with bin size 0.04 and normalizing it.

- *Characteristic path length L :*

The global characteristic path length L describes the average shortest path length d between two nodes in a network. The shortest path length measures the least number of steps it takes to travel from one node to another and indicates the integration level of a network. By these means, shorter path lengths imply stronger potential for integration between regions. The Characteristic path length L is given by:

$$L = \frac{1}{n} \sum_{i \in N} L_i = \frac{1}{n} \sum_{i \in N} \frac{\sum_{j \in N, j \neq i} d_{ij}}{n-1}, \quad (5.4)$$

where L_i is the average distance between node i and all other nodes, and d_{ij} is the shortest path length between nodes i and j .

- *Transitivity T :*

The transitivity T of a network is a variant of the clustering coefficient (CC) that takes into account the functional segregation of a network. Since it is normalized collectively through all the nodes of the network it is not influenced by nodes with low degree (Newman, 2003), as it appears to happen with the clustering coefficient. The transitivity of the network T was given by:

$$T = \frac{\sum_{i \in N} 2t_i}{\sum_{i \in N} k_i(k_i - 1)}, \quad (5.5)$$

where t_i is the sum of all triangles around node i involving other nodes, and k_i is the degree of the node i .

- *Global efficiency G_E and Local efficiency L_E :*

These measures captured the easiness for information flow across nodes or across the network, as illustrated in Figure 5.7. G_E (Latora and Marchiori, 2001) accounted for the capacity of neurons to exchange information across the entire network, and was defined as:

$$G_E = \frac{1}{N(N-1)} \sum_{0 \leq i, j \leq N} \frac{1}{d(i, j)}, \quad (5.6)$$

where N is the number of nodes and $d(i, j)$ is the length of the shortest topological path connecting nodes i and j , with non-connected nodes procuring $d(i, j) = \infty$. $G_E \simeq 0$

indicated that any node poorly communicates with any other in the network, while $G_E \simeq 1$ indicated that there was a strong capacity for information exchange at the whole-network scale (Figure 5.7).

The local efficiency L_E of each node of the network i was computed in an equivalent manner but considering only the subgraph formed by node i and its connected neighbourhood. High L_E values indicate the tendency for strong local communication in the network. The probability distribution function of L_E values was evaluated but computing the histogram of observed L_E values in a given network with bin size 0.04 and normalizing it.

- *Modularity index Q:*

The modularity index Q (Blondel et al., 2008) accounted for the tendency of neurons to form functional modules, *i.e.*, groups of neurons that are more connected within their groups than with neurons in other groups (Figures 5.6 and 5.7), and was defined as:

$$Q = \frac{1}{2m} \sum_{0 \leq i, j \leq N} (A_{ij} - \frac{k_i k_j}{2m}) \delta(c_i, c_j), \quad (5.7)$$

where N is the number of nodes, A_{ij} represents the weight of the connection between i and j , $k_i = \sum_{j=1}^N A_{ij}$ is the sum of the weights of the connections attached to neuron i , c_i is the community to which neuron i belongs, $m = (1/2) \sum_{i, j=1}^N A_{ij}$, and $\delta(u, v)$ is the Kronecker Delta with $\delta(u, v) = 1$ for $u = v$ and 0 otherwise. Optimal community structure was computed using the Louvain algorithm (Blondel et al., 2008). Q ranged between 0 (the entire network shapes a unique module) and 1 (each node is an isolated module). Values of $Q \gtrsim 0.3$ indicated the existence of modules in the network with a varying number of nodes and interconnected to one another, as illustrated in Figure 5.7.

- *Betweenness centrality BC:*

The betweenness centrality of a node i describes its importance in routing information flow across a network. The higher the BC, the larger the number of shortest path in a network that pass through it. BC was determined as the fraction of shortest paths between any pair of nodes j, k in the network that passed through the node i , and was given by:

$$BC_i = \sum_{j \neq k} \frac{n_{jk}(i)}{n_{jk}}, \quad (5.8)$$

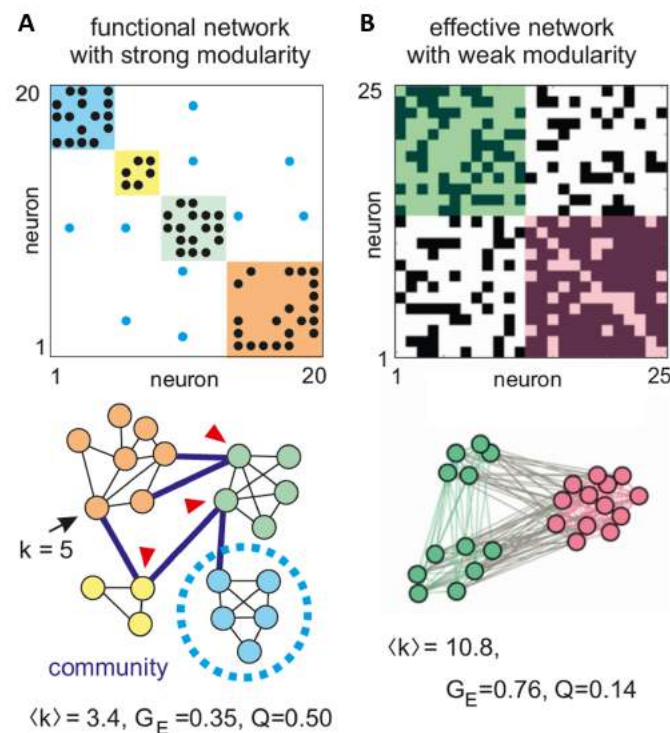


Fig. 5.7 Schematic representation of important concepts in complex networks. (A) Top: adjacency connectivity matrix of a sparse functional network (symmetric matrix, as in the *in vivo* recordings) with 20 nodes and four communities, with the matrix ordered to highlight communities (colour boxes). Black dots are intra-community connections and blue ones are inter-community connections. Bottom: representation of the matrix as a network map. Circles are neurons coloured according to the community they belong to, and lines are connections (black or blue for intra- or inter-community connections). Red arrowheads indicate hub nodes. The quantities k , $\langle k \rangle$, G_E , and Q indicate different network measures. (B) Example of a dense effective network (asymmetric matrix, as in the *in vitro* recordings) with two strongly bonded communities. Adapted from Soriano (2023).

where n_{jk} is the number of shortest paths that link j to k , and $n_{jk}(i)$ is the number of shortest paths connecting j with k that travel through i .

In all studied data, the set of BC values for a given network were scaled by the maximum, so that data was normalized between 0 and 1. The probability distribution function of BC values was then evaluated by computing the histogram of observed BC values in a given network with bin size 0.04 and normalizing it.

- *Smallworldness:*

A well-designed anatomical network may combine the presence of segregated modules with the presence of inter-modular integrating links (Rubinov and Sporns, 2010). This particular design of specialized functional modules integrated by strong links is commonly named small-world and it is measured by the smallworldness (SW) property of

the network. In terms of functional networks, it is commonly thought that a network with small-world architecture reflects an optimal balance between segregation and integration (Sporns and Honey, 2006).

Small-world networks was defined as significantly more clustered networks than random networks even though they have approximately the same characteristic path length (Watts and Strogatz, 1998). Humphries and Gurney (2008) proposed a single measure to capture the ensemble of networks taking into account the segregation and integration measures of the network. In this context, the smallworldness (SW) of the network was defined as:

$$\sigma = \frac{\gamma}{\lambda}, \quad (5.9)$$

where γ and λ are formally given by:

$$\gamma = \frac{CC_p^{net}}{CC_p^{random}}, \quad (5.10)$$

$$\lambda = \frac{L_p^{net}}{L_p^{random}}, \quad (5.11)$$

where CC_{net} and CC_{random} are the clustering coefficient measures of the tested network and a random one. Similarly, L_{net} and L_{random} are the characteristic path length of the same networks.

Small-world networks typically show a value of $\gamma > 1$ and a ratio lambda $\lambda \approx 1$.

5.5 Spatial compactness of functional modules

It was used to investigate whether functional modules in the *in vitro* networks were segregated in the Euclidean space, *e.g.*, as in Figure 5.7, which would indicate that the nodes within the community were physically close, for instance due to physical constraints imposed in the network.

Compactness C refers to the property of objects to exhibit a minimum perimeter P for a given area S , and is mathematically measured through the Polsby–Popper test, $C = 4\pi S/P^2$, with $C = 0$ for a lack of compactness, *e.g.*, randomly scattered spots, and 1 for a circle, the most compact shape. The compactness of the effective networks shown in the Results section of this Thesis was determined as described next, with Figure 5.8 providing representative

examples. For each functional module, its participating ROIs were drawn as solid white squares on a black background (Figure 5.8, left column). ROIs were laid down following a grid, so that two adjacent ROIs shaped a solid rectangle. The final white object containing all participating ROIs was then smoothed to eliminate single black squares surrounded by white regions (Figure 5.8, centre). This was necessary to prevent that few empty regions could dominate the perimeter of the object. The compactness C_i for the object (functional module) i was then computed, evaluating the area (Figure 5.8, centre) and perimeter (Figure 5.8, right).

To correct for the artifact associated with the square shape of the ROIs, which increased the perimeter of the object and procured lower compactness than expected, a reference compactness for the entire culture $C_{culture}$ was also determined by using all original ROIs of the experiment and that, by construction, shaped a circle (Figure 5.8A). The examples of Figures 5.8B to Figures 5.8D correspond, respectively, to a module in a homogeneous network, to one in the ‘tracks’ topographical configuration, and one for the ‘squares’ topographical configuration. We can observe that the presence of topography facilitated compact spots, *i.e.*, modules were formed by physically nearby neurons.

We observed that, typically, $C_{culture} \simeq 0.65$, smaller than the expected value of 1 associated to a perfect circle. Thus, for each functional module, its compactness was corrected as $C_i^* = C_i/C_{culture}$. The compactness values shown in Figure 5.8 and in the results section (see Chapter 6, Section 6.5) were finally obtained, for a given culture, as $C^* = (1/n_f) \sum_i C_i^*$, with n_f the number of functional modules.

5.6 Statistical analysis

Statistical and graphical analyses were conducted with Origin 9.1 and MATLAB 2018a software packages.

For neuronal cultures, the most widely used tests were One-way ANOVA verified with Mann–Whitney test and the t–Students’ test. The outcome of these tests is discussed in the context of the results (see Chapter 6).

For fMRI recordings we considered the following analysis:

To assess differences within the neuropsychological measures between the six age groups, IBM SPSS (v26) was used to perform ANOVA tests with Tukey’s multiple comparison correction, and $p < 0.05$ was set as significant. For statistical analysis of the six groups in fALFF and ReHo, DPABI was used with a voxel–wise ANOVA test with Tukey’s multiple comparison correction. As a precautionary measure and to avoid confusion effects head motion, Jenkinson’s FD (Jenkinson et al., 2002), TE and total GM volume were included as covariates in all analyses. In addition, the criteria used to assess multiple comparisons was

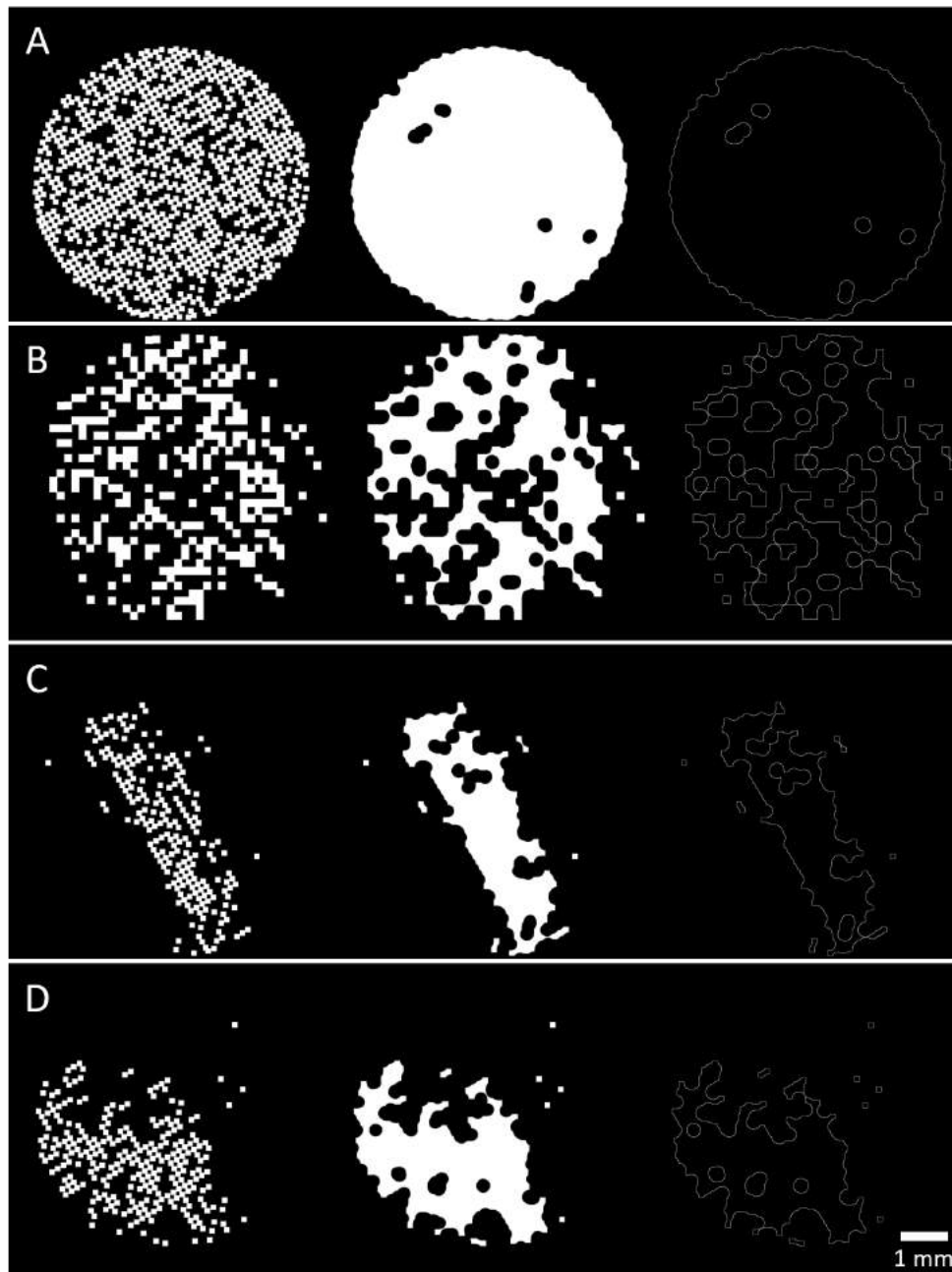


Fig. 5.8 Compactness of effective networks in a 6 mm neuronal culture. The left column portrays the ROIs involved in the analysis, the centre one the smoothed spot for the calculation of the area, and the right one the corresponding perimeter of the spot. **(A)** Reference data corresponding to all active ROIs in an experiment, which ideally should shape a perfect circle with $C = 1$, but effectually provided $C_{culture} \simeq 0.65$. **(B)** Analysis corresponding to a homogeneous culture, where neurons within a module are everywhere in the field of view, providing $C^* = C/C_{culture} \simeq 0.1$. **(C)** Analysis for a module in the ‘tracks’ configuration, with the module providing $C^* \simeq 0.4$. **(D)** Equivalent analysis for a module in the ‘squares’ configuration, with the module providing $C^* \simeq 0.3$.

the Gaussian random field (Eklund et al., 2016), with a voxel p value of 0.001 and a cluster threshold of $p = 0.05$. Additional thresholding, $n = 30$ voxels for ReHo and $n = 10$ voxels for fALFF, was set to exclude very small clusters, although they appeared to be significant after the strict Gaussian random field correction.

Moreover, the significant clusters found in the ANOVA test in fALFF and ReHo were extracted using DPABI and were correlated with age and grey matter volume. As the correlations were high a step-wise regression model was adjusted including as predictor variables the grey matter volume and the most common clusters through age groups found in the ANOVA analysis. Moreover, R Studio (R 4.1.2) was used for the correlations, regression analysis, and visualization matrices.

Complementary analyses considering age as a quantitative variable were performed to avoid a possible loss of information since age was previously considered a qualitative variable. Therefore, both whole-brain fALFF and ReHo values were correlated with age using the criteria of multiple comparisons with the threshold-free cluster enhancement (TFCE), which reaches the best balance between familywise error and test-retest reliability (Chen et al., 2018; Winkler et al., 2016). A total of 10000 permutations were performed, and the cluster p value was set to $p < 0.05$. As in the previous analyses, there was an additional threshold with a minimum extent threshold of 30 voxels for ReHo and 10 voxels for fALFF. For the correlation and regression analysis, only the areas which were common for the six groups were chosen in ReHo analysis. Regarding the right caudate and thalamus, as there were both regions regarding these clusters, they were both included in the correlation analysis.

Multiple comparisons

A common statistical issue that comes forth when diverse tests are computed to a great volume of data, *i.e.*, brain voxels, is the so called *multiple testing problem*. In standard statistics, a p -value of 0.05 implies that there is a 5% chance of obtaining a false result when there is no signal, just from the noise. Taking into account that voxel-based analysis usually parcel the brain in thousands of voxels, the false result, or false positive, appearance is likely to be inflated when using the standard p -value threshold (Han, 2020). It is essential, then, to apply some form of correction to control the number of false positive findings and address the multiple comparison problem.

Most methodologies choose one of two strategies to approach the multiple comparison issue: to adopt a more stringent threshold for the p -value or to adjust the rate of potential false positives. Consequently, the purpose of these correction techniques is to find a balance between trying to minimize false positives (Type I error) and not being too restrictive and

excluding true effects (Type II error) (Han and Glenn, 2018). The following tests are classic procedures used in the field of network analysis.

Family-wise error rate (FWER) correction techniques (Benjamini and Hochberg, 1995) control the probability of getting a Type I error when performing any multiple comparison. In the present Thesis, the next FWER methodologies were performed:

- **Bonferroni correction** is one of the most traditional methods (Han and Glenn, 2018). This technique divides the nominal significance level ($p < 0.05$) by the number of tests being performed (Martin Bland and Douglas Altman, 1995). Despite producing good results for controlling the Type I error, when it is applied in neuroimaging can remove both false and true positives (Han and Glenn, 2018).
- **Gaussian random field (GRF) theory correction** (Nichols, 2012) focuses on the maximum value (across voxels) of the test statistic, parametric approach. Unlike the traditional Bonferroni method, which only accounts for the total number of comparisons, this method assumes that the error fields can be a lattice approximation to an underlying random field usually with a Gaussian distribution (Brett et al., 2003; Eklund et al., 2016).
- **Monte Carlo simulations** estimate the overall significance level of the functional images (Ward, 2000). By means of Monte Carlo simulations and combining voxel probability thresholding and minimum cluster size thresholding, the probability of a false positive is estimated.
- **Permutation tests: Threshold-free cluster enhancement (TFCE)** is a strict multiple comparison correction strategy (Winkler et al., 2016), which reaches the best balance between family-wise error rate (under 5%) and test-retest reliability and replicability (Chen et al., 2018) for voxel wise multiple comparisons. This method provides improved sensitivity, with a richer and more interpretable output than other methodologies (Smith and Nichols, 2009).

False discovery rate (FDR) correction is more sensitive and less likely to produce Type II error than FWE correction methods (Han and Glenn, 2018). Unlike the precedent methods that control for the possibility of any false positives, this method focuses on the expected proportion of false positives only among survived entities (Genovese et al., 2002). In this type of correction, 5% of all voxels would be declared to be significant in the brain. Generally, it is not used in whole-brain, but mostly in network analysis (Chen et al., 2018).

Chapter 6

Results I: Understanding complex functional organization in neuronal assemblies

A fascinating yet intriguing property of living neuronal circuits is their capacity to exhibit a rich repertoire of activity patterns and functional states from a relatively hardwired structural architecture (Blankenship and Feller, 2010; Suárez et al., 2020). This property is most prominent in the human brain, enabling the realization of precise and fast-changing tasks with precision, from motor action to memory and cognition (Finc et al., 2020; Park and Friston, 2013), and that reveals the existence of intrinsic mechanisms and network traits for a swift dynamic reconfiguration of neural circuits. An established consensus is that modular and hierarchically modular network organization (Meunier et al., 2010) are fundamental hallmarks for the coexistence of diverse dynamic scenarios, allowing for both specialized computation at the scale of a module (functional segregation) and whole-network information exchange (functional integration; Deco et al. (2015); Sporns (2013)) with balanced wiring-efficiency cost (Bullmore and Sporns, 2012).

Modularity and integration-segregation balance are important actors in the functioning of neuronal circuits and play a key role in their robustness and flexibility (Finc et al., 2020). The sheer size of the brain and the intrinsic difficulty to monitor neuronal-level dynamics in detail, however, have fostered the development of *in vitro* preparations in which complex behaviour at the mesoscale can be investigated (Aebersold et al., 2016; Millet and Gillette, 2012a; Wheeler and Brewer, 2010). Culturing neurons in a controlled environment allows not only for an easy accessibility and manipulation of $\sim 100 - 1000$ neurons but also for the design of true 'structure-to-function' laboratories to investigate the relation between physical wiring and emerging complex behaviour (Bonifazi et al., 2013; Marconi et al., 2012;

Poli et al., 2015). Indeed, different experimental studies have pointed out the advantage of spatial constraints, connectivity guidance and modular designs (Neto et al., 2016) to tune neuronal culture functionality (Forró et al., 2018) and dynamics (Bisio et al., 2014; Park et al., 2021), or to facilitate the coexistence of segregated and integrated states (Yamamoto et al., 2018).

In this Chapter we detail the efforts that we undertook to shape rich dynamics in neuronal cultures through topographical patterning. Taking into consideration the PDMS topographical molds introduced in Chapter 3, Section 3.2.1, we first describe the rich repertoire of spatiotemporal activity patterns that the spatial constraints induce in the neuronal cultures. Second, we explore the alterations in burst initiation and velocity propagation due to the underlying topography. And third, we present an analysis on effective connectivity of the topographical cultures that reveal unique network organisation traits.

6.1 Coherent activity disruption in patterned cultures

6.1.1 The effect of PDMS topographical molds

We used printed board technology to generate a master mold formed by copper motifs $70\ \mu\text{m}$ high deposited on a fiberglass substrate. As described in Section 3.2.1, the motifs were designed using computer-aided design software in combination with printed circuit board technology and included two main configurations, namely parallel copper tracks (termed *tracks*) and randomly positioned squared copper blocks (*squares*) (see Figures 3.2 and 3.4). Briefly, the printed circuit board shaped a relief over which PDMS was poured and cured, giving rise to a topographical design that was the negative of the original mold. PDMS was then cut out as discs 6 mm in diameter that were firmly attached to a glass coverslip, and primary neuronal cultures from rat embryos were grown on the PDMS surface in a homogeneous manner. Cultures were later transduced with the genetically encoded calcium indicator GCaMP6s using adeno-associated viruses (AAVs) and spontaneous activity was monitored using calcium fluorescence imaging. The representative videos V1 and V2 provide a zoom-in detail of the prepared cultured and the characteristics of calcium fluorescence imaging, while videos V3 and V4 illustrate typical recordings and the raw data from which all analyses were conducted. All these videos are provided with this Thesis.

Measurements on the same culture extended from day *in vitro* (DIV) 7, in which the fluorescence signal was sufficiently strong for reliable analysis, to DIV 18, in which neurons started to degrade or detach from the PDMS surface. In all recordings, the field of view fitted the 6 mm diameter of the cultures (Figure 6.1A), *i.e.*, the entire culture of interest was

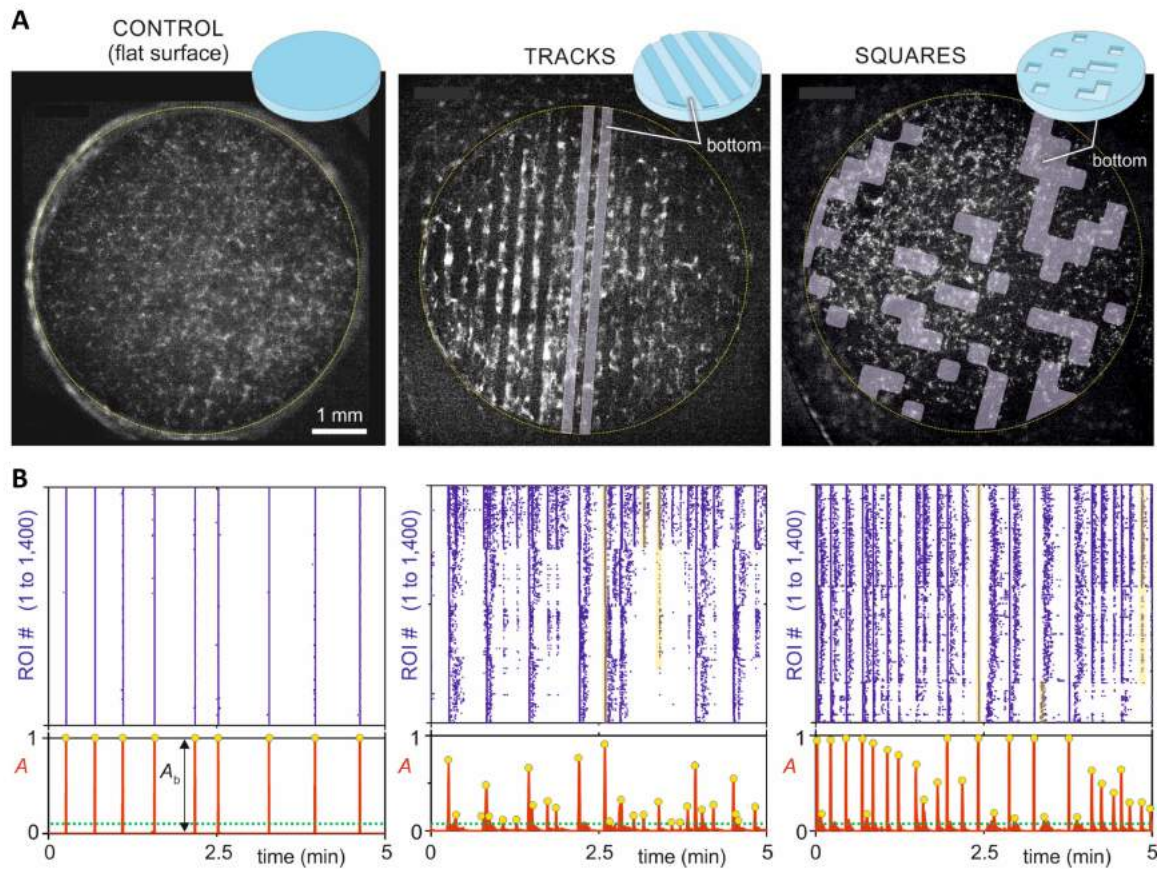


Fig. 6.1 Patterned culture activations. (A) Illustrative fluorescence images of the three studied topographical designs, namely a flat PDMS surface that serves as control (left), parallel tracks (centre) and randomly positioned square valleys (right). All cultures were 6 mm in diameter and were recorded at DIV 14. Bright spots on the fluorescence images reveal active neurons. (B) Corresponding raster plots (top) and population activity A (bottom). Events encompassing more than 10% of the monitored Regions of Interest (ROIs) (green lines) were considered significant (yellow dots) and shaped ‘network bursts’ of size A_b . Raster plots were ordered by ROIs similarity to highlight groups of coordinated activity.

monitored. All recordings were carried out at 25°C, with humidity and CO₂ control, for typically 30 min at 50 images/s.

Figure 6.1A provides illustrative fluorescence images of the prepared neuronal cultures (see also videos V3 and V4 to get a glimpse of the corresponding original data). We also included in our study control cultures plated on a flat PDMS surface, which provided a fundamental reference scenario to, first, investigate the capacity of PDMS patterning to suppress the persistent whole-network bursting of standard cultures, and second, to assess the impact of spatial anisotropies on network dynamics and functional organization. To

emphasize the differences between controls and tracks/squares, in all analyses carried out here the behaviour of control cultures is presented first.

To quantify the collective behaviour of the prepared cultures, we recorded spontaneous activity in each configuration for 30 min, to next extract the fluorescence traces in small Regions of Interest (ROIs) that contained 5 – 10 neurons each and that covered uniformly the area of the culture (Figure 6.2), giving rise to about 1,400 ROIs.

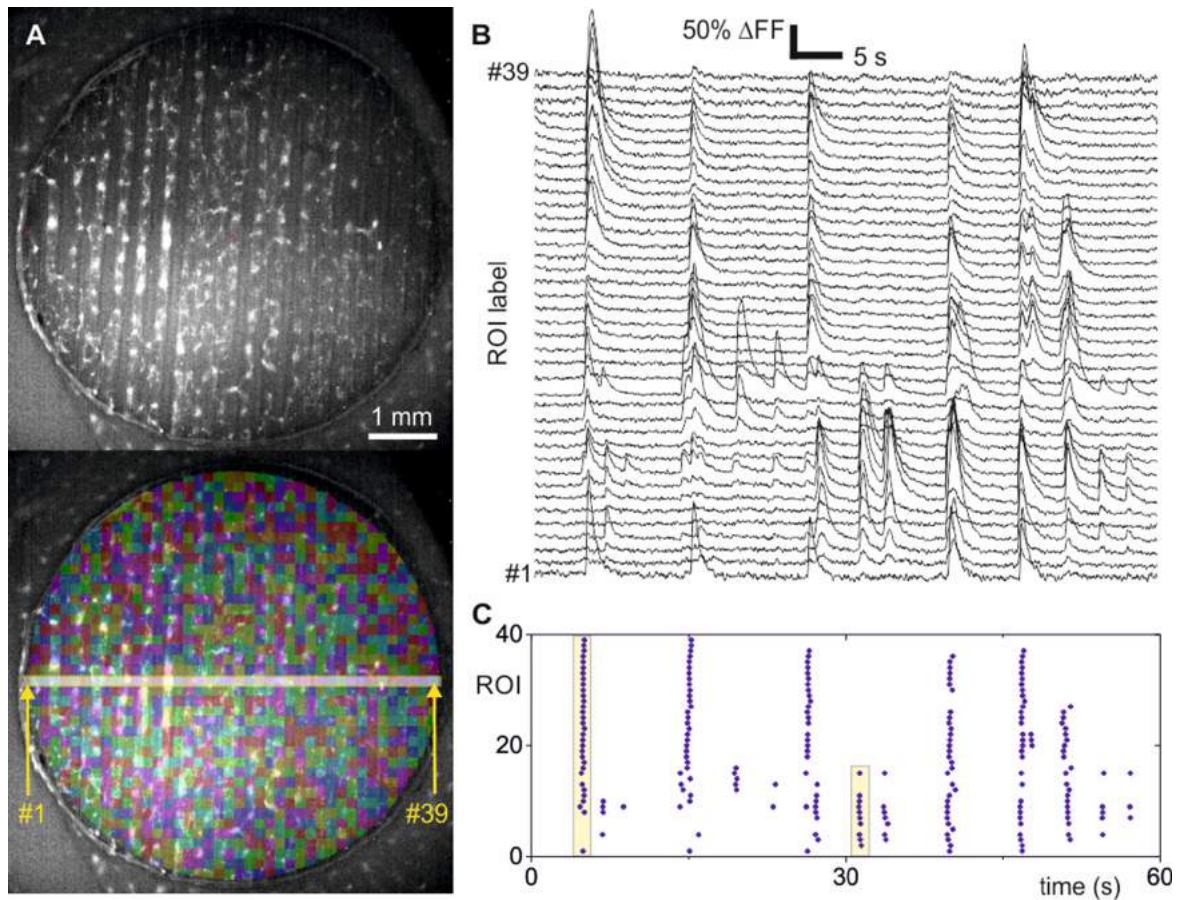


Fig. 6.2 ROI generation and data analysis. (A) Top, highly contrasted fluorescence image of a ‘tracks’ culture. Bottom, Regions of Interest (ROIs) set as squared boxes and covering the entire circular culture, with a total number of 1,400 ROIs. The ROIs labeled as 1 to 39 at the centre of the culture are used to provide representative fluorescence traces. (B) Normalized fluorescence traces of these 39 ROIs along the first minute of the recording, vertically shifted for clarity. Sharp peaks indicate neuronal activity. (C) Corresponding raster plot. Examples of coordinated neuronal activity events of large and small sizes are highlighted with yellow boxes.

The recorded fluorescence data was analysed to extract the activation time of each ROI, and data represented in the form of raster plots. Figure 6.1B shows 5 min of representative data for the cultures depicted in Figure 6.1A. Activity in control cultures was characterized

by episodes of highly coherent behaviour in which all ROIs activated together in a short time window of ~ 200 ms (network bursts) or remained practically silent. *Tracks* and *squares* configurations, by contrast, showed a much richer dynamic repertoire, in which network bursts of different sizes coexisted (yellow bands in Figure 6.1B). Network bursts extended longer periods of time (on the order of seconds) for these topographical configurations, and sporadic activity outside these bursts was also more abundant.

The rich variety of network burst sizes was reflected in the population activity A , which counts the fraction of ROIs that coactivate together (Figure 6.1B, bottom panels). Networks bursts whose size were above background activity (typically 10% of A) were considered significant and denoted A_b . While all events exhibited sizes $A_b=1$ for controls, the event sizes for the topographical designs richly varied from $A_b \gtrsim 0.1$ to $A_b \simeq 1$.

6.1.2 Bursting sizes and dynamical richness

A comparison of the distribution of bursting sizes in the different configurations is provided in the boxplots of Figure 6.3A. Data incorporate different experimental repetitions for the same configuration and compare young (DIV 7) and mature (DIV 14) cultures. For young cultures, while controls produced a narrow distribution with $\langle A_b \rangle \simeq 1$, tracks and squares were significantly shifted towards small values of A_b , with $\langle A_b \rangle \simeq 0.3$ and 0.35 , respectively (p -values $\ll 0.001$ for control vs. tracks/squares). Upon maturation, the distribution of bursting sizes remained high for controls, indicating that these cultures activate in a coherent manner in all its lifespan. For tracks and squares, the distributions shifted towards higher A_b values, with $\langle A_b \rangle \simeq 0.4$ and 0.6 , respectively but the A_b distributions were still significantly different than controls (p -values $\ll 0.001$). We hypothesize that this increase in busting sizes upon maturation is associated with either an overall stronger interconnectivity in the network, longer average axons, or both. These connectivity changes smoothed out the impact of topography on dynamics and favoured a higher presence of network-wide bursts. The validity of this hypothesis is discussed later in the context of effective connectivity analysis. On the other hand, we also observed that the A_b distributions for tracks and squares were also significantly different ($p = 7.5 \times 10^{-6}$ at DIV 7 and $p \ll 0.001$ at DIV 14), indicating that their repertoire of dynamic states was modulated by the specific PDMS pattern at play.

The variety in activity patterns, which is reflected both in the structure of the raster plots and the distribution of A_b values, can be quantified through a single parameter termed *dynamical richness* Θ (Yamamoto et al., 2018). As described in Chapter 5, Section 5.1, this parameter varies between $\Theta = 0$ for perfectly coherent or random activity and $\Theta = 1$ for maximally patterned activity, *i.e.*, with all possible neuronal coactivation patterns present, from few neurons to the entire network. Figure 6.3B shows the results for the evolution of Θ

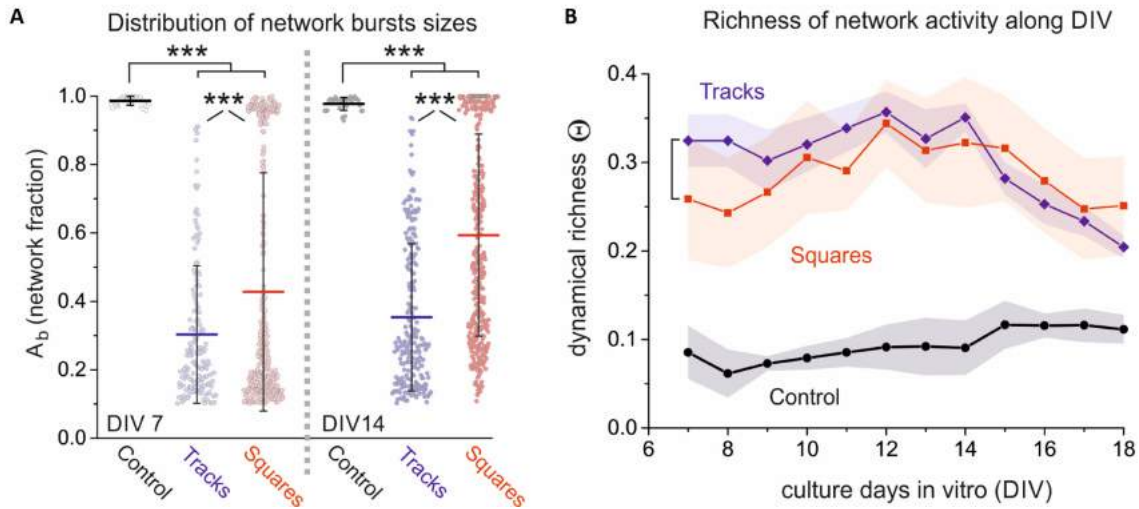


Fig. 6.3 Dynamical richness repertoire. (A) Distribution of bursting sizes A_b for the three configurations and comparing young (day in vitro, DIV 7) and mature (DIV 14) cultures. Data is plotted by pooling together all observations in $n=5$ cultures for controls, 5 for tracks, and 6 for squares. $***p < 0.001$ (one-way ANOVA). (B) Dynamical richness Θ along development. Θ portrays the variability in the raster plots, which is much higher in topographical cultures, particularly in the range DIV 7 – 14. Data are represented as mean \pm standard deviation of the mean.

as a function of DIV for the three configurations, averaged out among different experimental repetitions. While $\Theta \lesssim 0.1$ for controls, with small changes along development, Θ exhibits at short DIV a much larger $\Theta \simeq 0.33$ and $\Theta \simeq 0.25$ for tracks and squares, respectively, remaining high for about a week until it decreases after DIV 14, as network-wide bursting in the topographical designs strengthens, *i.e.*, A_b distributions shift towards higher values (Figure 6.3A).

6.2 Topography induces a rich repertoire of activity patterns

The burst size A_b captures the fraction of the network that activates coherently in a short time window but does not inform about the spatiotemporal structure of a burst. To explore this aspect, Figure 6.4A provides image plots of representative bursts' evolution across the culture for the flat surface configuration. For tracks (Figure 6.5A) and squares (Figure 6.6A), we included data for young (DIV 7) and mature (DIV 14) cultures since they changed in dynamic behaviour along maturation. This was not the case for control cultures, which exhibited whole-network bursts in all their evolution, and therefore only data at DIV 7 is shown. In the image plots we used a black–yellow colour scheme to portray the activation

time of each ROI, and marked the initiation point of the burst spatiotemporal front as a white circle. Regions of the culture with no activity are shown in grey.

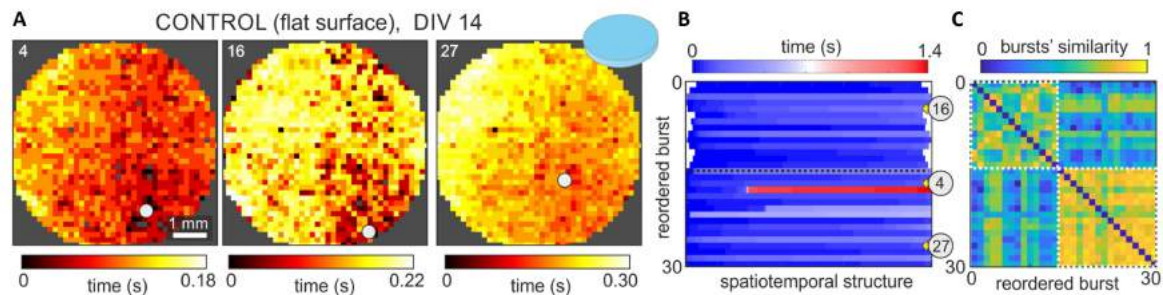


Fig. 6.4 Repertoire of spatiotemporal patterns in control cultures. (A) Representative examples of spatiotemporal activity fronts for controls. Each coloured dot in the image plots is an active ROI, with the colour coded according to the time of activation (from black to yellow). Grey regions indicate absence of active ROIs. The number on the top-left corner of each panel identifies the burst, while the big white dot signals the origin of activity. (B) Classification of burst sizes and propagation. Each band corresponds to a burst, which are ordered according to their similarity. The width of a band indicates the number of ROIs involved in the burst, while its colour indicates the propagation time. Bands with similar colour scheme portray bursts with akin spatiotemporal structure. The numbers within a grey circle indicate the position of the bursts represented in (A). The dotted black lines separate the different groups of bursts. (C) Detailed classification in the form of similarity matrix and following the same organization as in (B). The brighter the colour, the higher the similarity among bursts. White dashed boxes identify the groups of similar bursts.

For controls, activity encompassed the entire culture in all bursts and propagated as a quasi-circular front, which is reflected by a progressive change in colour (from black to yellow) for ROIs gradually further from the origin of activity. Activity propagation was fast, with the bursts crossing the 6 mm diameter of the culture in about 0.2 – 0.3 s. In controls, activity always comprises the entire network and propagates fast ($\Delta t \simeq 0.2 - 0.3$ s) while for tracks and squares, activity switches between few sections of the culture or its whole extent, and much slowly ($\Delta t \simeq 1 - 3$ s). Bursts also started approximately in the same location. Thus, the whole-network activation and the similar location of burst initiation shaped altogether a very rigid system.

In the tracks configuration (Figure 6.5), by contrast, different sizes and propagation schemes were present (videos V3 and V5), in combination with a richer variability in initiation points. Indeed, at DIV 7, some bursts encompassed just a couple of tracks (front #36), the entire culture (#42) or half of it (#53). Propagating fronts required about 3 – 4 s to propagate over the culture, *i.e.*, bursts were an order of magnitude slower than in controls. As the culture matured, the bursts maintained this variability in sizes and initiation points,

although there was a tendency for the sizes to encompass larger areas. Bursts extending only one or two tracks were rare in these mature networks.

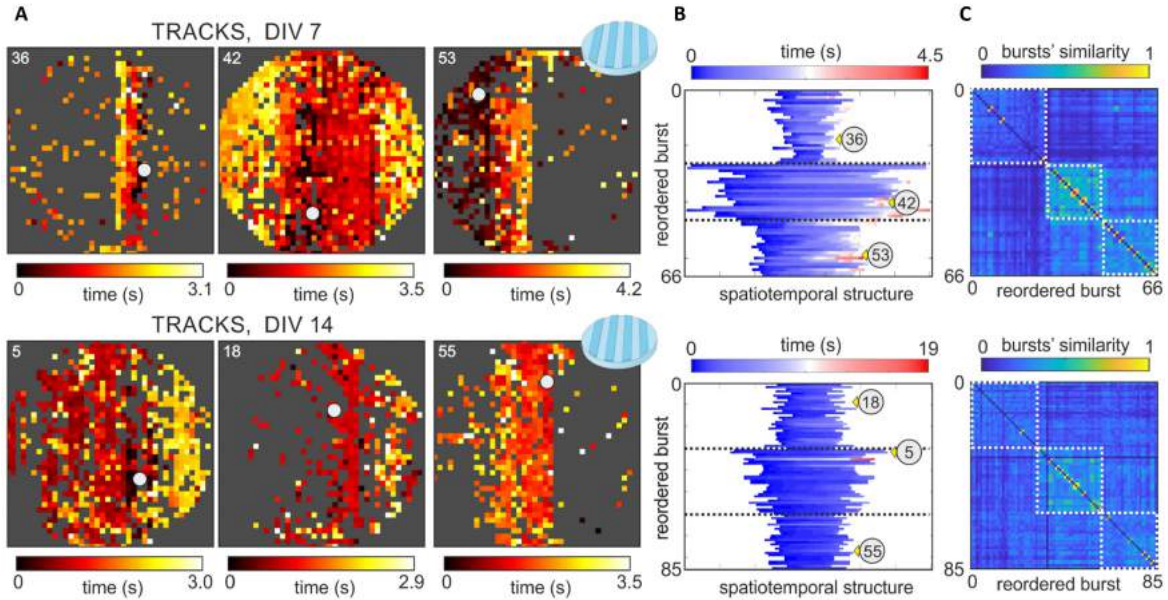


Fig. 6.5 Repertoire of spatiotemporal patterns in cultures with tracks configuration. (A) Representative examples of spatiotemporal activity fronts in young and mature developmental stages. Same colour palette is applied as in Figure 6.4. The number on the top-left corner of each panel identifies the burst, while the big white dot signals the origin of activity. In this case, image plots are drawn for the topographical tracks to coincide with the vertical direction. (B) Classification of burst sizes and propagation. As in Figure 6.4 each band corresponds to a burst, its width indicates the ROIs involved in the burst and the same colour palette is applied. Circled numbers indicate the position of the bursts represented in (A). The dotted black lines separate the different groups of bursts. (C) Detailed classification in the form of similarity matrix and following the same organization as in (B). The brighter the colour, the higher the similarity among bursts. White dashed boxes identify the groups of similar bursts.

For squares (Figure 6.6), we observed that young cultures exhibited a rich variability in burst structures (video V4), which encompassed either specific regions of the culture (bursts #1 and #148) or its entirety (#29). Burst propagation took about 1 – 2 s to cross the system, *i.e.*, in between controls and tracks. The most prominent characteristic of the square's configuration, however, is that for mature cultures at DIV 14 there was a tendency for the bursts to cover large areas. Fragmented activity was rare (bursts #7 and #45) and most of bursts filled the entire culture (#19).

In the B panels of Figures 6.4, 6.5, 6.6 we provide a diagram that compares in a compact manner the spatiotemporal structure of all bursts for each configuration and day *in vitro*. As explained in Chapter 3, each colour band in the diagram represents a burst. The width

of the band indicates the number of participating neurons in each burst, while the colour scale itself portrays the spatiotemporal evolution. Conceptually, those bursts that propagate similarly share the same colour structure. The bursts are ordered in the y-axis according to a similarity analysis that identifies groups of akin bursts. Similarity was based on Pearson's correlation among all pairs of bursts in combination with community detection (C panels in Figures 6.4, 6.5, 6.6, white boxes). The groups of similar bursts are separated by a black line (B panels), and the grey discs with a number show the id of the bursts portrayed in the A panels on Figures 6.4, 6.5, 6.6.

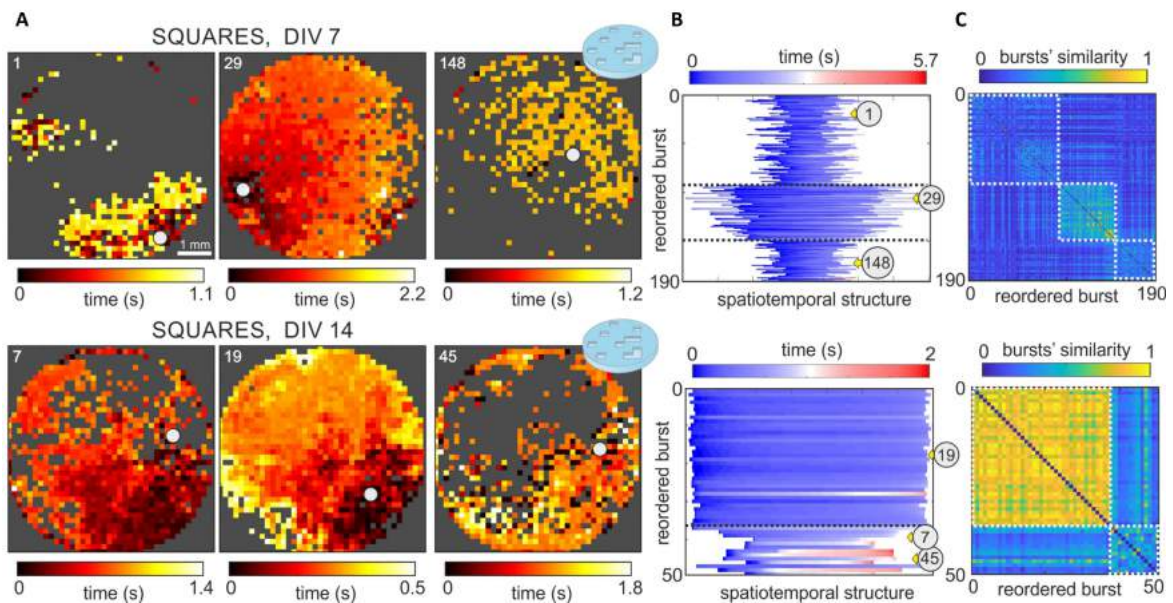


Fig. 6.6 Repertoire of spatiotemporal patterns in cultures with squares configuration. (A) Representative examples of spatiotemporal activity fronts in young and mature developmental stages. Same colour palette is applied as in Figure 6.4. The number on the top-left corner of each panel identifies the burst, while the big white dot signals the origin of activity. In this case, motifs are aligned with the image borders. (B) Classification of burst sizes and propagation. As in Figure 6.4 each band corresponds to a burst, its width indicates the ROIs involved in the burst and the same colour palette is applied. Circled numbers indicate the position of the bursts represented in (A). The dotted black lines separate the different groups of bursts. (C) Detailed classification in the form of similarity matrix and following the same organization as in (B). The brighter the colour, the higher the similarity among bursts. White dashed boxes identify the groups of similar bursts.

For controls, all bursts practically comprised the whole network and therefore they fill the width of the diagram. Additionally, most of the colour bands evolve from dark blue to clear blue, indicating a similar activity propagation across the culture. For tracks at DIV 7 three distinct groups appeared in the diagram and were associated to activity extending a couple of tracks (top group), most of the culture (central group) or half of it (bottom group).

The colour scheme of the bursts was richer than in controls, indicating that spatiotemporal propagation was more varied. These three distinct groups were preserved upon maturation, although the groups were more similar among themselves, and colour schemes were more uniform. A similar trend was observed in the square's configuration. Three distinct groups of bursts were clear at DIV 7, which correspond to typically small yet compact areas of the culture (top), quasi full-culture activations (centre), and small activations in scattered areas (bottom). These groups practically vanished at DIV 14 as most of the bursting events comprised the entire culture.

6.3 PMDS topography induces connectivity traits

To understand the origin of the rich repertoire of activity patterns, we carried out an immunohistochemical analysis on the tracks and squares configurations. As shown in Figure 6.7, we were interested in identifying neuronal processes (green), astrocytes (red) and cell nuclei (blue). For tracks (Figure 6.7A), confocal images covering a field of view on the order of mm ('overview', left) revealed that neuronal processes extended preferentially along the direction of the tracks, both at the top and at the bottom of the PDMS relief, and that connectivity in the transverse direction was by comparison very minor (see also video V1). Immunostaining also revealed that neuronal processes often tended to follow the edges of the relief, particularly at the top of the design (Figure 6.7A, detail, white arrowheads). Thus, topography provided guidance to connections, which were funneled along the tracks and shaped a highly anisotropic connectivity. A detail of the images (Figure 6.7A, right) allows to clearly visualize the difference in connectivity along and across tracks. This difference provided the seed for shaping track-oriented, weakly coupled microcircuits that ultimately rendered rich spatiotemporal patterns. The detail immunostaining images also reveal the abundant and uniform distribution of astrocytes in the cultures, which contrasts with the aggregation of cell nuclei (Figure 6.7A, bottom), a trait that could also help to enrich connectivity microcircuits and varied emerging dynamics.

The immunohistochemical analysis for the squares configuration is provided in Figure 6.7B, both at the mm scale (left) and in the detail (right). For this configuration, the relief favoured the formation of strongly connected islands at the bottom part of the relief which, in turn, connected with other islands or with the top part of the PDMS. Astrocytes and neurons were also abundant, although the latter were more homogeneously distributed as compared to tracks. Thus, for squares, the presence of spontaneous activity as 'patches' at DIV 7 in Figure 6.6A is most likely due to the activation of relatively isolated groups of neurons either at the top or at the bottom of the topographical relief. The interaction among the top

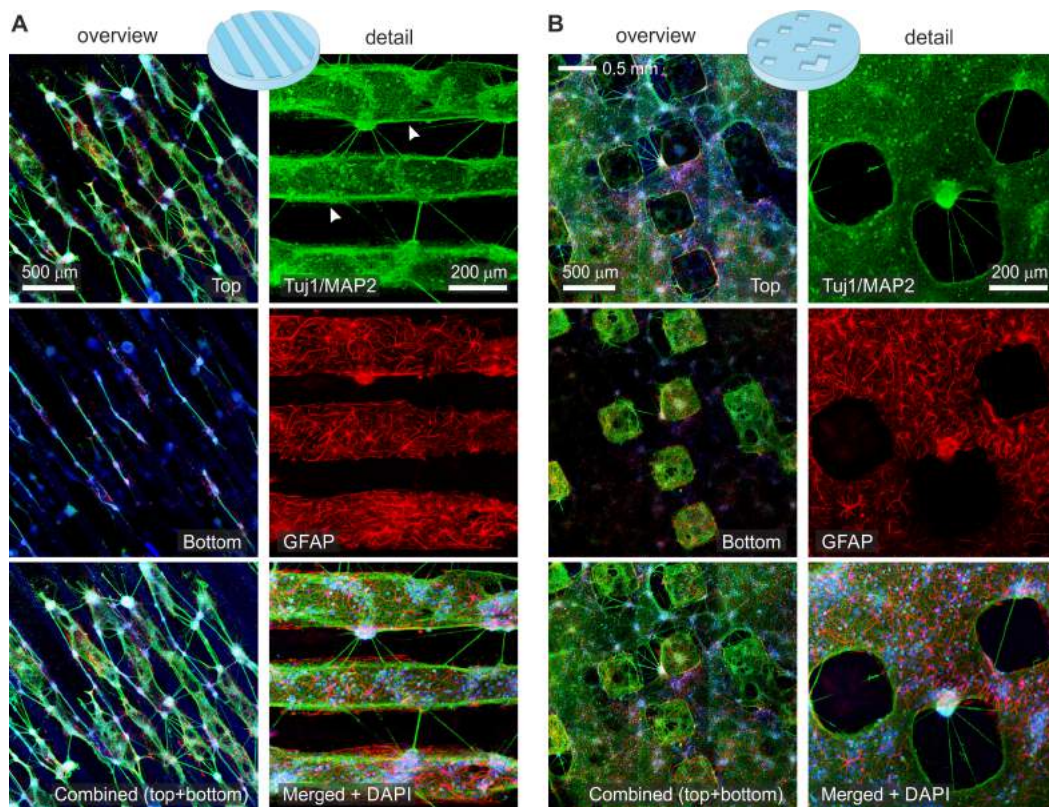


Fig. 6.7 Anisotropic connectivity in PDMS topographical cultures revealed by immunostaining. (A) Representative immunohistochemical images of neurons grown on PDMS topographical tracks at DIV 14, providing a broad overview (left) and a detail (right). For the overview, images show neuronal processes in green, astrocytes in red and cell nuclei in blue, with focus at the top part of the topography, the bottom part, and a combination of them. For the detail, images correspond to the top part of the design only and depict neuronal process (green), astrocytes (red), and the combination of these channels with cell nuclei (blue). Neuronal connections are more abundant in the direction of the tracks than transverse to them. White arrows mark neuronal processes that follow the edge of the topographical design. (B) Corresponding images for the square's configuration at DIV 14. Connectivity is abundant at the bottom part of the square designs, shaping small microcircuits by themselves that interconnect with the top part.

and bottom parts, however, is complex since the entire network sporadically activated in a coherent manner. We note that, as in tracks, the relief facilitates the formation of interacting distinctive microcircuits that shape a rich variety of spontaneous activity patterns. These microcircuits are not stable in time, but rather continuously evolve. Indeed, the observation that activity at DIV 14 mostly encompasses the entire network indicates that there is global tendency for the microcircuits to gradually blend together and cast a much more uniform overall connectivity that translates into whole-network bursting events.

6.4 PDMS topography impacts on burst initiation and velocity of burst propagation

Figure 6.8A provides the spatial distribution of burst initiation for the configurations shown in Figures 6.5, 6.6 at two stages of culture maturation (DIV 7 and DIV14). In the panels, the black dots represent the spatial location of each observed burst while the blue–yellow colourmap shows the corresponding probability distribution function of burst initiation. The degree of activity focalization, *i.e.*, the tendency for spontaneous activity to initiate in the same location, is quantified through the Gini coefficient λ , which is 0 for a spatially equiprobable initiation, and 1 for a point–concentrated initiation occurrence.

For controls (left), most of the bursts at DIV 7 started in the same neighbourhood, leading to highly focalized distribution function (yellow spot) with $\lambda \simeq 0.57$. This focalization was maintained at DIV 14 ($\lambda \simeq 0.51$), although the location of the most probable initiation points varied due to global connectivity changes during maturation. By contrast, activity initiation for the track’s configuration was substantially more extended at DIV 7 ($\lambda \simeq 0.20$), a trait that was maintained upon maturation ($\lambda \simeq 0.16$ at DIV 14). Hence, topographical tracks not only help shaping connectivity anisotropies that enriched spontaneous activity but that these anisotropies were maintained upon maturation. For squares, initiation was spatially extended at DIV 7 ($\lambda \simeq 0.28$) but became focalized upon maturation ($\lambda \simeq 0.72$ at DIV 14). This focalization is consistent with the observed whole–network bursting and the gradual loss of connectivity anisotropies upon maturation.

We extended the above analysis to all culture types and repetitions. As shown in Figure 6.8B, the overall distribution of λ values for controls at DIV 7 was significantly higher than in tracks or squares (grey asterisks, $p=0.017$ and $p=8.0 \times 10^{-4}$ respectively), indicating that activity initiation foci in patterned cultures were consistently more varied. At DIV 14, the λ distributions were not significantly different between controls and tracks/squares, indicating a trend towards a more concentrated activity initiation in all configurations. We note, however, that the dispersion of λ values for tracks/squares was important, and that it accentuated from DIV 7 to 14, with broader λ distributions for the latter day. Interestingly, the tracks configuration maintained an average λ that was similar at DIV 7 and 14, suggesting that the dynamic alterations caused by the track’s topography were preserved. For squares, there was a significant increase in overall λ values from DIV 7 to 14 ($p=0.0029$), and with an average λ comparable to the one of controls.

We also investigated the velocity of propagating fronts in detail. We considered data at DIV 14 since most fronts encompassed large areas of the 6 mm culture, which provided sufficient statistics for a reliable analysis. The top panels of Figure 6.9A show representative

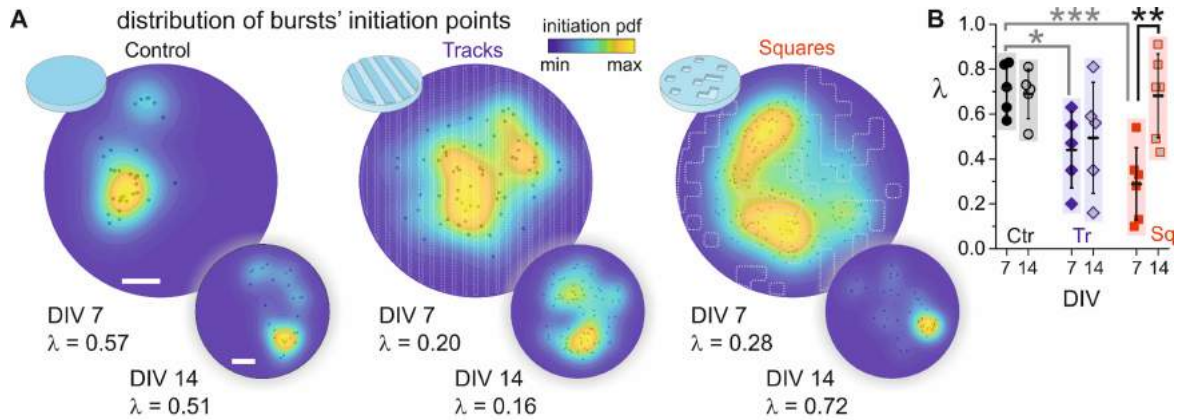


Fig. 6.8 Burst initiation point distribution and Gini coefficient. (A) Spatial distribution of burst initiation points (black dots) and probability density functions of burst initiation (pdf, blue–yellow colourmap) for the PDMS configurations shown in Figures 6.5, 6.6 and comparing two days in vitro, DIV 7 and DIV 14. λ is the Gini coefficient and indicates the degree of focalization of burst initiation. White scale bars are 1 mm and apply to all culture types. (B) Box plots of the distribution of λ values for all experimental repetitions. At DIV 7, the λ distribution for controls is significantly higher (grey asterisks) than for tracks/squares. The λ distribution for squares at DIV 14 is significantly higher than the one at DIV 7 (black asterisks). * $p < 0.05$, ** $p < 0.01$, *** $p < 0.001$ (Student’s t–test).

spatiotemporal fronts for the three configurations, which evolve as quasi–circular fronts from the origin of activity (white circle). As shown in the bottom graph of Figure 6.9A, their characteristic propagation velocity was obtained by linear regression of $d(t)$ data (solid lines), where d is the distance of each ROI to the origin of activity and t its activation time.

The measured velocity was $v \simeq 40$ mm/s for controls and substantially decayed to $v \simeq 13$ and 3 mm/s for squares and tracks, respectively. Pearson’s regression coefficients in all three cases were $r \gtrsim 0.95$. Despite the goodness of the linear regression approach there was, however, a noticeable dispersion in the data for squares and tracks that indicates strong changes in the propagation of the fronts at local scales. For squares, for instance, one could identify a first regime (in the range 0 – 0.2 s) of slow propagation with $v \simeq 13$ mm/s followed by a second one (0.2 – 0.3 s) of fast propagation with $v \simeq 30$ mm/s, which suggests an abrupt change of the underpinned local connectivity during front evolution. For tracks, an inspection of the data revealed that the strong dispersion of some points, with identical time activation of ROIs that were $\simeq 6$ mm apart, was associated with a much faster propagation of activity along the tracks than transverse to them, as discussed below. The analysis of the velocity using linear regression was consistent across experimental realizations (Figure 6.9B), with significantly different velocities between controls ($\langle v \rangle \simeq 42.2 \pm 14.7$ mm/s), tracks (4.7 ± 1.6 mm/s) and squares (23.4 ± 13.0 mm/s).

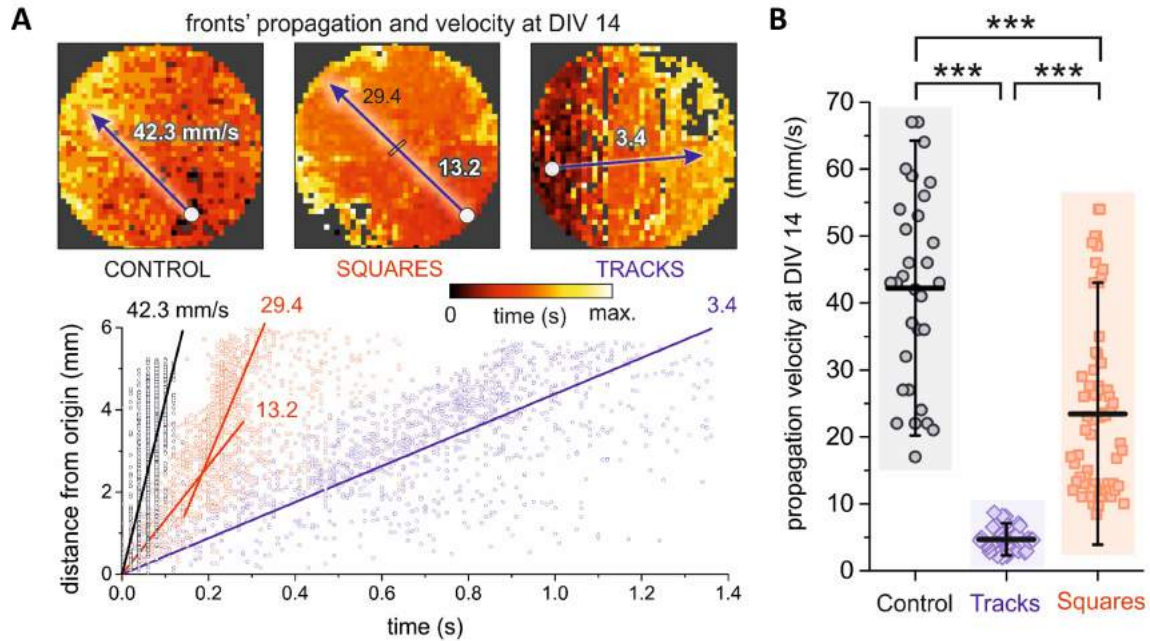


Fig. 6.9 Velocity of propagation bursts in PDMS topographical cultures. (A) Top, representative network bursts at DIV 14 that encompass the entire network and whose propagation is compatible with a circular or flat front. The white dot marks the origin of activity. Bottom, corresponding determination of velocity propagation as linear fits, where the Euclidean distance of each ROI to the origin of activity is plotted as a function of its activation time. The squares configuration exhibits a sudden, two-fold increase in velocity. All linear fits have Pearson's correlation coefficients $r \gtrsim 0.95$. (B) Box plots of propagation velocities for the three configurations, showing that fronts in tracks or squares configurations propagate much slowly than on controls. $***p < 0.001$ (Student's t-test).

The contrast in propagating velocities along PDMS tracks or transversally to them outlined above is analysed in more detail in Figure 6.10A–B (see also video V3). For the illustrative spatiotemporal front of Figure 6.10A we observed that the colour scheme along tracks (vertical axis of the image plot) was practically uniform, with characteristic black and red bands (white arrows) that revealed the fast activation of the whole track, typically in a time window on order of 0.3 s. Conversely, the colour variation transverse to tracks (horizontal axis) smoothly varied from black at the origin of activity to yellow at the right edge of the culture, leading to a propagation time of 4.3 s. The corresponding velocities were about an order of magnitude dissimilar, with $v_{\parallel} \simeq 9.1$ mm/s along tracks and $v_{\perp} \simeq 1.7$ mm/s transversally to them. This dissimilarity was preserved across experimental repetitions and was significantly different (Figure 6.10B, $p = 0.0027$), and on average we obtained $\langle v_{\parallel} \rangle = 17.4 \pm 9.6$ mm/s and $\langle v_{\perp} \rangle \simeq 3.3 \pm 2.2$ mm/s.

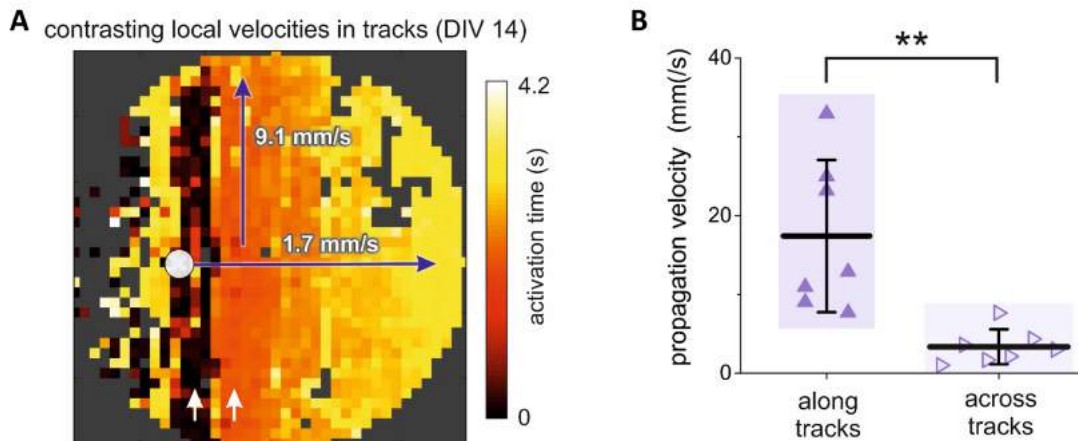


Fig. 6.10 Velocity of propagation bursts in tracks configuration. (A) Local velocities in the track's configuration, illustrating that activity propagation along the tracks (vertical direction) is much higher than across them (horizontal direction). Arrows marks tracks with high propagation speed and therefore very small colour variation. (B) Box plots of velocity propagation for different fronts of the same culture. On average, propagation along tracks is 18 mm/s, about 6 times larger than across tracks, which is of 3.5 mm/s. $** p < 0.01$ (Student's t-test).

6.5 Effective connectivity analysis identifies unique network organization traits

We used generalized transfer entropy (GTE) to infer causal relations among ROIs in the neuronal cultures (Figure 6.11), and from them extracted network measures that exposed functional organizational traits. In all cases we used the data presented in the previous figures and at DIV 14. Conceptually, the nodes of the computed effective networks are the ROIs in our experiments, whereas the links are the flow of information among those ROIs. The network traits that we explored include the Global efficiency (G_E) and the modularity index Q . The former captures the capacity of the network to share information as a whole, while the latter informs about the existence of functional modules, *i.e.*, groups of ROIs that tend to communicate within their group more strongly than with other groups in the network.

Figure 6.11, top, shows the obtained effective connectivity matrices for the three PDMS configurations, with the modules highlighted as colour boxes along the diagonal. In all configurations we observed an abundance of effective connections both within modules and between them. All networks indeed exhibited a similar $G_E \simeq 0.45$, indicating that neurons in the three configurations easily exchanged information globally. This is understandable in the context of the observed dynamics, in which whole-network correlated activity was present in the three cultures and thus global neuronal communication. The modularity Q , however, was clearly different among configurations, with $Q \simeq 0.26$ for controls, $Q \simeq 0.49$

for tracks and $Q \simeq 0.47$ for squares. The low Q for controls indicates that ROIs within a module connected similarly among themselves and the rest of the network, *i.e.*, the network effectually operated as a unique system. The high Q for the topographical designs indicates the presence of functional microcircuits, *i.e.*, strongly interconnected neuronal assemblies.

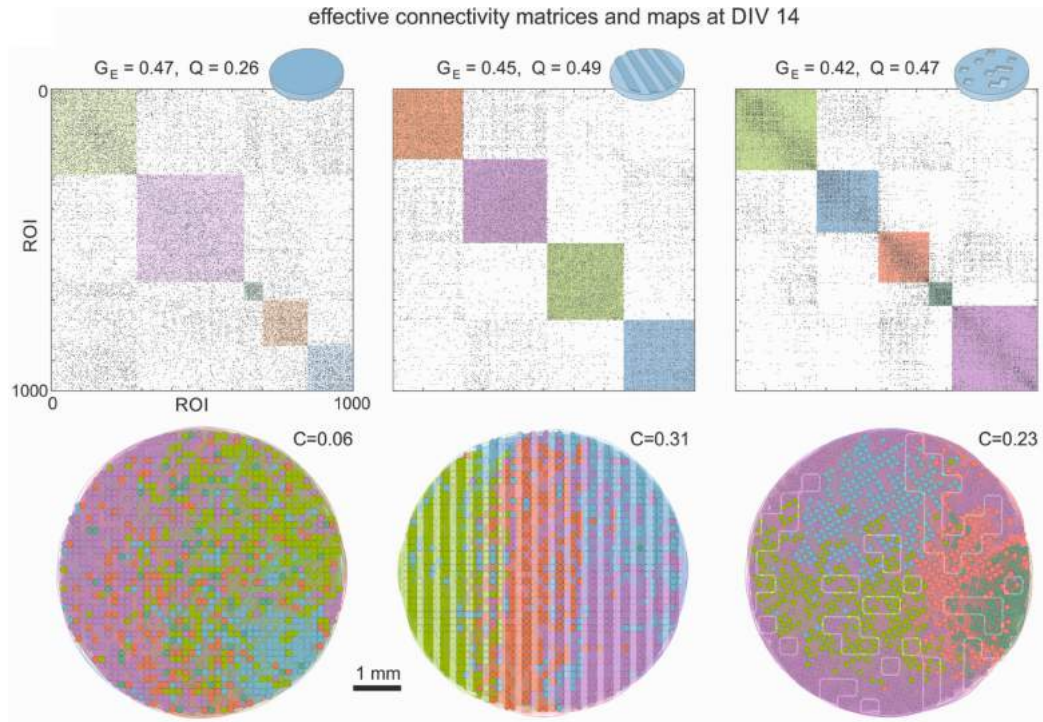


Fig. 6.11 Effective connectivity analysis in PDMS topographical cultures. Top, adjacency matrices of effective connectivity among ROI pairs for the three PDMS configurations at DIV 14. The global efficiency G_E and modularity Q values of the networks are indicated on the top. Colour boxes along the diagonal of the matrices highlight functional modules, with their colour intensity proportional to their strength. Bottom, corresponding network maps, where each dot is an ROI colour coded according to the functional module it belongs to. The value of C accompanying each map indicates the average spatial compactness of the functional modules, which is markedly high for tracks.

The network maps associated to the connectivity matrices (Figure 6.11, bottom) provide an additional insight into the impact of PDMS topography on neuronal network communication. These maps show the spatial location of the ROIs in the culture as circles, and colour coded according to the functional module they belong to. Effective connections are present, but their abundance masks their individual identification. For controls, the functional modules are spatially interwoven over the area of the culture, a feature that is quantified by the average compactness C of the spots (see Chapter 5, Section 5.5) and that provided $C \simeq 0$. This mixture of the modules indicates that a neuron tended to interact similarly with any other in the culture and at very long distances. By contrast, for the tracks configuration we

observed that functional modules shaped compact spots in the culture ($C \simeq 0.31$) that were aligned with the tracks themselves, indicating that the topographical relief orchestrated the functional organization of the culture. The spatial extent of the functional modules could be related to specific spatiotemporal activity patterns (see Figure 6.12 and video SV5), which indicates a relation between network dynamics and functional traits. A similar compact functional organization was observed for the square's configuration ($C \simeq 0.23$), although the shape of the modules did not concord with the arrangement of the PDMS design possibly due to the high connectivity between top and bottom parts at DIV 14.

The obtained results for functional organization in terms of G_E and Q were maintained across experimental realizations (Figure 6.13A). G_E was not significantly different for the three configurations, but Q for tracks and squares was significantly higher than for controls.

To complete the analysis, we investigated in more detail the emergence of local functional features in the topographical cultures. Given the capacity of tracks to funnel neuronal connectivity along their length, we first examined whether such a privileged direction was captured by the GTE effective connectivity analysis. For that, we computed the angle of effective connections relative to the horizontal axis and plotted the distribution of angles. As shown in Figure 6.13B, controls (black curve) showed a homogenous distribution of angles that indicated an isotropic effective connectivity. A similar result was observed for the squares configuration (red), although the distribution exhibited strong fluctuations. For tracks (blue), however, neat peaks appeared at -90 and 90 degrees, distinctly revealing a preferred vertical direction in neuronal communication. Thus, the effective connectivity analysis shown here demonstrated to be an invaluable tool to complete the activity and immunostaining analyses and brought to light additional evidence that the PDMS relief help dictating the way in which neurons wired and communicated.

6.5.1 Euclidean distance analysis in topographical cultures

The observation that effective connections were primarily oriented along the tracks themselves is interesting and made us inquire whether we could also observe differences in the distribution of effective connectivity distances, defined as the Euclidean separation between any pair of effectively connected ROIs. Since effective connectivity reflects dynamics or neuronal communication, in principle these distances could extend the entire culture diameter of $\varnothing = 6$ mm. For sake of discussion, we established that those effective connections that projected beyond 75% of the culture's diameter were considered 'long-range', which corresponds to 4.5 mm. The analysis of the distribution of these distances for DIV 7 and DIV 14 is provided in Figure 6.14, with the data for DIV 14 corresponding to the networks of Figure 6.11. The results show that, for controls, long-range effective connections were

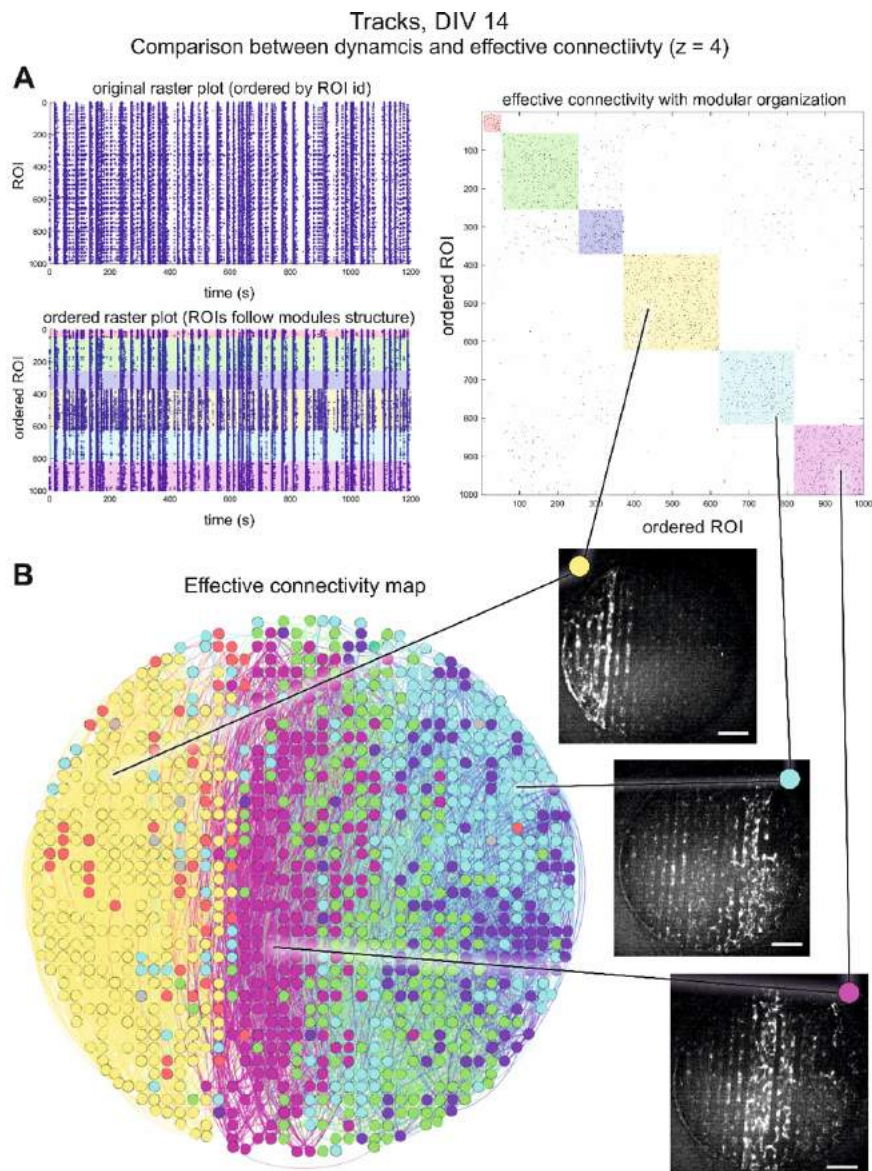


Fig. 6.12 Relationship between effective connectivity and dynamics in 'tracks' configuration. (A) Original raster plot of spontaneous activity (left-top) and effective connectivity matrix depicting the functional modules (right). The reordering of ROI indexes according to the modules shapes a new raster plot (left-bottom) in which dynamic features of the network can be linked to characteristic modules. The yellow module for instance corresponds to a group of ROIs (reordered indexes 400 to 600) with strong spontaneous activity and the presence of collective events that do not exist in the other groups, indicating that functional modules reflect specific activity patterns. (B) Network map of effective connections. ROIs are coloured according to the functional module they belong to. Some modules, particularly the yellow and the pink, coincide in spatial structure with activity patterns that appear often in the recording (fluorescence snapshots), which illustrates the link between dynamics and functional organization.

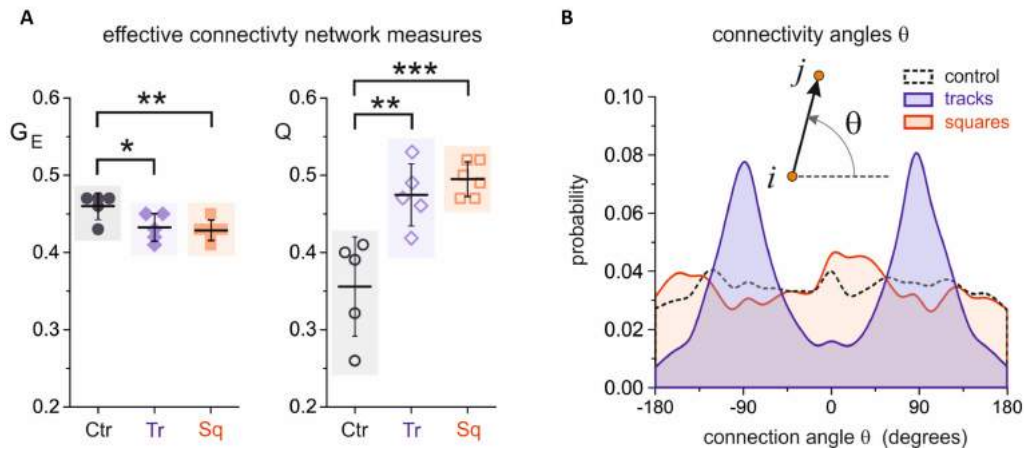


Fig. 6.13 Local and global functional features in PDMS topographical cultures. (A) Box plots of comparing the network measures G_E and Q for the three configurations and including all experimental repetitions. Flat PDMS cultures exhibit a significantly higher G_E and lower Q than the other configurations. $*p < 0.05$, $**p < 0.01$, $***p < 0.001$ (Student's t-test). (B) Distribution of connectivity angles θ , where θ is the angle formed between two effectively connected neurons $i \rightarrow j$ and the horizontal axis. The distributions for both controls and squares are approximately flat, while the one for tracks is markedly peaked at 90 and -90 degrees, indicating strong neuronal communication along the tracks.

abundant both at DIV 7 and DIV 14, which is compatible with the observed network-wide bursting in all their developmental stages, whereas for tracks/squares long-range connections were rare at DIV 7 and substantially increased at DIV 14.

For control, flat PDMS, the fraction of long-range effective connections is about 9% of all existing connections at day in vitro (DIV) 7 and remains practically constant along development, a result that is expected since whole-network communication occurs in the form of bursting both in young and mature cultures. For tracks, long-range connections are rare at young (DIV 7) cultures, comprising about 2% of all connections, a result that is consistent with the low occurrence of whole-network bursts. Long-range connections increase 4 times upon maturation and reach levels akin to controls, also in agreement with a stronger overall bursting. A similar trend is observed in squares. Altogether, this analysis shows that a higher presence of bursting events in mature tracks/squares cultures is consistent with stronger whole-network communication and longer-range effective connections. Numerical simulations (see Figure 6.15) show that, in turn, an increase in the average length of the axons (simulating development) leads to a stronger whole-network bursting and longer range effective connections.

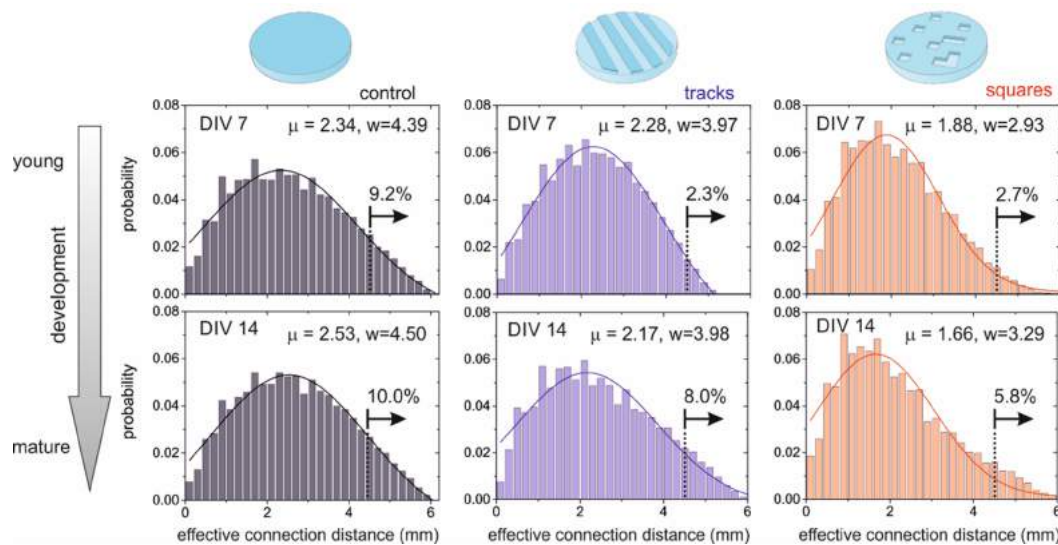


Fig. 6.14 Evolution of Euclidean distance between effectively connected neurons. The bar plots show the probability distribution functions of Euclidean distances d between effectively connected ROIs. All distributions show a Gaussian fit that is used to extract the mean μ and width w of the distributions. Long range effective connections are set as those that extend at least 75% of the diameter of the culture, *i.e.*, 4.5 mm (vertical dashed line and arrow).

6.5.2 Numerical simulations

Numerical simulations were carried out by the collaborator Akke Houben in Soriano's laboratory and allow to understand the impact of longer axons on effective connectivity. The rationale behind the effort of running such simulations is that, experimentally, the increase in long-range effective connectivity upon maturation raises the hypothesis that the induced PDMS anisotropy somehow blocked the capacity for fast whole-network communication at early stages of development that gradually diluted. Indeed, the impact of anisotropies was less prominent at later stages, possibly due to the growth of axons in all directions, which effectually integrated the entire network.

To provide evidence for this hypothesis, we carried out numerical simulations in which we used biologically realistic models of the three experimental culture types to, then, explore the emerging dynamics and effective connectivity as the average axonal lengths grew. An example of the constructed networks is provided in Figure 6.15A, and the results for the distribution of connectivity distances are provided in Figure 6.15B. The results show that longer axons clearly favoured network-wide bursting and substantially increased the presence of long-range effective connections. Thus, we conclude that young cultures most likely exhibited short axons which, in combination with the anisotropy induced by PDMS patterning, confined activity in small neighbourhoods, with rare network-wide bursting. Mature cultures, with long axons, favoured global connectivity that smoothed out the underlying anisotropy

and facilitated network-wide bursting. Numerical simulations also evinced that effective and structural connectivity are related, but that one cannot freely take the former as a proxy for the latter.

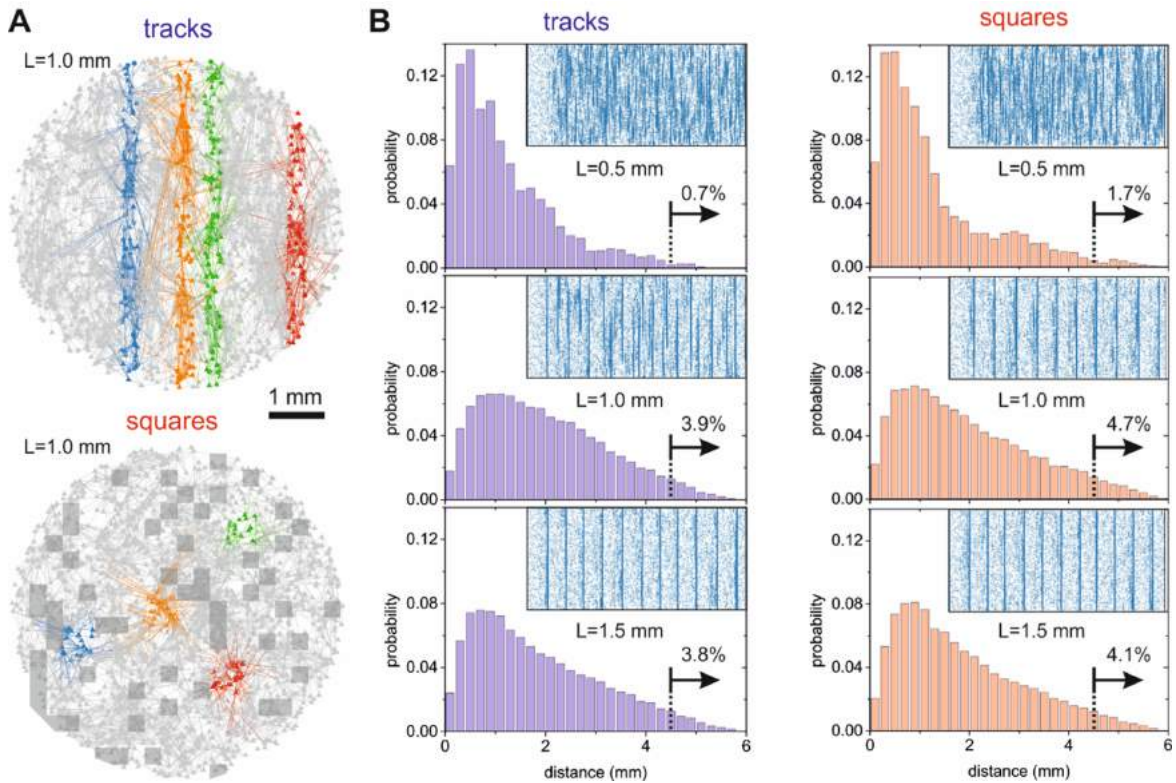


Fig. 6.15 Dependence of effective connectivity distance on average axonal length (numerical simulation). (A) Illustrative network maps of simulated networks with tracks or squares topographical patterns. Neuronal density is 400 neurons/mm² and average axonal length is 1 mm. Some neurons and their outgoing connections are colour coded according to the structural module they belong to. For the case of the track's configuration, the modules coincide with the position of the tracks themselves. For the case of squares, the modules form islands in the network. The position of the square valleys is indicated with a grey overlay. (B) Probability distribution functions of effective connectivity Euclidean distances, in both tracks and squares configurations, for gradually larger average axonal lengths L that replicate the maturation of the network. The insets show simulated raster plots of spontaneous activity from which effective connectivity data is obtained, using the same GTE inference approach and parameters as in the experiments.

Additionally, as seen in Figure 6.15, for both tracks and squares, short axonal lengths of $L = 0.5$ mm led to rich raster plots qualitatively similar to those observed in the experiments. The corresponding distributions of effective connection distances show that long-range connections (those larger than 4.5 mm, vertical dashed line) are rare, comprising about 1 – 2% of all occurrences, which is consistent with the lack of whole-network activity events in the raster plots. For $L = 1.0$ mm and 1.5 mm, however, long-range connections

substantially increase and are about 4 – 5% of all occurrences, a trait that is ascribed to the large-scale communication provided by abundant whole-network bursting. Altogether, the results show that an increase in the Euclidean distance of effective connections is consistent with an increase of axonal lengths and, in turn, a higher presence of whole-network bursts.

6.5.3 Local topological properties in patterned cultures

Given the interesting insight that effective connectivity provides, we investigated the local topological properties of the obtained effective networks, and considered the distribution of in-degrees, clustering coefficients and other properties. We initially focused on the analysis of in-degrees k_{in} (incoming connections to a given ROI), comparing the shape of k_{in} distributions between DIV 7 and 14 as well as the evolution of the average degree $\langle k_{in} \rangle$ along development. We considered the in-degree only since in a previous numerical study (Ludl and Soriano, 2020) we showed that k_{in} better captured the differences between neuronal networks grown in environments with strong spatial constraints. As shown in Figure 6.16A, $\langle k_{in} \rangle$ for controls did not substantially. This indicates that, in the context of the observed persistent network-wide bursting of these cultures since the very beginning, the network maintains a similar functional behaviour along development. Interestingly, very small in-degrees are not present at DIV 14, which hints at an overall stronger connectivity caused by maturation, *i.e.*, the realization of an overall well-connected network.

For tracks, a change is noticeable, with an abundance of small in-degree values at DIV 7 that disappear at DIV 14. $\langle k_{in} \rangle$ grows from 34 (DIV 7) to 47 (DIV 14), a 36% relative increase. For squares, an increase in overall connectivity is also observed, from about 40 to 45, a 12% relative increase, much smaller than tracks, which is possibly due to the fact that the PDMS square patterns do not completely dominate the surface of the culture, *i.e.*, substantial areas connect similarly as in a flat, control culture. However, the distribution of degree values for squares at DIV 14 is much broader than for controls, indicating that connectivity on the surface of the square's configuration may abruptly change. We believe that this broadness in k_{in} values is related to the abrupt changes in the propagation velocity of fronts shown in Figure 6.9A.

The evolution of $\langle k_{in} \rangle$ along DIV for the three configurations is shown in Figure 6.16B. For controls, $\langle k_{in} \rangle$ oscillates around $\langle k_{in} \rangle \simeq 40$ and no clear developmental trend can be observed. Again, we think that this is due to the dynamical locking of the system in network-wide bursting. For tracks and squares, however, a clear development is observed, changing for both configurations from $\langle k_{in} \rangle \simeq 34$ at DIV 7 to $\langle k_{in} \rangle \simeq 42$ after DIV 10, about 25% relative increase. This development of effective connections is consistent with a dynamic (and therefore neuronal communication) involving small regions of the culture at DIV 7 to,

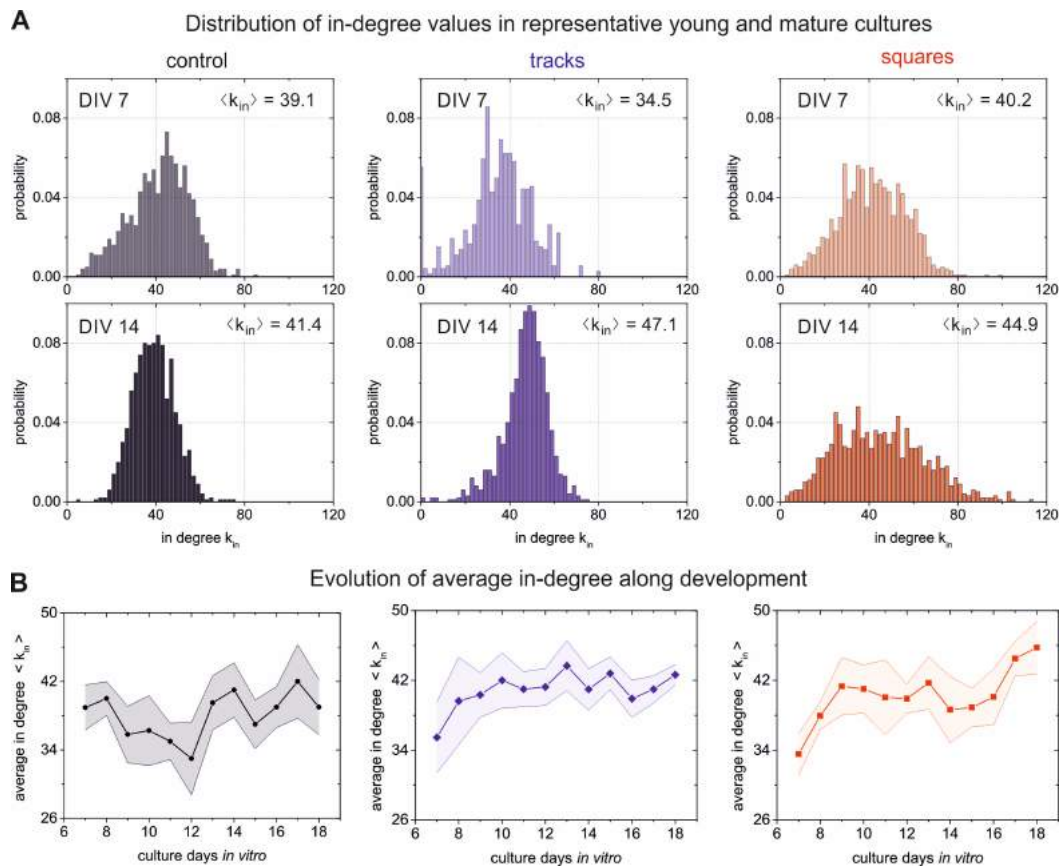


Fig. 6.16 In-degree connectivity distributions and evolution of average connectivity along development. (A) In-degree probability distribution functions for representative young (DIV 7) and mature (DIV 14) cultures, comparing controls with tracks and squares topographical cultures. The data at DIV 14 correspond to the matrices and maps provided in Figure 6.11. The value of $\langle k_{in} \rangle$ shown on the top-left corner of each distribution provides the average connectivity of the network. $\langle k_{in} \rangle$ is similar between DIV 7 and 14 for controls but increases by 36% and 12% (relative to the values at DIV 7) for tracks and squares, respectively. (B) Evolution of $\langle k_{in} \rangle$ for the three culture types along DIV and including all explored experimental repetitions ($n=5$ for controls, 5 for tracks, and 6 for squares). Data are represented as mean \pm standard deviation of the mean. For controls, $\langle k_{in} \rangle$ oscillates around 40 connections/ROI along DIV, while for tracks and squares a clear growing trend in average connectivity is observed from DIV 7 to DIV 9 – 10, when connectivity appears to stabilize and later fluctuate.

later, encompass its full entirety. We note that fluctuations in $\langle k_{in} \rangle$ values were strong, as revealed by the relatively large error bars, indicating that cultures prepared in similar conditions easily follow different developmental paths.

We finally inspected topological properties of the networks at DIV 14 that were related with the functional communication and organization at local scales. They include the distribution of clustering coefficients, local efficiencies and betweenness centralities, averaged over experimental repetitions. The results are provided in Figure 6.17 and complete the

global analyses (G_E and Q) provided in Figure 6.11 and Figure 6.13. In general, tracks and squares exhibited higher clustering coefficients and local efficiencies than controls, indicating a higher tendency for the topographical patterns to shape local subgraphs and functional communities, which in turn are related to the observed capacity of neurons to activate in small groups and not at unison as in controls. The betweenness centrality exhibited similar average values for the three configurations, although the distributions were strongly peaked towards zero except for tracks, possibly indicating that this configuration favoured hubs formation, *e.g.*, neurons connecting tracks transversally. We also included for completeness the averaged k_{in} distributions among repetitions, leading to results that were consistent with those provided in Figure 6.16, particularly the broadness of k_{in} values for squares. Altogether, these results show that there are differences in local network properties between culture types that are consistent with the overall results on dynamics, although these differences are not significant in statistical terms, an aspect that we elaborate in the Discussion section.

In general, tracks and squares exhibited higher clustering coefficients and local efficiencies than controls, indicating a higher tendency for the topographical patterns to shape local subgraphs and functional communities. Since effective connectivity reflects dynamics, these higher values for tracks/squares may indicate the tendency of neurons to activate in small groups, and not at unison as in controls. The betweenness centrality had similar average values for the 3 configurations, although the peak at zero was less prominent on tracks, possibly indicating that this configuration favoured hubs formation, *e.g.*, neurons connecting tracks transversally. The in-degree k_{in} distributions provided similar average value $\langle k_{in} \rangle$ around 40 connections/neuron, but the distributions for tracks and squares were right-skewed (peaked towards high values) as compared to controls, and the distribution for squares was broader than for tracks. It must be noted that the effective connectivity does not fully portray structural connectivity and therefore these comparisons may require further investigations.

To illustrate the difficulty in relating structural and effective connectivity, Figure 6.18 compares the distribution of clustering coefficients CC between the structural and effective connectivity data in simulations. As can be observed, for the structural blueprint, CC values were on average much higher in tracks than in controls or squares, but the two latter were similar, which indicates that it is difficult to strongly imprint local structural features in the squares configuration. For the effective connectivity, we can see that the distributions are broader and different in shape than the structural ones, indicating that a direct structure–function relationship cannot be established. However, the same trend is maintained, with the tracks configuration showing higher CC values on average than the rest. Thus, we conclude that, first, effective connectivity cannot be freely taken as a proxy of the structural one, and second, that clustering coefficients (and by extension other topological properties) may by

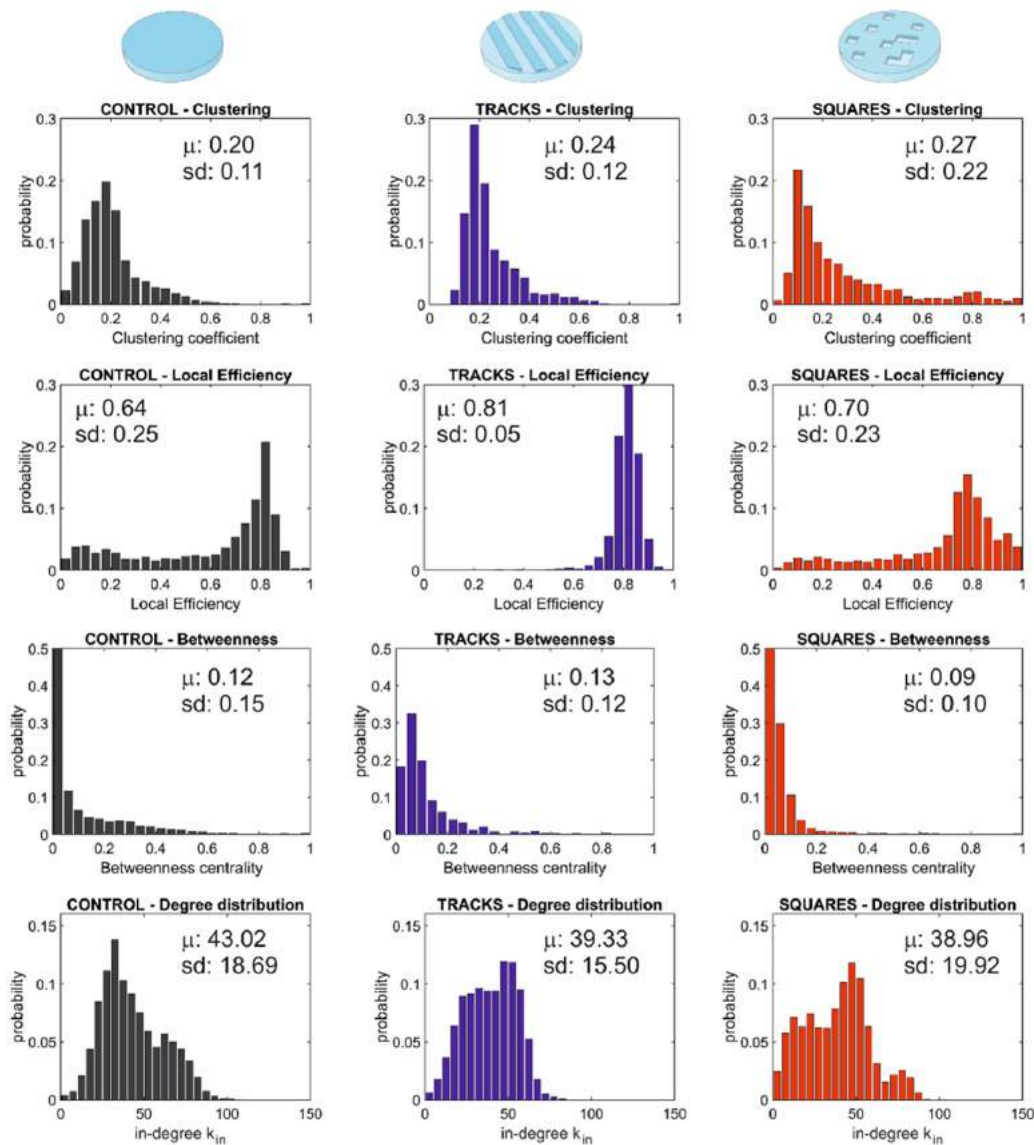


Fig. 6.17 Local network properties for effective connectivity in experimental data at DIV 14. The plots show probability density functions (pdf) of 4 local network metrics derived from the effective connectivity data, comparing control, 'tracks' and 'squares' configurations. All pdfs are averages over the 5 – 6 experimental realizations per configuration of Figure 6.13A. The values of μ and sd indicate, respectively, the average of the distributions and their standard deviation.

themselves not be sufficient to understand the observed rich dynamics in the topographical networks. Other traits may be necessary ingredients to render a full picture, such as strong anisotropies in the network's spatial connectivity (*e.g.*, the distribution of connectivity angles in Figure 6.13), metric correlations, or connectivity motifs that amplify or restrain neuronal activity. Understanding the relative impact of all these ingredients is an endeavour that requires future substantial investigation.

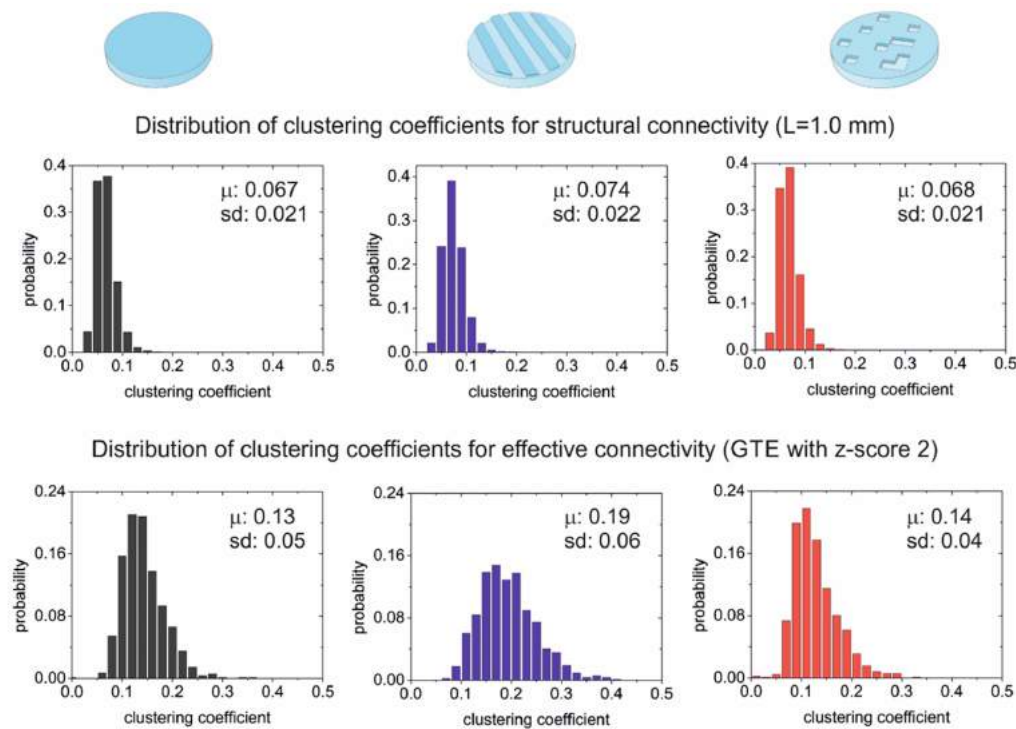


Fig. 6.18 Comparison between structural and effective clustering coefficients. The plots show probability density functions (pdf) of clustering coefficients (CC) values, comparing control, tracks, and squares configurations. Data is drawn from a single numerical repetition. Since data is extracted from simulations, both structural and effective connectivity layouts are accessible. In all three configurations, neuronal density was 400 neurons/ mm^2 , average axonal length $L = 1.0$ mm, and average in-degree $\langle k_{in} \rangle = 25$.

6.6 Discussion

Primary neuronal cultures are one of the most celebrated techniques in several multidisciplinary research fields, including physics of complex systems, neuroengineering and medicine. Their versatility, accessibility and ease of manipulation have made them ideal to investigate in a controlled manner phenomena as diverse as self-organization (Downes et al., 2012; Okujeni and Egert, 2019; Schroeter et al., 2015), repertoire of activity patterns (Wagenaar et al., 2006; Yamamoto et al., 2018), structure-to-function relationship (Bonifazi et al., 2013; Marconi et al., 2012; Tibau et al., 2018), resilience to perturbations (Estévez-Priego et al., 2020; Teller et al., 2020) and alteration upon disease (Fernández-García et al., 2020; Teller et al., 2015). However, primary cultures grown on flat surfaces typically exhibit a strong bursting behaviour in which all neurons activate together in a short time window and remain practically silent in between bursts. In the present study we showed that this all-or-none rigid behaviour can be relaxed by incorporating spatial anisotropies on the substrate, in the form of topographical reliefs, that substantially enrich the repertoire of activity patterns and

approach them to what is observed in vivo, where activations of different spatiotemporal structure coexist.

The spatial constraints promoted by the PDMS reliefs favoured local connectivity and facilitated activity at a microcircuit level, but without suppressing whole-network dynamics. Thus, our design promoted the emergence of neuronal networks with balanced integration and segregation, *i.e.*, where activity patterns comprising small regions of the culture coexisted with network-wide bursting (Figures 6.5, 6.6). In other words, for a given patterned culture, both local computation and whole-network communication coexisted. Other studies investigated the realization of this integration–segregation balance by using modular designs (Park et al., 2021; Shein-Idelson et al., 2011; Yamamoto et al., 2018), in which neurons were spatially confined in small areas. Our PDMS topographical modulation provides an alternative approach to such an ad hoc confinement, shaping dynamically rich networks in both space and time without fine tuning the position of neurons and axons. We note that a broader modulation of the dynamical repertoire in our cultures could be achieved by altering the ratio between excitatory or inhibitory neurons or by decreasing the strength of excitatory synapses. All our experiments were conducted with both excitation and inhibition active. Given the role of inhibition in modulating activity (Isaacson and Scanziani, 2011; Sukenik et al., 2021), we argue that the repertoire of activity patterns could additionally be tuned by blocking GABA receptors in inhibitory neurons, which would make bursting events more similar among themselves, or by reducing the amount of excitatory transmission by blocking AMPA–glutamate receptors. The latter was explored for instance in modular networks (Yamamoto et al., 2018), observing that the integration–segregation balance shifted towards higher segregation as excitation was reduced. The importance of inhibition in modulating the repertoire of activity patterns will be explored in future work, both in vitro and in silico.

We found a PDMS height of around $70\ \mu\text{m}$ to be optimal, since it promoted a coarse axonal positioning and orientation in a neuronal neighbourhood, *e.g.*, along a PDMS track, while allowing for easy interconnection with other neighbourhoods. Our observation that connections follow the track ridges is in agreement with other studies that investigated in detail the impact of geometrical cues on axonal growth (Basso et al., 2019). PDMS heights of $100\ \mu\text{m}$ or higher in our experiments often shaped isolated regions in the culture, whereas heights of $\approx 30\ \mu\text{m}$ did not cause sufficient structural alterations to markedly modify network dynamics. Other studies also used PDMS reliefs to control connectivity in neuronal circuits, most notably holes and pillars of characteristic scales in the range $10 - 100\ \mu\text{m}$ (Li et al., 2017, 2014), ultrasoft PDMS (Sumi et al., 2020), or by combining fine-tuned neuroengineering and microfluidics (Forró et al., 2018; Holloway et al., 2021; Liu et al., 2021; Marconi et al.,

2012; Nikolakopoulou et al., 2020). In these works, authors reported a richer repertoire of activity patterns or the suppression of extreme bursting. In the context of these studies, the relevance of our PDMS reliefs is that cells' neurite development is coarsely guided rather than fully delineated, allowing the circuit to retain its self-organization potential. The effort of imprinting 'mesoscale architecture' while allowing self-organization is conceptually similar to the studies on neuronal cultures with spatial aggregation (Okujeni and Egert, 2019; Okujeni et al., 2017; Tibau et al., 2018). Aggregation helped neurons to connect within their neighbourhood but without hindering long-range connectivity, shaping networks with a richer dynamic behaviour and more varied activity initiation, as in our case.

In our study we used effective connectivity, computed from spontaneous activity, to better understand communication across the neuronal cultures, and as a complementary analysis to the observed dynamical changes in the patterned networks. It is important to emphasize that effective connectivity reflects communication among neurons and not structural paths or synaptic efficiencies, and therefore a direct quantitative analysis of structural connectivity is not possible based solely on the analysis of the GTE-inferred effective data. We explored the difficulty of unravelling structural traits from effective connectivity by running simulations of the patterned networks and computing specific network descriptors for both the ground-truth topology (structure) and effective connectivity data. As illustrated in Figure 6.18, the distribution of structural clustering coefficients was similar among culture types even though the networks behave differently from a dynamical point of view. The effective clustering coefficients had some differences among configurations, but one could not easily infer structural traits from them. Thus, we hypothesize that to infer structural details from effective connectivity one needs, first, to combine as many descriptors as possible, *e.g.*, global and local properties, connectivity distances and angles, hubness and connectivity cliques, and many others (Bassett and Sporns, 2017; Farahani et al., 2019), and second, to combine recordings of spontaneous activity with electrical or optogenetic stimulation (Chiappalone et al., 2019; Emiliani et al., 2015) to unveil which neurons directly respond to a specific stimulus and gradually construct the network map of interactions.

The contrasting velocities of activity propagation in the tracks configuration, with measured velocities about 5 times larger along tracks than across them, can be put in context of theoretical models (Bressloff, 2000; Golomb and Ermentrout, 1999) and experiments on activity propagation in one-dimensional neuronal cultures (Feinerman et al., 2005; Jacobi and Moses, 2007; Jacobi et al., 2010). These studies revealed that the velocity of activity fronts depended on average neuronal connectivity and synaptic strength. If we assume that synaptic strength is similar in all neurons in the culture, then we conclude that connectivity along tracks was 5-fold higher than transverse to it. This difference is consistent with the

functional data of Figure 6.13B, in which effective connections along tracks were about 8 times more abundant than across tracks. We also remark that the maximum velocity that we measured along tracks was about 30 mm/s, which is slower compared to the data provided in the study of Feinerman and coworkers (Feinerman et al., 2005), who measured velocities in the range 40 – 80 mm/s. In Feinerman’s study, however, activity was solely driven by excitatory neurons, while in our networks both excitation and inhibition are active. Thus, the presence of inhibition, which effectually reduces average connectivity from a network dynamics perspective (Soriano et al., 2008; Tibau et al., 2018, 2013), is possibly the reason for the comparatively low velocities measured in our experiments.

Given the importance of spatial constraints in modelling neuronal circuitry architecture and function (Stiso and Bassett, 2018), it is interesting as a future exploration to investigate the impact of different degrees of connectivity restrictions. Chemical patterning (Liu et al., 2021; Yamamoto et al., 2018) offers the delineation of precise circuits but with restricted self-organization capacity, while PDMS topographical modulation offers a broader flexibility at an expense of a poorer control on physical wiring. We observed in our experiments that different repetitions of the tracks or squares designs led to neuronal circuits with similar global dynamic behaviour but with different functional details. For instance, the distribution of initiation points (Figure 6.8) and functional modules (Figure 6.11) varied across repetitions, indicating different mesoscopic evolution. Additionally, some of the explored cultures tended to become more integrated and with increasingly stronger network-wide bursting as they matured, suggesting that the initially imprinted inhomogeneities were erased at long term (Figure 6.17). This loss of richness was particularly strong in the square’s configuration. We hypothesize that, to better approach brain-like behaviour in vitro, an optimal experimental system would be one that combines topographical and chemical patterning, thus preserving key functional traits without the loss of flexible self-organization. We also conjecture that external stimulation, *e.g.*, as in Poli et al. (2015), may be a necessary ingredient to shape circuits with long-lasting functional features.

Our neuronal cultures were monitored using calcium imaging to detect neuronal activity at different heights of the PDMS patterns. Technologies based on planar electrodes such as MEAs were not suitable since for our investigation since they require the neurons to be located on the surface of the MEAs chip. However, the concept of constraining neurons or connections to enrich the dynamics of neuronal cultures has been widely explored using planar MEAs (Brofiga et al., 2021; Kim et al., 2014), with the additional advantage that neurons could be locally stimulated. Successful concepts related to our work included modular designs (Park et al., 2021), predefined connectivity through axonal guidance (Gladkov et al., 2017) and interconnected subpopulations of neurons (Bang et al., 2015; Brofiga et al., 2021;

Dauth et al., 2017; Kanagasabapathi et al., 2012). Studies using modularity and guidance shaped networks that qualitatively resembled our tracks configuration, and authors reported a richer dynamic repertoire when modularity and guidance were present as compared to non-modular isotropic configurations. The studies using interconnected subpopulations of neurons showed that the dynamical and functional richness of the networks substantially increased when neurons from diverse origin (*e.g.*, cortex or hippocampus) were wired together, overall shaping a true brain-on-chip system that not only captured functional complexity but also the intrinsic neuronal variability of the brain. In the context of our work, we hypothesize that the richness that we observed could be further increased by placing different neuronal types along groups of tracks or in the valleys of the square's configuration.

Finally, we note that our experiments may be of interest for those studies that use neuronal cultures as models for neurological disorders *in vitro*. These studies often explore the alterations in network collective activity caused by a disease. For instance, in a recent study of Parkinson *in vitro* (Carola et al., 2021), authors observed that the affected networks exhibited a much higher number of network-wide bursts as compared to healthy controls. Although their results were conclusive, the investigation was diffculted by the tendency of standard, glass-grown neuronal cultures to exhibit persistent whole-network bursting. Thus, we argue that the use of PDMS topographical substrates may help to prepare networks whose activity is much varied since early development, identify the impact of a disease in network formation, activity and functionality, as well as their evolution along time.

6.6.1 Limitations of the study

Neurons in our experiments were plated in a homogeneous manner in PLL-coated PDMS surfaces. However, we often observed that neurons strongly aggregated after few days, or that some areas of the PDMS relief, generally at the bottom, were not occupied by cells. This problem was present both in the tracks and squares configurations, and often led to large empty areas for the latter. We ascribe this lack of homogeneity to the PLL coating, which possibly was not sufficiently uniform for neurons to adhere to the surface, or to capillary forces that caused the trapping of air bubbles and blocked coating. These inhomogeneities can be observed for instance in the fluorescence image of the tracks configuration in Figure 6.1. We note that fluctuations in local density accentuated the anisotropies induced by the relief and, in turn, amplified the variability of the spatiotemporal fronts. Specifically, for the track's configuration, the distinct parallel and transverse velocities is possibly favoured by the contrasting neuronal densities between top and bottom parts. Nonetheless, we used high-resolution phase contrast images and immunostaining to reject cultures in which neurons grew as isolated patches. All studied cultures here contained neurons that were globally

interconnected and exhibited episodes of coordinated activity that encompassed from few neurons to the entire network.

On the other hand, in this study we were interested in the collective behaviour of mm-sized cultures rather than in the precise individual dynamics of their constituting neurons. The need to access a large field of view in combination with limitations in image resolution imposed by the fluorescence camera, made not possible to resolve single cells. Hence, we analysed network activity using an ROI approach. To investigate whether this approach could create artifacts, we run experiments in smaller, 4 mm diameter cultures in which both single neuron monitoring and ROIs could be used (Orlandi et al., 2013; Tibau et al., 2018). Similar qualitatively results were obtained when comparing both approaches for all major dynamic and functional descriptors. Thus, the ROIs analysis can be viewed as a coarse-graining approach, which suffices to capture interesting mesoscale phenomena as far as the spatial extent of these phenomena is larger than the characteristic neuron size. In our case, network bursts and functional modules covered areas on the order of few mm, much larger than the 10 μm diameter of a neuron. We believe that this coarse-graining may be a source of inspiration to explore neuronal circuits at different scales and may help bridging the gap between in vitro networks and naturally formed neuronal circuits. Related to this, it is important to emphasize that we considered rat primary cortical cultures for our experimental design. Alternative cells models such as human induced pluripotent stem cells (hiPSCs) may broaden the spectrum of dynamical and functional traits shown here. Indeed, hiPSCs cultures grown on flat substrates already exhibit a higher individual activity and a richer repertoire of coordinated activations (Carola et al., 2021; Kirwan et al., 2015), as opposed to rat primary cultures that show a strongly rigid bursting behaviour.

6.7 List of videos from experimental recordings

The supplementary videos can be found at the following link as published in the article for the IScience journal.

Open full-text with the supplementary videos:

URL: [https://www.cell.com/iscience/fulltext/S2589-0042\(22\)01952-6](https://www.cell.com/iscience/fulltext/S2589-0042(22)01952-6)

- **Supplementary video V1.** Spontaneous activity in a small region of the ‘tracks’ configuration at DIV 14. Spontaneous activity in a zoom-in region of the track’s configuration at DIV 14. Playback is 24x real time. At approximately recording time 54 s the processes (neurons and dendrites) in the culture can be appreciated. Several of these processes are aligned along the left track. The video is related to Figures 6.1 and 6.7.

- **Supplementary video V2.** Spontaneous activity in a small region of the ‘squares’ configuration at DIV 14. Spontaneous activity in a zoom-in region of the square’s configuration at DIV 14. Playback is 6x real time. The video is related to Figure 6.1.
- **Supplementary video V3.** Spontaneous activity in a full 6 mm diameter cultures with ‘tracks’ topography at DIV 14. Spontaneous activity for a ‘tracks’ culture at DIV 14 in which its entire extent (6 mm diameter PDMS disc) visualized. The video plays at approximately 5x speed and covers 2 min of actual recording. Different structures of spatiotemporal fronts can be observed, *e.g.*, extending half culture or two tracks. Contrasting velocities of activity propagation along or across tracks can be also appreciated. The video is related to Figures 6.1, 6.5, 6.9 and 6.10
- **Supplementary video V4.** Spontaneous activity in a full 6 mm diameter culture with ‘squares’ topography at DIV 7. Spontaneous activity for a ‘squares’ culture at DIV 7 in which in which its entire extent (6 mm diameter PDMS disc) visualized. The video plays at approximately 5x speed (covering 2 min of actual recording) for a better appreciation of the activity fronts and their propagation. The video is related to Figures 6.1 and 6.6.
- **Supplementary video V5.** 20 min of spontaneous activity in a full 6 mm diameter cultures with ‘tracks’ topography at DIV 14. Spontaneous activity for a ‘tracks’ culture at DIV 14. The video corresponds to the same culture as in SV3 but played at 40x speed to cover 20 min of actual recording. This allows to better appreciate the variability in activity patterns and how these patterns shape unique functional communities. The video is related to Figures 6.1, 6.5 and 6.9–6.12.

Chapter 7

Results II: Understanding complex functional organization in aging brain

In the last few years, interest in neuroimaging studies has substantially grown through many fields, including medicine, psychology and engineering. A popular and well-established technique is functional Magnetic Resonance imaging (fMRI), a non-invasive technique that measures the local fluctuations in cerebral blood flow. This approach enables scientists and researchers to study, in a controlled manner, the brain's structure and functioning of participants in a great variety of situations, either healthy or diseased.

In particular, healthy aging has caught substantial attention given the large number of elderly people across Europe, with fMRI providing toolboxes to monitor both structural and functional connectivity along years and detect possible markers of degeneration (Abellana-Pérez et al., 2022; Oschmann et al., 2020; Yamashita et al., 2021). Indeed, several studies have reported the changes in functional and structural connectivity during the aging process in healthy individuals and the importance to understand them in the context of behaviour and cognition (Farras-Permanyer et al., 2019; Oschwald et al., 2019; Vaqué-Alcázar et al., 2020). Regarding functional findings, aging has been associated with a decrease in functional connectivity (FC) in the default mode network (DMN) (Mowinckel et al., 2012), among other alterations (Chen, 2019; West et al., 2019). Aging has also been associated with decreased grey matter volume in frontal and parietal lobes (Hu et al., 2014). In turn, these regions have also been highlighted as the most vulnerable to aging (Marchitelli et al., 2018).

As experimental tool, the main goal of fMRI studies is to register the spontaneous blood oxygen level-dependent (BOLD) signal, which provides an indirect measure of the brain's hemodynamic (Gorges et al., 2014). Afterwards, a connectivity matrix can be extracted by computing the Pearson correlation coefficients between the recorded time-series of the brain regions. This matrix depicts the functional connectivity (FC) (Ystad et al., 2011) of

the brain, *i.e.*, the statistical relationship between signals in two or more brain areas. In further pre-processing steps these connectivity matrices are treated with filtering techniques to eliminate spurious or noise-derived signal while retaining the most relevant information.

Some techniques focus on node-based analysis and use *graphs* to summarize the relationship between recorded signals, which are associated to the activation of brain regions, finally shaping networks whose nodes are brain regions and links are statistical associations between activity patterns in those regions. We must note that, as a crucial step during graph construction, a threshold is applied to the raw correlation matrices derived from fMRI to obtain the adjacency matrices, *i.e.*, the representation of the nodes that are more importantly interacting to one another and that are therefore considered to be functionally connected. The threshold concept is indeed important to remove small link weights that may arise from spurious or random connections rather than real coactivations between brain regions. However, unfortunately, there is no a unique well-established criterion for setting such a threshold, which by itself illustrates the difficulty of such a procedure. Actually, new statistical approaches have arisen along the years to diminish the consequences of the selected threshold (Drakesmith et al., 2015; van den Heuvel et al., 2017). In this sense, three filtering methods, applied to graphs, are presently used: absolute thresholding (Buckner et al., 2009; Luo et al., 2015; Pedersini et al., 2020; Tomasi and Volkow, 2010), proportional thresholding (Dvorak et al., 2018; van den Heuvel et al., 2008) and the Triangulated Maximally Filtered Graph (TMFG; Mancho-Fora et al. (2020b)) approach. Other methodologies have been proposed, like Amplitude of low-frequency fluctuations (ALFF) and ReHo (Regional Homogeneity), but they are *data-driven analyses* of the brain signals and are conceptually very different from a graph approach. These methods, generally speaking, are based on revealing regional characteristics by using the raw data in resting-state functional magnetic resonance imaging (rs-fMRI). It is important to note that, by construction, ALFF and ReHo do not require a hypotheses on brain connectivity or *a priori* selection of the most interesting brain regions, which is a necessary step in graph theory to establish a minimum organizational map of the brain and its possible changes (Lee and Hsieh, 2017).

Both approaches, *i.e.*, graph theory and data-driven analyses, may be complementary to one another (Lee and Hsieh, 2017), but they may lead to different results and interpretations. They have been recently used in many psychiatric diseases (Gao et al., 2021; Lai et al., 2020; Wang et al., 2022), dementias (Liu et al., 2014; Yue et al., 2020) and healthy populations (Deng et al., 2022; Hu et al., 2014). For example, Cha et al. (2015) performed an interesting meta-analysis studying functional abnormalities in amnesic mild cognitive impairment and Alzheimer's disease (AD) patients using ReHo and ALFF, among other

techniques, and they found decreased functional characteristics that were consistent across all approaches.

Given the importance of the threshold method, and the possible differences between graph and data-driven approaches, in the present Thesis we dived into fMRI data to explore this difficult statistical problem in the context of aging. Thus, in this context, the present Chapter aims to study the whole-brain resting state of healthy participants to elucidate the functional connectivity through aging. To do so, two complementary approaches were explored. On the one hand, ALFF and ReHo strategies were used to find differences in spontaneous brain activity among healthy participants of different age groups from middle to advanced age. Despite the incongruencies between the studies, we reported differences in ALFF and ReHo in the frontal lobe and in the DMN. On the other hand, we considered different thresholding methods on weighted connectivity matrices to assess which threshold was more adequate to describe functional connectivity metrics. Afterwards, we extracted the connectivity traits and analysed their fit through the different thresholds on a healthy aging population. Specifically, we compared absolute thresholding, relative thresholding and TMFG (Triangulated maximally filtered graph) filtered matrices in an older healthy sample.

With this road map in mind, the chapter is organized as follows. We first present the analysis of the participant' demographic data. Next, we describe the detection of significant clusters obtained with ALFF and ReHo techniques from the registered functional data between age groups. Afterwards, we explore the key role of the age variable in the results obtained and present a model of linear regression. Finally, we describe the impact of applying different thresholding techniques to the correlation matrices, with special attention to the changes that these different thresholds cause on key network statistics (see Chapter 4), particularly those related to the functional segregation and integration of information.

7.1 ALFF and ReHo approaches to fMRI data

7.1.1 Participant characteristics analysis

In the last decades, the worldwide population mean age has increased due to an ageing population, the decrease of birth rates and the recent advances in medicine and pharmacology. This increase is particularly emphasized in the developed countries, where population has access to a health care system. Despite these advances in medicine and health care, aging is related to remarkable changes in both physical, *e.g.*, loss of muscular strength and bone and joint atrophy (Brooks and Faulkner, 1994), and cognitive, *e.g.*, short-term memory loss or a higher tendency to suffer from depression or anxiety (Association et al., 2017).

Table 7.1 Description of participant groups and movement measures between age groups

Age group	Age range ($\bar{x} \pm SD$)(years)	Size	FD Jenkinson ($\bar{x} \pm SD$)(mm)
Group 1	< 60 (54.67 \pm 3.91)	12	0.24 \pm 0.12
Group 2	60 – 64 (62.29 \pm 1.35)	21	0.22 \pm 0.12
Group 3	65 – 69 (67.13 \pm 1.28)	30	0.23 \pm 0.14
Group 4	70 – 74 (72.33 \pm 1.20)	21	0.24 \pm 0.13
Group 5	75 – 79 (76.72 \pm 1.36)	18	0.25 \pm 0.14
Group 6	\geq 80 (82.80 \pm 2.74)	10	0.21 \pm 0.13

The table shows the 6 age groups studied and their most fundamental traits. \bar{x} : mean; SD: standard deviation; FD: Framewise Displacement

For the study carried out in this Thesis, Table 7.1 summarizes the range of ages corresponding to each group of participants and the number of participants (defined as ‘size’). Additionally, since participants tend to move inside the scanner throughout the recording process, it is important to quantify their global movement and correct afterwards for possible artifacts. This movement includes linear displacements along the three Euclidean spatial directions as well as the rotational displacement on the three angular dimensions (roll, pitch and yaw). Jenkinson et al. (2002) defined the variable ‘framewise displacement’ (FD Jenkinson) to summarize these global movements as a lineal quantification of the total subject locomotion along the recording session. Such a displacement data is also shown in Table 7.1, as the extracted FD Jenkinson from the fMRI recordings. Subject locomotion is assessed post-recording to prevent a bias in the processed signal that could affect the results. We note that the FD Jenkinson movement was introduced as a covariable during all the procedures to remove any possible confound effect.

Table 7.2 shows the participants’ neuropsychological measures across age groups. The different tests are of common use in psychiatry to test cognitive functions. One of these tests, named ‘Mini-Mental State Examination’ (MMSE) is particularly important since reflects overall performance, and where a subject is considered to be healthy if it scores above 24. As can be seen, all the individuals in our sample had scores higher than 24, granting no cognitive decline. To assess differences between groups on the different neuropsychological measures, an analysis of variance (ANOVA) was performed. We used the ANOVA’s natural statistical test, the F-Snedecor test ($F(a, b)$). In this test, the term a inside the parenthesis indicates the degrees of freedom (df), *i.e.*, the age groups minus 1, and the term b indicates the number of imputations to the test, *i.e.*, the number of participants. It is important to highlight that some of

Table 7.2 Description of neuropsychological measures between age groups

Age group	BNT ($\bar{x} \pm SD$)	NART ($\bar{x} \pm SD$)	WAIS–Voc ($\bar{x} \pm SD$)	MMSE ($\bar{x} \pm SD$)
Group 1	55.50 ± 5.22	25.17 ± 3.81	40.22 ± 12.70	29.33 ± 0.89
Group 2	54.81 ± 2.94	24.86 ± 3.45	47.62 ± 16.11	28.76 ± 1.09
Group 3	57.07 ± 8.77	28.93 ± 3.58	46.36 ± 10.75	29.31 ± 0.97
Group 4	54.90 ± 3.70	28.71 ± 16.50	41.40 ± 9.04	28.90 ± 1.45
Group 5	54.29 ± 3.42	25.00 ± 5.21	41.18 ± 6.39	28.06 ± 1.75
Group 6	49.20 ± 4.02	23.00 ± 5.77	41.90 ± 9.68	28.20 ± 1.23

Comparison of the neuropsychological measures among the 6 age groups to show that all of them were relatively high, with all of them having MMSE scores above 24. \bar{x} : mean; SD: standard deviation; BNT: Boston naming test; NART: National Adult Reading Test; WAIS–Voc: WAIS Vocabulary; MMSE: mini–mental state examination

the participants had missing values and therefore the total number of imputations mismatches the total number of participants. Overall, no significant differences were observed between the groups in either the National Adult Reading Test (NART, $F(5, 106) = 0.925$, $p = 0.468$), the WAIS–Vocabulary ($F(5, 99) = 1.095$, $p = 0.368$) or the MMSE ($F(5, 106) = 0.887$, $p = 0.492$). Significantly lower scores in the Boston naming test (BNT) were detected in the oldest group compared with all of the others ($F(5, 105) = 3.089$, $p = 0.012$, Tukey’s HSD adjusted $p < 0.001$) (Table 7.2).

Regarding level of education, Table 7.3 shows the participants’ characteristics. Group 4 presents 43% of participants with primary studies whereas Group 5 presents a 45% of participants with university studies.

Table 7.3 Description of level of education between age groups

Age group	Primary (%)	Secondary (%)	University (%)
Group 1	42	33	25
Group 2	38	19	43
Group 3	12	44	44
Group 4	43	48	9
Group 5	33	22	45
Group 6	40	20	40

7.1.2 fALFF results between groups

The ‘Amplitude of Low-Frequency Fluctuations’ (ALFF) is a data-driven method that measures the strength of the regional intensity of spontaneous fluctuations in the BOLD signal (see Chapter 4, Section 4.4.1). Since the standard method is often considered sensitive to physiological noise, we decided to use its normalized *fractional* derivative (fALFF) proposed by Zou et al. (2008). This technique estimates local spontaneous activity and can reveal uncovered characteristics of resting state fMRI data (rs-fMRI). In the present Thesis, we compared the values of fALFF obtained from different age groups in healthy participants and investigated whether this marker could be related to the process of aging. Additionally, we explored the possible relationship between fALFF values and cognitive performance, *i.e.*, the neuropsychological measures, of the participants.

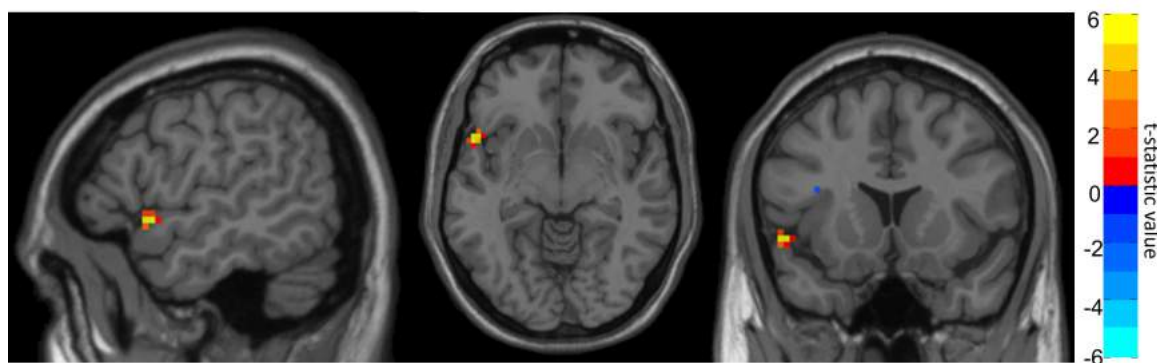


Fig. 7.1 fALFF analysis across significant age groups. Representation of significant differences between Group 1 and Group 5 in fALFF analysis. The colour bar indicates the intensity of the difference calculated with the *t*-statistic, with a score of 6 (yellow) representing positive differences and -6 (light blue) representing negative differences.

Table 7.4 shows the significant differences between age groups in the fALFF analysis. For clarity, the *contrast* formulates the hypothesis of the expected difference, the *area* refers to the anatomical brain region where the cluster is localized, and the *number of voxels* describes the size of the aforementioned cluster. Additionally, the *t(peak)* column expresses the value obtained in the *t*-Test, a statistical test similar to the *z*-score when the population size is small, used to support or reject the null hypothesis. The peak intensity of low-frequency fluctuations is localized in the Montreal Neurological Institute (MNI) coordinates, used in a spatially normalized brain. Finally, the AAL region identifies the positioning of the cluster peak within the nearest functional region defined by the Automatic Anatomical Labeling Atlas (AAL; Tzourio-Mazoyer et al. (2002)).

Figure 7.1 shows the graphical representation of the results in fALFF visualized with DPARSF (<http://rfmri.org/DPARSF>; Yan and Zang (2010)). No significant differences were found between Groups 2, 3, 4, and 6. Nevertheless, Group 1 showed increased fALFF in a cluster of voxels comprehending the superior temporal gyrus and inferior frontal gyrus compared with Group 5.

Table 7.4 Significant between–group differences in fALFF with their peak localization in MNI coordinates and the corresponding AAL ROI

Contrast	Area	Number of voxels	t(peak)	Peak MNI coordinates (mm)			AAL peak region
Group 1 > Group 5	Superior temporal gyrus and Inferior frontal gyrus	13	4.69	-54	15	-6	Temporal_Pole_Sup_L

t(peak):T–statistic value; MNI: Montreal Neurological Institute; AAL: Automatic Anatomical Labeling

7.1.3 ReHo results between groups

The regional homogeneity (ReHo) is another voxel–based method that estimates the temporal homogeneity of the signal between a voxel and its neighbours in the BOLD signal (see Chapter 4, Section 4.4.2). This technique evaluates local neuronal activity and regional abnormalities of rs-fMRI data. In the present Thesis, we compared the values of ReHo obtained from different age groups in healthy participants and exposed the key role of this indicator in the process of healthy aging. Additionally, we also explored the possible relationship between the ReHo values and the cognitive performance, *i.e.*, the neuropsychological measures, of the participants.

Table 7.5 shows the significant differences between groups in ReHo localized in MNI coordinates and the corresponding brain region defined by AAL. Figure 7.2 shows the graphical representation of the ReHo results, visualized with DPARSF (<http://rfmri.org/DPARSF>; Yan and Zang (2010)).

All groups showed significant differences with Group 6, where increased ReHo was always found in Group 6 compared with the other groups. More concretely, Group 6 showed increased ReHo in the temporal lobe (hippocampus) compared with Group 1. All groups also showed increased activity in the right hippocampus when compared with Group 2. Increased

Table 7.5 Significant between–group differences in ReHo with their peak localization in MNI coordinates and the corresponding AAL ROI

Contrast	Area	Number of voxels	t(peak)	Peak MNI coordinates (mm)			AAL peak region
Group 6 > Group 1	Temporal lobe (hippocampus)	318	5.42	9	-24	15	Thalamus_R
	Right caudate	44	5.31	9	15	3	Caudate_R
	Left precuneus	30	3.96	-24	-48	6	Precuneus_L
Group 6 > Group 2	Temporal lobe (hippocampus)	151	4.98	12	-27	15	Thalamus_R
Group 6 > Group 3	Right caudate	80	5.39	15	18	6	Caudate_R
	Right thalamus and right hippocampus	116	5.11	12	-36	9	Hippocampus_R
Group 6 > Group 4	Right caudate	39	4.94	12	18	3	Caudate_R
	Right precuneus	34	3.87	18	-42	9	Precuneus_R
Group 6 > Group 5	Right caudate	53	5.32	12	15	3	Caudate_R
	Left thalamus	30	4.15	0	-18	15	Thalamus_L

t(peak):t–statistic; MNI: Montreal Neurological Institute; AAL: Automatic Anatomical Labeling

ReHo activation in two separate clusters was found when comparing Group 6 to Group 3. The former showed an increase involving the right caudate, while the latter showed an increase in the right thalamus and right hippocampus. Interestingly, Group 6 again showed increased ReHo in the right caudate when compared with Groups 4 and 5.

Moreover, complementary correlation analyses between whole-brain fALFF and ReHo values were performed using age as a quantitative variable. No significant correlations were found between either whole-brain fALFF or ReHo values and age.

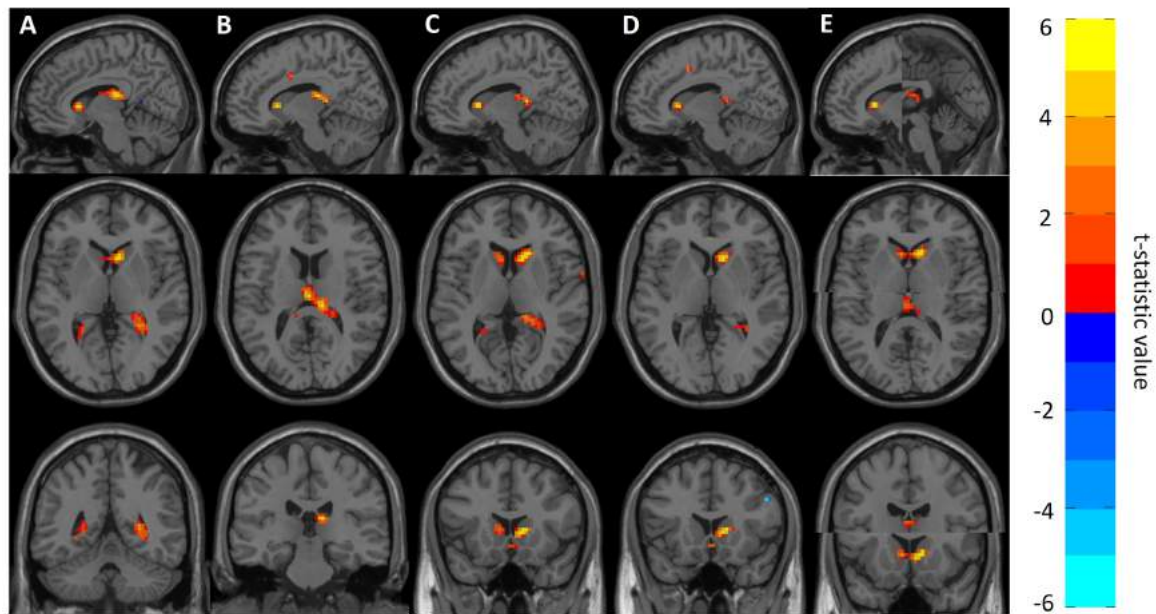


Fig. 7.2 ReHo analysis through age groups. Representation of significant differences between Group 6 and Groups 1 – 5 in the ReHo analyses. (A) shows the sagittal, axial and coronal planes with the differences between Group 6 and Group 1. Likewise, (B–E) represent the differences between Group 6 against Groups 2, 3, 4 and 5. (E) The two clusters (Right Caudate and Left Thalamus) that appeared to be significant; therefore, two images are shown in each plane. The colour bar indicates the intensity of the difference calculated with the *t*-statistic, with 6 (yellow) representing positive differences and –6 (light blue) negative differences.

7.1.4 Correlation analysis with neuropsychological outcome

Correlation analyses were performed using the clusters found in fALFF and ReHo when comparing the six groups to determine whether a relationship between the functional role of the clusters and patient's cognitive performance could be established.

We concluded that no significant relationship was found between the fALFF cluster and neuropsychological outcome. Similarly, no relationship was found between neuropsycholog-

ical measures and the signal from the clusters found in ReHo when comparing Groups 1 and 6, Groups 4 and 6 and Groups 5 and 6. Nonetheless, a significant relationship was found between BNT values and the signal from the cluster localized in the right hippocampus when comparing Groups 2 and 6 ($r_{xy} = -0.447$; $df = 29$; $p = 0.012$; $r^2 = 0.199$), where r_{xy} is the correlation coefficient, df is the degrees of freedom, p is the p -value and r^2 is the square power of the correlation coefficient. Moreover, a significant relationship was found between MMSE values and the signal of the first cluster involving right caudate when comparing Groups 3 and 6 ($r_{xy} = -0.345$; $df = 39$; $p = 0.031$; $r^2 = 0.119$).

Finally, regarding the clusters found in the correlation between age and ReHo values, significant correlations with cognitive outcomes were only found in the cluster involving occipital regions. WAIS–Vocabulary test showed a significant relationship ($r_{xy} = -0.202$; $df = 103$; $p = 0.038$; $r^2 = 0.041$) with ReHo signal in the same cluster (regions of the occipital lobe).

7.1.5 Correlations and regressions: fALFF, ReHo, and aging

Since some significant differences were found between age groups through both ReHo and fALFF techniques, we performed a correlation test to explore the possible relationship between the significant clusters. Also, an additional factor was taken into account in this analysis: the grey matter volume of the anatomical regions that were found to be significant in the seed–based analysis. As already explained in Chapter 5 Section 5.6, the structural images (T1-w) were segmented and introduced as a covariate in the voxel–based analysis to control possible confounds. We thought it would be interesting to inspect whether the grey volume matter of the regions where clusters were found to be significant would play any role at all in the healthy aging process.

Figure 7.3 shows the correlations between the significant clusters of fALFF and ReHo and the grey matter volume of these specific regions and age. All of them were significant, but it is important to highlight those surviving to the ‘multiple comparison correction’ (Bonferroni). Interestingly, high correlations were found between age and the ReHo signal of both right thalamus clusters, as well as the ReHo signal of both right caudate clusters, and their corresponding grey matter volume. Moreover, we also observed that age was also highly correlated with the fALFF signal of the frontal cluster, as well as their corresponding GM volume. All of them survived to Bonferroni correction, except the GM of the right caudate.

Additionally, since the correlations in some clusters of fALFF, ReHo and grey matter volume were high and significant after Bonferroni, a linear regression analysis was performed. The aim of such analysis was to explore if using the data of the most relevant clusters of fALFF, ReHo and grey matter volume as predictor variables of aging. In this case the lineal

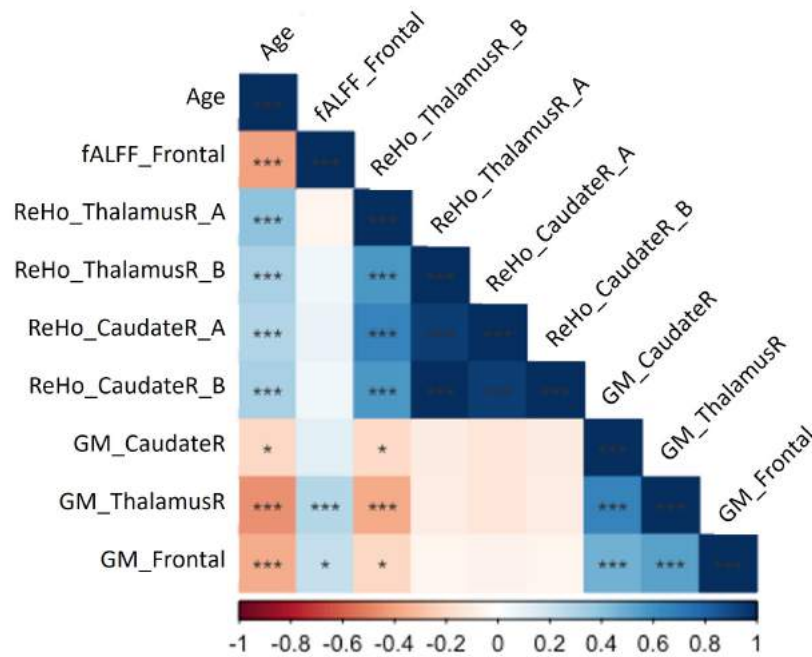


Fig. 7.3 Correlation analysis between significant clusters. Correlation regarding age, grey matter volume and significant clusters in fALFF and ReHo. Note: * $p < 0.05$; ** $p < 0.01$; *** $p < 0.00238$ (corrected by Bonferroni).

regression model we wanted to compute was the following:

$$Age = \beta_0 + \beta_1(\text{fALFF}) + \beta_2(\text{ReHo}) + \beta_3(\text{GreyMatter}), \quad (7.1)$$

where the different β are the coefficients accompanying the predictor variables.

In Table 7.6, the regression model predicting age is presented. The multiple regression (Figure 7.4) meets the conditions (no error autocorrelation, linearity, normality, and homoscedasticity of errors tested). It had high coefficient of determination (R^2) values, a parameter that evaluates the goodness of the fit, therefore indicating that a high level of prediction was achieved. Only some variables were included as predictors, including fALFF signal of the frontal lobe, ReHo signal of the right thalamus and the right thalamus grey matter volume. Here, F is the F-Snedecor test, R^2 is the aforementioned coefficient of determination and AIC (Akaike information criterion) is a metric used to compare the fit of several regression models. The AIC value is designed to find the model that explains the most variation in the data while penalizing models that use an excessive number of parameters. The lower the AIC value, the better the model fit.

Table 7.6 Parameter estimation (β) of the best stepwise linear model for age

fALFF, ReHo and Grey matter	Age
	F = 22.52
	$R^2 = 0.39$
	AIC = 738.21
Intercept	95.86
fALFF Frontal	$\beta = -6.33$ ($p < 0.001$)
ReHo Thalamus Right	$\beta = 6.26$ ($p < 0.001$)
Grey matter Thalamus right	$\beta = -7.07$ ($p < 0.001$)

F: F-test ANOVA; AIC: Akaike information criterion. All parameters have a $p < 0.001$ in the model ($df = 3; 108$) and a $p > 0.05$ in Anderson's Darling test of normality, the Ramsey Regression Equation Specification Error (RESET) test, Durbin Watson's test, and the Breusch-Pagan test.

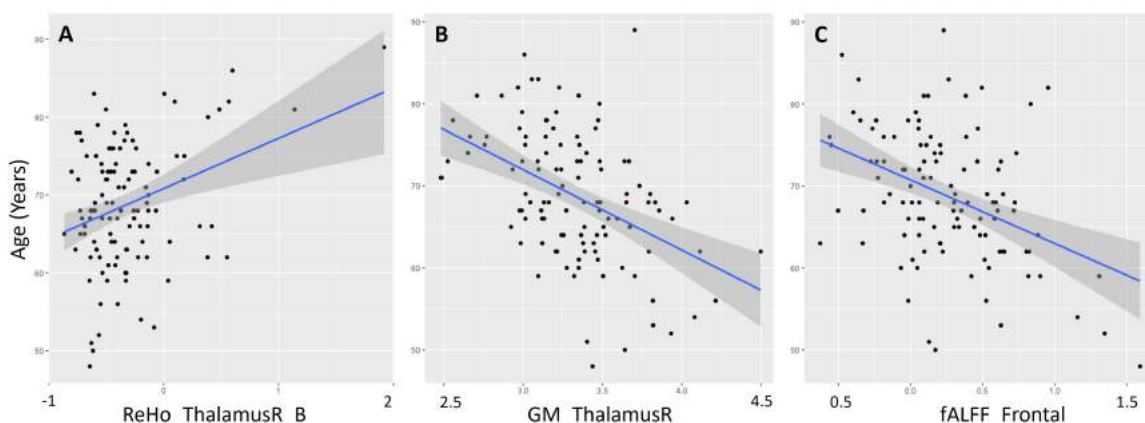


Fig. 7.4 Scatter plot and regression for age. (A) Relation between Age and ReHo signal of the right Thalamus. (B) Relation between Age and grey matter volume of the right Thalamus. (C) Relation between Age and fALFF signal of the Frontal lobe.

7.2 Graph-based analysis of fMRI data and thresholding

In this Section we describe the overall results obtained from the exploration of different thresholding techniques in the correlation matrices of fMRI signals. For each threshold, all graph indicators (Path Length L , clustering coefficient CC , global efficiency G_E , modularity Q , transitivity T and smallworldness (SW)) were computed, both from the real subject network and from the ones simulated with the null model. Since the small-world indicator already includes by definition the null model's computation of the characteristic path length and clustering coefficients, the comparison between the real and the simulated data is achieved by analysing the value of the graph metrics by itself.

Figures 7.5 to 7.9 portray, for each respective graph indicator, the null model and the subject's real graph measure for the different thresholding approaches. In a descriptive manner, each indicator value from subjects' data was plotted next to its corresponding simulated null model for every threshold. In all plots, subjects' data was coloured in red, and null models in blue. We note that the number of links is normalized, *i.e.*, they are provided as fraction of links, with '0' indicating that no links are preserved from the original matrix after thresholding, and '1' indicating that the totality of links were preserved, *i.e.*, the that the 100% of originally identified links in the matrix are present. To identify in the plots each threshold approach, we used the following scheme: (i) for the *proportional thresholding*, data is represented as a solid line (red or blue) together with a grey shading that indicates the SD; (ii) for the *TMFG threshold*, data is represented with a large triangle with the corresponding error bars; and (iii), for the *absolute thresholding*, data are represented as a coloured scatter plot. For this thresholding approach, we note that neither the SD nor the confidence interval are shown in the plot since the number of individual links may vary through subjects due to the inner nature of the absolute thresholding method. Finally, for each graph measure, subplots A and B differentiate the graph measure values for the two absolute thresholds used in this study, namely 0.5 and 0.7 thresholding value, respectively. We also note that Figure 7.10 represents the smallworldness without a null model, as previously justified.

7.2.1 Characteristic path length L

It provided the average shortest path length between any two nodes in a network. Low L values indicated that nodes needed several steps to reach one another, while high L values indicated an easy and, thus, overall fast network communication. Results are shown in Figure 7.5A. For the 'proportional threshold' (solid lines), the subject values separate well from the null model in the range of preserved links between 0.1 and 0.25, with no overlapping of the SD shadings, indicating that the observed values of L in subjects cannot occur by chance. However, in the range from 0.25 to 0.5, the deviations clearly overlap. In the case of 'absolute thresholding' and $r \geq 0.5$ (Figure 7.5A), L steeply declines as the number of preserved links increases, which range from 0.06 to 0.54. It is important to point out that values within this threshold present a high range of variability. Regarding the TMFG method, the subject's characteristic path length value is clearly separated from the null model. Finally, Figure 7.5B repeats the analysis but using an absolute thresholding criteria of $r \geq 0.7$. We note that, in this panel, the results for the proportional thresholding and TMFG are exactly the same as in panel A, and only those from the absolute thresholding varied. By comparing the panels, we observed that, on the one hand, L values are higher here than in $r \geq 0.5$ criterion and have a decreasing tendency even though the link range is shorter. On the other hand, a

larger overlap between the subject and the null model values is observed, with the red and blue dots crossing one another, especially when fewer links are considered.

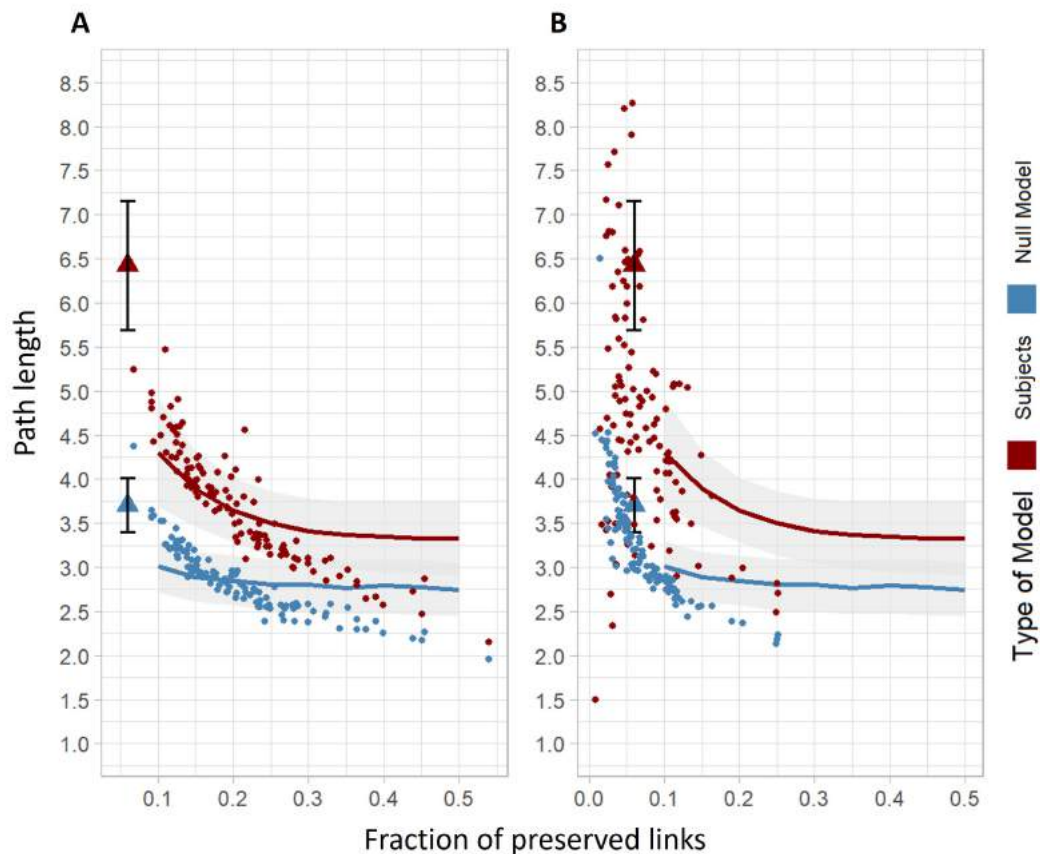


Fig. 7.5 Graphical representation of the subjects' characteristic path length L , together with the null model, for each threshold for varying links. In each subplot, the horizontal axis represents the fraction of links included in the graph, and vertical axis represents the value of the measured L . Data in red shows the subjects' results, and blue the one obtained from the null model. (A) Coloured solid lines show the results for the 'proportional threshold' values, with the shaded area representing the SD. Big triangles with error bars provide the TMFG threshold values. Coloured scatter plots show the 'absolute threshold' values using $r \geq 0.5$. (B) Equivalent representation but using 'absolute threshold' values for $r \geq 0.7$. Note that the range of the horizontal axis is slightly different.

7.2.2 Clustering coefficient CC

It captured the tendency of the nodes in the network to form triangles, a signature of strong local connectivity. As shown in Figure 7.6A, With regard to the proportional thresholding (solid lines), the subject's model values of clustering coefficients tend to be substantially higher than the null models as the preserved links grew up to the 20% of links, where a local

maximum value is reached. Then, the values of the subject's clustering coefficient decrease. Null model's clustering coefficient shows a different behaviour than the subject's values and shows a tendency of increasing its value as more links are added. In addition, an overlap of the SD is set on nearly 25% of the links and increases as more links are included. The value of the clustering coefficient's null model in the TMFG thresholding (triangles) is much higher for the subjects than for the null model, with the latter showing a very small variability as reflected by the much shorter error bar as compared to subjects' one. Regarding absolute thresholding, Figure 7.6A compares the for $r \geq 0.5$, while Figure 7.6B compares the data for $r \geq 0.7$. Both panels show a linear growth of CC along the included links and both show a slight overlap with the null model, especially at a higher fraction of preserved links.

7.2.3 Global Efficiency G_E

It captured the tendency of the network to exchange information globally as a whole, with large G_E indicating a highly integrated network. Figure 7.7 represents the values of G_E for the three thresholding methods. Overall, we note that, for this particular graph observable, the null-model values are always higher than the subjects'. The proportional thresholding analysis (solid lines) shows a logarithmic growth of the subjects' G_E , with a rapid increase of the measured indicator as more links are taken into account until a plateau is reached, around 25 – 30% of the links. Moreover, a local maxima in the null model G_E values is reached around the 25% of the links, then the values of global efficiency decrease. An overlap of the deviations is reached below the 10% and over the 35% of the links considered. In the case of TMFG thresholding (triangles), the null model and subject's values are clearly differentiated, also with the null model presenting higher efficiency, and the error bars show no overlap between them. Regarding absolute thresholding for $r \geq 0.5$ (scatter plots, panel A), both the null model and the individual values present a linear growth, with values aligning with the proportional analysis at lower links. In the case of $r \geq 0.7$ (panel B) the data for subjects' has a tendency similar to the null-model and the other thresholding approaches (TMFG and 'proportional'). Nevertheless, there is an evident overlapping of the values, especially when considering fewer links.

7.2.4 Modularity Q

It provided a measure of the segregation in the network by evaluating the likelihood that nodes organize in communities, *i.e.*, functional groups of nodes that are more connected within their group than with the rest of the network. As depicted in Figure 7.8A, the proportional thresholding analysis (solid lines) shows a decreasing tendency of the subject's modularity

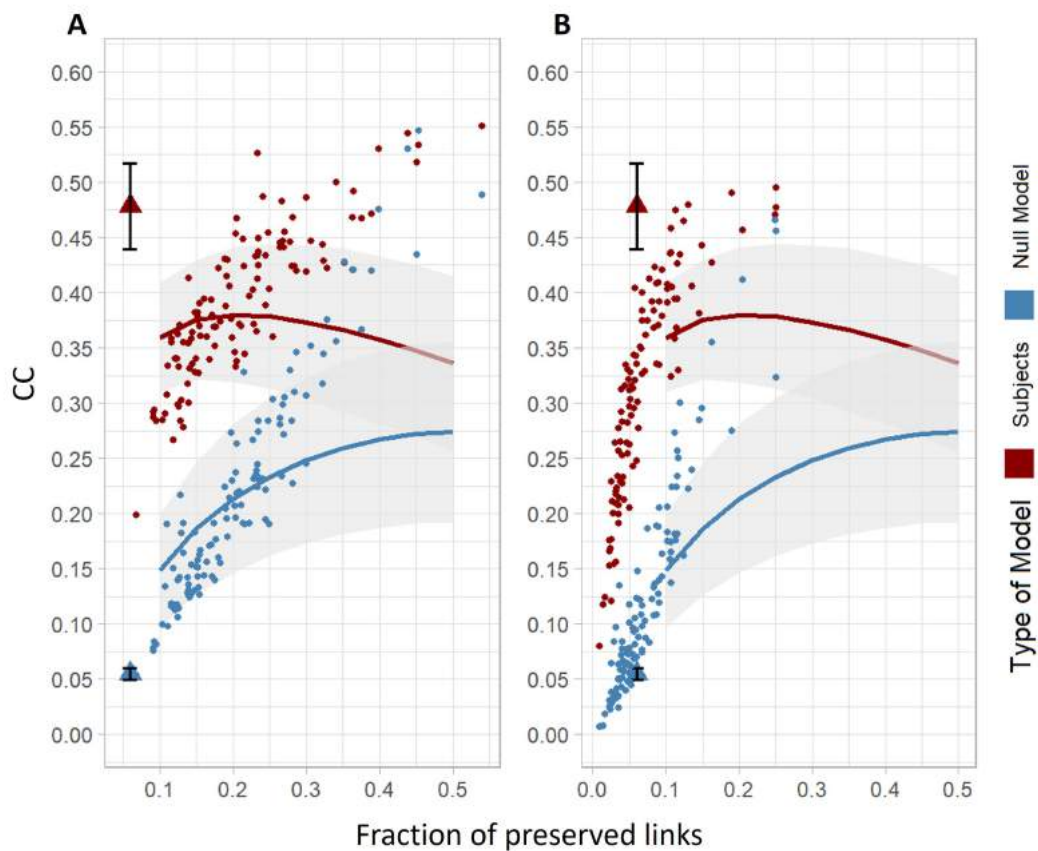


Fig. 7.6 Graphical representation of the subjects' clustering coefficient CC , together with the null model, for each threshold for varying links. In each subplot, the horizontal axis represents the fraction of links included in the graph, and vertical axis represents the value of the measured CC . Data in red shows the subjects' results, and blue the one obtained from the null model. (A) Coloured solid lines show the result for 'proportional threshold' values, with the shaded area representing the SD. Big triangles with error bars provide the TMFG threshold values. Coloured scatter plots show the 'absolute threshold values using $r \geq 0.5$. (B) Equivalent representation but using 'absolute threshold' values for $r \geq 0.7$. Note that the range of the horizontal axis is slightly different.

and the null model values. We note that the null model presents a low dispersion and hence a lower SD, while the subject values are sparser. Even with this fact, there is clearly no overlap between the distributions at any range of links. In the case of TMFG thresholding (triangles), the null model and subject's values are clearly differentiated and seem to follow the same tendency as the proportional thresholding values. Also, the error bars show a low dispersion in both the null model and the subject values. Regarding absolute thresholding for $r \geq 0.5$ (panel A, scatter plots), both the null model and the individual values align with the proportional thresholding tendency, especially at lower links. In the case of $r \geq 0.7$ (panel B) the tendency of the modularity values adjusts to a potential decrease as more links are taken into account for both the null model and subject values. Nevertheless, it is important to note

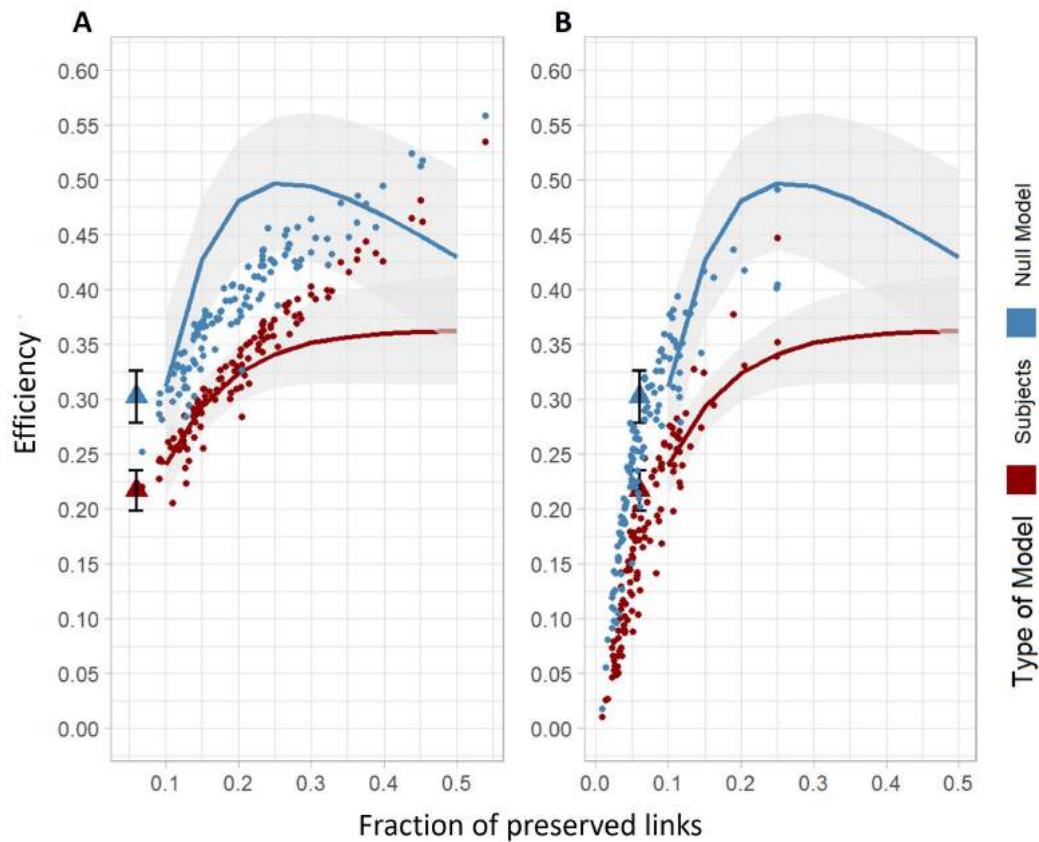


Fig. 7.7 Graphical representation of the subjects' global efficiency G_E , together with the null model, for each threshold for varying links. In each subplot, the horizontal axis represents the fraction of links included in the graph and vertical axis represents the value of the measured efficiency G_E . Data in red shows the subjects' results, and blue the one obtained from the null model. (A) Coloured solid lines show the results for the 'proportional threshold' values, with the shaded area representing the SD. Big triangles with error bars provide the TMFG threshold values. Coloured scatter plots show the 'absolute threshold' values using $r \geq 0.5$. (B) Equivalent representation but using 'absolute threshold' values for $r \geq 0.7$. Note that the range of the horizontal axis is slightly different.

that even though there is no clear overlap of the distributions, the dispersion of the subject values (red data) is higher, either in the 0.5 and 0.7 absolute thresholding.

7.2.5 Transitivity T

This metric is a complementary measure to the clustering coefficient that quantifies the density of triangles in the network, *i.e.*, also informs about a tendency towards local connectivity. Figure 7.9 provides the results for this metric. With regard to the proportional threshold, the null model and the subject values follow two different tendencies. On the one hand, the null

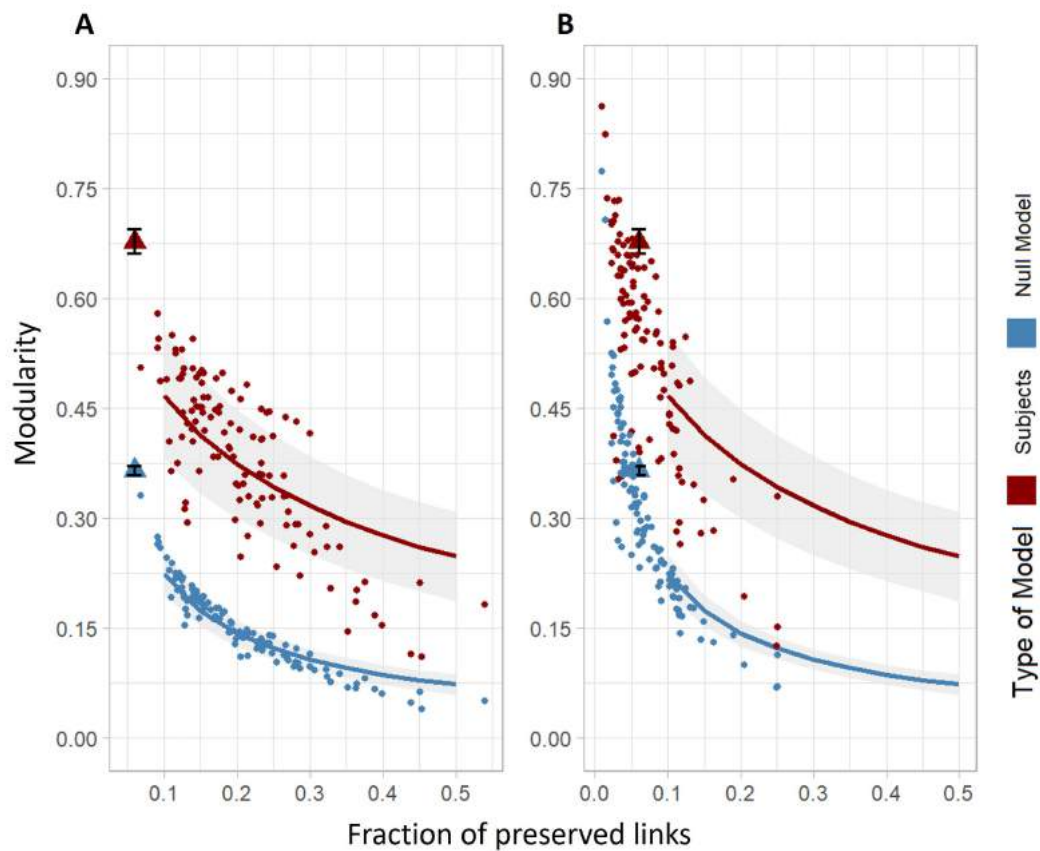


Fig. 7.8 Graphical representation of the subjects' modularity Q , together with the null model, for each threshold for varying links. In each subplot, the horizontal axis represents the fraction of links included in the graph and vertical axis represents the value of the measured modularity Q . Data in red shows the subjects' results, and blue the one obtained from the null model. (A) Coloured solid lines show the results for the 'proportional threshold' values, with the shaded area representing the SD. Big triangles with error bars provide the TMFG threshold values. Coloured scatter plots show the 'absolute threshold' values using $r \geq 0.5$. (B) Equivalent representation but using 'absolute threshold' values for $r \geq 0.7$. Note that the range of the horizontal axis is slightly different.

model shows an increase of the transitivity and a high dispersion along the range of considered links. On the other hand, the subjects' values show a linear decreasing transitivity as more links are taken into account. In addition, the SD is also high in the subjects' transitivity, and an overlap between subjects and null model values is reached at the 25% of preserved links. The values obtained with the TMFG thresholding show a clear difference between the null model and the subjects' transitivity, being the latter value higher and with wider error bars but with no overlap. Finally, regarding the absolute thresholding, the scatter plots show a linear increase tendency of the transitivity for the subject values and for the null model with a slight overlap at higher percentages of considered links in both cases $r \geq 0.5$ (Figure 7.9A) and $r \geq 0.7$ (Figure 7.9B).

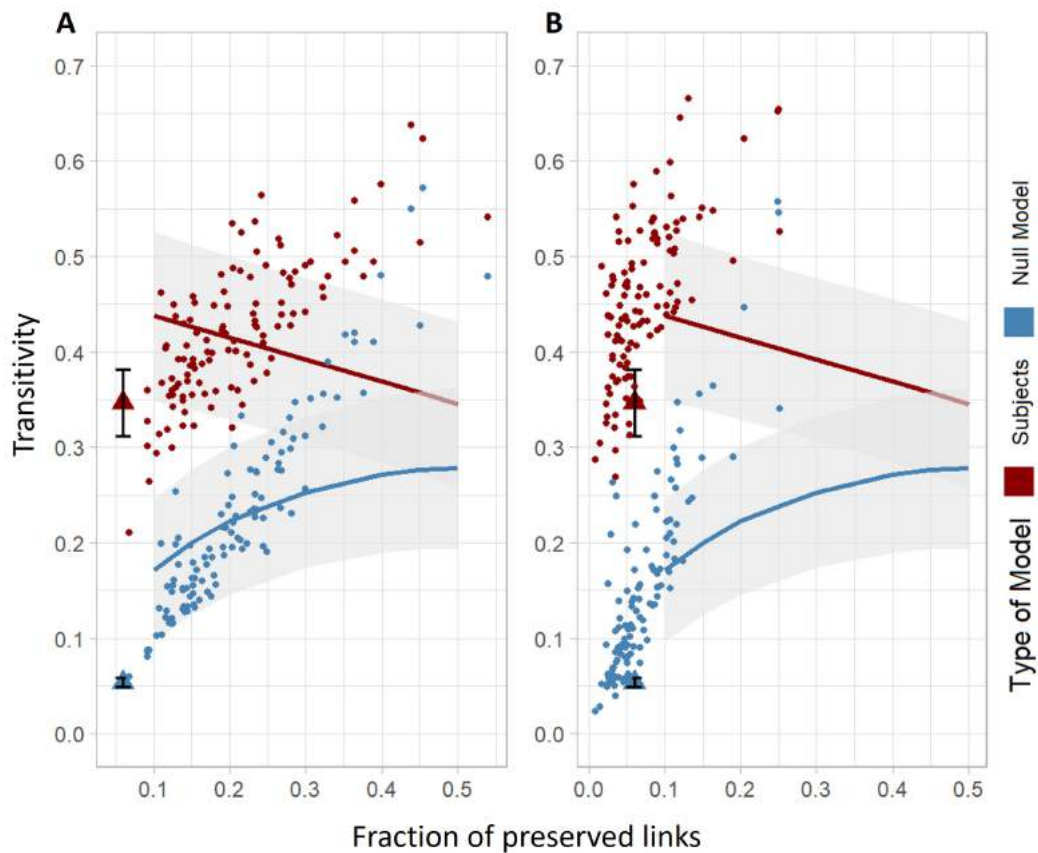


Fig. 7.9 Graphical representation of the subjects' transitivity T , together with the null model, for each threshold for varying links. In each subplot, the horizontal axis represents the fraction of links included in the graph, and vertical axis represents the value of the measured transitivity T . Data in red shows the subjects' results, and blue the one obtained from the null model. **(A)** Coloured solid lines show the results for the 'proportional threshold' values, with the shaded area representing the SD. Big triangles with error bars provide the TMFG threshold values. Coloured scatter plots show the 'absolute threshold' values using $r \geq 0.5$. **(B)** Equivalent representation but using 'absolute threshold' values for $r \geq 0.7$. Note that the range of the horizontal axis is slightly different.

7.2.6 Smallworldness

This graph statistic quantifies the likelihood that the network balances regularity and randomness, which is achieved by having a network with high clustering coefficients CC and short distances L . A small-world organization, which is a hallmark of a healthy brain, is considered optimal to facilitate the functional communication between any two brain areas with relatively few steps. The results of such analysis are provided in Figure 7.10. As mentioned before, the null model is not represented in this graphic due to the mathematical definition of the small world, which already includes the null model. It is typically considered that a network

has a small–world organization when its sigma value exceeds 1 ($\sigma > 1$) (Humphries and Gurney, 2008), represented as a dotted line in the plots.

We note that the vertical axis of both panels in Figure 7.10 are not equally escalated. Figure 7.10A shows a decreasing tendency of the small–world’s indicator regarding the proportional thresholding. The TMFG thresholding method presents the higher value of the small–world. It is important to highlight that all the thresholds, except some values for the absolute 0.5 threshold, surpass the > 1 condition for smallworldness, and thus they can be considered networks characterized with such a trait. Concerning the proportional threshold, it is shown that the small world value decreases as more links are considered but the metric never decreases below 1. We can assume, then, that all the proportional thresholds also have a smallworldness structure. As for absolute thresholding ($r \geq 0.5$), small world values diminish as the number of links increases. It is important to point out that values within this threshold present a high range of variability. Finally, Figure 7.10B compares the absolute thresholding criterion ($r \geq 0.7$) with the TMFG and proportional thresholding already detailed in Figure 7.10A. Small world values are much higher than in $r \geq 0.5$ criterion and also tend to decrease even though the link range is shorter.

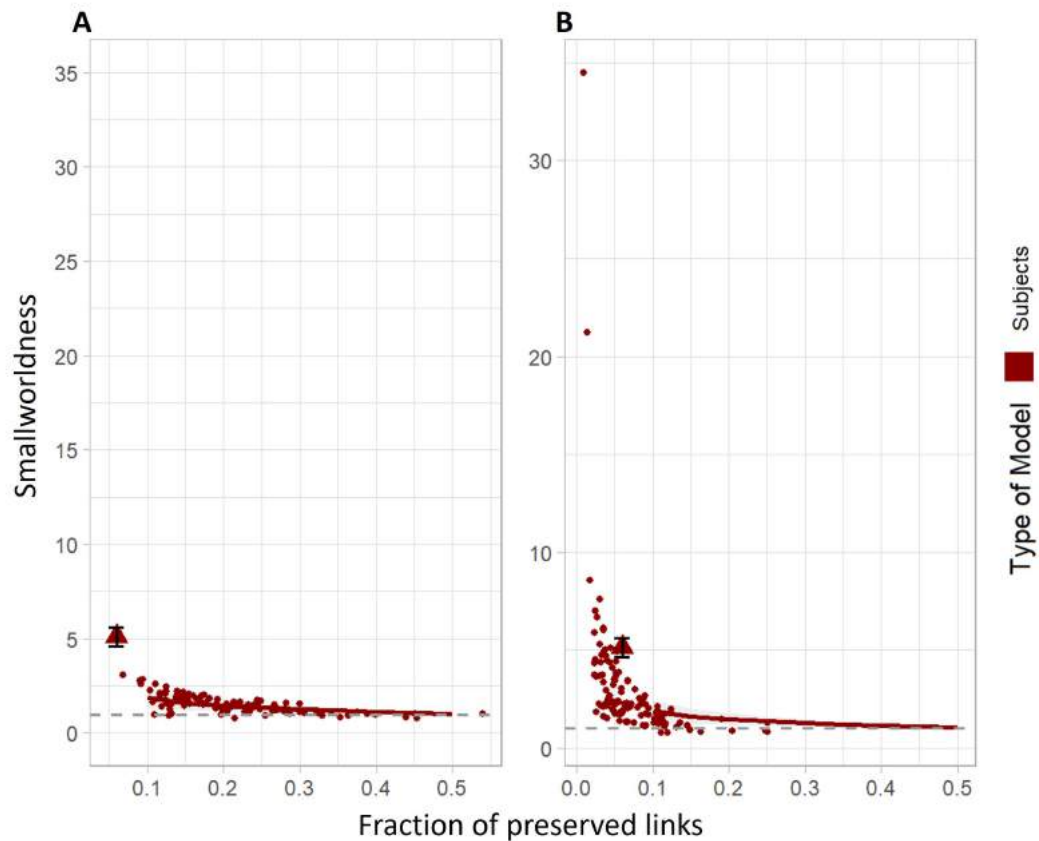


Fig. 7.10 Graphical representation of the subjects' small-world SW metric for each threshold for varying links. In each subplot, the horizontal axis represents the fraction of links included in the graph and vertical axis represents the value of the measured smallworldness SW . Data in red shows the subjects' results. **(A)** Coloured solid lines show the results for the 'proportional threshold' values. Big triangles with error bars provide the TMFG threshold values. Coloured scatter plots show the 'absolute threshold' values using $r \geq 0.5$. **(B)** Equivalent representation but using 'absolute threshold' values for $r \geq 0.7$. Note that the range of the horizontal axis is slightly different.

7.2.7 Accuracy measure

Table 7.8 represents the accuracy ratio (%) for every graph indicator for both two and three SD, estimated as explained in the methods section. Be noted that the global efficiency's accuracy is estimated subtracting instead of adding the two SD, because the values of efficiency in the null model are higher than in the subject's model.

Regarding characteristic path length, for both deviations the accuracy is 100%, except for absolute 0.7 and relative 0.1. For the modularity and transitivity metrics, all the accuracies are of 100%, both for 2 and 3 deviations. Regarding clustering coefficient indicator, we find only a 100% of accuracy for TMFG thresholding. Finally, in the case of global efficiency, a 100% of accuracy was found for all the thresholds except relative 0.1. It is important to mention also that there are not big differences between two and three deviations. Finally, in Table 7.7, the total accuracy for every threshold considering all the graphs indicators is shown. Although all accuracy values are very high, the unique thresholding method with a 100% of accuracy in all the measures is the TMFG.

Table 7.7 Total accuracy for every threshold considering all the graph indicators used previously

Threshold	Accuracy for 2 SD	Accuracy for 3 SD
Absolute 0.5	99.649%	99.474%
Absolute 0.7	97.368%	97.193%
TMFG	100%	100%
Relative 0.1	97.719%	98.596%
Relative 0.15	99.649%	99.649%
Relative 0.2	99.474%	99.474%
Relative 0.25	99.649%	99.474%
Relative 0.3	99.649%	99.474%
Relative 0.35	99.474%	99.947%
Relative 0.4	99.649%	99.947%
Relative 0.45	99.825%	99.649%
Relative 0.5	99.825%	99.825%

SD: standard deviation

Table 7.8 Accuracy for every threshold in every connectivity indicator

Threshold	Char. path length			Modularity			Transitivity			Clustering Coefficient			Global Efficiency		
	Acc	2 SD	3 SD	Acc	2 SD	3 SD	Acc	2 SD	3 SD	Acc	2 SD	3 SD	Acc	2 SD	3 SD
Absolute 0.5	100%	100%	100%	100%	100%	100%	100%	100%	100%	100%	100%	100%	100%	100%	100%
Absolute 0.7	87.7%	86.8%	86.8%	100%	100%	100%	100%	100%	100%	100%	100%	100%	100%	100%	100%
TMFG	100%	100%	100%	100%	100%	100%	100%	100%	100%	100%	100%	100%	100%	100%	100%
Relative 0.1	99.1%	99.1%	99.1%	100%	100%	100%	100%	100%	100%	100%	100%	100%	90.4%	94.7%	94.7%
Relative 0.15	100%	100%	100%	100%	100%	100%	100%	100%	100%	100%	100%	100%	100%	100%	100%
Relative 0.2	100%	100%	100%	100%	100%	100%	100%	100%	100%	100%	100%	100%	100%	100%	100%
Relative 0.25	100%	100%	100%	100%	100%	100%	100%	100%	100%	100%	100%	100%	100%	100%	100%
Relative 0.3	100%	100%	100%	100%	100%	100%	100%	100%	100%	100%	100%	100%	100%	100%	100%
Relative 0.35	99.1%	96.5%	96.5%	100%	100%	100%	100%	100%	100%	100%	100%	100%	100%	100%	100%
Relative 0.4	100%	100%	100%	100%	100%	100%	100%	100%	100%	100%	100%	100%	100%	100%	100%
Relative 0.45	100%	100%	100%	100%	100%	100%	100%	100%	100%	100%	100%	100%	100%	100%	100%
Relative 0.5	100%	100%	100%	100%	100%	100%	100%	100%	100%	100%	100%	100%	100%	100%	100%

Char: Characteristic; Acc: Accuracy; SD: standard deviation

7.3 Discussion

7.3.1 Discussion fALFF and ReHo

In the last few years, the importance of healthy aging has increased substantially due to the higher levels of life expectancy in the population together with the appearance of dementia in the general population, which dramatically increases societal healthcare costs. Therefore, disentangling the brain mechanisms of healthy aging has been a subject of interest for researchers. The aims of the present study were to study the whole-brain resting state using fALFF and ReHo strategies to explore differences in spontaneous brain activity among healthy participants of different age groups, from middle to advanced age.

Regarding the whole-brain fALFF analysis, the results showed significant differences in low-frequency fluctuations between Groups 1 and 6 in the superior temporal gyrus and inferior frontal gyrus (Table 7.4). More concretely, group one (the youngest one) showed increased fALFF in this area.

These results are in line with those reported by other authors. The superior temporal gyrus appeared to show a volume decrease (atrophy) in healthy aging, revealing a relationship between age and the rate of atrophy (Fjell et al., 2009). This atrophy could also explain the decrease in fALFF values among this population. Moreover, Galiano et al. (2020) also found higher intrinsic connectivity contrast and higher cerebral blood flow between young and elderly groups. Oschmann et al. (2020) also reported significantly decreased FC in this area in a longitudinal study (4-year follow-up) when using the right inferior parietal sulcus as a seed. The inferior frontal gyrus, which is an area involved in language functions, has also been found to have a decreased grey matter density in older adults (Pistono et al., 2021).

Moreover, the detected cluster appears to be disrupted by aging, and the significant differences would be expected to involve the oldest group. However, the differences found in this study involve the second oldest group (Group 5) and not the oldest-most group. This fact is consistent with Farras-Permanyer et al. (2019), who suggested that this phenomenon could be a survival mechanism, meaning that the participants of Group 6 would have a higher degree of resilience.

In relation to the ReHo results, significant differences between all groups and Group 6 were found, indicating higher synchronization of rs-fMRI signals among neighbouring voxels in Group 6. More specifically, Group 6 had increased ReHo values in some areas of the temporal lobe (hippocampus) compared with Groups 1 and 2. However, this cluster has different volumes depending on the groups compared. It has its maximum size (318 voxels) when comparing age Groups 1 and 6, and as the age of the participants increases, it decreases to 151 voxels when comparing Groups 2 and 6. It is important to highlight that, even if it

is smaller, the cluster is significant also in group 3 (involving the right thalamus and right hippocampus, 116 voxels). As individual effects, it is also important to remark that group 6 shows increased ReHo compared with group 1 in the left precuneus whereas group six shows increased ReHo in the right precuneus. The left thalamus is increased in ReHo values when comparing group 5 and 6. All these structures that show significant group differences among age groups include the default mode network (DMN), which is one of the intrinsic resting-state networks that has been most studied with respect to aging.

Fjell et al. (2014) highlighted the hippocampus as a vulnerable region to aging. The FC of the hippocampus also decreases in Alzheimer's disease (AD) (Greicius et al., 2004; Sheline et al., 2010). In healthy elderly individuals, Bartrés-Faz et al. (2008) examined the FC of the hippocampus during an encoding memory task and found increased connectivity with the anterior cingulate, inferior parietal lobe, and caudate in Apolipoprotein E (APOE- ϵ 4) carriers. Oschmann et al. (2020) points out the importance of other networks, as the frontoparietal network, apart from the DMN. Despite these unclear conclusions (Hu et al., 2014), the hippocampus appears to be a key structure that changes with age. It is clear that a broad individual heterogeneity emerges in this population; Abellana-Pérez et al. (2022) proposed a combination of non-invasive brain stimulations (NIBS) and fMRI to understand how fundamental brain plasticity mechanisms operate in advancing age.

The second cluster (right caudate) shows increased ReHo values in Group 6 compared with Groups 1, 3, 4 and 5. However, as shown in Table 7.5, the size of this second cluster varies through age group comparisons which is higher on Group 3. These results are also in line with those reported in other studies. Bennett et al. (2011) found age-related decreases in caudate-dorsolateral prefrontal cortex tract integrity that mediated age-related differences in late-stage sequence learning. In a task-fMRI study, Bowen et al. (2020) found that older but not younger adults exhibited enhanced subsequent memory for high-reward items, supported by greater connectivity between the caudate and bilateral inferior frontal gyrus. Tang et al. (2021) found decreased FC within the right caudate and some regions of the cerebellum in AD.

Our results show that, even scaling by grey matter volume, fALFF and ReHo show significant differences in healthy aging. The correlation matrix demonstrates the clear relationship between age and neuroimaging signals, beginning with ReHo signals in the right thalamus, which correlates positively with age. The ReHo signal of the right caudate also correlates positively with age. Nonetheless, fALFF signal in the frontal cluster is negatively linked with age, showing a decrease of fractional amplitude of low frequency fluctuations in these areas. Remarkably, structural changes are also associated with age, finding a negative correlation with this variable. In this sense, grey matter volumes of the right thalamus, the

right caudate and the frontal cluster are negatively associated with age, having therefore decreased volume as age advances. These structural abnormalities have also been reported in Pergher et al. (2019). They also show negative correlations with sociodemographic variables such as age. As high correlations were found between these measures and age, we performed step-wise regression to try to predict age by neuroimaging data. Results show a high variability explained by these structural and spontaneous brain activity measures, suggesting its utility as biomarkers of age. However, more studies are needed to demonstrate its potential. Other authors have suggested already the ability of fALFF and ReHo measures as potential biomarkers owing to their high test-retest reliability (Küblböck et al., 2014; Zuo and Xing, 2014).

Both fALFF and ReHo techniques have been shown to be valuable and usable tools for disentangling brain changes in activation in different groups of healthy aging. fALFF and ReHo techniques measure different outcomes in the brain; therefore, differences in groups suggest two features involved in aging. On the one hand, the fALFF results indicate a significant difference in low-frequency fluctuations between Groups 1 and 5 despite not being translated into a significant change in performance in terms of the neuropsychological measures. However, interestingly, this result is in line with the results of Farras-Permanyer et al. (2019) using the same sample concerning progressive FC decrease either in number or intensity of connections. On the other hand, the ReHo results indicate an increase in regional synchronization between Group 6 and the other age groups. Other studies have also reported increased ReHo measures and have considered it to offset functional decrease or impairment, *i.e.*, a compensatory mechanism (Kong et al., 2015; Zhang et al., 2012). This finding may be crucial because it directly links the increase in ReHo signal with healthy aging; furthermore, there is no evidence of impairment and no decrease in the neuropsychological performance. The differences in the findings of fALFF and ReHo, which remained in Groups 5 and 6, could be linked to the fact that both groups were healthy-aging participants without any suspicion of dementia or any other cognitive decline. Meanwhile, Group 6 included more elderly individuals who therefore have higher resilience. These results demonstrate that increased ReHo values could be directly linked with compensatory mechanisms due to brain aging.

Limitations on the study

The described techniques and analyses have some limitations, though. First, an important limitation is found in the sample size. Although the study cohort contains 112 participants, the size of each age group was not entirely homogeneous, leaving the oldest group with only 10 participants. Therefore, sample size, distribution and dispersion may introduce a bias

in the final results, especially concerning the older group. The lack of a replication dataset could also have limited the results. Second, low-frequency BOLD signals, especially in the brain regions that comprise the DMN (Birn et al., 2006), are affected by physiological noises (Birn et al., 2008; Chang and Glover, 2009). We cannot truly assess the impact of these physiological noises or any blood pressure-induced hemodynamic response fluctuation as we did not monitor respiratory and cardiovascular data. Finally, motion, even if well controlled, might affect the results.

Some strengths of the presented work are also worth mentioning. As there is a fundamental need to better understand the neurobiological changes associated with healthy aging given the globally aging population, elucidating the differences in spontaneous brain activity between age groups of healthy aging is of major importance. Our investigation demonstrates that changes in spontaneous brain activity may occur in very low intervals of years, and those changes could be targeted as specific therapeutic areas in cognitive rehabilitation. Finally, a highly restrictive correction for multiple comparisons was performed in this analysis to ensure that the strongest differences remained significant. The results have a large effect size, so we can affirm that significant differences in regional spontaneous brain activity using fALFF and ReHo were found between the six groups of an elderly population. Finally, the strong relationship between age and structural and spontaneous brain activity measures suggests the possibility of using them as potential biomarkers.

7.3.2 Discussion on thresholds

Our exploration confirms that the choice of a threshold dramatically affects the results obtained for different graph metrics, mainly due to the big variability found in all the metrics by using different types of thresholding techniques. This conclusion is in line with other studies published before, mainly in binary matrices (Drakesmith et al., 2015; Garrison et al., 2015; van den Heuvel et al., 2017). The comparison between two groups (mainly one healthy and one with a certain disorder) and the possibility to generalize the results may depend on the threshold choice, and therefore, it is of great value to standardize which threshold may be more adequate. Moreover, the two methodologies used in this study, null model comparison and the accuracy measure, have demonstrated to be useful in order to decide which is the best threshold.

Based on the comparison between the subjects' graph metrics and null models' we can affirm that our results are neither spurious nor noise driven. Within a certain thresholding range, it's guaranteed that the subject values and their SD are far from the null model, and therefore, the included links are not randomly organized. The null models' network is a randomized complex system that preserves some important characteristics of the original

network, such as the degree and the number of links, but not the network arrangement. Thus, the graph metrics values of this network are different from the ones obtained for the subjects'.

Regarding the proportional thresholding, the range from 0.1 to 0.25 of included links shows no overlapping of the null model deviations in all the graph measures. In this sense, this indicates that when we have 10 – 25% of the network's strongest links, we can be sure that these values are sufficiently separated from the null model. More concretely, an overlap is found at the range from 0.25 to 0.5 of included links for the clustering coefficient, characteristic path length and transitivity. Caution must be taken when using threshold values comprehended within this range due to the similarity of the measure with its null model. In the global efficiency graph measure, the overlap does not appear until 0.35, and there is no overlapping found in modularity using this thresholding technique, independently of the proportion of links included. In this sense, this graph measure indicates the subdivision into a set of modules, indicating that when this value is high, there are dense connections between the nodes within modules but sparse connections between nodes in different modules. When we use a random network then, the modularity is difficult to find. It is also important to remark that all the proportional thresholds had a small-world structure. Nevertheless, the inclusion of more links in the network (with less strength) decreases the small world graph measure.

Regarding the TMFG thresholding method, as we can see in the results section, the subject's model is always clearly separated from the null model's distribution throughout all the estimated graph measures. It is also essential to highlight the differences between clustering coefficient and transitivity using this type of threshold. Despite being both indicators of segregation, as well as to reflect both the prevalence of clustered connectivity around individual nodes (Rubinov and Sporns, 2010), the values in this threshold for both graph metrics are different. We find a higher clustering coefficient than the transitivity measure using the TMFG thresholding method due to the influence of nodes with a low degree on the clustering coefficient measure. This phenomenon is also represented in other thresholding methods but is much smoother. This result is a consequence of the different criteria based on the degree when filtering the original correlation matrices. In the case of the TMFG thresholding method, the matrices are constructed by trying to maximize a score function linked with the information retained in the network (Christensen, 2018). Therefore, in this thresholding, links with a lower degree can be included in the matrix, which directly impacts the estimation of the clustering coefficient measure. In contrast, CC is compensated when calculating the transitivity measure with this threshold. Finally, this occurrence is also affecting the small world measure, due to the inherent estimation of this measure, which

is based on the clustering coefficient. Therefore, we can see that the small world values estimated with the TMFG thresholding are really high.

Finally, a main issue that arises from the absolute thresholding technique is that the number of links considered through individuals cannot remain constant. A direct consequence of this limitation is that no mean value could be extracted and hence it could not be compared as a whole with the other thresholding values. To solve this inconvenience, we decided to plot the individual values as a scatter plot and observe whether the individual values followed the tendency of the proportional and the TMFG thresholding techniques. It is important to remark that graph metrics using the absolute thresholding show a tendency resembling to the proportional ones, especially when fewer links are considered in the correlation matrices. This affirmation does not apply to the clustering coefficient and the transitivity, where the values obtained from the absolute thresholding follow a completely different behaviour. In addition, since scatter plots represent individual values, both in $r \geq 0.5$ and in $r \geq 0.7$, a high variability is found not only on the graph metrics calculated but also in the number of links included.

Overall, as a general trend, we observed that the proportional threshold preserves the number of links used to create the graphs. In studies with a group comparison approach where two groups are used, it is undeniable the importance of keeping the number of nodes and the number of edges constant. Many graph measures rely on the degree, so it is important to preserve this characteristic in order to have meaningful comparisons. On the one hand, the proportional thresholding method does not allow to control the lower correlation cutoff and the differences in strength of the included links can also be relevant. On the other hand, the absolute thresholding method sets a determined value as a cutoff point from which correlations will be included, but the number of included links vary significantly from subject to subject. It is also important to mention that an approach where links and correlation values are maintained stable for all the subjects would be ideal but is unachievable because of the individual differences across the subjects. TMFG thresholding methodology could be a suitable solution, where the number of links is preserved and also the structure of the graph composition. Nevertheless, this approach includes lower correlations and may exclude higher correlations from the original matrix when trying to maximize the score function associated with the information retained in the network.

The computed graph variables analysed in this work are the most commonly used to characterize networks as measures of segregation and integration. In this sense, segregation metrics (clustering coefficient, transitivity, modularity) evaluate the brain capacity to functionally split up into different interconnected groups. Integration metrics (characteristic path length, global efficiency) indicate the ability of the brain to merge specialized information

from distributed regions (Rubinov and Sporns, 2010). Finally, the small world is a global measure that combines path length and clustering coefficient and that reveals an optimal flow of information across brain areas.

In addition to the description and interpretation of the different thresholding techniques, a deeper discussion about the graph metrics' interpretation is needed. Regarding the segregation measures, the selected threshold may strongly affect the metrics of interested. Indeed, as mentioned before, since the clustering coefficient is especially influenced by low-degree links, the value of this measure is relatively higher in the TMFG in comparison to the other thresholding methods. This effect is corrected in the transitivity measure and thus the TMFG value is closer to the ones of the proportional and absolute thresholding. In addition, the linear tendency presented in both graph metrics for the absolute thresholding might be explained by the fact that, by fixing an absolute value of correlation, we are losing possible interactions within ROIs and, by extension, the clustering coefficient and the transitivity are lower.

In this regard, modularity is a core attribute of systems in neuroscience which measures the presence of functional communities of densely connected ROIs with hubs that mediate the information flow, bringing a more complex dynamics to the system (Alexander-Bloch et al., 2010). In our work, modularity appears to be a consistent measure through all the three thresholding techniques and shows a decreasing tendency when more links are taken into account. This similar trend for all thresholds is reasonable since, by relaxing the threshold criteria and accepting more links into the network, a stronger overall connectivity is induced despite incorporating weaker links. It is interesting to point out the modularity value obtained with the TMFG thresholding because, despite including only the 6% of the network links, it was able to maximize the modularity. This result increases the interest of using this filtering technique in neuroscience, since fewer links saves substantial computational resources with the reward of a consistent output.

Regarding integration metrics, we observed that the characteristic path length decreases as more links are included in the matrix. This is consistent with the modularity results discussed above. Indeed, a densely connected network increases the ability of the system to communicate with other ROIs, which is translated into a lower characteristic path length. Also, the null model values are expected to be lower because of the random nature of the null model matrix itself. In addition, it is plausible to conjecture that the global efficiency of the system should behave somehow as the inverse of the characteristic path length. Longer paths means that the information needs to travel through several regions before reaching its final destination, which lowers the global efficiency of the network. Also, we note that the null model global efficiency is higher than the subjects', meaning that a random arrangement

of the links enhances the efficiency. However, again, this random distribution is far from describing a high complex system which is a human brain (van den Heuvel et al., 2017).

It is important to remark that all the thresholding techniques have a small–world structure, except some individual cases in absolute thresholding. This small–world structure reflects an optimal stability of functional integration and segregation (Sporns and Honey, 2006). These results confirm that, although the choice of the thresholding technique may vary the graph measure value and thus cause difficult future comparisons, the global network description is not substantially affected. As said before, small–world attributes balance functional integration and segregation, and therefore allow efficient information transmission at low wiring cost. They also reflect a high resilience to random loss of connections (Kaiser et al., 2007) and this indicates that the matrix filtering throughout all the thresholding techniques used in this study is far from random.

Finally, regarding the accuracy analysis, it seems that two and three SD are enough in order to discriminate between those values that get in the confidence interval of the null model's values distribution. The analysis by graph measure may be interesting if different thresholds are applied. Modularity and transitivity seem to behave very differently in the subject's and null model's values, and we can assume that throughout all the thresholds tested in this study, the subject's values will be far away from a random distribution. Moreover, regarding the accuracy per threshold, it is important to highlight that only one of the twelve tested thresholds, the TMFG, classified all the values far from the null model distribution over all the 5 graph metrics compared.

Graph metrics have become very popular to analyse extensive datasets of resting–state fMRI. However, the thresholding choice to clean the original functional interactions has been frequently done in an arbitrary way. Given the dependence of the graph metrics values from the thresholding technique performed (Drakesmith et al., 2015; Garrison et al., 2015; van den Heuvel et al., 2017), the aim of the present work was to study different thresholding methods on weighted connectivity matrices and assess which technique is more adequate to extract functional connectivity measures. Particularly, we investigated three thresholding methods were addressed: absolute thresholding, relative thresholding and TMFG filtered matrices.

In this sense, we conclude that important differences were found between the computed graph measures for the different thresholding techniques. Thus, more studies in this area are needed to fully grasp the impact of this variability. For instance, it is expected to have off–balanced values when extreme thresholding criteria are used, *i.e.*, by including most of the links or very few; or by acting in a very restrictive way when setting a cutoff correlation value. These extreme thresholding values lead to essentially disconnected graphs or strongly connected, almost complete ones (Garrison et al., 2015). However, what is most

important is that these differences in graph metrics are not only found in extreme thresholding values but also when using the most commonly used thresholds. Thus, attention must be paid when choosing the thresholding technique that better suits the acquired data, and also when interpreting results from graph models. Our study demonstrates a high variability in the number of links in absolute thresholding which can directly affect group comparisons. Proportional thresholding techniques seem to be accurate but may not be the best option since values can fall closer to a random distribution. In the last few years, it has also become popular to apply a large range of thresholds to the data (Cao et al., 2020; Song et al., 2014b), but this can lead to misleading results or difficult interpretations. TMFG thresholding methodology has demonstrated, in our study, to be very far from the null model's distribution in all the metrics evaluated. Nevertheless, these results should be replicated.

Summarizing, graph analysis applied to resting-state is a powerful tool to characterize brain networks and make comparisons with healthy and diseased populations. The TMFG thresholding method has shown to be the most stable, less close to the null model and with consistent measures when compared to the other thresholding techniques. Nevertheless, more studies are needed to elucidate a more robust conclusion and caution must be taken into account when choosing the adequate threshold to filter the connectivity matrices, due to the absolute value differences between graph metrics through thresholds.

Limitations of the study

It is worth mentioning some limitations to this study that need to be considered in conjunction with the results. Resting state fMRI data captures low intensity fluctuations of the BOLD signal through time and is viewed as an indirect measure of brain activity. In our study, a unique run of 5 minutes was evaluated for each subject. More runs could have been done in order to figure out the stability of the extracted measures across runs. Nevertheless, Garrison et al. (2015) investigated this aspect and concluded that results were consistent across runs for the absolute and proportional thresholds, when preserving the type of threshold and the preprocessing method.

A second limitation of this study is that analyses were carried out using the cortical and subcortical parcellations of the AAL of 90 ROIs atlas Tzourio-Mazoyer et al. (2002) instead of a larger brain atlas or a voxel-based approach. The voxel-based approach does not assume the a priori parcellation of the brain and may be therefore much more accurate when defining smaller functional units. This is especially useful when studying a neurological disorder (Scheinost et al., 2012) but at the cost of increasing the computational cost and statistical inferences. Consequently, as both approaches are complementary, we decided to simplify the analysis to a 90 ROI brain parcellation.

On a more computational level, more null models and with more iterations could have been done. Finally, more weighted studies comparing thresholding techniques should be done in order to have a confirmation of the results obtained here.

Notwithstanding these limitations, we procured key strengths that must be mentioned. To our knowledge, this is the first study that compares three types of thresholding techniques. Moreover, the sample size of the study is higher than others in the same field and this fact increases the generalization possibilities and decreases the false positives. It is also important to remark that the sample used comprises older population and that some differences may arise when reproducing this study with a broader age population. Finally, our results are in the line of some others already published with healthy populations (Drakesmith et al., 2015; Garrison et al., 2015; van den Heuvel et al., 2017), and the results are similar despite the age differences between samples.

Chapter 8

General discussion

8.1 General discussion

This Thesis approached functional connectivity from two main perspectives, a whole-brain investigation on the one hand and a mesoscopic study in the form of neuronal cultures on the other. Both perspectives are complementary since they provide different yet rich multi-scale information that is relevant when describing the mechanisms that dictate the functioning of living neuronal networks. There is an innate urge for the scientific community to understand how neuronal circuits process the surrounding environment. During the last century, many efforts have been devoted to exploring and understanding the brain, the mechanisms that govern its functions as well as its disorders and syndromes. The path towards this understanding has needed, and will need, the combination of multi-scale approaches, from the simplest neuronal networks up to the brain. Thus, modern neuroscience needs to build bridges across different research domains and disciplines to fully understand how the brain works. Such an effort is conceptually summarized in Figure 8.1.

In this quest to understand the brain, resting state fMRI provides a huge advantage when analysing functional connectivity, because it is a harmless non-invasive technique that does not require ionizing radiation. Additionally, it gives access to both spatial and temporal information at the whole-brain level with a reasonably good resolution. Among all the non-invasive imaging techniques, it is the one with the highest spatial resolution that reaches both cortical and subcortical structures. Finally, it enables to inspect a great variety of brain functions—within the cognitive, emotional and motoric domains— while subjects perform a specific task. The major drawback of the fMRI technique is that the BOLD signal is an indirect measure of neuronal activity that combines spiking activity, local field potentials, glial cell function and vascular smooth muscle cells. Also, the BOLD response can vary across brain regions and is rather slow, which can complicate the analysis of small structures.

In this Thesis, we explored the whole-brain resting state functional connectivity using fMRI recordings of spontaneous brain activity of healthy participants. Specifically, we aimed to disentangle the brain mechanisms of the healthy aging process by distributing the participants in 6 age groups. Our results point towards the direction that the amplitude of low-frequency fluctuations (fALFF) and the regional homogeneity (ReHo) measures are disrupted by aging on specific brain areas. The youngest group presented increased the values of fALFF in the superior temporal gyrus and inferior frontal gyrus, while the oldest group presented higher synchronization (ReHo values) among neighbouring voxels in the hippocampus, the thalamus and the precuneus. Interestingly, the differences observed in brain fluctuations and synchronization did not translate in a change in performance in terms of neuropsychological measures.

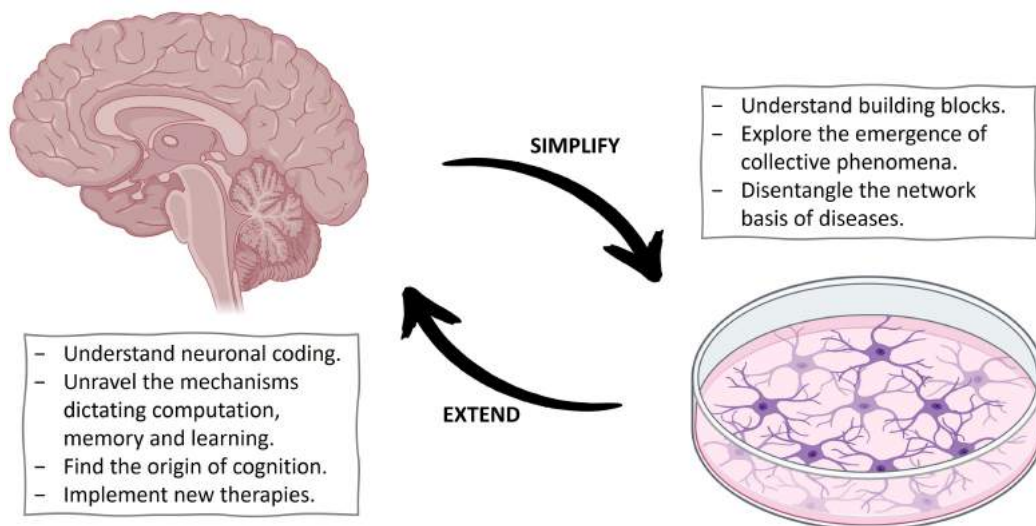


Fig. 8.1 Simplification and expansion processes to understand the brain functioning. Sketch that represents the feedback and feed forward from a whole-brain model to a *in vitro* model and vice-versa.

We hypothesize that some mechanisms, such as resilience due to a higher cognitive reserve or the influence of a compensatory mechanism to offset the functional decrease, may be playing a key role in the brain functioning. All the structures involved in the statistically significant differences between age groups involved the *default mode network* (DMN), a large-scale network that is active when the brain is at rest and not performing any particular task.

Therefore, the description of the whole-brain functioning is a challenging task due to the inherent complexity of the system, so alternative strategies that involve less complexity must come into play. A mesoscopic approach, *i.e.*, a neuronal culture, offers a simplified version of

a complex system with a controlled repertoire of dynamical activations. The implementation of controlled perturbations on a system enables the possibility to modify specific traits and evaluate how these perturbations impact on the dynamical repertoire of the system.

In the present Thesis, we implemented the use of topographical cultures, *i.e.*, homogeneous cultures where neurons are plated on top of a designed structural pattern to modulate their self-organization and the spatiotemporal structure of activity patterns. Topographical cultures have proven to be a valuable tool to tune a simple, yet very interesting, complex system from which we can study the structure-to-function relationship. In our study, spatial constraints promoted by the PDMS reliefs favoured local connectivity and facilitated activity at a microcircuit level, but without suppressing whole-network dynamics. Specifically, we observed that velocity propagation along the *tracks* was five times faster than in the transversal direction. This finding was consistent with computing of the effective connections, which were 8 times more abundant along tracks than transversely to them.

The use of *in vitro* techniques combined with calcium fluorescence imaging is an excellent way to investigate in a controlled manner the emergence of collective behaviour. In a sense, neuronal cultures offer the possibility to understand the building blocks that conform a complex system and how these building blocks assemble to bring to light rich collective behaviour. The interactions between neurons, or groups of neurons, is key to understand the emergent dynamics and functional organization of the whole system. In our study, we explored various dynamic and network traits derived from spontaneous activity, such as the initiation points, propagation velocity or the organization of the network in functional modules, to better understand the organizational features in the neuronal cultures as different spatial constraints were imposed. A richer dynamic repertoire was observed in cultures arranged in interconnected modules —track and square configurations— as compared to non-modular, isotropic configurations, *i.e.*, homogeneous cultures on a flat surface. This broader dynamic repertoire was specially observed at early days of development (DIV 7) until the initial inhomogeneities disappeared after maturation. We note, however, that this effective connectivity did not reflect the underlying structural pathways, although we could coarsely inspect them with immunostaining and, as a complementary approach, explore their impact by running numerical simulations of the patterned networks.

Also, the use of neuronal cultures could be of interest to further understand neurological disorders *in vitro*. The alterations in network activity caused by a specific neuronal disease could be mimicked in a neuronal culture and, afterwards, implement treatments and therapies that may recover the system functionality.

We believe that, by combining a mesoscale approach with the causal techniques applied on the fMRI signal, the scientific community will improve the interpretation of the measures

extracted from human participants. This novel scenario will yield a better understanding on the existing biophysical models that expose the mechanisms underlying higher-level brain functions.

8.2 Limitations of the Thesis

As already stated in the particular discussions, Chapter 6, Section 6.6.1 and Chapter 7, Sections 7.3.1 and 7.3.2, there are some limitations worth mentioning.

Regarding the experiments *in vitro*, one of the limitations was the presence of areas with strongly aggregated neurons and other regions where there were none, due to a lack of homogeneity of the adhesive protein coating. This inhomogeneity was translated in an amplification of the variability of the spatiotemporal fronts. Nonetheless, all studied cultures presented neurons that were fully interconnected and did not present isolated patches.

A second limitation resided on the scale we performed our observations. We decided to analyse cultures with a diameter of 6 mm. The need to record with a wide field of view and the limitation in image resolution made impossible to resolve single cell events. To conclude this part, a last limitation is use of rat primary cultures over human induced pluripotent stem cells (hiPSCs). Indeed, hiPSCs cultures provide a higher individual activity and a richer repertoire of coordinated activations as opposed to rat primary cultures that show a strongly rigid bursting behaviour.

Considering the study of fMRI BOLD signal *in vivo*, an important limitation concerned the size of each age group, which was not entirely homogeneous and with the oldest group containing only 10 participants. Therefore, sample size, distribution and dispersion may introduce a bias in the final results. Secondly, since we did not collect any respiratory or cardiovascular data, we cannot assess the impact of physiological noises that might affect the signal from the brain regions that comprise the DMN (Birn et al., 2006; Chang and Glover, 2009). Also, motion during the data acquisition might affect the results, even if well controlled.

Another limitation arises from the stability of the BOLD signal itself. Since resting state fMRI data captures low intensity fluctuations, it would be interesting to guarantee that these fluctuations are indeed stable through time. More recordings or longer ones could have been done in order to ensure the stability of the extracted measures across runs.

Regarding the preprocessing of the BOLD signal, in the analysis of the threshold filtering techniques we used the cortical and subcortical parcellations of the AAL of 90 ROIs atlas Tzourio-Mazoyer et al. (2002) instead of a larger brain atlas or a voxel-based approach. The latter approach provides a much more accurate analysis of the functional units

but also vastly increases the computational cost. Consequently, as both approaches are complementary, we decided to simplify the analysis to a 90 ROI brain parcellation.

Chapter 9

Conclusions

9.1 Conclusions

1. PDMS topographical modulations provide an interesting approach to impose spatial constraints that enrich the connectivity of *in vitro* neuronal networks, shaping dynamically rich networks in both space and time without finely tuning the position of neurons and axons.
2. The spatial constraints promoted by the PDMS reliefs favoured local connectivity and facilitated activity at a microcircuit level, but without suppressing whole-network dynamics.
3. Effective connectivity, computed from spontaneous activity, has proven to be an adequate tool to describe communication across the neuronal cultures, providing a complementary analysis to the observed dynamical changes in the patterned networks.
4. The effective connectivity extracted from spontaneous activity enabled the understanding of information flow throughout the neuronal culture, but could not infer the structural connections between neurons or groups of neurons.
5. The contrasting velocities of activity propagation in the tracks configuration, with measured velocities about 5 times larger along tracks than across them, is consistent with the fact that effective connections, extracted from activity data, were about 8 times more abundant along tracks than across them.
6. Some of the explored cultures tended to become more integrated and with increasingly stronger network-wide bursting as they matured, suggesting that the initially imprinted

inhomogeneities were erased at long term. This loss of richness was particularly strong in the square's configuration.

7. A mesoscopic approach that focuses on the alterations of the network collective activity may be of interest for those studies that use neuronal cultures as models for neurological disorders *in vitro*.
8. fMRI and graph analysis granted the extraction of functional network traits that help to understand the aging process in a healthy population.
9. The filtering technique applied to the correlation matrices had a significant impact on the computed network functional features, such as clustering coefficient or global efficiency.
10. The TMFG thresholding method has shown to be the most stable, furthest to the null model, *i.e.*, random values due to signal fluctuations or noise, and with consistent measures when comparing to the other filtering techniques. Since TMFG preserved the overall links between participants, and thus the matrix structure, it enabled the possibility to perform transversal analysis.
11. All three filtering techniques captured a small-world structure of the brain network, and thus a consistent measure of modularity, which means that the integration-segregation balance was preserved.
12. fALFF (amplitude of low-frequency fluctuations) and ReHo (Regional homogeneity) have proven to be valuable tools to discern functional brain changes in short age intervals through healthy aging.
13. fALFF analysis showed significant differences at the superior temporal gyrus and the inferior frontal gyrus between groups involving the youngest and oldest participants, being the former the ones with increased values of fALFF.
14. The most significant differences in fALFF signal were found between Group 1 (< 60 years old) and Group 5 (75 – 79 years old), instead than with the oldest group. This could reveal a survival mechanism, meaning that the participants of Group 6 would have a high degree of cognitive reserve and thus, higher resilience.
15. ReHo analysis found significant differences between all age groups and the oldest one, which had increased ReHo values. Group 6 showed higher synchronization between neighbouring voxels, specially at the hippocampus, a vulnerable structure that changes with age.

16. Increased ReHo values of the oldest group were also reported in a cluster comprising regions of the prefrontal cortex, a brain area commonly related to difficulties in late-stage sequence learning.
17. A correlation analysis spotted a clear relationship between age and neuroimaging signal. Regional synchronization increases with age, while low-frequency fluctuations and grey matter volume decrease.
18. The complementary use of fMRI measurements and non-invasive brain stimulation techniques would be a qualitative improvement to fully understand the interaction of the underlying plasticity mechanisms (network structure) with the functional evolution of the brain.

References

- Abellaneda-Pérez, K., Vaqué-Alcázar, L., Solé-Padullés, C., and Bartrés-Faz, D. (2022). Combining non-invasive brain stimulation with functional magnetic resonance imaging to investigate the neural substrates of cognitive aging. *Journal of neuroscience research*, 100(5):1159–1170.
- Achard, S., Salvador, R., Whitcher, B., Suckling, J., and Bullmore, E. (2006). A resilient, low-frequency, small-world human brain functional network with highly connected association cortical hubs. *Journal of Neuroscience*, 26(1):63–72.
- Aebbersold, M. J., Dermutz, H., Forró, C., Weydert, S., Thompson-Steckel, G., Vörös, J., and Demkó, L. (2016). “brains on a chip”: Towards engineered neural networks. *TrAC Trends in Analytical Chemistry*, 78:60–69.
- Alexander-Bloch, A. F., Gogtay, N., Meunier, D., Birn, R., Clasen, L., Lalonde, F., Lenroot, R., Giedd, J., and Bullmore, E. T. (2010). Disrupted modularity and local connectivity of brain functional networks in childhood-onset schizophrenia. *Frontiers in systems neuroscience*, 4:147.
- Alon, U. (2007). Network motifs: theory and experimental approaches. *Nature Reviews Genetics*, 8(6):450–461.
- Alvarez-Lacalle, E. and Moses, E. (2009). Slow and fast pulses in 1-d cultures of excitatory neurons. *Journal of computational neuroscience*, 26:475–493.
- Ashburner, J. (2007). A fast diffeomorphic image registration algorithm. *Neuroimage*, 38(1):95–113.
- Ashburner, J. and Friston, K. J. (2005). Unified segmentation. *Neuroimage*, 26(3):839–851.
- Association, A. P. et al. (2017). Older adults’ health and age-related changes: Reality versus myth [internet]. *Washington, DC: Office of Public Communications*.
- Aurich, N. K., Alves Filho, J. O., Marques da Silva, A. M., and Franco, A. R. (2015). Evaluating the reliability of different preprocessing steps to estimate graph theoretical measures in resting state fmri data. *Frontiers in neuroscience*, 9:48.
- Ayasreh, S., Jurado, I., López-León, C. F., Montalà-Flaquer, M., and Soriano, J. (2022). Dynamic and functional alterations of neuronal networks in vitro upon physical damage: A proof of concept. *Micromachines*, 13(12):2259.
- Bang, S., Na, S., Jang, J. M., Kim, J., and Jeon, N. L. (2015). Engineering-aligned 3d neural circuit in microfluidic device. *Advanced Healthcare Materials*, 5(1):159–166.

- Barabási, A.-L. and Albert, R. (1999). Emergence of scaling in random networks. *science*, 286(5439):509–512.
- Barabási, A.-L. and Bonabeau, E. (2003). Scale-free networks. *Scientific american*, 288(5):60–69.
- Barrat, A., Barthelemy, M., and Vespignani, A. (2008). *Dynamical processes on complex networks*. Cambridge university press.
- Bartrés-Faz, D., Serra-Grabulosa, J. M., Sun, F. T., Solé-Padullés, C., Rami, L., Molinuevo, J. L., Bosch, B., Mercader, J. M., Bargalló, N., Falcón, C., et al. (2008). Functional connectivity of the hippocampus in elderly with mild memory dysfunction carrying the apoe ϵ 4 allele. *Neurobiology of Aging*, 29(11):1644–1653.
- Baruchi, I., Volman, V., Raichman, N., Shein, M., and Ben-Jacob, E. (2008). The emergence and properties of mutual synchronization in in vitro coupled cortical networks. *European Journal of Neuroscience*, 28(9):1825–1835.
- Bassett, D. S. and Sporns, O. (2017). Network neuroscience. *Nature neuroscience*, 20:353–364.
- Basso, J. M. V., Yurchenko, I., Simon, M., Rizzo, D. J., and Staii, C. (2019). Role of geometrical cues in neuronal growth. *Physical Review E*, 99(2):022408.
- Bastian, M., Heymann, S., and Jacomy, M. (2009). Gephi: an open source software for exploring and manipulating networks. *Proceedings of the international AAAI conference on web and social media*, 3(1):361–362.
- Battaglia, D., Witt, A., Wolf, F., and Geisel, T. (2012). Dynamic effective connectivity of inter-areal brain circuits. *PLoS computational biology*, 8(3):e1002438.
- Beggs, J. M. and Plenz, D. (2003). Neuronal avalanches in neocortical circuits. *Journal of neuroscience*, 23(35):11167–11177.
- Beggs, J. M. and Plenz, D. (2004). Neuronal avalanches are diverse and precise activity patterns that are stable for many hours in cortical slice cultures. *Journal of neuroscience*, 24(22):5216–5229.
- Ben-Ari, Y. (2001). Developing networks play a similar melody. *Trends in neurosciences*, 24(6):353–360.
- Benjamini, Y. and Hochberg, Y. (1995). Controlling the false discovery rate: a practical and powerful approach to multiple testing. *Journal of the Royal statistical society: series B (Methodological)*, 57(1):289–300.
- Bennett, I. J., Madden, D. J., Vaidya, C. J., Howard Jr, J. H., and Howard, D. V. (2011). White matter integrity correlates of implicit sequence learning in healthy aging. *Neurobiology of aging*, 32(12):2317–e1.
- Berridge, M. J., Lipp, P., and Bootman, M. D. (2000). The versatility and universality of calcium signalling. *Nature reviews Molecular cell biology*, 1(1):11–21.

- Bijsterbosch, J., Smith, S. M., and Beckmann, C. F. (2017). *Introduction to Resting State fMRI Functional Connectivity*. Oxford: Oxford University Press.
- Birn, R. M., Diamond, J. B., Smith, M. A., and Bandettini, P. A. (2006). Separating respiratory-variation-related fluctuations from neuronal-activity-related fluctuations in fmri. *Neuroimage*, 31(4):1536–1548.
- Birn, R. M., Smith, M. A., Jones, T. B., and Bandettini, P. A. (2008). The respiration response function: the temporal dynamics of fmri signal fluctuations related to changes in respiration. *Neuroimage*, 40(2):644–654.
- Bisio, M., Bosca, A., Pasquale, V., Berdondini, L., and Chiappalone, M. (2014). Emergence of bursting activity in connected neuronal sub-populations. *PloS one*, 9(9):e107400.
- Biswal, B., Zerrin Yetkin, F., Haughton, V. M., and Hyde, J. S. (1995). Functional connectivity in the motor cortex of resting human brain using echo-planar mri. *Magnetic resonance in medicine*, 34(4):537–541.
- Blamire, A. M., Ogawa, S., Ugurbil, K., Rothman, D., McCarthy, G., Ellermann, J. M., Hyder, F., Rattner, Z., and Shulman, R. G. (1992). Dynamic mapping of the human visual cortex by high-speed magnetic resonance imaging. *Proceedings of the National Academy of Sciences*, 89(22):11069–11073.
- Blankenship, A. G. and Feller, M. B. (2010). Mechanisms underlying spontaneous patterned activity in developing neural circuits. *Nature Reviews Neuroscience*, 11(1):18–29.
- Blazer, D. G., Yaffe, K., and Karlawish, J. (2015). Cognitive aging: a report from the institute of medicine. *Jama*, 313(21):2121–2122.
- Blondel, V. D., Guillaume, J.-L., Lambiotte, R., and Lefebvre, E. (2008). Fast unfolding of communities in large networks. *Journal of statistical mechanics: Theory and experiment*, pages 1–12.
- Boccaletti, S., Latora, V., Moreno, Y., Chavez, M., and Hwang, D. (2006). Complex networks: Structure and dynamics. *Physics Reports*, 424:175–308.
- Bonifazi, P., Difato, F., Massobrio, P., Breschi, G. L., Pasquale, V., Levi, T., Goldin, M., Bornat, Y., Tedesco, M., Bisio, M., et al. (2013). In vitro large-scale experimental and theoretical studies for the realization of bi-directional brain-prostheses. *Frontiers in neural circuits*, 7:40.
- Bonifazi, P., Goldin, M., Picardo, M. A., Jorquera, I., Cattani, A., Bianconi, G., Represa, A., Ben-Ari, Y., and Cossart, R. (2009). Gabaergic hub neurons orchestrate synchrony in developing hippocampal networks. *Science*, 326(5958):1419–1424.
- Bowen, H. J., Ford, J. H., Grady, C. L., and Spaniol, J. (2020). Frontostriatal functional connectivity supports reward-enhanced memory in older adults. *Neurobiology of Aging*, 90:1–12.
- Breskin, I., Soriano, J., Moses, E., and Tlusty, T. (2006). Percolation in living neural networks. *Physical review letters*, 97(18):188102.

- Bressler, S. L. (1995). Large-scale cortical networks and cognition. *Brain Research Reviews*, 20(3):288–304.
- Bressloff, P. C. (2000). Traveling waves and pulses in a one-dimensional network of excitable integrate-and-fire neurons. *Journal of Mathematical Biology*, 40:169–198.
- Brett, M., Penny, W., and Kiebel, S. (2003). Introduction to random field theory. *Human brain function*, 2:867–879.
- Brofiga, M., Pisano, M., Raiteri, R., and Massobrio, P. (2021). On the road to the brain-on-a-chip: a review on strategies, methods, and applications. *Journal of Neural Engineering*, 18(4):041005.
- Brooks, S. V. and Faulkner, J. A. (1994). Skeletal muscle weakness in old age: underlying mechanisms. *Medicine and science in sports and exercise*, 26(4):432–439.
- Buckner, R. L., Sepulcre, J., Talukdar, T., Krienen, F. M., Liu, H., Hedden, T., Andrews-Hanna, J. R., Sperling, R. A., and Johnson, K. A. (2009). Cortical hubs revealed by intrinsic functional connectivity: mapping, assessment of stability, and relation to alzheimer’s disease. *Journal of neuroscience*, 29(6):1860–1873.
- Bullmore, E. and Sporns, O. (2012). The economy of brain network organization. *Nature reviews neuroscience*, 13(5):336–349.
- Buzsaki, G. and Draguhn, A. (2004). Neuronal oscillations in cortical networks. *science*, 304(5679):1926–1929.
- Cao, C. and Slobounov, S. (2009). Alteration of cortical functional connectivity as a result of traumatic brain injury revealed by graph theory, ica, and sloreta analyses of eeg signals. *IEEE Transactions on Neural Systems and Rehabilitation Engineering*, 18(1):11–19.
- Cao, H., Chung, Y., McEwen, S. C., Bearden, C. E., Addington, J., Goodyear, B., Cadenhead, K. S., Mirzakhani, H., Cornblatt, B. A., Carrion, R., et al. (2020). Progressive reconfiguration of resting-state brain networks as psychosis develops: Preliminary results from the north american prodrome longitudinal study (napls) consortium. *Schizophrenia research*, 226:30–37.
- Cao, M., Wang, J.-H., Dai, Z.-J., Cao, X.-Y., Jiang, L.-L., Fan, F.-M., Song, X.-W., Xia, M.-R., Shu, N., Dong, Q., et al. (2014). Topological organization of the human brain functional connectome across the lifespan. *Developmental cognitive neuroscience*, 7:76–93.
- Carola, G., Malagarriga, D., Calatayud, C., Pons-Espinal, M., Blasco-Agell, L., Richaud-Patin, Y., Fernandez-Carasa, I., Baruffi, V., Beltramone, S., Molina, E., et al. (2021). Parkinson’s disease patient-specific neuronal networks carrying the lrrk2 g2019s mutation unveil early functional alterations that predate neurodegeneration. *npj Parkinson’s Disease*, 7(1):55.
- Cha, J., Hwang, J.-M., Jo, H. J., Seo, S. W., Na, D. L., Lee, J.-M., et al. (2015). Assessment of functional characteristics of amnesic mild cognitive impairment and alzheimer’s disease using various methods of resting-state fmri analysis. *BioMed research international*, 2015.

- Chang, C. and Glover, G. H. (2009). Relationship between respiration, end-tidal co₂, and bold signals in resting-state fmri. *Neuroimage*, 47(4):1381–1393.
- Chen, J. J. (2019). Functional mri of brain physiology in aging and neurodegenerative diseases. *Neuroimage*, 187:209–225.
- Chen, T.-W., Wardill, T. J., Sun, Y., Pulver, S. R., Renninger, S., Baohan, A., Schreiter, E. R., Kerr, R. A., Orger, M. B., Jayaraman, V., Looger, L. L., Svoboda, K., and Kim, D. S. (2013). Ultra-sensitive fluorescent proteins for imaging neuronal activity. *Nature*.
- Chen, X., Lu, B., and Yan, C.-G. (2018). Reproducibility of r-fmri metrics on the impact of different strategies for multiple comparison correction and sample sizes. *Human brain mapping*, 39(1):300–318.
- Chiappalone, M., Pasquale, V., and Frega, M. (2019). *In vitro neuronal networks: From culturing methods to neuro-technological applications*, volume 22. Springer.
- Christensen, A. P. (2018). Networktoolbox: Methods and measures for brain, cognitive, and psychometric network analysis in r. *R J.*, 10(2):422.
- Cohen, E., Ivenshitz, M., Amor-Baroukh, V., Greenberger, V., and Segal, M. (2008a). Determinants of spontaneous activity in networks of cultured hippocampus. *Brain research*, 1235:21–30.
- Cohen, E., Ivenshitz, M., Amor-Baroukh, V., Greenberger, V., and Segal, M. (2008b). Determinants of spontaneous activity in networks of cultured hippocampus. *Brain research*, 1235:21–30.
- Cohen, J. (1988). *Statistical power analysis for the behavioral sciences*. Lawrence Erlbaum Associates, Hillsdale, NJ.
- Cohen, J. R. and D’Esposito, M. (2016). The segregation and integration of distinct brain networks and their relationship to cognition. *The Journal of neuroscience: the official journal of the Society for Neuroscience*, 36 48:12083–12094.
- Corlew, R., Bosma, M. M., and Moody, W. J. (2004). Spontaneous, synchronous electrical activity in neonatal mouse cortical neurones. *The journal of physiology*, 560 Pt 2:377–90.
- Czarnecki, A., Tschertter, A., and Streit, J. (2012). Network activity and spike discharge oscillations in cortical slice cultures from neonatal rat. *European journal of neuroscience*, 35(3):375–388.
- Dahlgren, K. N., Manelli, A. M., Stine, W. B., Baker, L. K., Krafft, G. A., and LaDu, M. J. (2002). Oligomeric and fibrillar species of amyloid- β peptides differentially affect neuronal viability. *Journal of Biological Chemistry*, 277(35):32046–32053.
- Damasio, A. R. (1989). The brain binds entities and events by multiregional activation from convergence zones. *Neural computation*, 1(1):123–132.
- Damoiseaux, J. S. (2012). Resting-state fmri as a biomarker for alzheimer’s disease? *Alzheimer’s research & therapy*, 4:1–2.

- Damoiseaux, J. S. (2017). Effects of aging on functional and structural brain connectivity. *Neuroimage*, 160:32–40.
- Damoiseaux, J. S., Beckmann, C., Arigita, E. S., Barkhof, F., Scheltens, P., Stam, C., Smith, S., and Rombouts, S. (2008). Reduced resting-state brain activity in the “default network” in normal aging. *Cerebral cortex*, 18(8):1856–1864.
- Dauth, S., Maoz, B. M., Sheehy, S. P., Hemphill, M. A., Murty, T., Macedonia, M. K., Greer, A. M., Budnik, B., and Parker, K. K. (2017). Neurons derived from different brain regions are inherently different in vitro: a novel multiregional brain-on-a-chip. *Journal of neurophysiology*, 117(3):1320–1341.
- Dawson Ted M., Golde Todd E., L.-T. C. (2018). Animal models of neurodegenerative diseases. *Nature neuroscience*, 21:1370–1379.
- de No, R. L. and Fulton, J. F. (1938). *Architectonics and structure of the cerebral cortex*. Oxford University Press.
- de Santos-Sierra, D., Sendina-Nadal, I., Leyva, I., Almendral, J. A., Anava, S., Ayali, A., Papo, D., and Boccaletti, S. (2014). Emergence of small-world anatomical networks in self-organizing clustered neuronal cultures. *PloS one*, 9(1):e85828.
- Deco, G. and Jirsa, V. K. (2012). Ongoing cortical activity at rest: criticality, multistability, and ghost attractors. *Journal of Neuroscience*, 32(10):3366–3375.
- Deco, G., Jirsa, V. K., and McIntosh, A. R. (2010). Emerging concepts for the dynamical organization of resting-state activity in the brain. *Nature reviews neuroscience*, 12:43–56.
- Deco, G., Jirsa, V. K., and McIntosh, A. R. (2011). Emerging concepts for the dynamical organization of resting-state activity in the brain. *Nature reviews neuroscience*, 12(1):43–56.
- Deco, G., Jirsa, V. K., Robinson, P. A., Breakspear, M., and Friston, K. J. (2008). The dynamic brain: From spiking neurons to neural masses and cortical fields. *PLoS Computational Biology*, 4:861–870.
- Deco, G., Tononi, G., Boly, M., and Kringelbach, M. (2015). Rethinking segregation and integration: Contributions of whole-brain modelling. *Nature reviews neuroscience*, 16:430–9.
- DeFelipe, J. (2011). The evolution of the brain, the human nature of cortical circuits, and intellectual creativity. *Frontiers in Neuroanatomy*, 5:29.
- DeFelipe, J., Markram, H., and Rockland, K. S. (2012). The neocortical column. *Frontiers in neuroanatomy*, 6:22.
- Deitcher, Y., Eyal, G., Kanari, L., Verhoog, M. B., Kahou, G. A. A., Mansvelder, H. D., de Kock, C. P. J., and Segev, I. (2017). Comprehensive morpho-electrotonic analysis shows 2 distinct classes of I2 and I3 pyramidal neurons in human temporal cortex. *Cerebral cortex*.

- Deng, S., Franklin, C. G., O'Boyle, M., Zhang, W., Heyl, B. L., Jerabek, P. A., Lu, H., and Fox, P. T. (2022). Hemodynamic and metabolic correspondence of resting-state voxel-based physiological metrics in healthy adults. *Neuroimage*, 250:118923.
- Dennis, E. L. and Thompson, P. M. (2014). Functional brain connectivity using fmri in aging and alzheimer's disease. *Neuropsychology review*, 24:49–62.
- Dichter, M. A. (1978). Rat cortical neurons in cell culture: culture methods, cell morphology, electrophysiology, and synapse formation. *Brain research*, 149(2):279–293.
- Dorogovtsev, S. N. and Mendes, J. F. (2003). *Evolution of networks: From biological nets to the Internet and WWW*. Oxford university press.
- Downes, J. H., Hammond, M. W., Xydas, D., Spencer, M. C., Becerra, V. M., Warwick, K., Whalley, B. J., and Nasuto, S. J. (2012). Emergence of a small-world functional network in cultured neurons. *PLoS computational biology*, 8(5):e1002522.
- Drakesmith, M., Caeyenberghs, K., Dutt, A., Lewis, G., David, A., and Jones, D. K. (2015). Overcoming the effects of false positives and threshold bias in graph theoretical analyses of neuroimaging data. *Neuroimage*, 118:313–333.
- Dvorak, D., Radwan, B., Sparks, F. T., Talbot, Z. N., and Fenton, A. A. (2018). Control of recollection by slow gamma dominating mid-frequency gamma in hippocampus ca1. *PLoS Biology*, 16(1):e2003354.
- Eckmann, J.-P., Feinerman, O., Gruendlinger, L., Moses, E., Soriano, J., and Tlusty, T. (2007). The physics of living neural networks. *Physics Reports*, 449(1-3):54–76.
- Eckmann, J.-P., Jacobi, S., Marom, S., Moses, E., and Zbinden, C. (2008). Leader neurons in population bursts of 2d living neural networks. *New Journal of Physics*, 10(1):015011.
- Eckmann, J.-P., Moses, E., Stetter, O., Tlusty, T., and Zbinden, C. (2010). Leaders of neuronal cultures in a quorum percolation model. *Frontiers in computational neuroscience*, 4:132.
- Eklund, A., Nichols, T. E., and Knutsson, H. (2016). Cluster failure: Why fmri inferences for spatial extent have inflated false-positive rates. *Proceedings of the national academy of sciences*, 113(28):7900–7905.
- Emiliani, V., Cohen, A. E., Deisseroth, K., and Häusser, M. (2015). All-optical interrogation of neural circuits. *Journal of Neuroscience*, 35(41):13917–13926.
- Estévez-Priego, E., Teller, S., Granell, C., Arenas, A., and Soriano, J. (2020). Functional strengthening through synaptic scaling upon connectivity disruption in neuronal cultures. *Network Neuroscience*, 4(4):1160–1180.
- Eyal, G., Verhoog, M. B., Testa-Silva, G., Deitcher, Y., Lodder, J. C., Benavides-Piccione, R., Morales, J. I., DeFelipe, J., de Kock, C. P. J., Mansvelder, H. D., and Segev, I. (2016). Unique membrane properties and enhanced signal processing in human neocortical neurons. *eLife*.
- Eytan, D. and Marom, S. (2006). Dynamics and effective topology underlying synchronization in networks of cortical neurons. *Journal of Neuroscience*, 26(33):8465–8476.

- Faci-Lázaro, S., Soriano, J., and Gómez-Gardeñes, J. (2019). Impact of targeted attack on the spontaneous activity in spatial and biologically-inspired neuronal networks. *Chaos: An Interdisciplinary Journal of Nonlinear Science*, 29(8):083126.
- Fan, J., Meng, J., Ludescher, J., Chen, X., Ashkenazy, Y., Kurths, J., Havlin, S., and Schellnhuber, H. J. (2021). Statistical physics approaches to the complex earth system. *Physics reports*, 896:1–84.
- Farahani, F. V., Karwowski, W., and Lighthall, N. R. (2019). Application of graph theory for identifying connectivity patterns in human brain networks: a systematic review. *frontiers in Neuroscience*, 13:585.
- Farras-Permanyer, L., Mancho-Fora, N., Montalà-Flaquer, M., Bartrés-Faz, D., Vaqué-Alcázar, L., Peró-Cebollero, M., and Guàrdia-Olmos, J. (2019). Age-related changes in resting-state functional connectivity in older adults. *Neural regeneration research*, 14(9):1544.
- Farràs-Permanyer, L., Mancho-Fora, N., Montalà-Flaquer, M., Gudayol-Ferré, E., Gallardo-Moreno, G. B., Zarabozo-Hurtado, D., Villuendas-González, E., Peró-Cebollero, M., and Guàrdia-Olmos, J. (2019). Estimation of brain functional connectivity in patients with mild cognitive impairment. *Brain Sciences*, 9(12):350.
- Feinerman, O. and Moses, E. (2003). A picoliter ‘fountain-pen’ using co-axial dual pipettes. *Journal of neuroscience methods*, 127(1):75–84.
- Feinerman, O., Segal, M., and Moses, E. (2005). Signal propagation along unidimensional neuronal networks. *Journal of neurophysiology*, 94(5):3406–3416.
- Feinerman, O., Segal, M., and Moses, E. (2007). Identification and dynamics of spontaneous burst initiation zones in unidimensional neuronal cultures. *Journal of neurophysiology*, 97(4):2937–2948.
- Feldt, S., Bonifazi, P., and Cossart, R. (2011). Dissecting functional connectivity of neuronal microcircuits: experimental and theoretical insights. *Trends in neurosciences*, 34(5):225–236.
- Fernández-García, S., Orlandi, J. G., García-Díaz Barriga, G., Rodríguez, M., Masana, M., Soriano, J., and Alberch, J. (2020). Deficits in coordinated neuronal activity and network topology are striatal hallmarks in huntington’s disease. *BMC biology*, 18(1):1–16.
- Finc, K., Bonna, K., He, X., Lydon-Staley, D. M., Kühn, S., Duch, W., and Bassett, D. S. (2020). Dynamic reconfiguration of functional brain networks during working memory training. *Nature communications*, 11(1):2435.
- Fjell, A. M., McEvoy, L., Holland, D., Dale, A. M., Walhovd, K. B., Initiative, A. D. N., et al. (2014). What is normal in normal aging? effects of aging, amyloid and alzheimer’s disease on the cerebral cortex and the hippocampus. *Progress in neurobiology*, 117:20–40.
- Fjell, A. M. and Walhovd, K. B. (2010). Structural brain changes in aging: courses, causes and cognitive consequences. *Reviews in the Neurosciences*, 21(3):187–222.

- Fjell, A. M., Walhovd, K. B., Fennema-Notestine, C., McEvoy, L. K., Hagler, D. J., Holland, D., Brewer, J. B., and Dale, A. M. (2009). One-year brain atrophy evident in healthy aging. *Journal of Neuroscience*, 29(48):15223–15231.
- Folstein, M. F., Folstein, S. E., and McHugh, P. R. (1975). “mini-mental state”: a practical method for grading the cognitive state of patients for the clinician. *Journal of psychiatric research*, 12(3):189–198.
- Fornito, A., Zalesky, A., and Bullmore, E. (2016). *Fundamentals of brain network analysis*. Academic press.
- Fornito, A., Zalesky, A., and Bullmore, E. T. (2010). Network scaling effects in graph analytic studies of human resting-state fmri data. *Frontiers in systems neuroscience*, 4:1373.
- Forró, C., Thompson-Steckel, G., Weaver, S., Weydert, S., Ihle, S., Dermutz, H., Aebersold, M. J., Pilz, R., Demkó, L., and Vörös, J. (2018). Modular microstructure design to build neuronal networks of defined functional connectivity. *Biosensors and Bioelectronics*, 122:75–87.
- Fox, M. and Greicius, M. (2010). Clinical applications of resting state functional connectivity. *Frontiers in systems neuroscience*, 4:19.
- Fox, M. D. and Raichle, M. E. (2007). Spontaneous fluctuations in brain activity observed with functional magnetic resonance imaging. *Nature reviews neuroscience*, 8(9):700–711.
- Frega, M., Pasquale, V., Tedesco, M., Marcoli, M., Contestabile, A., Nanni, M., Bonzano, L., Maura, G., and Chiappalone, M. (2012). Cortical cultures coupled to micro-electrode arrays: a novel approach to perform in vitro excitotoxicity testing. *Neurotoxicology and teratology*, 34(1):116–127.
- Friedrich, J., Zhou, P., Paninski, L., Staneva, V., Chklovskii, D., and Pnevmatikakis, E. (2017). Fast online deconvolution of calcium imaging data. *PLOS Computational Biology*, 13(3):e1005423.
- Friston, K. J. (1997). Imaging cognitive anatomy. *Trends in cognitive sciences*, 1(1):21–27.
- Friston, K. J. (2009). Modalities, modes, and models in functional neuroimaging. *Science*, 326(5951):399–403.
- Friston, K. J. (2011). Functional and effective connectivity: a review. *Brain connectivity*, 1(1):13–36.
- Friston, K. J., Williams, S., Howard, R., Frackowiak, R. S., and Turner, R. (1996). Movement-related effects in fmri time-series. *Magnetic resonance in medicine*, 35(3):346–355.
- Gabay, T., Jakobs, E., Ben-Jacob, E., and Hanein, Y. (2005). Engineered self-organization of neural networks using carbon nanotube clusters. *Physica A: Statistical Mechanics and its Applications*, 350(2-4):611–621.
- Galiano, A., Mengual, E., García de Eulate, R., Galdeano, I., Vidorreta, M., Recio, M., Riverol, M., Zubieta, J. L., and Fernández-Seara, M. A. (2020). Coupling of cerebral blood flow and functional connectivity is decreased in healthy aging. *Brain imaging and behavior*, 14:436–450.

- Gao, Y., Wang, X., Xiong, Z., Ren, H., Liu, R., Wei, Y., and Li, D. (2021). Abnormal fractional amplitude of low-frequency fluctuation as a potential imaging biomarker for first-episode major depressive disorder: a resting-state fmri study and support vector machine analysis. *Frontiers in neurology*, 12:751400.
- Garrison, K. A., Scheinost, D., Finn, E. S., Shen, X., and Constable, R. T. (2015). The (in) stability of functional brain network measures across thresholds. *Neuroimage*, 118:651–661.
- Geerligs, L., Renken, R. J., Saliassi, E., Maurits, N. M., and Lorist, M. M. (2015). A brain-wide study of age-related changes in functional connectivity. *Cerebral cortex*, 25(7):1987–1999.
- Geerligs, L., Tsvetanov, K. A., and Henson, R. N. (2017). Challenges in measuring individual differences in functional connectivity using fmri: the case of healthy aging. *Human brain mapping*, 38(8):4125–4156.
- Genovese, C. R., Lazar, N. A., and Nichols, T. (2002). Thresholding of statistical maps in functional neuroimaging using the false discovery rate. *Neuroimage*, 15(4):870–878.
- Gevens, A., Brickett, P., Costales, B., Le, J., and Reutter, B. (1990). Beyond topographic mapping: towards functional-anatomical imaging with 124-channel eegs and 3-d mris. *Brain topography*, 3(1):53–64.
- Gladkov, A., Pigareva, Y., Kutyina, D., Kolpakov, V., Bukatin, A., Mukhina, I., Kazantsev, V., and Pimashkin, A. (2017). Design of cultured neuron networks in vitro with predefined connectivity using asymmetric microfluidic channels. *Scientific reports*, 7(1):15625.
- Gobel, W. and Helmchen, F. (2007). In vivo calcium imaging of neural network function. *Physiology*, 22(6):358–365.
- Goldman-Rakic, P., Chafee, M., and Friedman, H. (1993). Allocation of function in distributed circuits. *Brain mechanisms of perception and memory: From neuron to behavior*, pages 445–456.
- Golomb, D. and Ermentrout, G. B. (1999). Continuous and lurching traveling pulses in neuronal networks with delay and spatially decaying connectivity. *Proceedings of the National Academy of Sciences*, 96(23):13480–13485.
- Gong, G., He, Y., Concha, L., Lebel, C., Gross, D. W., Evans, A. C., and Beaulieu, C. (2009). Mapping anatomical connectivity patterns of human cerebral cortex using in vivo diffusion tensor imaging tractography. *Cerebral cortex*, 19(3):524–536.
- Goodglass, H., Kaplan, E., Weintraub, S., et al. (1983). Boston naming test.
- Gorges, M., Müller, H.-P., Ludolph, A. C., Rasche, V., Kassubek, J., et al. (2014). Intrinsic functional connectivity networks in healthy elderly subjects: a multiparametric approach with structural connectivity analysis. *BioMed research international*, 2014.
- Greicius, M. D., Krasnow, B., Reiss, A. L., and Menon, V. (2003). Functional connectivity in the resting brain: a network analysis of the default mode hypothesis. *Proceedings of the national academy of sciences*, 100(1):253–258.

- Greicius, M. D., Srivastava, G., Reiss, A. L., and Menon, V. (2004). Default-mode network activity distinguishes alzheimer's disease from healthy aging: evidence from functional mri. *Proceedings of the National Academy of Sciences*, 101(13):4637–4642.
- Greig, L. C. C., Woodworth, M. B., Galazo, M. J., Padmanabhan, H., and Macklis, J. D. (2013). Molecular logic of neocortical projection neuron specification, development and diversity. *Nature Reviews Neuroscience*, 14:755–769.
- Grewe, B. F., Langer, D., Kasper, H., Kampa, B. M., and Helmchen, F. (2010). High-speed in vivo calcium imaging reveals neuronal network activity with near-millisecond precision. *Nature methods*, 7(5):399–405.
- Grienberger, C. and Konnerth, A. (2012). Imaging calcium in neurons. *Neuron*, 73(5):862–885.
- Grigorov, M. G. (2005). Global properties of biological networks. *Drug discovery today*, 10(5):365–372.
- Grober, E. and Buschke, H. (1987). Genuine memory deficits in dementia. *Developmental neuropsychology*, 3(1):13–36.
- Gross, G. W. and Kowalski, J. M. (1999). Origins of activity patterns in self-organizing neuronal networks in vitro. *Journal of Intelligent Material Systems and Structures*, 10(7):558–564.
- Habets, A., Van Dongen, A., Van Huizen, F., and Corner, M. (1987). Spontaneous neuronal firing patterns in fetal rat cortical networks during development in vitro: a quantitative analysis. *Experimental brain research*, 69:43–52.
- Hagmann, P., Cammoun, L., Gigandet, X., Meuli, R., Honey, C. J., Wedeen, V. J., and Sporns, O. (2008). Mapping the structural core of human cerebral cortex. *PLoS biology*, 6(7):e159.
- Ham, M. I., Bettencourt, L. M., McDaniel, F. D., and Gross, G. W. (2008). Spontaneous coordinated activity in cultured networks: analysis of multiple ignition sites, primary circuits, and burst phase delay distributions. *Journal of computational neuroscience*, 24:346–357.
- Han, H. (2020). Implementation of bayesian multiple comparison correction in the second-level analysis of fmri data: With pilot analyses of simulation and real fmri datasets based on voxelwise inference. *Cognitive neuroscience*, 11(3):157–169.
- Han, H. and Glenn, A. L. (2018). Evaluating methods of correcting for multiple comparisons implemented in spm12 in social neuroscience fmri studies: an example from moral psychology. *Social neuroscience*, 13(3):257–267.
- Hartley, D. M., Walsh, D. M., Chianping, P. Y., Diehl, T., Vasquez, S., Vassilev, P. M., Teplow, D. B., and Selkoe, D. J. (1999). Protofibrillar intermediates of amyloid β -protein induce acute electrophysiological changes and progressive neurotoxicity in cortical neurons. *Journal of Neuroscience*, 19(20):8876–8884.
- He, Y., Chen, Z. J., and Evans, A. C. (2007). Small-world anatomical networks in the human brain revealed by cortical thickness from mri. *Cerebral cortex*, 17(10):2407–2419.

- He, Y., Wang, J., Wang, L., Chen, Z. J., Yan, C., Yang, H., Tang, H., Zhu, C., Gong, Q., Zang, Y., et al. (2009). Uncovering intrinsic modular organization of spontaneous brain activity in humans. *PloS one*, 4(4):e5226.
- Herculano-Houzel, S. (2009). The human brain in numbers: a linearly scaled-up primate brain. *Frontiers in human neuroscience*, page 31.
- Hernández-Navarro, L., Orlandi, J. G., Cerruti, B., Vives, E. G., and Soriano, J. (2017). Dominance of metric correlations in two-dimensional neuronal cultures described through a random field ising model. *Physical review letters*, 118(20):208101.
- Hilgetag, C.-C., Burns, G. A., O'Neill, M. A., Scannell, J. W., and Young, M. P. (2000). Anatomical connectivity defines the organization of clusters of cortical areas in the macaque and the cat. *Philosophical Transactions of the Royal Society of London. Series B: Biological Sciences*, 355(1393):91–110.
- Hirsiger, S., Koppelmans, V., Mérellat, S., Liem, F., Erdeniz, B., Seidler, R. D., and Jäncke, L. (2016). Structural and functional connectivity in healthy aging: associations for cognition and motor behavior. *Human brain mapping*, 37(3):855–867.
- Holloway, P. M., Willaime-Morawek, S., Siow, R., Barber, M., Owens, R. M., Sharma, A. D., Rowan, W., Hill, E., and Zagnoni, M. (2021). Advances in microfluidic in vitro systems for neurological disease modeling. *Journal of Neuroscience Research*, 99(5):1276–1307.
- Honey, C. J., Kötter, R., Breakspear, M., and Sporns, O. (2007). Network structure of cerebral cortex shapes functional connectivity on multiple time scales. *Proceedings of the National Academy of Sciences*, 104(24):10240–10245.
- Hu, S., Chao, H. H.-A., Zhang, S., Ide, J. S., and Li, C.-S. R. (2014). Changes in cerebral morphometry and amplitude of low-frequency fluctuations of bold signals during healthy aging: correlation with inhibitory control. *Brain Structure and Function*, 219:983–994.
- Huang, C.-C., Hsieh, W.-J., Lee, P.-L., Peng, L.-N., Liu, L.-K., Lee, W.-J., Huang, J.-K., Chen, L.-K., and Lin, C.-P. (2015). Age-related changes in resting-state networks of a large sample size of healthy elderly. *CNS Neuroscience & Therapeutics*, 21(10):817–825.
- Huang, Y. and Mucke, L. (2012). Alzheimer mechanisms and therapeutic strategies. *Cell*, 148(6):1204–1222.
- Humphries, M. D. and Gurney, K. (2008). Network ‘small-world-ness’: a quantitative method for determining canonical network equivalence. *PloS one*, 3(4):e0002051.
- Isaacson, J. S. and Scanziani, M. (2011). How inhibition shapes cortical activity. *Neuron*, 72(2):231–243.
- Izhikevich, E. M. (2003). Simple model of spiking neurons. *IEEE Transactions on neural networks*, 14(6):1569–1572.
- Jacobi, S. and Moses, E. (2007). Variability and corresponding amplitude–velocity relation of activity propagating in one-dimensional neural cultures. *Journal of neurophysiology*, 97(5):3597–3606.

- Jacobi, S., Soriano, J., and Moses, E. (2010). Bdnf and nt-3 increase velocity of activity front propagation in unidimensional hippocampal cultures. *Journal of neurophysiology*, 104(6):2932–2939.
- Jenkinson, M., Bannister, P., Brady, M., and Smith, S. (2002). Improved optimization for the robust and accurate linear registration and motion correction of brain images. *Neuroimage*, 17(2):825–841.
- Kaiser, M., Martin, R., Andras, P., and Young, M. P. (2007). Simulation of robustness against lesions of cortical networks. *European Journal of Neuroscience*, 25(10):3185–3192.
- Kamioka, H., Maeda, E., Jimbo, Y., Robinson, H. P., and Kawana, A. (1996). Spontaneous periodic synchronized bursting during formation of mature patterns of connections in cortical cultures. *Neuroscience letters*, 206(2-3):109–112.
- Kanagasabapathi, T. T., Massobrio, P., Barone, R. A., Tedesco, M., Martinoia, S., Wadman, W. J., and Decré, M. M. (2012). Functional connectivity and dynamics of cortical–thalamic networks co-cultured in a dual compartment device. *Journal of neural engineering*, 9(3):036010.
- Kandel, E. R., Schwartz, J. H., Jessell, T. M., Siegelbaum, S., Hudspeth, A. J., Mack, S., et al. (2000). *Principles of neural science*, volume 4. McGraw-hill New York.
- Kessler, R. C., Birnbaum, H., Bromet, E., Hwang, I., Sampson, N., and Shahly, V. (2010). Age differences in major depression: results from the national comorbidity survey replication (ncs-r). *Psychological medicine*, 40(2):225–237.
- Kim, R., Joo, S., Jung, H., Hong, N., and Nam, Y. (2014). Recent trends in microelectrode array technology for in vitro neural interface platform. *Biomedical Engineering Letters*, 4:129–141.
- Kirwan, P., Turner-Bridger, B., Peter, M., Momoh, A., Arambepola, D., Robinson, H. P., and Livesey, F. J. (2015). Development and function of human cerebral cortex neural networks from pluripotent stem cells in vitro. *Development*, 142(18):3178–3187.
- Kong, F., Wang, X., Hu, S., and Liu, J. (2015). Neural correlates of psychological resilience and their relation to life satisfaction in a sample of healthy young adults. *Neuroimage*, 123:165–172.
- Kotlikoff, M. I. (2007). Genetically encoded ca²⁺ indicators: using genetics and molecular design to understand complex physiology. *The Journal of physiology*, 578(1):55–67.
- Kriegstein, A. R. and Dichter, M. A. (1983). Morphological classification of rat cortical neurons in cell culture. *Journal of Neuroscience*, 3(8):1634–1647.
- Kruschwitz, J., List, D., Waller, L., Rubinov, M., and Walter, H. (2015). Graphvar: a user-friendly toolbox for comprehensive graph analyses of functional brain connectivity. *Journal of neuroscience methods*, 245:107–115.
- Küblböck, M., Woletz, M., Höflich, A., Sladky, R., Kranz, G. S., Hoffmann, A., Lanzenberger, R., and Windischberger, C. (2014). Stability of low-frequency fluctuation amplitudes in prolonged resting-state fmri. *Neuroimage*, 103:249–257.

- Lai, J., Xu, T., Zhang, H., Xi, C., Zhou, H., Du, Y., Jiang, J., Wu, L., Zhang, P., Xu, Y., et al. (2020). Fractional amplitude of low frequency fluctuation in drug-naïve first-episode patients with anorexia nervosa: A resting-state fmri study. *Medicine*, 99(9).
- Latora, V. and Marchiori, M. (2001). Efficient behavior of small-world networks. *Physical review letters*, 87(19):198701.
- Lee, H.-H. and Hsieh, S. (2017). Resting-state fmri associated with stop-signal task performance in healthy middle-aged and elderly people. *Frontiers in psychology*, 8:766.
- Leinekugel, X., Khazipov, R., Cannon, R. C., Hirase, H., Ben-Ari, Y., and Buzsáki, G. (2002). Correlated bursts of activity in the neonatal hippocampus in vivo. *Science*, 296 5575:2049–52.
- Lezak, M. D. (2004). *Neuropsychological assessment*. Oxford University Press, USA.
- Li, M., Liu, R.-R., Lü, L., Hu, M.-B., Xu, S., and Zhang, Y.-C. (2021). Percolation on complex networks: Theory and application. *Physics Reports*, 907:1–68.
- Li, S., Kuddannaya, S., Chuah, Y. J., Bao, J., Zhang, Y., and Wang, D. (2017). Combined effects of multi-scale topographical cues on stable cell sheet formation and differentiation of mesenchymal stem cells. *Biomaterials science*, 5(10):2056–2067.
- Li, W., Xu, Z., Huang, J., Lin, X., Luo, R., Chen, C.-H., and Shi, P. (2014). Neuroarray: a universal interface for patterning and interrogating neural circuitry with single cell resolution. *Scientific reports*, 4(1):4784.
- Liu, W., Fu, W., Sun, M., Han, K., Hu, R., Liu, D., and Wang, J. (2021). Straightforward neuron micropatterning and neuronal network construction on cell-repellent polydimethylsiloxane using microfluidics-guided functionalized pluronic modification. *Analyst*, 146(2):454–462.
- Liu, X., Wang, S., Zhang, X., Wang, Z., Tian, X., and He, Y. (2014). Abnormal amplitude of low-frequency fluctuations of intrinsic brain activity in alzheimer’s disease. *Journal of Alzheimer’s Disease*, 40(2):387–397.
- Liu, X., Zhang, N., Chang, C., and Duyn, J. H. (2018). Co-activation patterns in resting-state fmri signals. *Neuroimage*, 180:485–494.
- Lodato, S. and Arlotta, P. (2015). Generating neuronal diversity in the mammalian cerebral cortex. *Annual review of cell and developmental biology*, 31:699–720.
- Logothetis, N. K. (2008). What we can do and what we cannot do with fmri. *Nature*, 453(7197):869–878.
- Lonardoni, D., Amin, H., Di Marco, S., Maccione, A., Berdondini, L., and Nieuws, T. (2017). Recurrently connected and localized neuronal communities initiate coordinated spontaneous activity in neuronal networks. *PLOS Computational Biology*, 13(7):e1005672.
- Ludl, A.-A. and Soriano, J. (2020). Impact of physical obstacles on the structural and effective connectivity of in silico neuronal circuits. *Frontiers in computational neuroscience*, 14:77.

- Luo, C. Y., Guo, X. Y., Song, W., Chen, Q., Cao, B., Yang, J., Gong, Q. Y., and Shang, H.-F. (2015). Functional connectome assessed using graph theory in drug-naive parkinson's disease. *Journal of neurology*, 262:1557–1567.
- Macis, E., Tedesco, M., Massobrio, P., Raiteri, R., and Martinoia, S. (2007). An automated microdrop delivery system for neuronal network patterning on microelectrode arrays. *Journal of Neuroscience Methods*, 161(1):88–95.
- Maeda, E., Robinson, H., and Kawana, A. (1995). The mechanisms of generation and propagation of synchronized bursting in developing networks of cortical neurons. *Journal of Neuroscience*, 15(10):6834–6845.
- Maldjian, J. A., Laurienti, P. J., and Burdette, J. H. (2004). Precentral gyrus discrepancy in electronic versions of the talairach atlas. *Neuroimage*, 21(1):450–455.
- Maldjian, J. A., Laurienti, P. J., Kraft, R. A., and Burdette, J. H. (2003). An automated method for neuroanatomic and cytoarchitectonic atlas-based interrogation of fmri data sets. *Neuroimage*, 19(3):1233–1239.
- Mancho-Fora, N., Montalà Flaquer, M., Farràs Permanyer, L., Bartrés Faz, D., Vaqué Alcázar, L., Peró, M., and Guàrdia Olmos, J. (2020a). Resting-state functional dynamic connectivity and healthy aging: A sliding-window network analysis. *Psicothema*, 2020, vol. 32, num. 3, p. 337-345.
- Mancho-Fora, N., Montalà-Flaquer, M., Farràs-Permanyer, L., Bartrés-Faz, D., Vaqué-Alcázar, L., Peró-Cebollero, M., and Guàrdia-Olmos, J. (2020b). Resting-state functional connectivity dynamics in healthy aging: An approach through network change point detection. *Brain Connectivity*, 10(3):134–142.
- Mancho-Fora, N., Montalà-Flaquer, M., Farràs-Permanyer, L., Zarabozo-Hurtado, D., Gallardo-Moreno, G. B., Gudayol-Farré, E., Peró-Cebollero, M., and Guàrdia-Olmos, J. (2020c). Network change point detection in resting-state functional connectivity dynamics of mild cognitive impairment patients. *International Journal of Clinical and Health Psychology*, 20(3):200–212.
- Marchitelli, R., Aiello, M., Cachia, A., Quarantelli, M., Cavaliere, C., Postiglione, A., Tedeschi, G., Montella, P., Milan, G., Salvatore, M., et al. (2018). Simultaneous resting-state fdg-pet/fmri in alzheimer disease: relationship between glucose metabolism and intrinsic activity. *Neuroimage*, 176:246–258.
- Marconi, E., Nieus, T., Maccione, A., Valente, P., Simi, A., Messa, M., Dante, S., Baldelli, P., Berdondini, L., and Benfenati, F. (2012). Emergent functional properties of neuronal networks with controlled topology. *PloS one*, 7(4):e34648.
- Markram, H., Muller, E., Ramaswamy, S., Reimann, M. W., Abdellah, M., Sanchez, C. A., Ailamaki, A., Alonso-Nanclares, L., Antille, N., Arsever, S., et al. (2015). Reconstruction and simulation of neocortical microcircuitry. *Cell*, 163(2):456–492.
- Martin Bland, J. and Douglas Altman, G. (1995). Statistics notes: Multiple significance tests: the bonferroni method. *Br Med J*.

- Massara, G. P., Di Matteo, T., and Aste, T. (2016). Network filtering for big data: Triangulated maximally filtered graph. *Journal of complex Networks*, 5(2):161–178.
- Matthews, P., Clare, S., and Adcock, J. (1999). Functional magnetic resonance imaging: Clinical applications and potential. *Journal of inherited metabolic disease*, 22(4):337–352.
- Mazzatenta, A., Giugliano, M., Campidelli, S., Gambazzi, L., Businaro, L., Markram, H., Prato, M., and Ballerini, L. (2007). Interfacing neurons with carbon nanotubes: electrical signal transfer and synaptic stimulation in cultured brain circuits. *Journal of Neuroscience*, 27(26):6931–6936.
- Mazzoni, A., Broccard, F. D., Garcia-Perez, E., Bonifazi, P., Ruaro, M. E., and Torre, V. (2007). On the dynamics of the spontaneous activity in neuronal networks. *PloS one*, 2:e439.
- Medaglia, J. D. and Bassett, D. S. (2018). *Network Analyses and Nervous System Disorders*. Oxford University Press.
- Mesulam, M.-M. (1990). Large-scale neurocognitive networks and distributed processing for attention, language, and memory. *Annals of Neurology: Official Journal of the American Neurological Association and the Child Neurology Society*, 28(5):597–613.
- Meunier, D., Lambiotte, R., and Bullmore, E. T. (2010). Modular and hierarchically modular organization of brain networks. *Frontiers in neuroscience*, 4:200.
- Millet, L. J. and Gillette, M. U. (2012a). New perspectives on neuronal development via microfluidic environments. *Trends in neurosciences*, 35(12):752–761.
- Millet, L. J. and Gillette, M. U. (2012b). Over a century of neuron culture: from the hanging drop to microfluidic devices. *The Yale journal of biology and medicine*, 85(4):501–521.
- Ministerio de sanidad (2021). Esperanzas de vida en España. [https://sanidad.gob.es/Esperanzas de vida en salud en España 2021.pdf](https://sanidad.gob.es/Esperanzas_de_vida_en_salud_en_España_2021.pdf).
- Ministerio de sanidad política social e igualdad (2010). Esperanzas de vida en salud en España (1986-2007). [https://sanidad.gob.es/Esperanzas de vida en salud en España 1986-2007.pdf](https://sanidad.gob.es/Esperanzas_de_vida_en_salud_en_España_1986-2007.pdf).
- Mitchell, A. J. (2009). A meta-analysis of the accuracy of the mini-mental state examination in the detection of dementia and mild cognitive impairment. *Journal of psychiatric research*, 43(4):411–431.
- Montalà-Flaquer, M., Cañete-Massé, C., Vaqué-Alcázar, L., Bartrés-Faz, D., Però-Cebollero, M., and Guàrdia-Olmos, J. (2023). Spontaneous brain activity in healthy aging: An overview through fluctuations and regional homogeneity. *Frontiers in aging neuroscience*, 14:1002811.
- Montalà-Flaquer, M., López-León, C. F., Tornero, D., Houben, A. M., Fardet, T., Monceau, P., Bottani, S., and Soriano, J. (2022). Rich dynamics and functional organization on topographically designed neuronal networks in vitro. *Isience*, 25(12):105680.
- Mountcastle, V. B. (1997). The columnar organization of the neocortex. *Brain: a journal of neurology*, 120(4):701–722.

- Mowinckel, A. M., Espeseth, T., and Westlye, L. T. (2012). Network-specific effects of age and in-scanner subject motion: a resting-state fmri study of 238 healthy adults. *Neuroimage*, 63(3):1364–1373.
- Murphy, T. H., Blatter, L. A., Wier, W. G., and Baraban, J. (1992). Spontaneous synchronous synaptic calcium transients in cultured cortical neurons. *Journal of Neuroscience*, 12(12):4834–4845.
- Nelson, H. E. and Willison, J. (1991). *National adult reading test (NART)*. Nfer-Nelson Windsor.
- Neto, E., Leitão, L., Sousa, D. M., Alves, C. J., Alencastre, I. S., Aguiar, P., and Lamghari, M. (2016). Compartmentalized microfluidic platforms: the unrivaled breakthrough of in vitro tools for neurobiological research. *Journal of Neuroscience*, 36(46):11573–11584.
- Newman, M. (2010). *Networks: an Introduction*. Oxford university press.
- Newman, M. E. (2003). The structure and function of complex networks. *SIAM review*, 45(2):167–256.
- Nichols, T. E. (2012). Multiple testing corrections, nonparametric methods, and random field theory. *Neuroimage*, 62(2):811–815.
- Nikolakopoulou, P., Rauti, R., Voulgaris, D., Shlomy, I., Maoz, B. M., and Herland, A. (2020). Recent progress in translational engineered in vitro models of the central nervous system. *Brain*, 143(11):3181–3213.
- Ogura, A., Iijima, T., Amano, T., and Kudo, Y. (1987). Optical monitoring of excitatory synaptic activity between cultured hippocampal neurons by a multi-site ca²⁺ fluorometry. *Neuroscience letters*, 78(1):69–74.
- Okujeni, S. and Egert, U. (2019). Self-organization of modular network architecture by activity-dependent neuronal migration and outgrowth. *Elife*, 8:e47996.
- Okujeni, S., Kandler, S., and Egert, U. (2017). Mesoscale architecture shapes initiation and richness of spontaneous network activity. *Journal of Neuroscience*, 37(14):3972–3987.
- Onoda, K. and Yamaguchi, S. (2013). Small-worldness and modularity of the resting-state functional brain network decrease with aging. *Neuroscience letters*, 556:104–108.
- Opitz, T., De Lima, A. D., and Voigt, T. (2002). Spontaneous development of synchronous oscillatory activity during maturation of cortical networks in vitro. *Journal of neurophysiology*, 88(5):2196–2206.
- Orlandi, J., Comella-Bolla, A., Masana, M., et al. (2017). Netcal: an interactive platform for large-scale, network and population dynamics analysis of calcium imaging recordings. *Neuroscience*.
- Orlandi, J. G., Soriano, J., Alvarez-Lacalle, E., Teller, S., and Casademunt, J. (2013). Noise focusing and the emergence of coherent activity in neuronal cultures. *Nature Physics*, 9(9):582–590.

- Ornstein, R. E. and Thompson, R. F. (1986). *The amazing brain*. Houghton Mifflin Harcourt.
- Oschmann, M., Gawryluk, J. R., and Initiative, A. D. N. (2020). A longitudinal study of changes in resting-state functional magnetic resonance imaging functional connectivity networks during healthy aging. *Brain Connectivity*, 10(7):377–384.
- Oschwald, J., Guye, S., Liem, F., Rast, P., Willis, S., Röcke, C., Jäncke, L., Martin, M., and Mérillat, S. (2019). Brain structure and cognitive ability in healthy aging: a review on longitudinal correlated change. *Reviews in the Neurosciences*, 31(1):1–57.
- Otsu, Y. and Murphy, T. H. (2003). Miniature transmitter release: accident of nature or careful design? *Science's STKE*, 2003(211):pe54–pe54.
- Pakkenberg, B., Pelvig, D., Marnier, L., Bundgaard, M. J., Gundersen, H. J. G., Nyengaard, J. R., and Regeur, L. (2003). Aging and the human neocortex. *Experimental gerontology*, 38(1-2):95–99.
- Palop, J. J. and Mucke, L. (2016). Network abnormalities and interneuron dysfunction in alzheimer disease. *Nature Reviews Neuroscience*, 17:777–792.
- Park, H.-J. and Friston, K. (2013). Structural and functional brain networks: from connections to cognition. *Science*, 342(6158):1238411.
- Park, M. U., Bae, Y., Lee, K.-S., Song, J. H., Lee, S.-M., and Yoo, K.-H. (2021). Collective dynamics of neuronal activities in various modular networks. *Lab on a Chip*, 21(5):951–961.
- Pasquale, V., Massobrio, P., Bologna, L., Chiappalone, M., and Martinoia, S. (2008). Self-organization and neuronal avalanches in networks of dissociated cortical neurons. *Neuroscience*, 153(4):1354–1369.
- Pedersini, C. A., Guàrdia-Olmos, J., Montalà-Flaquer, M., Cardobi, N., Sanchez-Lopez, J., Parisi, G., Savazzi, S., and Marzi, C. A. (2020). Functional interactions in patients with hemianopia: A graph theory-based connectivity study of resting fmri signal. *PloS one*, 15(1):e0226816.
- Pergher, V., Demaerel, P., Soenen, O., Saarela, C., Tournoy, J., Schoenmakers, B., Karrasch, M., and Van Hulle, M. M. (2019). Identifying brain changes related to cognitive aging using vbm and visual rating scales. *NeuroImage: Clinical*, 22:101697.
- Petersen, R. C. and Morris, J. C. (2005). Mild cognitive impairment as a clinical entity and treatment target. *Archives of neurology*, 62(7):1160–1163.
- Pistono, A., Guerrier, L., Péran, P., Rafiq, M., Giméno, M., Bézy, C., Pariente, J., and Jucla, M. (2021). Increased functional connectivity supports language performance in healthy aging despite gray matter loss. *Neurobiology of Aging*, 98:52–62.
- Poli, D., Pastore, V. P., and Massobrio, P. (2015). Functional connectivity in in vitro neuronal assemblies. *Frontiers in neural circuits*, 9:57.
- Posner, M. I. and Rothbart, M. K. (1994). Constructing neuronal theories of mind. *Large-scale neuronal theories of the brain*, pages 183–199.

- Pu, J., Gong, H., Li, X., and Luo, Q. (2013). Developing neuronal networks: self-organized criticality predicts the future. *Scientific reports*, 3(1):1081.
- Ramon y Cajal, S. (1899). Comparative study of the sensory areas of the human cortex. *Book*, page 325.
- Rey, A. (1958). L'examen clinique en psychologie.
- Robinson, H., Kawahara, M., Jimbo, Y., Torimitsu, K., Kuroda, Y., and Kawana, A. (1993). Periodic synchronized bursting and intracellular calcium transients elicited by low magnesium in cultured cortical neurons. *Journal of neurophysiology*, 70(4):1606–1616.
- Rochefort, N. L., Jia, H., and Konnerth, A. (2008). Calcium imaging in the living brain: prospects for molecular medicine. *Trends in molecular medicine*, 14(9):389–399.
- Rolston, J., Wagenaar, D., and Potter, S. (2007). Precisely timed spatiotemporal patterns of neural activity in dissociated cortical cultures. *Neuroscience*, 148:294–303.
- Rubinov, M. and Sporns, O. (2010). Complex network measures of brain connectivity: uses and interpretations. *Neuroimage*, 52(3):1059–1069.
- S. von Bartheld, C., Bahney, J., and Herculano-Houzel, S. (2016). The search for true numbers of neurons and glial cells in the human brain: A review of 150 years of cell counting. *The journal of comparative neurology*, 524:3865–3895.
- Sala-Llonch, R., Bartrés-Faz, D., and Junqué, C. (2015). Reorganization of brain networks in aging: a review of functional connectivity studies. *Frontiers in psychology*, 6:663.
- Scannell, J. W., Blakemore, C., and Young, M. P. (1995). Analysis of connectivity in the cat cerebral cortex. *Journal of Neuroscience*, 15(2):1463–1483.
- Scheinost, D., Benjamin, J., Lacadie, C., Vohr, B., Schneider, K. C., Ment, L. R., Papademetris, X., and Constable, R. T. (2012). The intrinsic connectivity distribution: a novel contrast measure reflecting voxel level functional connectivity. *Neuroimage*, 62(3):1510–1519.
- Schroeter, M. S., Charlesworth, P., Kitzbichler, M. G., Paulsen, O., and Bullmore, E. T. (2015). Emergence of rich-club topology and coordinated dynamics in development of hippocampal functional networks in vitro. *Journal of Neuroscience*, 35(14):5459–5470.
- Schröter, M. S., Paulsen, O., and Bullmore, E. T. (2017). Micro-connectomics: probing the organization of neuronal networks at the cellular scale. *Nature reviews neuroscience*, 18:131–146.
- Seeley, W. W., Crawford, R. K., Zhou, J., Miller, B. L., and Greicius, M. D. (2009). Neurodegenerative diseases target large-scale human brain networks. *Neuron*, 62:42–52.
- Segev, R., Baruchi, I., Hulata, E., and Ben-Jacob, E. (2004). Hidden neuronal correlations in cultured networks. *Physical Review Letters*, 92(11):118102.
- Segev, R., Benveniste, M., Shapira, Y., and Ben-Jacob, E. (2003). Formation of electrically active clusterized neural networks. *Physical review letters*, 90(16):168101.

- Seidler, R. D., Bernard, J. A., Burutolu, T. B., Fling, B. W., Gordon, M. T., Gwin, J. T., Kwak, Y., and Lipps, D. B. (2010). Motor control and aging: links to age-related brain structural, functional, and biochemical effects. *Neuroscience & Biobehavioral Reviews*, 34(5):721–733.
- Serra, M., Guaraldi, M., and Shea, T. B. (2010). Inhibitory neurons modulate spontaneous signaling in cultured cortical neurons: density-dependent regulation of excitatory neuronal signaling. *Physical Biology*, 7(2):026009.
- Shein, M., Greenbaum, A., Gabay, T., Sorkin, R., David-Pur, M., Ben-Jacob, E., and Hanein, Y. (2009). Engineered neuronal circuits shaped and interfaced with carbon nanotube microelectrode arrays. *Biomedical microdevices*, 11:495–501.
- Shein-Idelson, M., Ben-Jacob, E., and Hanein, Y. (2011). Engineered neuronal circuits: a new platform for studying the role of modular topology. *Frontiers in neuroengineering*, 4:10.
- Sheline, Y. I., Morris, J. C., Snyder, A. Z., Price, J. L., Yan, Z., D’Angelo, G., Liu, C., Dixit, S., Benzinger, T., Fagan, A., et al. (2010). Apoe4 allele disrupts resting state fmri connectivity in the absence of amyloid plaques or decreased csf a β 42. *Journal of neuroscience*, 30(50):17035–17040.
- Siegenfeld, A. F. and Bar-Yam, Y. (2020). An introduction to complex systems science and its applications. *Complexity*, 2020:1–16.
- Siegle, G. J., Carter, C. S., and Thase, M. E. (2006). Use of fmri to predict recovery from unipolar depression with cognitive behavior therapy. *American Journal of Psychiatry*, 163(4):735–738.
- Simon, E. J., Reece, J. B., and Dickey, J. (2013). *Campbell essential biology with physiology*. Pearson.
- Smetters, D., Majewska, A., and Yuste, R. (1999). Detecting action potentials in neuronal populations with calcium imaging. *Methods*, 18(2):215–221.
- Smith, S. M., Fox, P. T., Miller, K. L., Glahn, D. C., Fox, P. M., Mackay, C. E., Filippini, N., Watkins, K. E., Toro, R., Laird, A. R., et al. (2009). Correspondence of the brain’s functional architecture during activation and rest. *Proceedings of the national academy of sciences*, 106(31):13040–13045.
- Smith, S. M. and Nichols, T. E. (2009). Threshold-free cluster enhancement: addressing problems of smoothing, threshold dependence and localisation in cluster inference. *Neuroimage*, 44(1):83–98.
- Song, J., Birn, R. M., Boly, M., Meier, T. B., Nair, V. A., Meyerand, M. E., and Prabhakaran, V. (2014a). Age-related reorganizational changes in modularity and functional connectivity of human brain networks. *Brain connectivity*, 4(9):662–676.
- Song, Y., Mu, K., Wang, J., Lin, F., Chen, Z., Yan, X., Hao, Y., Zhu, W., and Zhang, H. (2014b). Altered spontaneous brain activity in primary open angle glaucoma: a resting-state functional magnetic resonance imaging study. *PloS one*, 9(2):e89493.

- Soriano, J. (2023). Neuronal cultures: Exploring biophysics, complex systems, and medicine in a dish. *Biophysica*, 3(1):181–202.
- Soriano, J., Rodríguez Martínez, M., Tlustý, T., and Moses, E. (2008). Development of input connections in neural cultures. *Proceedings of the National Academy of Sciences*, 105(37):13758–13763.
- Soriano-Paños, D., Cota, W., Ferreira, S. C., Ghoshal, G., Arenas, A., and Gómez-Gardeñes, J. (2022). Modeling communicable diseases, human mobility, and epidemics: a review. *Annalen der Physik*, 534(6):2100482.
- Sotiropoulos, S. N., Bai, L., Morgan, P. S., Constantinescu, C. S., and Tench, C. R. (2010). Brain tractography using q-ball imaging and graph theory: Improved connectivities through fibre crossings via a model-based approach. *Neuroimage*, 49(3):2444–2456.
- Sporns, O. (2013). Network attributes for segregation and integration in the human brain. *Current opinion in neurobiology*, 23(2):162–171.
- Sporns, O. (2018). Graph theory methods: applications in brain networks. *Dialogues Clin Neurosci*, 20:111–120.
- Sporns, O. and Honey, C. J. (2006). Small worlds inside big brains. *Proceedings of the National Academy of Sciences*, 103(51):19219–19220.
- Sporns, O. and Kötter, R. (2004). Motifs in brain networks. *PLoS biology*, 2(11):e369.
- Sporns, O., Tononi, G., and Edelman, G. M. (2000). Theoretical neuroanatomy: relating anatomical and functional connectivity in graphs and cortical connection matrices. *Cerebral cortex*, 10(2):127–141.
- Sporns, O. and Zwi, J. D. (2004). The small world of the cerebral cortex. *Neuroinformatics*, 2:145–162.
- Srinivas, K. V., Jain, R., Saurav, S., and Sikdar, S. K. (2007). Small-world network topology of hippocampal neuronal network is lost, in an in vitro glutamate injury model of epilepsy. *European Journal of Neuroscience*, 25(11):3276–3286.
- Srinivasan, R., Russell, D. P., Edelman, G. M., and Tononi, G. (1999). Increased synchronization of neuromagnetic responses during conscious perception. *Journal of Neuroscience*, 19(13):5435–5448.
- Stam, C. J. (2014). Modern network science of neurological disorders. *Nature Reviews Neuroscience*, 15(10):683–695.
- Stern, Y. (2002). What is cognitive reserve? theory and research application of the reserve concept. *Journal of the international neuropsychological society*, 8(3):448–460.
- Stetter, O., Battaglia, D., Soriano, J., and Geisel, T. (2012). Model-free reconstruction of excitatory neuronal connectivity from calcium imaging signals.
- Stiso, J. and Bassett, D. S. (2018). Spatial embedding imposes constraints on neuronal network architectures. *Trends in cognitive sciences*, 22(12):1127–1142.

- Streit, J., Tschertter, A., Heuschkel, M. O., and Renaud, P. (2001). The generation of rhythmic activity in dissociated cultures of rat spinal cord. *European journal of neuroscience*, 14(2):191–202.
- Strogatz, S. (2018). *Nonlinear Dynamics and Chaos: With Applications to Physics, Biology, Chemistry and Engineering*. CRC Press, Boca Raton, FL, USA.
- Suárez, L. E., Markello, R. D., Betzel, R. F., and Misić, B. (2020). Linking structure and function in macroscale brain networks. *Trends in cognitive sciences*, 24(4):302–315.
- Sukenik, N., Vinogradov, O., Weinreb, E., Segal, M., Levina, A., and Moses, E. (2021). Neuronal circuits overcome imbalance in excitation and inhibition by adjusting connection numbers. *Proceedings of the National Academy of Sciences*, 118(12):e2018459118.
- Sumi, T., Yamamoto, H., and Hirano-Iwata, A. (2020). Suppression of hypersynchronous network activity in cultured cortical neurons using an ultrasoft silicone scaffold. *Soft Matter*, 16(13):3195–3202.
- Sun, D. A., Sombati, S., Blair, R. E., and DeLorenzo, R. J. (2002). Calcium-dependent epileptogenesis in an in vitro model of stroke-induced “epilepsy”. *Epilepsia*, 43(11):1296–1305.
- Sun, D. A., Sombati, S., Blair, R. E., and DeLorenzo, R. J. (2004). Long-lasting alterations in neuronal calcium homeostasis in an in vitro model of stroke-induced epilepsy. *Cell calcium*, 35(2):155–163.
- Sun, J.-J., Kilb, W., and Luhmann, H. J. (2010). Self-organization of repetitive spike patterns in developing neuronal networks in vitro. *European Journal of Neuroscience*, 32(8):1289–1299.
- Sun, Y., Huang, Z., Liu, W., Yang, K., Sun, K., Xing, S., Wang, D., Zhang, W., and Jiang, X. (2012). Surface coating as a key parameter in engineering neuronal network structures in vitro. *Biointerphases*, 7:1–14.
- Tang, F., Zhu, D., Ma, W., Yao, Q., Li, Q., and Shi, J. (2021). Differences changes in cerebellar functional connectivity between mild cognitive impairment and alzheimer’s disease: a seed-based approach. *Frontiers in Neurology*, 12:645171.
- Teller, S., Estévez-Priego, E., Granell, C., Tornero, D., Andilla, J., Olarte, O. E., Loza-Alvarez, P., Arenas, A., and Soriano, J. (2020). Spontaneous functional recovery after focal damage in neuronal cultures. *Eneuro*, 7(1).
- Teller, S., Granell, C., De Domenico, M., Soriano, J., Gomez, S., and Arenas, A. (2014). Emergence of assortative mixing between clusters of cultured neurons. *PLoS computational biology*, 10(9):e1003796.
- Teller, S., Tahirbegi, I. B., Mir, M., Samitier, J., and Soriano, J. (2015). Magnetite-amyloid- β deteriorates activity and functional organization in an in vitro model for alzheimer’s disease. *Scientific Reports*, 5(1):17261.
- Tetzlaff, C., Okujeni, S., Egert, U., Wörgötter, F., and Butz, M. (2010). Self-organized criticality in developing neuronal networks. *PLoS computational biology*, 6(12):e1001013.

- Thakor, N. V. and Tong, S. (2004). Advances in quantitative electroencephalogram analysis methods. *Annu. Rev. Biomed. Eng.*, 6:453–495.
- Tian, L., Hires, S. A., Mao, T., Huber, D., Chiappe, M. E., Chalasani, S. H., Petreanu, L., Akerboom, J., McKinney, S. A., Schreiter, E. R., et al. (2009). Imaging neural activity in worms, flies and mice with improved gcamp calcium indicators. *Nature methods*, 6(12):875–881.
- Tibau, E., Ludl, A.-A., Rüdiger, S., Orlandi, J. G., and Soriano, J. (2018). Neuronal spatial arrangement shapes effective connectivity traits of in vitro cortical networks. *IEEE Transactions on Network Science and Engineering*, 7(1):435–448.
- Tibau, E., Valencia, M., and Soriano, J. (2013). Identification of neuronal network properties from the spectral analysis of calcium imaging signals in neuronal cultures. *Frontiers in neural circuits*, 7:199.
- Tomasi, D. and Volkow, N. D. (2010). Functional connectivity density mapping. *Proceedings of the National Academy of Sciences*, 107(21):9885–9890.
- Tombaugh, T. N. and McIntyre, N. J. (1992). The mini-mental state examination: a comprehensive review. *Journal of the American Geriatrics Society*, 40(9):922–935.
- Tononi, G., Sporns, O., and Edelman, G. M. (1994). A measure for brain complexity: relating functional segregation and integration in the nervous system. *Proceedings of the National Academy of Sciences*, 91(11):5033–5037.
- Tzourio-Mazoyer, N., Landeau, B., Papathanassiou, D., Crivello, F., Etard, O., Delcroix, N., Mazoyer, B., and Joliot, M. (2002). Automated anatomical labeling of activations in spm using a macroscopic anatomical parcellation of the mni mri single-subject brain. *Neuroimage*, 15(1):273–289.
- Valenzuela, M. J. and Sachdev, P. (2006). Brain reserve and cognitive decline: a non-parametric systematic review. *Psychological medicine*, 36(8):1065–1073.
- van den Heuvel, M. P., de Lange, S. C., Zalesky, A., Seguin, C., Yeo, B. T., and Schmidt, R. (2017). Proportional thresholding in resting-state fmri functional connectivity networks and consequences for patient-control connectome studies: Issues and recommendations. *Neuroimage*, 152:437–449.
- Van Den Heuvel, M. P., Sporns, O., Collin, G., Scheewe, T., Mandl, R. C., Cahn, W., Goñi, J., Pol, H. E. H., and Kahn, R. S. (2013). Abnormal rich club organization and functional brain dynamics in schizophrenia. *JAMA psychiatry*, 70(8):783–792.
- van den Heuvel, M. P., Stam, C. J., Boersma, M., and Pol, H. H. (2008). Small-world and scale-free organization of voxel-based resting-state functional connectivity in the human brain. *Neuroimage*, 43(3):528–539.
- Vaqué-Alcázar, L., Sala-Llonch, R., Abellaneda-Pérez, K., Coll-Adrós, N., Valls-Pedret, C., Bargalló, N., Ros, E., and Bartrés-Faz, D. (2020). Functional and structural correlates of working memory performance and stability in healthy older adults. *Brain Structure and Function*, 225:375–386.

- Vecchio, F., Miraglia, F., Curcio, G., Altavilla, R., Scrascia, F., Giambattistelli, F., Quattrocchi, C. C., Bramanti, P., Vernieri, F., and Rossini, P. M. (2015). Cortical brain connectivity evaluated by graph theory in dementia: a correlation study between functional and structural data. *Journal of Alzheimer's Disease*, 45(3):745–756.
- Vicente, R., Wibral, M., Lindner, M., and Pipa, G. (2011). Transfer entropy—a model-free measure of effective connectivity for the neurosciences. *Journal of computational neuroscience*, 30:45–67.
- Volman, V., Baruchi, I., and Ben-Jacob, E. (2005). Manifestation of function-follow-form in cultured neuronal networks. *Physical biology*, 2(2):98.
- Von Neumann, J. and Kurzweil, R. (2012). *The computer and the brain*. Yale university press.
- Wagenaar, D. A., Pine, J., and Potter, S. M. (2006). An extremely rich repertoire of bursting patterns during the development of cortical cultures. *BMC neuroscience*, 7(1):1–18.
- Wandelt, S., Sun, X., Menasalvas, E., Rodríguez-González, A., and Zanin, M. (2019). On the use of random graphs as null model of large connected networks. *Chaos, Solitons & Fractals*, 119:318–325.
- Wang, J., Wang, L., Zang, Y., Yang, H., Tang, H., Gong, Q., Chen, Z., Zhu, C., and He, Y. (2009). Parcellation-dependent small-world brain functional networks: A resting-state fmri study. *Human brain mapping*, 30(5):1511–1523.
- Wang, Q., Wang, C., Deng, Q., Zhan, L., Tang, Y., Li, H., Antwi, C. O., Xiang, A., Lv, Y., Jia, X., et al. (2022). Alterations of regional spontaneous brain activities in anxiety disorders: a meta-analysis. *Journal of affective disorders*, 296:233–240.
- Ward, B. D. (2000). Simultaneous inference for fmri data.
- Watts, D. J. and Strogatz, S. H. (1998). Collective dynamics of ‘small-world’ networks. *nature*, 393(6684):440–442.
- West, K. L., Zupichini, M. D., Turner, M. P., Sivakolundu, D. K., Zhao, Y., Abdelkarim, D., Spence, J. S., and Rypma, B. (2019). Bold hemodynamic response function changes significantly with healthy aging. *NeuroImage*, 188:198–207.
- Wheeler, B. C. and Brewer, G. J. (2010). Designing neural networks in culture. *Proceedings of the IEEE*, 98(3):398–406.
- Winkler, A. M., Ridgway, G. R., Douaud, G., Nichols, T. E., and Smith, S. M. (2016). Faster permutation inference in brain imaging. *Neuroimage*, 141:502–516.
- World Health Organization (2016). Global strategy and action plan on ageing and health (2016-2020). <https://www.who.int/publications/Global strategy and action plan on ageing and health 2016-2020.pdf>.
- Wu, J. Y., Huang, X., and Zhang, C. (2008). Propagating waves of activity in the neocortex: what they are, what they do. *The Neuroscientist: a review journal bringing neurobiology, neurology and psychiatry*, 14 5:487–502.

- Xu, X., Kuang, Q., Zhang, Y., Wang, H., Wen, Z., and Li, M. (2015). Age-related changes in functional connectivity between young adulthood and late adulthood. *Analytical Methods*, 7(10):4111–4122.
- Yamamoto, H., Matsumura, R., Takaoki, H., Katsurabayashi, S., Hirano-Iwata, A., and Niwano, M. (2016). Unidirectional signal propagation in primary neurons micropatterned at a single-cell resolution. *Applied Physics Letters*, 109(4):043703.
- Yamamoto, H., Moriya, S., Ide, K., Hayakawa, T., Akima, H., Sato, S., Kubota, S., Tanii, T., Niwano, M., Teller, S., et al. (2018). Impact of modular organization on dynamical richness in cortical networks. *Science advances*, 4(11):eaau4914.
- Yamashita, K., Kuwashiro, T., Ishikawa, K., Furuya, K., Harada, S., Shin, S., Wada, N., Hirakawa, C., Okada, Y., and Noguchi, T. (2021). Identification of predictors for minimal state examination and revised hasegawa's dementia scale scores using mr-based brain morphometry. *European Journal of Radiology Open*, 8:100359.
- Yan, C. and Zang, Y. (2010). Dparsf: a matlab toolbox for" pipeline" data analysis of resting-state fmri. *Frontiers in systems neuroscience*, 4:1377.
- Yan, C.-G., Cheung, B., Kelly, C., Colcombe, S., Craddock, R. C., Di Martino, A., Li, Q., Zuo, X.-N., Castellanos, F. X., and Milham, M. P. (2013). A comprehensive assessment of regional variation in the impact of head micromovements on functional connectomics. *Neuroimage*, 76:183–201.
- Yan, C.-G., Wang, X.-D., Zuo, X.-N., and Zang, Y.-F. (2016). Dpabi: data processing & analysis for (resting-state) brain imaging. *Neuroinformatics*, 14:339–351.
- Yang, J., Gohel, S., and Vachha, B. (2020). Current methods and new directions in resting state fmri. *Clinical imaging*, 65:47–53.
- Yi, Y., Park, J., Lim, J., Lee, C., and Lee, S.-H. (2015). Central nervous system and its disease models on a chip. *Trends in biotechnology*, 33 12:762–776.
- Young, M. P. (1993). The organization of neural systems in the primate cerebral cortex. *Proceedings of the Royal Society of London. Series B: Biological Sciences*, 252(1333):13–18.
- Ystad, M., Hodneland, E., Adolfsdottir, S., Haász, J., Lundervold, A. J., Eichele, T., and Lundervold, A. (2011). Cortico-striatal connectivity and cognition in normal aging: a combined dti and resting state fmri study. *Neuroimage*, 55(1):24–31.
- Yu, H., Li, M.-L., Li, Y.-F., Li, X.-J., Meng, Y., Liang, S., Li, Z., Guo, W., Wang, Q., Deng, W., et al. (2020). Anterior cingulate cortex, insula and amygdala seed-based whole brain resting-state functional connectivity differentiates bipolar from unipolar depression. *Journal of Affective Disorders*, 274:38–47.
- Yue, Y., Jiang, Y., Shen, T., Pu, J., Lai, H.-Y., and Zhang, B. (2020). Alff and reho mapping reveals different functional patterns in early-and late-onset parkinson's disease. *Frontiers in Neuroscience*, 14:141.

- Yuste, R. (2015). From the neuron doctrine to neural networks. *Nature Reviews Neuroscience*, 16(8):487–497.
- Zang, Y., Jiang, T., Lu, Y., He, Y., and Tian, L. (2004). Regional homogeneity approach to fmri data analysis. *Neuroimage*, 22(1):394–400.
- Zanin, M., Papo, D., Sousa, P. A., Menasalvas, E., Nicchi, A., Kubik, E., and Boccaletti, S. (2016). Combining complex networks and data mining: why and how. *Physics Reports*, 635:1–44.
- Zhang, Z., Liu, Y., Jiang, T., Zhou, B., An, N., Dai, H., Wang, P., Niu, Y., Wang, L., and Zhang, X. (2012). Altered spontaneous activity in alzheimer’s disease and mild cognitive impairment revealed by regional homogeneity. *Neuroimage*, 59(2):1429–1440.
- Zhou, Y., Dougherty Jr, J. H., Hubner, K. F., Bai, B., Cannon, R. L., and Hutson, R. K. (2008). Abnormal connectivity in the posterior cingulate and hippocampus in early alzheimer’s disease and mild cognitive impairment. *Alzheimer’s & Dementia*, 4(4):265–270.
- Zou, Q.-H., Zhu, C.-Z., Yang, Y., Zuo, X.-N., Long, X.-Y., Cao, Q.-J., Wang, Y.-F., and Zang, Y.-F. (2008). An improved approach to detection of amplitude of low-frequency fluctuation (alf) for resting-state fmri: fractional alf. *Journal of neuroscience methods*, 172(1):137–141.
- Zuo, X.-N. and Xing, X.-X. (2014). Test-retest reliabilities of resting-state fmri measurements in human brain functional connectomics: a systems neuroscience perspective. *Neuroscience & Biobehavioral Reviews*, 45:100–118.

Appendix A

Informed consent documents

In this Appendix we include the informed consent documents procured to the participants of the three different studies that provided the fMRI data.

CONSENTIMIENTO INFORMADO

Título del estudio: “Índices de plasticidad cerebral regional como biomarcadores de estado y progresión en la enfermedad de Alzheimer preclínica. Estudio combinado con estimulación magnética transcranial y resonancia magnética”

Yo, (nombre del participante):

He leído la hoja de información general que se me ha entregado.

He leído las hojas de información sobre la EMT y la punción lumbar y entiendo los riesgos que puede tener.

He podido hacer preguntas sobre el estudio

He recibido suficiente información sobre el estudio

He hablado con (nombre del investigador):

Comprendo que mi participación es voluntaria

Comprendo que puedo retirarme del estudio:

1. Cuando quiera
2. Sin tener que dar explicaciones
3. Sin que esto repercuta en mi atención médica.

Consiento que los datos obtenidos para este proyecto sean almacenados de forma anónima para su posible uso en futuros proyectos aprobados por el comité ético (CEIC) del centro (de lo contrario, éstos serán destruidos tras la realización de las determinaciones previstas en este estudio).

Consiento que los posibles resultados obtenidos con mi participación en el estudio sean fuente de publicaciones científicas, siempre que se vele por mi completo anonimato.

Accedo a que la información obtenida para el estudio pueda ser utilizada en el futuro para nuevos análisis relacionados no previstos en el protocolo actual.

SI

NO

Presto libremente mi conformidad para participar en el estudio de estimulación no invasiva, de biomarcadores, cognitivo y radiológico.

Firma del participante:
investigador:

Firma del

Lugar y fecha:

FULL D'INFORMACIÓ PER ALS VOLUNTARIS PARTICIPANTS EN L'ESTUDI

Investigadors de la Universitat de Barcelona de l'Hospital Clínic de Barcelona i metges de tres Centres d'Atenció Primària de la ciutat de Barcelona, estem realitzant un treball de recerca finançat pel Ministerio de Ciencia e Innovación del Govern d'Espanya. En aquest estudi investigarem la influència de mesures com els anys d'educació, el tipus d'ocupació així com característiques de personalitat i d'hàbits alimentaris i de son, en combinació amb informació genètica tenen sobre l'estructura i funcionalitat del cervell en l'edat adulta, tant en persones sanes, com és el seu cas com en persones amb alteració cognitiva.

Per a participar en aquesta investigació cal donar un consentiment per escrit en un full que se li proporcionarà. Aquest consentiment indica que vostè està d'acord en participar a l'estudi i sotmetre's a un seguit de proves, totes elles sense risc i indolores.

En primer lloc es realitzarà una avaluació de les funcions cognitives com ara la memòria, l'atenció o el llenguatge a partir de l'aplicació d'una sèrie de tests psicològics. També, a partir de qüestionaris l'interrogarem sobre la seva educació, l'ocupació realitzada al llarg de la vida així com les seves aficions i hàbits de son i d'ingesta. Finalment li passarem un qüestionari de personalitat reduït per a tenir una estimació de les principals característiques en el seu cas. Aquesta part de l'estudi té una duració aproximadament d'entre 60 a 90 minuts depenent de la persona.

En segon lloc es realitzarà una exploració amb ressonància magnètica a l'Hospital Clínic de Barcelona. L'examen amb aquesta tècnica ens permetrà avaluar la integritat del cervell estructural i funcionalment. El procediment que utilitzarem durant l'exploració de RMf serà aproximadament el següent: vostè serà col·locat en posició horitzontal en la ressonància magnètica; un cop posicionat se li col·locaran unes ulleres especials que permeten la presentació d'imatges sobre les quals vostè haurà de realitzar opinions o tractar de recordar-les, segons les instruccions que li facilitem en el moment. També hi haurà estones en que vostè no haurà de fer res dins la màquina i pot restar quiet amb els ulls tancats. El temps total de l'exploració mitjançant RM serà d'aproximadament 30-45 minuts. Existeix un sistema de comunicació permanent amb el personal sanitari fora de la sala de la màquina de RM a través del qual se li anirà donant informació en cada cas. També pot utilitzar aquest sistema per a comunicar-se amb el personal sanitari quan ho desitgi. La ressonància magnètica no empra raigs X ni cap altre tipus de radiacions ionitzants, essent un procediment del tot segur. No causa cap dolor ni molèstia. Els únics inconvenients que poden aparèixer és sentir una mica de claustrofòbia al dur-se a terme l'exploració en un túnel amb poc espai. D'altra banda, l'equip emet una sèrie de sorolls que també poden resultar molestos, si bé, son completament normals.

El tercer tipus d'avaluacions que es realitzaran en aquest projecte serà la obtenció de determinada informació genètica, sobre gens que s'han relacionat prèviament amb les funcions cognitives (memòria, atenció, etc) en persones d'edat avançada. Aquesta informació es determinarà a partir de mostres de saliva que ens proporcionarà amb uns tubs que li facilitarem, essent per tant un procediment totalment indolor i segur. És important que li quedi clar que la informació genètica obtinguda en aquest estudi no té cap mena de valor mèdic en termes de diagnòstic. En aquest sentit el procediment establert en el projecte implica que la informació genètica no li serà revelada.

Tota la informació obtinguda d'aquesta investigació serà mantinguda de forma confidencial. Queda així mateix entès que la participació en el projecte no modifica ni condiona en cap mesura l'atenció o assistència que pugui rebre de l'Hospital Clínic o del seu CAP de referència.

Manifesto que quedo assabentat de les característiques de l'estudi i que accepto participar-hi.

Nom del voluntari/a:

Lloc i data:

FULL DE CONSENTIMENT INFORMAT

Sr./Sra.manifesto que he llegit i se m'ha aclarit qualsevol dubte del 'FULL D'INFORMACIÓ ALS VOLUNTARIS O PACIENTS PARTICIPANTS EN EL PROJECTE' en referència a les característiques principals sobre l'estudi que s'està duent a la Universitat de Barcelona, l'Hospital Clínic de Barcelona i tres Centres d'Atenció Primària de la ciutat de Barcelona per a estudiar la influència de determinades variables com l'educació, les característiques de personalitat, els hàbits de son i alimentaris així com certes variants genètiques sobre l'estructura i funció cerebrals en l'envelliment.

En aquest sentit, autoritzo el meu consentiment per a que els resultats de les proves que se m'administrin siguin utilitzats per a dur a terme aquesta recerca. En concret, manifesto també haver entès que la informació genètica que s'obtindrà en el present estudi a partir de mostres de saliva no proporciona cap informació mèdica rellevant i per tant no em serà revelada.

L'equip d'investigadors em garanteix la confidencialitat de les dades i que en qualsevol moment puc decidir no continuar participant en el projecte, la qual cosa significaria la immediata destrucció de totes les meves dades obtingudes fins al moment. En aquest cas se'm garanteix que seguiré rebent assistència psicològica o mèdica si fos necessària.

Ei/La sotasignat/da

**RESONANCIA MAGNÉTICA
PROTOCOLO DE INVESTIGACION**

Título del Proyecto de Investigación:

Relación entre variables de *reserva cerebral* de tipo ambientales y genéticas y la función y estructura cerebrales en el envejecimiento sano y patológico.

Investigador principal:

Nombre del participante:

Dirección y Teléfono del participante:

C/:

**Población:
Teléfono:**

C. Postal:

Gracias por participar en este proyecto de investigación, que tiene como objetivo último mejorar el conocimiento en Medicina, y así, el tratamiento de pacientes.

La duración aproximada de esta RM es de 30-45 min en una sola sesión. Los datos obtenidos de este estudio están sometidos a los mismos procedimientos de protección de datos y confidencialidad que los de todos los pacientes del Hospital Clínic.

Su estudio será valorado por un Radiólogo, que si encuentra algo anómalo, lo comunicará a su médico en el hospital.

Si tiene alguna pregunta, por favor, no deje de interrogar al Personal Técnico que le realiza la exploración, o al investigador responsable.

Los detalles del proyecto de investigación y su finalidad me han sido explicados por el Dr/Dra.

Fdo. El Dr./Dra.

Consiento en la realización de este estudio

Fdo.

El estudio será realizado por el ATS/Técnico Sr./Sra. _____

_____, que firma como testigo de que el paciente

ha sido debidamente informado y que consiente libremente en la realización de esta RM.

Barcelona, con fecha _____

Se solicita un examen de Resonancia Magnética (RM) para su evaluación y diagnóstico. Esta exploración se consigue mediante la conjunción de un fuerte campo magnético, ondas de radiofrecuencia i un ordenador para reproducir las imágenes. En esta tecnología no se utilizan radiaciones ionizantes (RX) ni material radioactivo.

La Resonancia Magnética es una exploración no agresiva que no comporta efectos secundarios al organismo. Por ello, le pedimos que conteste a las siguientes preguntas marcando con una "X" la respuesta adecuada:

		si	no
Marcapasos cardíaco			
Cirugía previa: aneurisma o bypass intracraneal			
Prótesis de válvula cardíaca			
Prótesis de oído medio			
Prótesis articular o miembro artificial			
Fragmentos de metal, metralla o bala en su organismo			
Ha tenido traumatismos oculares	(1)		
Actualmente embarazada o madre lactante	(2)		
Lleva cualquier objeto metálico o magnético integrado en su cuerpo			

(1) Si ha habido traumatismos oculares con duda de material metálico ocular, solicitar Rx de órbitas.

(2) En caso de embarazo, tiempo de gestación

Otras complicaciones, si bien poco frecuentes, son la aparición de hematomas en el lugar de la punción, o incluso una trombosis u obstrucción de una arteria que podría requerir una intervención quirúrgica urgente.

Deberá entrar en la sala de exploraciones sin objetos metálicos, joyas, gafas, maquillaje, puentes metálicos no fijos, tarjetas de crédito o magnéticas i deberá permanecer inmóvil durante el tiempo que el personal facultativo le indicará.

Pregunte cualquier duda. Nuestro personal médico y de enfermería le atenderán en todo momento.

Nombre: _____

Fecha: _____

Firma,
Enterado y conforme

CONSENTIMIENTO INFORMADO

Título del estudio: “Mecanismos de neuroplasticidad en el envejecimiento sano revelada mediante el uso de la estimulación magnética transcraneal (EMT) con neuronavegación: Impacto de las diferencias individuales en medidas de reserva cognitiva”

Yo, (nombre del participante):

He leído la hoja de información general que se me ha entregado.
He leído las hojas de información sobre la EMT y entiendo los riesgos que puede tener.
He podido hacer preguntas sobre el estudio
He recibido suficiente información sobre el estudio
He recibido respuesta satisfactoria a mis preguntas
He hablado con (nombre del investigador):

Comprendo que mi participación es voluntaria
Comprendo que puedo retirarme del estudio:
1. Cuando quiera
2. Sin tener que dar explicaciones
3. Sin que esto repercuta en mis cuidados médicos

Consiento que los datos obtenidos para este proyecto sean almacenados de forma anónima para su posible uso en futuros proyectos aprobados por el comité ético (CEIC) del centro (de lo contrario, éstos serán destruidos tras la realización de las determinaciones previstas en este estudio).

Consiento que los posibles resultados obtenidos con mi participación en el estudio sean fuente de publicaciones científicas, siempre que se vele por mi completo anonimato.

Presto libremente mi conformidad para participar en el estudio clínico, de estimulación no invasiva, cognitivo y radiológico.

Firma del participante:

Firma del investigador:

Lugar y fecha:

